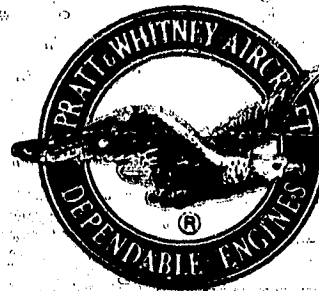


# STUDY OF CAVITATING INDUCER INSTABILITIES

FINAL REPORT



(NASA-CR-123939) STUDY OF CAVITATING  
INDUCER INSTABILITIES Final Report, 1  
Jul. 1971 - 15 May 1972 W.E. Young, et  
al (Pratt and Whitney Aircraft) 31 Aug.  
1972 163 p

N73-13299

CSSL 20D

G3/12

Unclas  
50895

For  
George C. Marshall Space Flight Center  
National Aeronautics and Space Administration  
Marshall Space Flight Center, Alabama 35812

**Pratt & Whitney Aircraft** DIVISION OF UNITED AIRCRAFT CORPORATION

U  
A.

## CONTENTS

SECTION	PAGE
LIST OF ILLUSTRATIONS . . . . .	v
LIST OF TABLES . . . . .	x
FOREWORD . . . . .	1
ABSTRACT . . . . .	1
SUMMARY . . . . .	1
1. INTRODUCTION . . . . .	3
2. REVIEW OF PREVIOUS WORK . . . . .	5
2.1 Experimental Observations . . . . .	5
2.2 Modeling Attempts . . . . .	10
2.3 Discussion of Previous Results . . . . .	11
3. APPROACH TO INSTABILITY ANALYSIS . . . . .	14
3.1 Mechanisms That Cause Instabilities . . . . .	14
3.2 Definition of Required Experimental Data . . . . .	18
4. EXPERIMENTS . . . . .	19
4.1 Cascade Experiment . . . . .	19
4.1.1 Facility . . . . .	19
4.1.2 Cascade Configuration . . . . .	23
4.1.3 Instrumentation . . . . .	25
4.1.4 Test Procedure . . . . .	27
4.1.5 Data Reduction . . . . .	29
4.1.6 Test Results . . . . .	30
4.2 Inducer Experiment . . . . .	40
4.2.1 Facility . . . . .	40
4.2.2 Inducers . . . . .	44
4.2.3 Instrumentation . . . . .	46
4.2.4 Test Procedure . . . . .	47
4.2.5 Data Reduction . . . . .	51
4.2.6 Test Results . . . . .	53
5. ANALYSIS AND DATA CORRELATION . . . . .	77
5.1 Cavitation Cavity Geometry . . . . .	77
5.1.1 Analytic Model . . . . .	77
5.1.2 Correlation of Cavity Model Predictions and Refinements of Model . . . . .	79

## CONTENTS (Continued)

SECTION	PAGE	
5.2	Cascade Tunnel Instability . . . . .	89
5.2.1	Analytic Model . . . . .	89
5.2.2	Comparison of Cascade Instability Predictions to Test Results . . . . .	100
5.3	Inducer Instabilities . . . . .	103
5.3.1	Analytic Model . . . . .	103
5.3.2	Model Predictions . . . . .	115
5.3.3	Correlation of Model Predictions With Test Results . . . . .	118
5.3.4	Parametric Effects of System Variables on Stability . . . . .	130
5.4	Simplified Inducer System Model . . . . .	135
6.	CONCLUSIONS AND RECOMMENDATIONS . . . . .	141
6.1	Conclusions . . . . .	141
6.2	Recommendations . . . . .	141
7.	REFERENCES . . . . .	143
	APPENDIX - Nomenclature . . . . .	145
	DISTRIBUTION LIST . . . . .	149

## ILLUSTRATIONS

FIGURE		PAGE
1	Cavity Response to Flowrate; Continuity De-stabilizing Mechanism Above Head Breakdown . . . . .	15
2	Path of "Continuity" Mechanism Oscillation . . . . .	15
3	Headrise Response to Flowrate; Performance De-stabilizing Mechanism Below Head Breakdown . . . . .	17
4	Path of "Performance" Mechanism Instability . . . . .	17
5	Water Cascade Tunnel . . . . .	20
6	Hydrofoil Cascade Installed in Water Tunnel . . . . .	21
7	Cascade Test Section . . . . .	22
8	Cascade Configuration . . . . .	24
9	Cascade Hydrofoil . . . . .	25
10	View of Left Side of Hydrofoil Cascade . . . . .	26
11	View of Right Side of Hydrofoil Cascade . . . . .	26
12	Cascade Cavitation Looking at Hydrofoil Profiles - Incidence = 0.28 rad (16 deg), Velocity $\approx$ 6.56 m/s (21.5 ft/sec) . . . . .	33
13	Cascade Cavitation Looking at Top of Cascade - Incidence = 0.28 rad (16 deg), Velocity $\approx$ 6.56 m/s (21.5 ft/sec) . . . . .	34
14	Typical Cascade Tunnel Dynamic Pressure Oscillographs . . . . .	37
15	Variation of Cascade Dynamic Pressure Data With Cavitation Number . . . . .	39
16	Inducer Test Loop . . . . .	41
17	Accumulator System Schematic . . . . .	42
18	Inducer Test Rig . . . . .	43
19	Inducer Installed in Test Facility . . . . .	43
20	Definition of Inducer Leading Edge Sweepback Angle . . . . .	44
21	Inducer with 0.28 rad (16 deg) Leading Edge Sweepback . . . . .	45
22	Inducer Pressure Instrumentation Locations . . . . .	46
23	Data Tape Analyzer System . . . . .	53
24	Noncavitating Inducer Performance . . . . .	56
25	Cavitating Performance, Radial Leading Edge Inducer . . . . .	58

ILLUSTRATIONS (Continued)

FIGURE		PAGE
26	Cavitating Performance, 0.28 rad (16 deg) Swept Leading Edge Inducer . . . . .	58
27	Normalized Cavitating Performance, Radial Leading Edge Inducer . . . . .	59
28	Normalized Cavitating Performance, 0.28 rad (16 deg) Swept Leading Edge Inducer . . . . .	59
29	Oscillograph Tracing Typical of Inducer Instability; Test 8.04, 513.1 rad/s (4900 rpm), $\bar{\phi} = 0.090$ , $\bar{k} = 0.038$ . . . . .	61
30	Inducer Discharge Dynamic Pressure Spectrum Plots; Radial Leading Edge, $\bar{\phi} = 0.070$ (Test 8.06) . . . . .	62
31	Inducer Discharge Dynamic Pressure Spectrum Plots; Radial Leading Edge, $\bar{\phi} = 0.084$ (Test 8.05) . . . . .	63
32	Inducer Discharge Dynamic Pressure Spectrum Plots; Radial Leading Edge, $\bar{\phi} = 0.084$ (Test 8.08) . . . . .	64
33	Inducer Discharge Dynamic Pressure Spectrum Plots; Radial Leading Edge, $\bar{\phi} = 0.090$ (Test 8.04) . . . . .	65
34	Inducer Discharge Dynamic Pressure Spectrum Plots; Radial Leading Edge, $\bar{\phi} = 0.090$ (Test 8.07) . . . . .	66
35	Inducer Discharge Dynamic Pressure Spectrum Plots; Swept Leading Edge, $\bar{\phi} = 0.070$ (Test 8.11) . . . . .	67
36	Inducer Discharge Dynamic Pressure Spectrum Plots; Swept Leading Edge, $\bar{\phi} = 0.084$ (Test 8.10) . . . . .	68
37	Inducer Discharge Dynamic Pressure Spectrum Plots; Swept Leading Edge, $\bar{\phi} = 0.090$ (Test 8.09) . . . . .	69
38	Inducer Inlet Dynamic Pressure Spectrum Plots; Typical Points . . . . .	70
39	Variation of Inducer Discharge Dynamic Pressure Data With Cavitation Number, Radial Leading Edge . . . .	71
40	Variation of Inducer Discharge Dynamic Pressure Data With Cavitation Number, 0.28 rad (16 deg) Swept Leading Edge . . . . .	72
41	Comparison of Relatively Deaerated With Non- deaerated Dynamic Pressure Data, Radial Leading Edge . . . . .	74
42	Variation of Inlet Tip Prerotation With Cavitation Number, Radial Leading Edge Inducer . . . . .	75

ILLUSTRATIONS (Continued)

FIGURE		PAGE
43	Variation of Inlet Tip Prerotation With Cavitation Number, 0.28 rad (16 deg) Swept Leading Edge Inducer . . . . .	76
44	Distinct Vapour Cavity on Inducer Blade Suction Surface . . . . .	78
45	Cavitation Cavity Profile . . . . .	78
46	Comparison of Cavity Height Predictions With Exact Predictions; Ideal Hydrofoil Cascade, $i = 0.78$ rad (16 deg) . . . . .	80
47	Comparison of Cavity Height Predictions With Exact Predictions, Ideal Inducer Cascade . . . . .	80
48	Comparison of Cavity Height Predictions With Cascade Test Data . . . . .	81
49	Comparison of Cavity Length-to-Maximum Height Predictions With Exact Predictions; Ideal Hydrofoil Cascade, $i = 0.78$ rad (16 deg) . . . . .	83
50	Comparison of Cavity Length to Maximum Height Predictions With Exact Predictions, Ideal Inducer Cascade . . . . .	84
51	Flow Separation Downstream of a Backward Facing Step (Data From Abbott and Kline). . . . .	84
52	Flow Separation Data Compared With Empirical Cavity Collapse Function . . . . .	85
53	Comparison of Cavity Profiles for an Inducer Cascade ( $\beta^* = 0.15$ rad, 8.83 deg; $i = 0.07$ rad, 3.8 deg) . . . . .	86
54	Comparison of Cavity Length Predictions With Inducer Test Data, Tip Streamline . . . . .	87
55	Comparison of Cavity Length Predictions With Inducer Test Data; Midspan Streamline . . . . .	87
56	Comparison of Cavity Length Predictions With Cascade Test Data . . . . .	88
57	Predicted Suction Surface Cavity Volume, Radial Leading Edge Inducer . . . . .	89
58	Measured Effect of Sweep Angle on Inducer Cavity Length . . . . .	90
59	Cascade Tunnel Dimensions . . . . .	91
60	Cascade Instability Model . . . . .	92
61	Cascade Cavity Relationships . . . . .	96

ILLUSTRATIONS (Continued)

FIGURE		PAGE
62	Cascade Pressure Drop Ratio Curves (Cavitating/Noncavitating) . . . . .	98
63	Cascade Pressure Drop Ratio, Cavitating to Noncavitating . . . . .	101
64	Dimensions of Inducer Water Loop . . . . .	104
65	Schematic of Inducer Loop Dynamic Model . . . . .	105
66	Discharge Throttling Valve Linear Resistance, Radial Inducer . . . . .	108
67	Pressure Gains; Radial Leading Edge Inducer . . . . .	112
68	Flow Gains, Radial Leading Edge Inducer . . . . .	113
69	Internal Resistance, Radial Leading Edge Inducer . . . . .	113
70	Pressure Compliance, Radial Leading Edge Inducer . . . . .	114
71	Flow Compliance, Radial Leading Edge Inducer . . . . .	115
72	Definitions of Damping Ratio and Natural Frequency in the Complex Plane . . . . .	116
73	Linear Model Predictions of Inducer Loop Oscillatory Characteristics With No Head Falloff; Radial Leading Edge Inducer; $\bar{\phi} = 0.070$ . . . . .	119
74	Linear Model Predictions of Inducer Loop Oscillatory Characteristics With No Head Falloff; Radial Leading Edge Inducer; $\bar{\phi} = 0.084$ . . . . .	120
75	Linear Model Predictions of Inducer Loop Oscillatory Characteristics With No Head Falloff; Radial Leading Edge Inducer; $\bar{\phi} = 0.090$ . . . . .	121
76	Linear Model Predictions of Inducer Loop Ramping Characteristics, Radial Leading Edge Inducer. . . . .	122
77	Comparison of Inducer Instability Predictions With Test Results, $\bar{\phi} = 0.070$ . . . . .	123
78	Comparison of Inducer Instability Predictions With Test Results, $\bar{\phi} = 0.084$ . . . . .	124
79	Comparison of Inducer Instability Predictions With Test Results, $\bar{\phi} = 0.090$ . . . . .	125
80	Location of Trapped Air Pocket . . . . .	127
81	Pipe Section at Trapped Air Pocket . . . . .	128
82	Effect of Trapped Air On Oscillatory Predictions; Radial Leading Edge Inducer; $\bar{\phi} = 0.084$ , $\bar{k} = 0.16$ . . . . .	128

ILLUSTRATIONS (Continued)

FIGURE		PAGE
83	Effect of Pressure Compliance on Oscillatory Predictions; Radial Leading Edge Inducer; $\bar{\phi} = 0.084$ , $\bar{k} = 0.16$ .....	129
84	Effect of Line Inertances on Oscillatory Predictions; $\bar{\phi} = 0.084$ , $\bar{k} = 0.16$ .....	130
85	Effect of Flow Compliance on Oscillatory Predictions; Radial Leading Edge Inducer; $\bar{\phi} = 0.084$ , $\bar{k} = 0.16$ .....	131
86	Effect of Pressure Gain on Oscillatory Predictions; Radial Leading Edge Inducer; $\bar{k} = 0.04$ .....	132
87	Effect of Flow Gain on Oscillatory Predictions; Radial Leading Edge Inducer; $\bar{k} = 0.04$ .....	133
88	Effect of Flow Gain on Ramping Predictions; Radial Leading Edge Inducer; $\bar{k} = 0.04$ .....	134
89	Effect of Inlet Line Compliance on Oscillatory Predictions; Radial Leading Edge Inducer, $\bar{\phi} = 0.084$ ...	135
90	Simplified Inducer System Model .....	136
91	Graphical Representation of System Parameters .....	138
92	Spring-Mass-Damper System .....	139

## TABLES

TABLE		PAGE
1	Cascade Features .....	24
2	Cascade Test Points .....	31
3	Measured Cavity Lengths and Heights .....	35
4	Cascade Dynamic Pressure Data and Observed Cavity Motion .....	38
5	Inducer Design Parameters .....	45
6	Inducer Test Instrumentation .....	48
7	Summary of Inducer Test Points .....	54
8	Blade and Flow Angles for Inducer Measurement Streamlines .....	88
9	Values of Inducer Loop Inertance, Compliance, and Resistance .....	107
10	Inducer Representation in Dynamic Model .....	109
11	Noncavitating Values of Damping Ratio and Natural Frequency, Radial Leading Edge Inducer .....	117

## FOREWORD

This report documents the work conducted under Contract NAS8-27026, "Study of Cavitating Inducer Instabilities," during the period 1 July 1971 through 15 May 1972. The work was sponsored by the George C. Marshall Space Flight Center, National Aeronautics and Space Administration, Marshall Space Flight Center, Alabama, and was administered technically by Mr. H. P. Stinson, Jr.

Pratt & Whitney Aircraft's Florida Research and Development Center at West Palm Beach, Florida, was the contractor, and Mr. W. E. Young was the Program Manager. All work was performed at PRDC with the exception of the cascade tests, which were conducted at United Aircraft Research Laboratories, East Hartford, Connecticut, by Mr. W. E. Taylor. Inducer tests were conducted by Mr. A. E. Wemmell.

## ABSTRACT

An analytic and experimental investigation into the causes and mechanisms of cavitating inducer instabilities was conducted. Hydrofoil cascade tests were performed, during which cavity sizes were measured. The measured data were used, along with inducer data and potential flow predictions, to refine an analysis for the prediction of inducer blade suction surface cavitation cavity volume. Cavity volume predictions were incorporated into a linearized system model, and instability predictions for an inducer water test loop were generated. Inducer tests were conducted and instability predictions correlated favorably with measured instability data.

## SUMMARY

An analytic and experimental investigation into the causes and mechanisms of cavitating inducer instabilities was conducted. Two possible instability mechanisms were analytically identified: (1) a "continuity" mechanism that results from the response of inducer cavitation volume to inlet flowrate; and (2) a "performance" mechanism that results from the relationship of inducer headrise to inlet flowrate in the cavitating head falloff region of operation. The continuity mechanism requires only the presence of flowrate-sensitive inducer cavitation for an instability to be possible, and this mechanism can cause instabilities at relatively high cavitation numbers where there is no head falloff (i.e., in the usual range of inducer operation). The performance mechanism is operable in the head falloff region. An analytic system model, in which the inducer and its system are treated as a series of lumped resistances, inertances, and compliances, can predict the occurrence of both types of instabilities. The model consists of a series of equations that define (1) the inlet and discharge line: resistances, inertances, and compliances; and (2) the inducer: cavitating head vs inlet pressure and flow curves (head falloff map), head vs flow curves (head flow map), and cavitation volume vs pressure and flow curves (cavitation volume map). The rate of change of cavitation volume with inlet pressure is defined as "pressure compliance" and the rate of change of cavitation volume

with flowrate is defined as "flow compliance." The most significant parameters, and the most difficult to accurately define with regard to "continuity" instabilities, are pressure compliance and flow compliance. "Performance" type instabilities require definition of the head falloff map, which can usually be obtained through the use of parameter measured data from similar inducers.

Two experiments were conducted: (1) a cascade experiment whose objective was to obtain measured cavity geometry data for refinement of inducer blade suction surface cavitation volume prediction (pressure compliance and flow compliance); and (2) an inducer experiment whose objective was to provide data for substantiation of the analytic instability predictions technique. Results of the cascade experiment were largely inconclusive because of apparent flow nonuniformities. Cavity volume predictions, therefore, were correlated and refined using limited inducer measured data and potential flow predictions. The inducer experiment resulted in the measurement of "continuity" and "performance" instabilities whose characteristics correlated with linear inducer system model predictions in all significant areas. Agreement between predicted and measured frequency magnitude was poor, but measured frequencies were known to be affected by system compliances that were not accounted for in the prediction analysis. Such compliances were of sufficient magnitude to explain the difference in frequencies. The analytic model of the inducer system indicated that "flow compliance" was the most significant parameter with regard to system stability. If the inducer had no flowrate sensitive cavitation, it would have been predicted to be stable regardless of the value of other parameters.

It was concluded that the analytically derived instability mechanisms explain the instabilities encountered in the inducer test program. The analytic technique employed can be generally used to predict instabilities and define stabilizing system changes.

## SECTION 1 INTRODUCTION

Inducers are widely used in liquid rocket engine propellant feed systems to increase propellant pressure before the propellant enters the main turbopumps. The turbopumps are thereby permitted to operate at relatively high rotational speeds with sufficient inlet pressure to preclude cavitation performance loss. The inducers themselves operate with significant cavitation, but they are designed such that the effect of cavitation on overall inducer-turbopump system pressure rise and efficiency are minimal.

The existence of cavitation in the feed system raises the possibility that "self-induced instabilities" may occur. These instabilities are characterized by oscillations in inducer inlet and discharge pressure which can, if their amplitude is sufficiently large, result in unacceptable variations in engine thrust because of their effect on propellant flowrate. Such oscillations have been observed during inducer and vehicle system tests by a number of investigators, and their occurrence has been generally linked to inducer blade suction surface cavitation; however, there has been little success in developing an analytic method for predicting the occurrence of an instability or for the definition of system changes that would be required to avoid instabilities.

The objective of this program was to develop an analytical system capable of predicting the occurrence of self-induced instabilities in cavitating inducers. The technical effort consisted of four phases, the scope of which can be described as follows:

- I. Review of Existing Models - Literature concerning instability models was reviewed and the most promising approach selected.
- II. Design of Experiments - Two experiments were designed: A two-dimensional cascade experiment to provide measured cavitation cavity geometry data as a function of incidence angle and inlet pressure, and rotating inducer experiment to provide measured instability data over a range of operating points.
- III. Conduct Experiments - The experiments planned in Phase II were conducted.
- IV. Data Correlation - Cavity geometry data from the cascade tests was correlated with analytic predictions from the cavity model of (1)\*, and the model was refined as indicated. The developed cavity model was used, in conjunction with a system model, to predict the unstable operating region of an inducer.

The program results indicate that an analytic system modeling technique that accounts for (1) inducer inlet and discharge line characteristics, (2) inducer head rise as a function of cavitation number and flow coefficient, and (3) inducer

\*Underlined numbers in parentheses denote references, which are listed in Section 7 on page 143.

blade suction surface cavity volume as a function of cavitation number and flow coefficient can predict the occurrence of an instability, and the technique can be used to define stabilizing system changes. Results are reported in detail in the following sections.

## SECTION 2 REVIEW OF PREVIOUS WORK

A literature survey was conducted to identify reported instances of instability and related modeling attempts. Literature pertinent to both rotating inducer and stationary tunnel tests was reviewed because apparently similar instabilities have been noted in both. Because of flow similarities between inducer and cascade flows, it seemed likely that a modeling approach that would explain inducer instabilities would also be adaptable to two-dimensional water tunnel instabilities. Verification of this similarity would demonstrate that the fluid dynamic effects that lead to an instability are understood and can be adequately modeled, increasing the degree of confidence in the inducer instability model.

The literature that was found in the survey is listed in References (2) through (22). The reported experimental observations and modeling attempts are summarized in the following sections, after which our conclusions are discussed.

### 2.1 EXPERIMENTAL OBSERVATIONS

Cavitation-induced oscillations in water tunnel tests of a single hydrofoil were reported by Wade and Acosta (2) who studied the growth of cavitation on a plano-convex hydrofoil as inlet pressure was lowered. They were the first investigators to report frequencies and amplitudes during unstable cavitation on a hydrofoil. They observed that the cavitation cavity, which began at the hydrofoil leading edge on the suction side, was steady and that measured hydrofoil normal force amplitudes were small whenever cavity length was less than about 60% of chord length. With further lowering of inlet pressure the characteristic low frequency, large amplitude cavitation-induced oscillations began. With still further lowering of inlet pressure the oscillations persisted, with hydrofoil force and cavity length amplitudes first increasing and then decreasing, until the cavity reached a length of about 120% chord. At lower inlet pressures and longer cavities the flow became quite steady. Cavity length oscillations reached a peak-to-peak amplitude of about 1/2 chord, with hydrofoil force varying  $\pm 10\%$  of mean value in phase with the cavity. The instabilities occurred in a region where hydrofoil mean lift and drag forces first increased, then decreased as inlet pressure was lowered. Typical frequencies found were about 12 to 25 Hz, depending upon tunnel speed, angle of attack, and cavitation number. Two regions of high frequency (270 Hz and 50-60 Hz), low amplitude "noise" were also found, but these do not appear to have a direct bearing on the instability presently in question. During one cycle of oscillation, the cavity was seen to grow smoothly from its minimum length until, as it approached the hydrofoil trailing edge, a reentrant jet formed and began to gradually fill the rearward portion of the cavity. The cavity surface became irregular and a large volume of cavity was abruptly shed into the stream. The cycle then repeated. No mention is made of tip vortex cavitation, nor is any appreciable amount discernible in the photographs.

Kaplan and Lehman (3) investigated cavitation on a semiwedge hydrofoil mounted in a 2-degree of freedom suspension in a water tunnel, finding that "for cavity lengths in the range from 0.5 to 1.0 chord the cavity itself becomes unstable and severe fluctuations occur in the entire system." The surface

cavity began at the hydrofoil leading edge. The hydrofoil was cantilevered from one end (essentially flush with tunnel wall) while the other end protruded into the freestream. Tip vortex cavitation occurred on the free end, and "---appears to be independent of the cavity on the foil upper surface." A trace of hydrofoil rotational and translational motion at one operating point (cavity length of 75% chord) indicates a frequency of oscillation of 8 Hz. No data are presented that would allow a comparison of the unstable region with the hydrofoil lift breakdown point.

Bosch (4) tested a semiwedge hydrofoil mounted in a 2-degree of freedom suspension in a water tunnel, finding that oscillations in cavity length, with amplitudes as much as 25% chord, occurred when the cavity was between 40 and 140% chord length. Frequency of oscillation varied from 4 to 18 Hz, decreasing as cavity length increased. The cavity sprang from the hydrofoil leading edge. No mention is made of tip vortex cavitation, nor of how the unstable region compared to the hydrofoil lift breakdown point.

Wade and Acosta (5) experimented with two-dimensional cascades of 3 to 5 plano-convex hydrofoils in a water tunnel and found an instability similar to that reported for the single hydrofoil of the same shape (2). They were the first to experiment with a cascade far enough into the cavitating region to uncover unstable cavitation. When the cavities, which extended from the blade leading edges, became about 1/3 chord in length, periodic oscillations of the cavities and static pressure upstream of the cascade occurred. With further reduction of tunnel pressure the cavities became longer than the chord, and oscillations ceased. Static pressure oscillations reached an amplitude of about 1/2 the approaching velocity head at a frequency of about 12 Hz. Wade and Acosta note that there was "---some time lag in the development of oscillating cavitation from one vane to the next ---." Presumably this means that the cavities on some hydrofoils began to oscillate at higher values of tunnel pressure than the others. It is not stated whether the cavities oscillated in phase once they all began to oscillate. The only reference to tip vortex cavitation is a statement that "--- noticeable tip clearance cavitation---" occurred. No mention is made of a propagating cavitation pattern. The data indicate that the instabilities occurred at or after cascade lift breakdown began.

Wade and Acosta (6) investigated another cavitating cascade to study instabilities. They measured the amplitudes and phase angles of the cascade lift and drag forces and of pressures and velocities upstream and downstream of the cascade. Motion pictures were made of the cavity oscillations. Both a surface cavity springing from the leading edge and tip vortex cavities at each end of the hydrofoil were formed. Oscillations began when the cavities became approximately 50% chord in length, and affected all measured parameters. "This oscillating or chugging mode of cavitation persists and grows more intense as the pressure is lowered until the maximum length of the cavity bubble formed during the oscillation cycle is approximately 15 to 20% longer than the chord of the hydrofoil. At this time the fluctuations in lift and pressure throughout the cascade are greatest. Then with a slight, but still further decrease in pressure, the cavities become considerably longer than the chord and the oscillations cease entirely---." Frequencies found were from 8 to 20 Hz. From high speed motion pictures an attempt was made to detect any propagating phenomenon that might be responsible for the observed instabilities. The authors state "-- after many repeated viewings of these motion pictures we could not conclude that there was a progressive disturbance across the cascade in the sense of a propagating stall

which is responsible for the instability that is observed." The data indicate that the instabilities occurred in a band around the point where cascade lift breakdown occurs.

Taylor, Murrin and Columbo (7) investigated the performance and point of incipient cavitation of a cascade of double circular-arc hydrofoils, and noted a propagating form of cavitation. Photographs show a single irregular-shaped surface cavity propagating along the cascade. Propagation velocity was approximately 3 m/s (10 ft/sec). There was no visible tip vortex cavitation. The authors attribute the phenomenon to nonuniform inlet conditions, and state: "when the inlet flow nonuniformity was less severe ---, the cavitation did not propagate and the bubble size changed simultaneously on all hydrofoils." The reference to simultaneous change refers to change when inlet pressure was changed, since the investigation did not go sufficiently far into the cavitating region for a severe cavitation-induced oscillation to have occurred.

Acosta (8) reported cavity oscillations on a four-bladed helical inducer with radial leading edges. He found that as inlet pressure was lowered a "patch of cavitation" with a "frosty appearance," formed at the blade tip. Photographs show the cavitation originating near the leading edge on the blade suction side. Acosta states that the "--greatest part of the fuzzy cavitation patch arises from a tip clearance flow--" and "-- is confined largely to the outer portions of the annulus, but at the lowest cavitation numbers it does occur from root to tip." At low inlet pressure the cavities formed only on alternate blades, but not always on the same blades. At high flowrates the alternate blade cavitation pattern was stable. At flowrates lower than the best efficiency point the alternate blade cavitation appeared to propagate from blade to blade, with the frequency of propagation decreasing as inlet pressure was lowered and decreasing to zero just before head breakdown of the inducer. No numerical oscillation amplitudes or frequencies were reported. Three modifications to the inducer were made in an attempt to suppress the oscillations. Increasing the tip clearance offered some help; sweeping back the blade leading edge depressed the occurrence to lower cavitation numbers; and using a variable head helix (0.1 to 0.16 rad, 6 to 9 deg) greatly reduced the extent and severity of the oscillating mode. In a discussion of (8) by Iura, observations are presented of alternate blade cavities on four-bladed inducers which began to oscillate in length as cavitation number was lowered. In one instance a rotating propagation pattern at one-tenth rotor speed was observed. The oscillations are reported to have ceased once head breakdown occurred.

Wood (9) visually noted cavity oscillations in three different mixed flow impellers. In one, a three-bladed model, a low frequency (18 Hz) oscillation of the cavity formed at the impeller inlet occurred. In the other two impellers, with four blades and eight blades each, higher frequency (42 to 175 Hz) oscillations occurred in cavitation formations in the rear channels. The rear channel cavitation extended across much of the channel, for some conditions completely filling the channel, and appeared to be unrelated to the "leading edge cavitation formations." Wood states that rear channel cavitation was "instigated by the tip cavitation vortexes." No description of the leading edge cavitation is given. Wood does not mention alternate blade cavitation nor circumferential propagation, but notes that he had a limited field of vision. It may be of significance that the low frequency impeller inlet cavity oscillations (18 Hz) occurred when the impeller was operating at an NPSH above that at which head breakdown begins, while the

high frequency rear channel oscillations (42 to 175 Hz) occurred below the head breakdown point.

Badowski (10) discussed an instability occurring in four-bladed inducers. He found that at reduced flowrates and a certain value of NPSH the four-blade cavitation pattern makes a sudden transition to cavitation only on alternate blades. Additional reduction of NPSH causes cavities to reestablish on the two noncavitating blades. An instability occurs when the reestablished cavities reach one blade spacing in length. No description of a cavity is given although reference to a surface cavity model is made. He states that two instabilities have been experienced when the two reestablished cavities are unequal in length, one instability occurring each time a cavity grows to a length of one blade spacing. By reducing NPSH so that the cavities become longer than one blade spacing stable flow was generally restored. The instability is described as "low frequency, high amplitude vibration," with no numerical values quoted. No mention is made of a propagating pattern. The instability is reported as occurring in a band of NPSH immediately prior to head breakdown, with the flow stable in the head breakdown region. Badowski attributes the instability to the existence of "backflow-induced pre-rotation" in the inlet line.

Etter (11) reported cavitation instabilities on two- and three-bladed inducers designed to operate with blade cavities longer than chord length (supercavitating). Only the supercavitating region was investigated. Instabilities were found when the two-bladed model was operated at flow coefficients below 0.090 and the cavity lengths became less than about 240% of chord. Instabilities were found when the three-bladed model was operated at flow coefficients below 0.075 and the cavity lengths became less than about 180% of chord. In both cases the cavities extended back to or slightly past the leading edge of adjacent blades when the instabilities occurred. Flow was stable for shorter cavities. Each blade cavity consisted of a suction surface cavity springing from the leading edge and a tip vortex cavity said to be of equal length, which sometimes merged with the leading edge cavity. Observed instabilities were described as "large magnitude, low frequency" oscillations in cavity length, with no numerical values given. It was noted that cavities on the two-bladed model were of equal length, while cavities on the three-bladed model were of unequal lengths, by as much as 20% but usually less than 10%, over a large operating region. In most instances two cavities were of one length and the third shorter or longer. In a few instances all three were different. The pattern could not be predicted to occur on any particular blades, and it was concluded that the phenomenon was not caused by geometry deviations among the blades. The region of observed instabilities seemed to have no particular relationship to the region of unequal cavity lengths. It is not stated whether the cavities oscillated in unison. The instabilities occurred when the inducers were operating in the head breakdown region.

Hartmann and Soltis (12) made observations of cavitation in an axial flow pump with 19 blades. They found that in addition to blade surface cavitation a large part of the total vapor cavity resulted from tip vortex cavitation. At low inlet pressure and low flow coefficients both vapor formations were observed to be unstable, with the tip vortex cavity fluctuating between a position close to the blade and a considerable distance away. At still lower flowrates the cavitation moved "in and out of the blade passage" such that at one instance the passage was almost free of cavitation and at another almost filled with vapor. No numerical values are given and no mention is made whether all blade passages were acting in unison.

Mildebrand (13) reported cavitation-induced oscillation of the J2 engine oxidizer pump during engine firing tests. Frequency, as determined by static pressure probes, varied from 14 to 24 Hz depending upon engine operating point and NPSH. Pump inlet and discharge pressures reached peak-to-peak amplitudes of approximately  $14 \text{ N/cm}^2$  (20 psi) while engine chamber pressure oscillated with a peak-to-peak amplitude of as much as  $7 \text{ N/cm}^2$  (10 psi). It is stated that as pump inlet pressure was lowered the oscillations, which began before the head breakdown point was reached, did not cease but the frequency decreased. Addition of a helium-filled accumulator near pump inlet reduced both the frequency and amplitude of oscillation. No observations of cavity formations were made. Previous tests of the same pump, reported in (14), had shown that the oscillations would cease if inlet pressure were lowered sufficiently. It is not stated in (13) whether inlet pressure was lowered to the same levels as in the earlier tests.

Soltis (15) investigated cavitation formations on two different three-bladed helical inducers and an axial flow pump with 19 blades. Both a surface cavity with a rather distinct closure point and a tip vortex cavity formed. It is stated that at low flowrates and low inlet pressures "--- cavitation of a highly unsteady nature is observed. Significant pressure oscillations occur within the system and are observed as cavitation pulsations within the blade passages. In general, this unsteady cavitation occurs when the cavity closure point reaches inside the passage formed with an adjacent blade." The tip vortex cavitation and the surface cavitation both followed the same pattern of fluctuation, which "-- is evidenced as a chugging movement of the cavity both in and out of the blade passage." This seems to imply that the cavities on all blades oscillated in unison. However, in references to a film strip of cavitation on an (unidentified) helical inducer it is stated, "Here, large amounts of vapor fill some of the blade passages, while the other passages are almost entirely vapor free. Closer analysis of the individual frames indicates that the full and empty blade passages occur in a regular pattern such that the cavitating zones rotate around the rotor at an angular speed lower than that of the rotor." And in reference to the axial flow pump (19 blades), "-- the vaporous regions have moved out ahead of the rotor and, again, flow conditions are such that these regions rotate around the annulus at a speed lower than the blade speed of the pump. A variation of flow from this operating point affects the speed of rotation of the cavitating zone about the annulus." No information on oscillation frequency or amplitude is presented. The instabilities are depicted as beginning before head breakdown begins. It is not stated whether stable operation is restored after head breakdown begins.

Miller and Gross (16) noted cavitation-induced oscillations during testing of a shrouded, hubless, helical inducer close-coupled to a centrifugal impeller in water and liquid nitrogen. "High-amplitude, low-frequency inlet and discharge pressure oscillations characteristic of cavitating pump inducer systems were observed at all lower than design flowrates. At design flowrates and higher, the low-frequency oscillations were observable; however, the amplitude was severely diminished." Oscillation frequency and amplitude were dependent upon inlet pressure and flowrate, with frequency varying from 4 to 12 Hz. Inducer inlet pressure reached a peak-to-peak amplitude of about  $24 \text{ N/cm}^2$  (35 psi). Both frequency and amplitude decreased as inlet pressure was lowered. No observations of cavity motion were made. The data presented indicate that the instabilities occurred prior to head breakdown.

## 2.2 MODELING ATTEMPTS

The reported models, employed to explain cavitation-induced oscillation in inducers, fall into the categories of rotating stall and system modeling. One attempt at employing a rotating stall analysis and three attempts at employing system modeling were made. None were satisfactorily correlated with test results. One attempt to model the instability in a cascade was made but agreement with test data was not achieved.

In a rotating stall analysis, originally developed for axial flow compressors, the only geometry considered is that of the inducer blading, with the inlet and discharge piping systems assumed to have no influence. Presence of a vapor cavity is not directly considered. The major feature of an instability is assumed to be a circumferential blade-to-blade variation or distortion in pressure and flowrate. Etter (11) used an analysis by Yeh (17) in an attempt to explain the instabilities encountered on the two-bladed and three-bladed supercavitating inducers. It was found that the predicted occurrence of an instability did not correlate, even trendwise, with the observed unstable operating regions. Etter concluded that it was unlikely that rotating stall was responsible for the observed "large magnitude low frequency instabilities."

In a system modeling approach all geometry is considered; the inducer blading as well as that of the inlet and discharge piping systems. Each element in the system is modeled individually and the equations are combined into a set of equations representing overall system motion. Stability is determined either from linear stability analysis techniques or by simulation on an analog computer, depending upon the form of the equations. The presence of blade cavities is directly considered through application of the law of continuity of mass to the fluid entering and discharging from the inducer. It is assumed that discharge flowrate can be different from inlet flowrate because total vapor cavity size can change. The major feature of an instability is assumed to be oscillation in inlet and discharge flowrates, with no variation in pressure and flowrate between any two blade passages. This implies that the cavities are equal in size and move in unison. The three reported modeling attempts have all neglected tip vortex cavitation, treating only the blade suction surface cavity.

Gross (18) modeled a shrouded, hubless, helical inducer close-coupled to a centrifugal stage operating in a water test facility. The facility exhibited low frequency (3 to 14 Hz) high amplitude (up to  $\pm 70\%$ ) inlet pressure oscillations over a wide range of inlet pressures and flowrates. Only the region above the head breakdown point was investigated. Both frequency and amplitude decreased as inlet pressure was lowered. A system model of the facility was programmed on an analog computer. Calculation of cavity volume was based on an assumed parabolic profile with the height computed from the Stripline and Acosta (19) two-dimensional cavity model and the length-to-height ratio based on an experimental point. The resulting model would not exhibit an instability.

Sack and Nottage (20) modeled a four-bladed helical inducer operating in a liquid oxygen test loop. The loop is stated to have been unstable, without specifying the exact operating region of instabilities. A typical frequency mentioned is 5 Hz, and discharge pressure oscillation is shown to have reached an amplitude of  $\pm 8 \text{ N/cm}^2$  ( $\pm 12 \text{ psi}$ ). A system model of the loop was programmed on an analog computer. Calculation of cavity volume was based on an assumed circular

arc profile tangent to the fluid incidence angle, with the height computed from the Stripling and Acosta cavity model (19). Operating regions both above and below the head breakdown point were investigated with the model. The model exhibited instabilities in both regions for certain bands of inlet pressure. The only correlation with test results presented are the statements that "frequencies and wave shapes were representative" and, "the real system as tested was observed to limit cycle when unstable. The simulation was noted to have a limit-cycling amplitude which also followed observed trends with cavitation number. The simulation had a limit-cycle amplitude higher than the test inducer and was unstable for a wider range of cavitation number."

A three-bladed helical inducer operating in a water loop was modeled in (21) on an analog computer. Calculation of cavity volume was based on the exact profile computed by the Stripling and Acosta cavity model (19). It is stated that the resulting system model was unstable, but work was terminated and no correlation with test results was presented.

Acosta (6) modeled a cascade in which unisonous cavity oscillations occurred. The details of the model were not presented, but it apparently was a system model. It is stated, "It is easy to show that the dynamic system consisting of the nozzle flow, the cavitating flow in the working section, plus some allowance for the inertia of the diffuser flow leads to a third order system that is inherently stable provided only that the total pressure loss due to cavitation in the working section increases as the ambient pressure decreases. Total pressure loss across the cascade was computed as a function of time from a knowledge of the instantaneous velocities and pressure levels upstream and downstream of the cascade. In this calculation the effect of the accelerating main stream from the point of measurement of the pressures was taken into account. This is a difficult calculation to make because of the spikiness of the velocity traces; these in turn caused large changes in pressure between the cascade and the reference point due to the large acceleration of the main stream. Nevertheless, it does appear that the total pressure loss is least when static pressure upstream of the cascade is greatest..."

### 2.3 DISCUSSION OF PREVIOUS RESULTS

Experimental observations of cavitation-induced oscillation reported in the literature do not present a completely clear picture of the phenomenon. The observations on individual hydrofoils (2, 3, 4) and cascades (5, 6) strongly indicate that the blade surface cavity is a major factor. However, Wood (9) and Hartmann and Soltis (12) indicate that additional cavity formations in the tip vortex or instigated by the tip vortex may also be involved. The hydrofoil and cascade tests indicate that unisonous cavity oscillations occur. However, some of the inducer tests show circumferentially propagating cavitation (8, 15), or alternate blade cavity oscillations (8, 10).

There could easily be more than one vapor cavity involved in the observed instabilities. In general, in both an inducer and a cascade, there will exist both a blade surface cavity springing from the leading edge and a tip vortex cavity. The tip vortex cavity generally forms at higher NPSH than the surface cavity. It is reasonable to assume that as NPSH is lowered the tip vortex cavity could form and begin to fluctuate in position (or form and detach) while the blade surface cavity remained steady or had not yet formed. This could occur because of the

different locations of the two cavities, being exposed to different parts of the flow field, and because of the different flow processes creating the cavities. However, a tip vortex cavity fluctuating in position is more likely to produce only random noise in pressure readings instead of the low frequency, high amplitude oscillations characteristic of cavitation-induced oscillation. At lower NPSII both the blade surface cavity and the tip vortex cavity grow and could both become factors in initiating cavitation-induced oscillation.

A key consideration, particularly when attempting to model the instability, is whether all cavities oscillate in unison when more than one blade is present. In the two-dimensional cascade tests Wade and Acosta (5) mention that high-speed motion pictures showed "--some time lag in the development of oscillating cavitation from one vane to the next--," but do not comment on blade-to-blade variations after all cavities began to oscillate. Had the cavities been oscillating significantly out of phase, or had a definite propagation pattern along the cascade occurred, it should have been evident from the high-speed motion pictures. In another series of cascade tests Wade and Acosta (6) searched for a propagating disturbance, but could not find one. We must conclude that a propagating disturbance was not responsible for the observed cascade instabilities. Taylor, et al (7) saw a single propagating cavity, but could attribute it to nonuniform cascade inlet conditions. The propagating cavity Taylor saw appears to be a distinct phenomenon from the instability observed by Wade and Acosta.

The single hydrofoil tests (in which propagation is not possible) and the cascade tests imply that propagation is not a major feature of cavitation-induced oscillation. However, such an inference is not so clearly made in the case of inducers. In testing a four-bladed helical inducer, Acosta (8) noted alternate blade cavitation that appeared to propagate from blade to blade. Iura (8) found alternate blade cavities on a four-bladed inducer, which oscillated in length, and in one instance propagated circumferentially. Soltis (15) noted circumferentially propagating cavitation on a helical inducer and on an axial flow pump with 19 blades. Badowski (10) found alternate blade cavitation on a four-bladed inducer, but instead of a propagation, he reports two instabilities, one occurring each time a blade cavity reached a length of one blade spacing. Badowski's observation is similar to the "time lag" noted by Wade and Acosta (5) in the case of a cascade. Etter (11) obtained unequal cavity lengths with a three-bladed inducer, but mentions neither a propagation nor a multiple instability. The other visual observers (9, 12) do not comment upon blade-to-blade variations.

There could easily be more than one phenomenon involved in the observed inducer instabilities. The propagating cavity found in the cascade tests of (7) indicates that it should be possible for circumferentially propagating distortion to produce a circumferentially propagating cavitation pattern. Under such circumstances only a local distortion of pressure and flowrate would be expected, with overall inducer flowrate unaffected. This may have been the instability seen by Acosta (8) and in one instance by Iura (8), but apparently was not the instability reported by Hildebrand (13). In the latter instance the engine chamber pressure oscillation indicates that overall oxidizer pump flowrate was affected by the instability. The propagating pattern reported in (8) and (15) may also be the result of the combination of two phenomena. Alternate blade cavitation may be the result of local zones of pressure and flowrate distortions rotating at rotor speed and related to backflow from the inducer. The unequal cavity lengths reported by Etter (11) on a three-bladed inducer probably have the same cause. Whatever

the mechanism of the phenomenon it was found not to favor any certain blades. If cavitation-induced oscillation occurs with the cavities moving in unison during alternate blade cavitation, then as the cavities collapse during one cycle of oscillation the tendency to re-form on the other two blades may be greater than the tendency to re-form on the same two blades. The combination of cavitation-induced oscillation and alternate blade cavitation could then appear as a circumferentially propagating cavitation pattern.

From consideration of the observed cavitation phenomena, it is concluded that modeling of cavitation-induced oscillation should consider as major features (1) a suction surface cavity starting at the leading edge of each blade, and (2) oscillation of these cavities in unison. Tip vortex cavitation caused by leakage flow through the blade tip clearance space should be considered of secondary importance in initial modeling. Propagating cavitation should be considered a different phenomenon from cavitation-induced oscillation.

Experimental evidence to support the above conclusions is scant, primarily because of the lack of a systematic investigation of cavitation formations and their relationship to instabilities. Oscillation of the blade surface cavity is the major feature mentioned in the individual hydrofoil tests (2, 3, 4), and in the cascade tests (5). In the inducer tests a surface cavity is either stated to be present (9, 11, 12, 15), implied to be present (8, 9, 10), or no visual observation was made (13, 16). There is no reported case of an instability in which it is known that there were no blade surface cavities.

The experimental evidence indicates that although there may be more than one mode of cavity motion - propagation as well as oscillation - the most likely mode occurring during most instances of low frequency, high amplitude cavitation-induced oscillation is that of nonpropagating oscillation with all cavities moving in unison. This is inferred from the individual hydrofoils tests in which no propagation is possible and from the absence of a propagation pattern in the cascade tests. The strongest evidence that propagation is not the major feature of the instability in question is the overall flowrate oscillation indicated by chamber pressure oscillations in (13). A purely propagating cavitation pattern would not be expected to cause an oscillation in overall inducer flowrate.

It is likely that tip vortex cavitation can influence stability and under certain conditions become an important factor. The presence of tip vortex cavitation during an instability was noted in the cascade tests (5, 11) and most of the inducer tests (8, 9, 11, 12). However, the tip vortex cavity was treated as a secondary consideration in this program because there exists no verified model for computing vapor volume of the tip vortex cavity. The only known published model is by Ghahremani (22). The influence of the tip vortex cavity can be estimated by the success in predicting instabilities when it is ignored, allowing an estimate of the level of effort which should be directed toward a tip vortex model.

## SECTION 3 APPROACH TO INSTABILITY ANALYSIS

After consideration of the reported descriptions of cavity motion during cavitation-induced oscillation in inducer, cascade, and hydrofoil tests, and of previous modeling attempts, we concluded that the system modeling approach offered the greatest potential for the prediction of instabilities. There is no evidence that rotating stall or blade-to-blade distortion (which are not considered in a system model) were significant factors in most known instances of cavitation-induced oscillation. The system modeling approach can, however, qualitatively explain all reported instances of instability and appears to be representative of the actual flow process.

### 3.1 MECHANISMS THAT CAUSE INSTABILITIES

Two basic mechanisms can create an instability under cavitating conditions:

1. The continuity mechanism, which results from the relationship of cavity volume to inducer inlet flowrate, and requires only the presence of cavitation cavities on the inducer blades for an instability to be possible.
2. The performance mechanism, which results from the relationship of inducer headrise to inlet flowrate, and requires that cavitation affect the inducer performance for an instability to be possible.

The first mechanism begins at a cavitation number well above head breakdown, and can be physically understood by considering that the blade suction surface cavity streamline constitutes a flow boundary. Since the streamline can change position in response to flowrate changes, it can be considered a movable wall. A momentary increase in flowrate reduces the fluid incidence angle, causing a reduction in cavity volume and a corresponding increase in the local space available for liquid. This is illustrated in figure 1. Continuity requires that inlet flowrate accelerate to fill the newly created liquid space, but this reduces incidence angle and causes a further collapse of the cavity. Inertia of the fluid mass in the inlet line causes the accelerating flowrate to be accompanied by a reduction in static pressure at the inducer inlet. The reduced inlet pressure acts to counter cavity collapse, since lower static pressure causes a cavity volume to increase, and at some point the static pressure reduction is sufficient to prevent further cavity collapse. Fluid inertia then causes an overshoot to a reverse trend, during which the increase in flowrate (with accompanying decrease in pressure) results in an increase in cavity volume. The flowrate increase is eventually halted and a deceleration begins with an accompanying increase in pressure. The deceleration continues back through the original operating point, where a decrease in flowrate causes an increase in cavity volume, and at some point the accompanying pressure increase causes the cavity to cease growing and begin to collapse again. Inertia causes an undershoot, the deceleration is halted, and the flowrate acceleration begins again. The path of oscillation is depicted in figure 2.

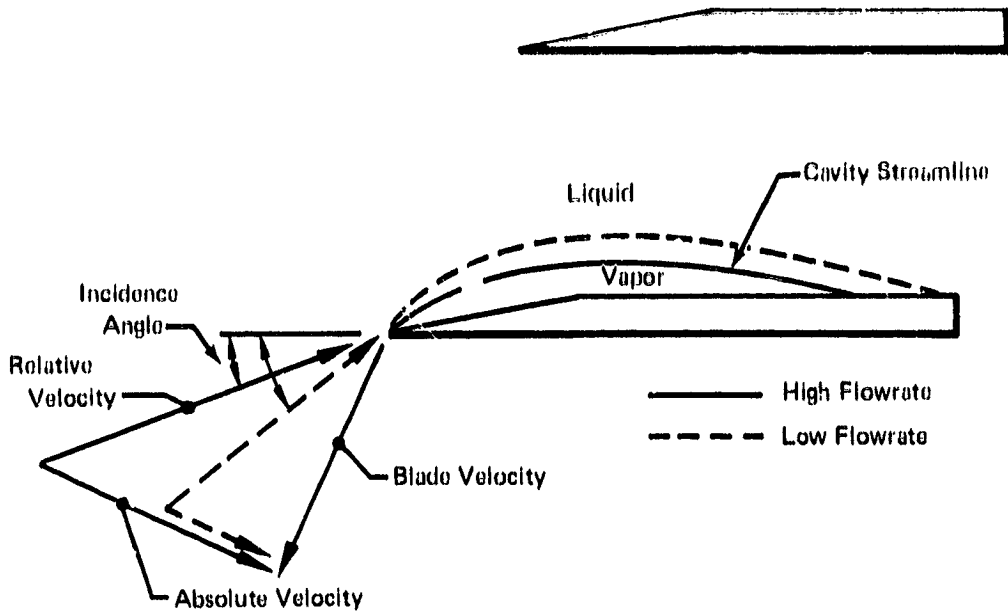


Figure 1. Cavity Response to Flowrate; Continuity Destabilizing Mechanism Above Head Breakdown

FD 62371

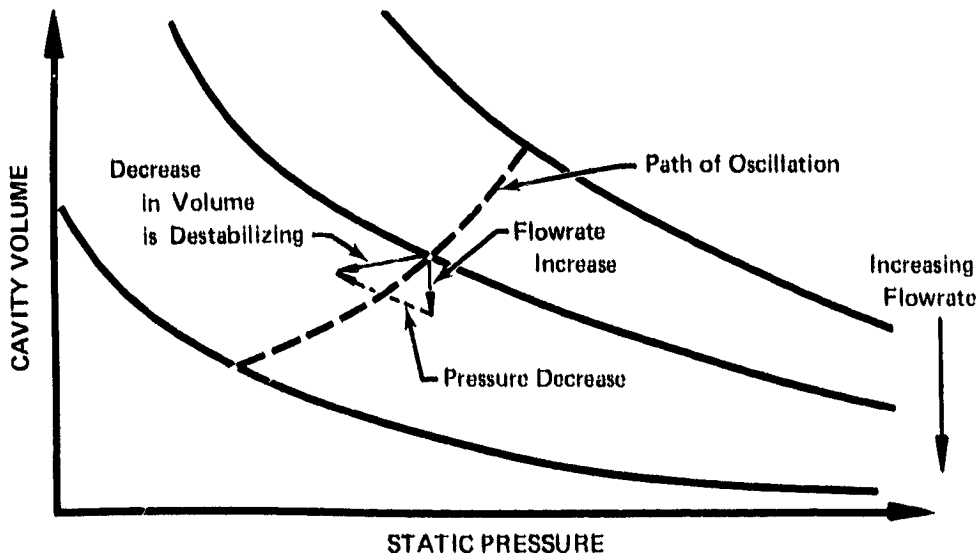


Figure 2. Path of "Continuity" Mechanism Oscillation

FD 62372

This is descriptive of the mechanism that causes inducer instabilities at cavitation numbers above the head breakdown point. The mechanism also exists at cavitation numbers below the point at which head breakdown begins, but head breakdown introduces a stabilizing effect. In the head breakdown region the lowering inlet pressure accompanying a flowrate acceleration not only acts to counter cavity collapse, but also to lower inducer discharge pressure (through pump gain), which tends to reduce the flowrate that can be forced through the discharge system. The deceleration of discharge flowrate helps to fill the newly created fluid space and reduce the acceleration required of inlet flowrate. This explains why the oscillations have generally been noted to diminish once head breakdown begins.

The second mechanism begins in the head breakdown region and involves the way cavitation can affect inducer headrise. If an inducer is operating at a point at which a momentary increase in flowrate causes an increase in headrise, as shown in figure 3, the instantaneously higher head available becomes greater than the head required to maintain flow and the flowrate increases further. Accompanying the flowrate increase, increasing frictional resistance in the inlet line lowers inducer inlet static pressure, which tends to increase the degree of head breakdown, and the inducer operating point shifts to lower values of headrise on the head vs flow map. Both effects tend to reduce the head available. The increasing flowrate also causes greater pressure drops across discharge restrictions, increasing the head required to maintain flow. These effects gradually stop the flowrate increase. An inertial overshoot causes head available to drop below head required to maintain flow, and flowrate begins to decrease. At this point it is speculated that hysteresis in the inducer system keeps head available below head required until flowrate drops below the original operating point. An inertial undershoot then causes head available to jump above head required, and flowrate begins to increase again. The path of oscillation is depicted in figure 4.

Both destabilizing mechanisms are influenced by the hydraulic system in which the inducer is operating, because the system has an effect on the exact relationship between pressure and flowrate. The system can therefore influence the point at which oscillations begin and the frequency and amplitude of oscillation. For this reason, the entire hydraulic system must be considered in an analysis of cavitation-induced instabilities.

Both mechanisms can occur in inducers, while only the latter is believed to occur in a cascade. In an inducer, an increase in flow decreases incidence and cavitation No. The incidence decrease generally is a stronger effect on cavity size than the cavitation No. decrease, so that cavity size decreases. In a cascade, incidence is fixed so that an increase in flow causes an increase in cavity size. Thus the continuity mechanism would not be expected to cause an instability in a cascade. The performance mechanism can cause a cascade instability. As cavitation number is lowered, the experimental observations show that steady-state lift and drag forces on the cascade remain constant until a point is reached at which both forces begin to change. Further lowering of cavitation number causes first one force and then the other to usually increase, reach a peak, and then rapidly decrease (2, 5, 6). The reported cascade (and hydrofoil) instabilities occurred in this lift and drag breakdown region. Since the lift and drag forces are forces exerted by the cascade on the fluid, they create pressure-area forces

at the cascade inlet and exit planes. The pressure-area forces in turn act on the flow approaching and leaving the cascade. If an increase in flow causes the lift, drag, and pressure-area forces to change so as to accelerate the flow, the resulting flow increase will further change the forces and an unstable trend develops. This trend will continue until a change in flow or pressure causes the force changes to reverse direction.

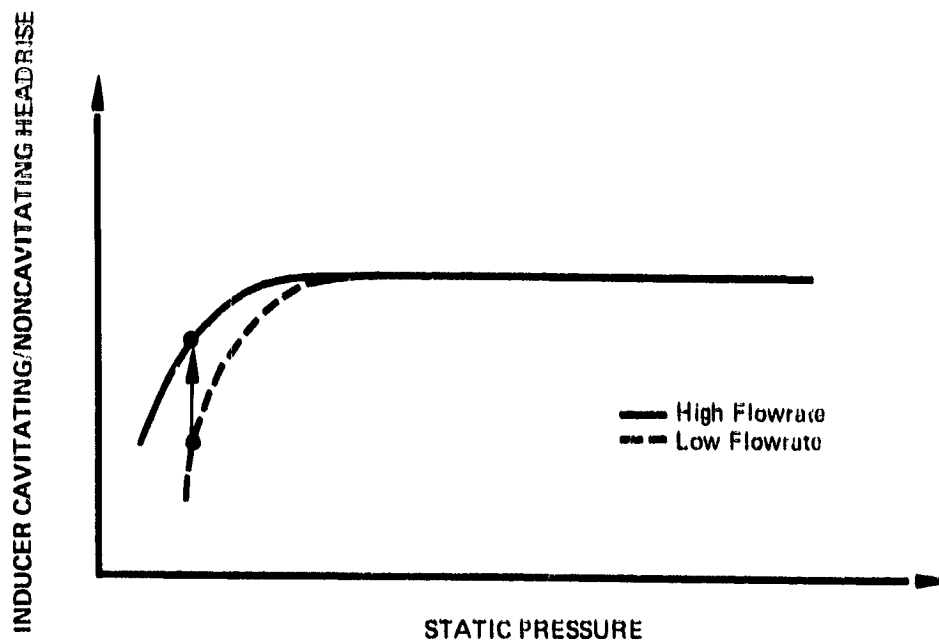


Figure 3. Headrise Response to Flowrate; Performance Destabilizing Mechanism Below Head Breakdown FD 62373

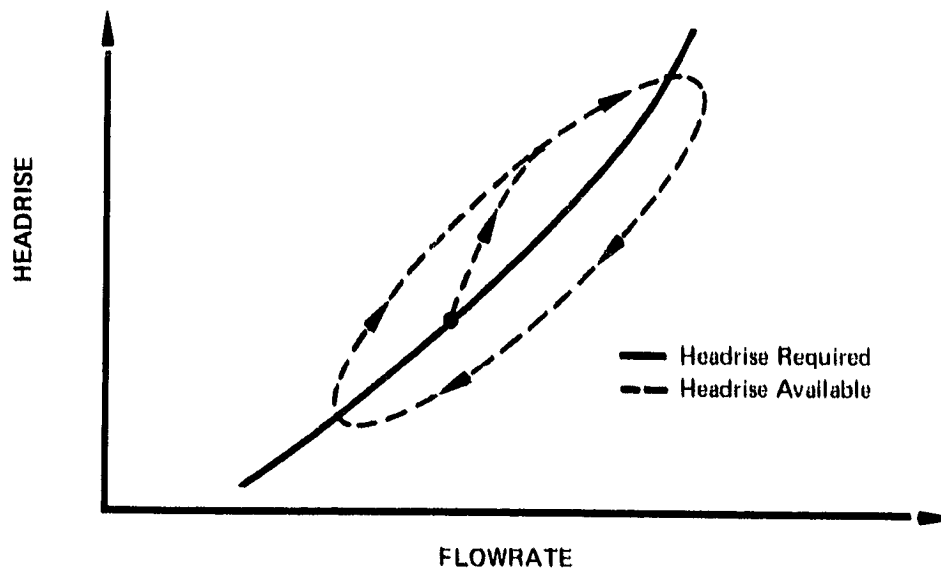


Figure 4. Path of "Performance" Mechanism Instability FD 62374

It should be pointed out that these mechanisms are not modeled individually. Only a single model is developed, and that model contains both mechanisms of an instability. Identifying the separate mechanisms was an aid in determining the effects required in a model.

### 3.2 DEFINITION OF REQUIRED EXPERIMENTAL DATA

There are two functions (apart from the readily predictable inlet and discharge line characteristics) that require accurate quantitative definition for the analytic prediction of the occurrence and characteristics of self-induced instabilities in cavitating inducers. The first of these is cavitation cavity volume as a function of inducer inlet pressure and flowrate, and the second is inducer head rise as a function of inlet pressure and flowrate. These functions are associated with the "continuity" and "performance" instability mechanisms, respectively.

At present, the cavity volume function is considered the most important because it affects the occurrence of instabilities in the usual inducer operating regime - reasonably above the head falloff pressure. It should be noted that total cavity volume (blade suction surface and tip vortex cavitation) must be defined in a rigorous analysis. The fact that the continuity instability mechanism requires that cavity volume be sensitive to flowrate, and that a qualitative consideration of tip clearance cavitation indicates that its volume may be much less sensitive to flowrate than is suction surface cavitation volume, led to the conclusion that an initial analytic modeling attempt would provide a reasonable degree of accuracy if only the suction surface cavity were considered.

Suction surface cavity volume for arbitrary inducer geometries and flow conditions is predictable with the computer program of (1), but the predictions did not provide the accuracy required because of the poor reported correlation of predicted with measured cavity length data. Additional experimental data were therefore required on the geometry of blade suction surface cavitation as a function of inlet pressure and incidence angle (flow coefficient) for refinement of the cavity model from (1).

A second set of experimental data were required to demonstrate the adequacy of the analytic instability modeling technique, to provide a qualitative indication of the accuracy of the suction surface cavity model, and to provide a qualitative indication of the relative importance of tip vortex cavitation.

The experiments that were planned and conducted to satisfy these requirements are reported in the next section of this report.

## SECTION 4 EXPERIMENTS

Two experiments were conducted: a cascade experiment and an inducer experiment. The primary objective of the cascade experiment was to provide cavity geometry data, and a secondary objective was to provide instability data for correlation with analytic predictions. The objective of the inducer experiment was to provide instability data for correlation with predictions. The experiments and their results are discussed in this Section.

### 4.1 CASCADE EXPERIMENT

#### 4.1.1 Facility

The cascade experiment was conducted in the water cascade tunnel at The United Aircraft Research Laboratories. A drawing of the tunnel is shown in figure 5. The tunnel was originally designed and constructed to permit the measurement of two dimensional performance and cavitation inception points of various cascade configurations. These previous programs are reported in (7). The tunnel is vertical and is oriented so that the inlet plane of the cascade is horizontal, which eliminates gravitational hydrostatic pressure gradients along the length of the cascade.

Water is circulated in the closed-loop tunnel by four pumps, which are located below floor level to increase available pump inlet head. The flow is discharged from the pumps, diffused and turned in a system of ducts, and settled in a rectangular chamber containing both a honeycomb flow straightener and graded-porosity screens for reducing large-scale turbulence. A subsequent guide vane section aligns the flow and delivers it to the cascade inlet nozzle. The flow is accelerated by the inlet nozzle, then passed through the cascade test section, and finally discharged into the plenum tank from which the flow is drawn into the circulating pumps.

Four interchangeable cascade inlet nozzles are available for inlet flow angles of 0.87, 1.05, 1.22, and 1.31 rad (50, 60, 70, and 75 deg), as measured from the nozzle axis to a line that is normal to the cascade inlet plane. The 1.31-rad (75-deg) nozzle was used in this program because it most nearly approximates the blade angles typical of inducers. Installation of the 1.31-rad (75-deg) inlet nozzle with the test section assembly is shown in figure 6. A section in the top wall of the nozzle is transparent to permit observation of cascade inlet flow conditions from a position above the test section. The cascade section is normally assembled with porous side walls in place of the illustrated transparent acrylic walls to provide for removal of the cascade boundary layer. The transparent walls were used in this program to permit visualization of cavitation profiles. The resulting partial loss of cascade two dimensionality was not considered significant to this program in view of other experience with cavitating cascades (2, 4, 5, 6).

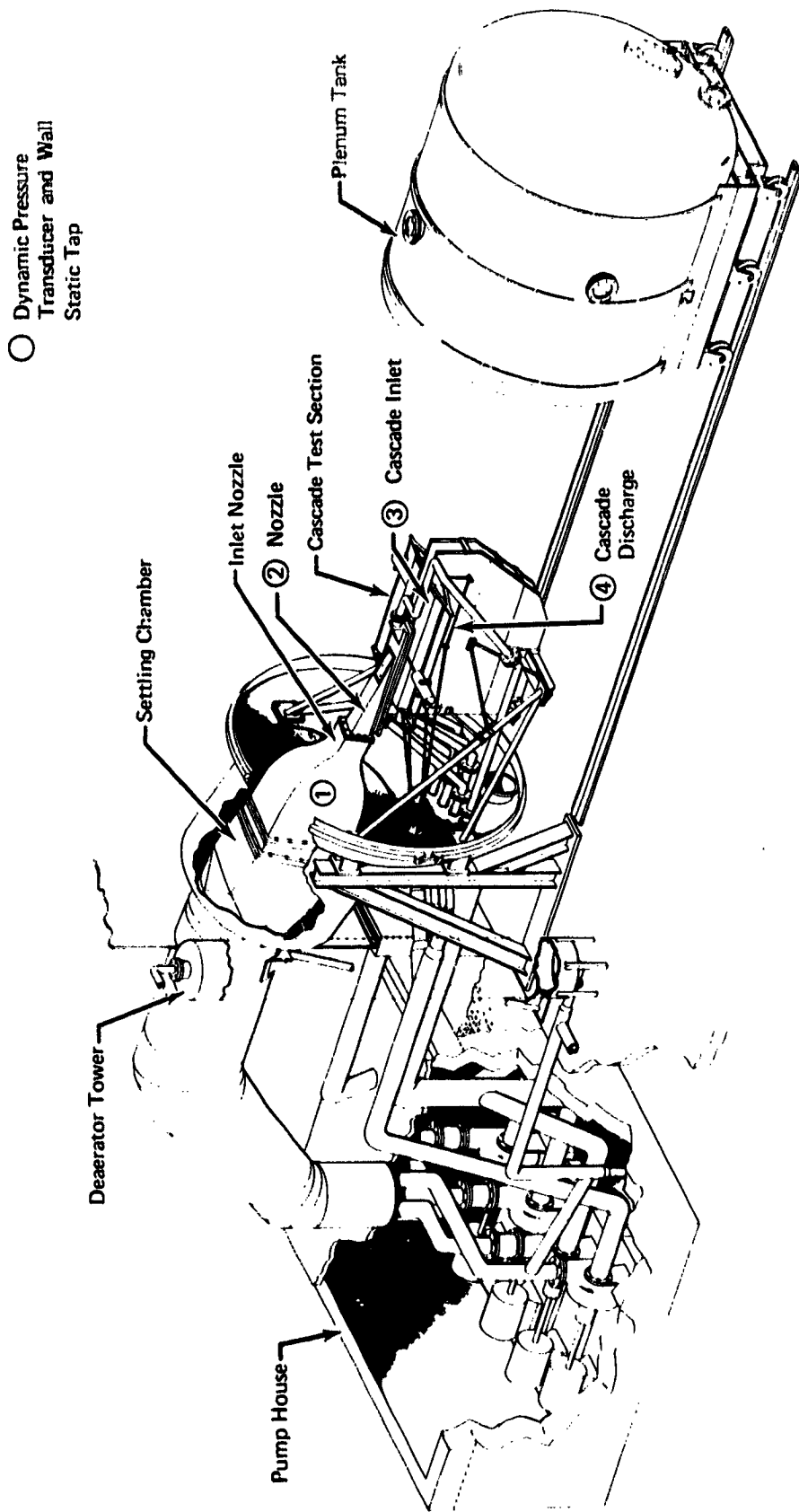


Figure 5. Water Cascade Tunnel

FD 53038

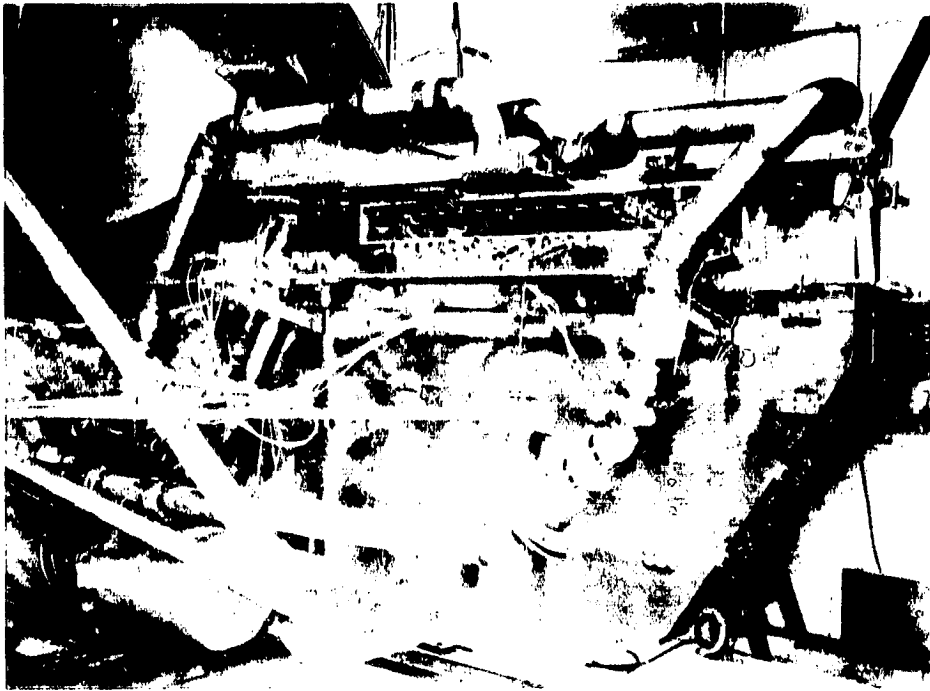


Figure 6. Hydrofoil Cascade Installed in Water Tunnel

FE 113784

A drawing of the cascade test section area is shown in figure 7. The test section inlet is rectangular, having a 15.24-cm (6-in.) span and a 91.44-cm (36-in.) length. The test section was designed to establish both a uniform flow along the cascade inlet plane and a periodic (blade-to-blade) flow downstream of the cascade. These are necessary conditions to ensure that the flow about each blade is identical; accomplishment of these goals provides a flow that is representative of the flow through an infinite cascade. Approximations of flow uniformity and periodicity are achieved by removal of the wall boundary layers and by contouring the cascade end walls to minimize their effect on the mainstream flow. The boundary layers which develop along the walls of the inlet nozzle are removed upstream of the test section by means of step-type slots located on all four walls of the nozzle. Flow intercepted by each of the four step slots is ducted through individual throttling valves to one of the four pumps.

Adjustments of flow streamlines (to obtain uniformity) are accomplished by means of variable geometry end walls located at each end of the cascade. These end walls are comprised of three sections; a flexible wall that connects the rigid inlet nozzle to an adjustable end wall, an adjustable end wall that is analogous to one surface of a cascade blade, and a tailboard that extends downstream from the adjustable end wall. Actuation of these end-wall sections enables independent adjustment of (1) the gap between the end blades of the cascade and the adjustable end wall, (2) the angle of the adjustable end wall, and (3) the angle of the tailboard. The convex, flexible end wall is porous to permit removal of the end wall boundary layer, thereby decreasing any tendency toward separation from this surface.

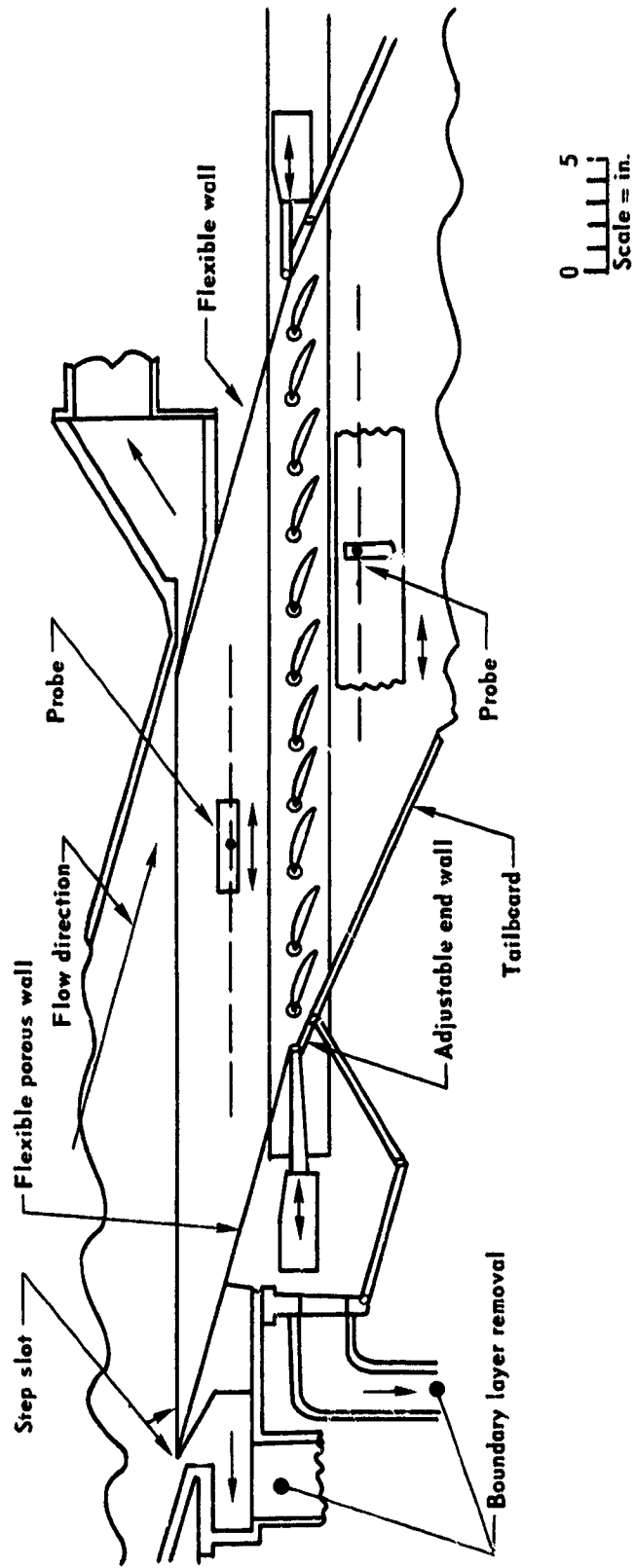


Figure 7. Cascade Test Section

FD 62056

The cascade test section assembly is supported from the fixed side of the 3.05-meter (10-ft) diameter plenum tank and completely enclosed within the tank. Tank water level during tests is just above the test section. The tank has an operating pressure capability of 0.7 to 69 N/cm<sup>2</sup> (1 to 100 psia). The three main flow pumps and one boundary layer pump are fabricated from zinc-free bronze and stainless steel. Each pump is driven by a 7457-watt (10-hp) motor and is capable of delivering water flows at a rate of 6.44 m<sup>3</sup>/min (1700 gpm) with a head rise of 4.88 m (16 ft).

Contamination of the water used in the facility is minimized by special water processing equipment. In addition, the facility is constructed primarily of stainless steel to avoid solid particle shedding. Solid particles contained in the water are removed by various filters, one of which provides continuous  $3 \times 10^{-6}$  m ( $3\mu$ ) filtration at a flowrate of 0.38 m<sup>3</sup>/min (100 gpm). Dissolved minerals are removed from the test water by a commercial ion-exchange-type demineralizer that provides water comparable to distilled water in conductivity, a measure of dissolved mineral content. The conductivity of the water from this unit was approximately 1 micro ohm/cm. Dissolved gases may be removed by a cold-water deaerator that can reduce the gas content to 3 ppm. The deaerator was not used in this program, however, as the natural deaeration resulting from the low test pressure was found to be more efficient.

#### 4.1.2 Cascade Configuration

The test cascade was designed to be as nearly representative of inducer blading as practical within the limits of existing tunnel hardware. The selected cascade features are listed in table 1 and a drawing of the cascade is shown in figure 8. The flat plate profile is the cascade equivalent of helical inducer blades. A cascade solidity of 2.0 was selected as being representative of inducers (but on the low end of the usual range) to permit large, easily measurable cavities to form. Hydrofoil chord was established near the upper limit of the test section capability so that the selected solidity would result in as large a blade spacing, and as high a cavitation cavity (for measurement), as possible. Leading edge wedge angle was determined by the requirement that the blade suction surface clear the free flow streamline at minimum incidence, and the leading edge was made relatively sharp (inducer design guide lines for best suction performance). The trailing edge configuration was unimportant in this program, where cavitation and not performance was to be studied, so the trailing edge was merely rounded to simplify manufacturing. Hydrofoil thickness was selected to make blade bowing negligible, yet not so thick as to result in unrepresentative blade blockage effects. Hydrofoil span was set solely by the test section capability and the number of hydrofoils resulted from the selected solidity, chord, and the length of the cascade test section (91.4 cm, 36.0 in.). Inlet flow angle was set by the existing tunnel facility nozzle. The nozzle with the highest angle (1.31 rad, 75 deg) was used to approximate, as nearly as possible, the blade angles of a typical inducer (1.36 to 1.48 rad, 78 to 85 deg from axial).

Table 1. Cascade Features

Hydrofoil Profile	Flat Plate
Solidity	2.0
Hydrofoil Chord	15.2 cm (6.0 in.)
Hydrofoil Spacing	7.62 cm (3.00 in.)
Loading Edge Shape	0.09-rad (5-deg) wedge angle cut on suction surface
Loading Edge Radius	0.025 cm (0.010 in.)
Trailing Edge Radius	0.25 cm (0.10 in.)
Hydrofoil Thickness	0.51 cm (0.20 in.)
Hydrofoil Span	15.2 cm (6.0 in.)
Number of Hydrofoils	11
Inlet Flow Angle	1.31 rad (75 deg)

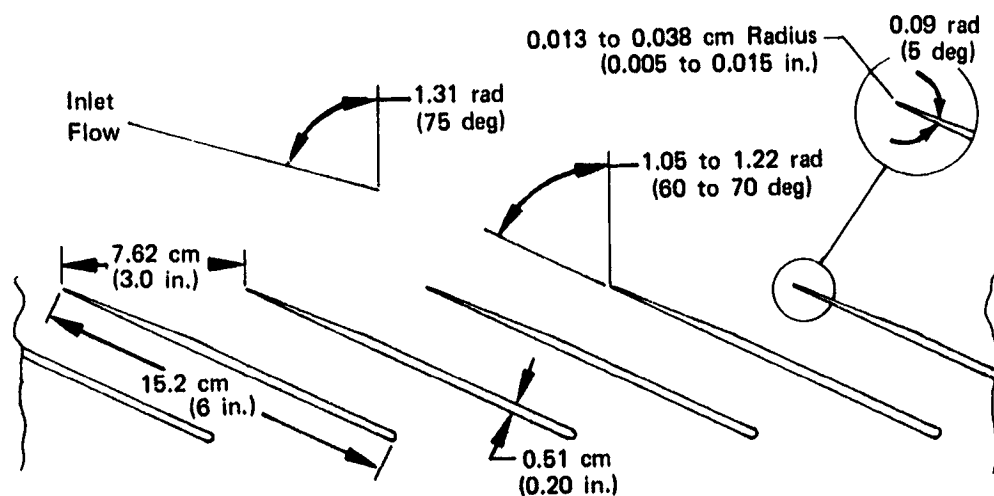


Figure 8. Cascade Configuration

FD 62668

The hydrofoils were machined from AISI-type 304 stainless steel and were welded to studs, one at either end of the hydrofoil. A photograph of a completed hydrofoil is shown in figure 9. The hydrofoil surfaces were not polished after machining because the exact cavitation inception point and performance were not of interest. Surface roughness measurements of a typical hydrofoil were:

Roughness (RMS)

Suction Surface	
Wedge	3.8 $\mu\text{m}$ (150 $\mu\text{in.}$ ) chordwise 0.6 $\mu\text{m}$ (25 $\mu\text{in.}$ ) spanwise
Flat	1.3 $\mu\text{m}$ (50 $\mu\text{in.}$ )
Pressure Surface	6.4 $\mu\text{m}$ (250 $\mu\text{in.}$ )

The cascade hydrofoils were assembled in the tunnel test section between acrylic plastic sidewalls, as shown in figures 10 and 11. The hydrofoil studs extended through holes in the sidewalls so that the foils pivoted about the stud centerline when incidence angle was changed. Foil end clearance was just

sufficient to permit smooth pivot operation and was approximately 0.013 cm (0.005 in.) for all foils (total for both ends). A series of reference lines, one at each hydrofoil location, were scribed on the far sidewall prior to assembly to facilitate setting the foils at a uniform incidence angle. The studs were locked to an actuation linkage with setscrews along the scribed lines so that subsequent actuation of the linkage, which was accomplished remotely, moved all the foils simultaneously through the same angle.

#### 4.1.3 Instrumentation

Cascade tunnel instrumentation was installed to provide data on (1) cavity geometry as a function of operating condition, (2) cascade pressure loss, and (3) tunnel dynamic pressures.

Cavity geometry measurements were obtained from photographs taken looking through the acrylic cascade sidewall at the hydrofoil profile and through the window in the top of the nozzle at the hydrofoil suction surfaces. The photographs were taken from outside the tunnel through portholes in the plenum tank. A speedgraphic 4 x 5 camera using Kodak Tri X film and a Calumet 4 x 5 long focus view camera using polaroid type 47 film were used with illumination provided by a Graphic Strobeflash - 1 strobe light.

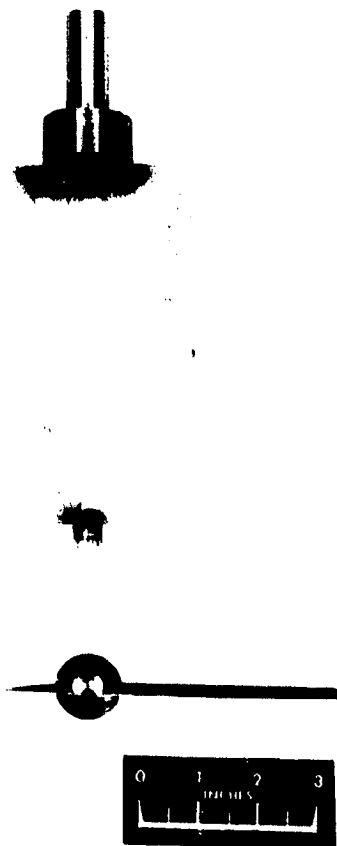


Figure 9. Cascade Hydrofoil

FE 119531

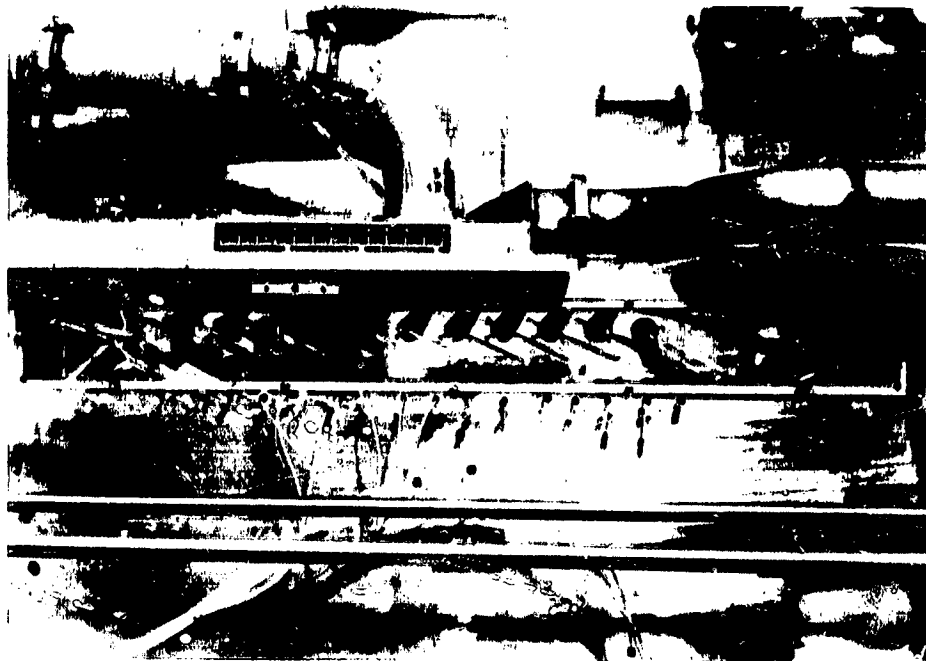


Figure 10. View of Left Side of Hydrofoil Cascade

FE 113783



Figure 11. View of Right Side of Hydrofoil Cascade

FE 119530

Cascade inlet total pressure, static pressure, and velocity pressure were obtained from a Kiel probe at the entrance to the inlet nozzle and a wall static tap approximately 4.6 cm (1.8 in.) upstream of the cascade leading edge plane. Each parameter was read from its own mercury manometer. A series of wall static taps spaced at 2.5-cm (1-in.) intervals along the length of the cascade at the cascade inlet and discharge and a Kiel probe approximately 25 cm (10 in.) downstream of the cascade were connected to a 254-cm (100-in.) tall, 50-tube manometer to indicate cascade flow uniformity and discharge total pressure, respectively. These measurements were later found to be inaccurate under cavitating conditions because of air bubbles that developed in the long manometer lines. Water temperature was measured with an immersed mercury thermometer. Plenum tank ambient pressure (above the water free surface) was measured with a pressure gage. Maximum instrumentation error is estimated at  $\pm 0.065$  cm Hg ( $\pm 0.025$  in. Hg) for the manometer measurements,  $\pm 1.25$  cm Hg ( $\pm 0.5$  in. Hg) for the pressure gage, and  $\pm 0.3^\circ\text{K}$  ( $\pm 0.5^\circ\text{F}$ ) for the thermometer.

Dynamic pressure data were measured by means of four Kistler model 601 H piezoelectric transducers with Kistler model 568 charge amplifiers. The transducers were located in the tunnel as follows:

1. In the large section at the nozzle entrance, 238 cm (94 in.) upstream of the cascade leading edge plane
2. In the convergent portion of the nozzle, 165 cm (65 in.) upstream of the cascade leading edge plane
3. At the cascade inlet, 1 cm (0.4 in.) upstream of the leading edge plane
4. At the cascade discharge, 46 cm (18 in.) downstream of the leading edge.

These locations are indicated on figure 5. Data were recorded using a Honeywell Model 5600 magnetic tape recorder for the first 18 test points and a visicorder Model 1108 oscillograph for test points 19 through 41.

#### 4.1.4 Test Procedure

The cascade was initially tested at high (noncavitating) pressures and attempts were made to obtain uniform inlet and exit flow distributions through control of boundary layer flow and positioning of endwalls and tailboards. The degree of flow uniformity was determined by inspection of the manometer pressure profiles from the inlet and discharge static wall taps. It was necessary to adjust boundary removal flow, endwall setting, and tailboard setting to maintain an acceptable uniformity over a range of incidence angles from 0.09 to 0.26 rad (5 to 15 deg). Under cavitating conditions, manometer pressure profiles could not be used to determine the uniformity of flow because of uncertainties in the individual pressure values caused by air bubbles trapped in the long lengths of small diameter tubing that ran to the manometer board. Under these conditions, flow uniformity was assumed when cavity lengths on the various foils were equal.

Endwall and tailboard settings that established the most uniform flow during noncavitating operation did not necessarily maintain uniformity after cavitation inception. Adjustments were usually required after the setting of cavitating test points, and the attainable degree of uniformity became progressively worse as inlet pressure was lowered and the cavities became larger.

During noncavitating tunnel operation, cascade inlet and discharge span-wise velocity profiles were measured at mid length along the cascade to obtain an indication of cascade two-dimensionality. The measurements were taken with the hydrofoils set at 0.17-rad (10-deg) incidence angle. An upstream boundary layer thickness of approximately 1 cm (0.4 in., 6.67% span) and a downstream thickness of 4.5 cm (1.75 in., 29% span) were measured. Thickness is defined as the distance to 90% of freestream velocity. These values were considered acceptable for the purposes of this investigation. The velocity probes could only be used during noncavitating operation (cavitation developed on the probes), and they were removed before the cavity geometry test points were run.

Hydrofoil pressure surface cavitation was noted at incidence angles from 0.09 to 0.23 rad (5 to 13 deg) and to a small extent at incidence angles of 0.24 and 0.26 rad (14 and 15 deg). The cause of the pressure surface cavitation was not determined conclusively but it was believed to be caused by deviations of the inlet flow angle from the presumed 1.31-rad (75-deg) nozzle angle. Such deviations could have been caused by cavitation choking in the step-slot boundary layer removal system, with consequent loss of the infinite cascade simulation. Flow angle, and incidence, would vary from blade to blade in such a situation and this variation would be manifested in nonuniform cavity geometries (that were observed) and in pressure surface cavitation.

A tuft was inserted in the cascade inlet flow at one location approximately 1 cm (0.4 in.) upstream of the leading edge plane to gain a qualitative indication of the magnitude of any flow angle variation. The location is probably within the region of normal cascade inlet flow adjustment, and, as such, was only used to roughly indicate the freestream direction. The tuft was near the top of the acrylic sidewall and could not be located any appreciable amount further upstream. A flow angle of approximately 1.25 rad (66 deg) was indicated by the tuft at a typical cavitating test point, which is 0.16 rad (9 deg) less than the nozzle angle. The apparent 0.16 rad upstream flow adjustment was somewhat larger than would be expected from normal two-dimensional considerations (0.03 to 0.10 rad in potential flow calculations for a similar cascade), and the tuft angle, therefore, was considered to indicate that flow adjustment was taking place upstream of the cascade.

Modifications to the facility, which may have alleviated the upstream flow adjustment problem, such as redesign or elimination of the step-slot boundary layer control system, were beyond the scope of this program and could not be accomplished. Alternatively, the cascade was operated at an indicated incidence angle that was sufficiently high to produce suction surface cavitation exclusively, so that the resulting test data would give a qualitative indication of the required cavity geometry vs incidence angle and inlet pressure functions. Step-slot boundary layer (b/l) flow was removed at full capacity for all test points because of previous experience which indicated that excess b/l flow had a lesser effect on two-dimensionality than insufficient flow. In addition, several points were taken with no b/l removal flow to permit an evaluation of the effects of b/l bleed. Additional inducer test data were available from (1) to permit quantitative evaluation of the data.

Cascade data were taken at indicated incidence angles of 0.28, 0.31, and 0.35 rad (16, 18, and 20 deg). These were the lowest values at which no pressure surface cavitation occurred and which produced reasonably sized suction surface cavities. All three incidence angles were tested with an inlet velocity of approximately 6.56 m/s (21.5 ft/sec), and the 0.28-rad incidence was repeated with a velocity of approximately 5.61 m/s (18.5 ft/sec). Blade chord Reynolds numbers were approximately  $1.4 \times 10^6$  and  $1.2 \times 10^6$ , respectively. At each incidence angle, inlet pressure was reduced to a level where the cascade was super-cavitating (cavity length was one chord or longer), and pressure was increased in approximately ten steps until the cavitation disappeared. At each inlet pressure test point endwall and tail settings were adjusted until blade-to-blade cavitation was as uniform as possible, photographs of the cascade profile and suction side were taken, a tape or an oscillograph recording of the dynamic pressure transducer signals was made, operating condition data were manually recorded, and visual observations concerning the cavitation were noted.

The water was deionized before testing was started in an ion-exchange-type demineralizer and was continuously filtered at a rate of 0.38 cubic meters per minute (100 gpm). A low air content was achieved by maintaining the system at pressures below 5 centimeters (2 in.) of mercury absolute at all times except during the actual testing periods. Air content was not measured, but this procedure resulted in values of less than 3 parts per million in previous programs.

#### 4.1.5 Data Reduction

All measurements and data reduction calculations were done in the English system of units (pressure in inches of mercury, lengths in inches or feet, etc.), and converted to the SI for presentation in this report. The originally measured or calculated data are shown as the secondary units in tables and figures. Symbols are defined in the Appendix.

Cascade inlet velocity ( $V_i$ ) was calculated from the measured difference between total pressure upstream of the inlet nozzle and static pressure at the cascade inlet plane ( $q_i$ )

$$V_i = \sqrt{2g \frac{\rho_{\text{mercury}}}{\rho_{\text{water}}} q_i}$$

The cavitation number ( $k$ ) was calculated from the cascade inlet static pressure ( $p_i$ ), the vapor pressure of water ( $p_v$ ) at the measured temperature, and the inlet dynamic pressure ( $q_i$ )

$$k = \frac{p_i - p_v}{q_i}$$

Cascade pressure loss ( $D$ ) was defined as the difference between total pressure at the entrance to the inlet nozzle and plenum tank static pressure and was calculated from the measured data as follows:

$$D = p_i + q_i - p_t - p_a$$

An uncertainty estimate was performed for the cascade pressure drop and cavitation number calculations since inflections in their relationship were significant to the instability correlation. The estimated measurement error in each of the values used in the calculations was:

	<u>Max Error, in. Hg</u>
Inlet Static Pressure, $p_1$	± 0.03
Fluid Vapor Pressure, $p_v$	± 0.02
Inlet Velocity Pressure, $q_1$	± 0.03
Tank Static Pressure, $p_t$	± 0.50
Atmospheric Pressure, $p_a$	Negligible

The uncertainty analysis was performed as detailed in (29) for nominal data values that were representative of data points over the tested range of cavitation number. The maximum uncertainty was ± 2% for cavitation number ( $k$ ) and ± 9% for pressure loss.

Cavitation cavity length and height were measured from the cascade suction surface and profile photographs, respectively. Scale for the profile photographs was obtained from a grid on the transparent cascade sidewall and suction surface photograph scale was obtained from the known length of the hydrofoil leading edge wedge. Both sets of measurements were corrected for viewing angle. Height measurements were taken from the suction surface in a direction normal to the surface, and length measurements were taken parallel to the suction surface. Both measurements were divided by foil tangential spacing (7.6 cm, 3.0 in.) for correlation with predictions.

Dynamic pressure amplitude and frequency were read from an oscillograph for the nozzle, cascade inlet, and cascade discharge transducers. The reported amplitude is the measured peak-to-peak amplitude of the total signal, which was not a simple sine wave, and frequency was calculated from the period of the most prominent frequency. The reported frequencies are approximate because the signal was erratic.

#### 4.1.6 Test Results

A list of test points showing the controlled parameters, fluid conditions, plenum tank static pressure, calculated pressure loss, vapor pressure, inlet velocity, and cavitation number is shown in table 2. Forty-one test points were run at the listed incidence angles, inlet velocities, and inlet static pressures. All points were run with the tunnel boundary layer bleed slots in operation at full capacity, with the exceptions of points 19, 31, and 41. These were run with no bleed flow to define the effects of the bleed on dynamic pressure characteristics.

Table 2. Cascade Test Points

Test Point	Incidence Angle, $\theta$ rad	MEASURED DATA										CORRECTED DATA			Calibration Number, $K$	
		Barometer N/cm <sup>2</sup> in. Hg	Water Temperature, T °K °F	Inlet Static Pressure, $P_i$ N/cm <sup>2</sup> in. Hg abs	Inlet Velocity Pressure, $q_i$ N/cm <sup>2</sup> in. Hg	Tank Static Pressure, $P_t$ N/cm <sup>2</sup> in. Hg vacuum vacuum	Pressure Loss, $\Delta P$ N/cm <sup>2</sup> in. Hg	Pressure Loss, $\Delta P$ N/cm <sup>2</sup> in. Hg	Velocity, $V$ m/s ft/sec	Correction Factor, $C$						
1	0.28	10.21	301.1	92.3	1.21	3.58	2.16	6.39	6.22	27.6	2.47	1.54	0.77	1.11	0.55	1.07
2	0.25	13.26	301.4	95.0	1.24	3.69	2.14	6.34	6.25	27.4	2.44	1.52	0.75	1.10	0.55	1.07
3	0.28	16	301.7	93.5	1.27	3.77	2.14	6.34	6.22	27.3	2.44	1.54	0.75	1.10	0.55	1.07
4	0.28	16	302.4	84.7	1.29	3.82	2.16	6.39	6.19	27.2	2.47	1.50	0.75	1.10	0.55	1.07
5	0.28	16	302.9	85.5	1.34	3.99	2.25	6.67	6.15	27.1	2.61	1.42	0.72	1.09	0.55	1.07
6	0.28	16	302.4	86.2	1.36	4.03	2.30	6.81	6.12	27.0	2.68	1.38	0.70	1.09	0.55	1.07
7	0.28	16	303.2	86.2	1.36	4.03	2.30	6.81	6.12	27.0	2.68	1.38	0.70	1.09	0.55	1.07
8	0.28	16	304.3	87.2	1.31	3.87	2.11	6.25	6.05	26.5	2.35	1.67	0.70	1.09	0.55	1.07
9	0.28	16	304.3	88.0	1.41	4.17	2.09	6.70	6.11	26.5	2.11	1.93	0.70	1.09	0.55	1.07
10	0.28	16	304.7	89.7	1.34	3.97	2.17	6.44	6.03	26.4	1.84	2.22	0.70	1.09	0.55	1.07
11 (1)	0.28	16	305.5	90.2	4.90	14.52	7.13	6.30	6.30	9.0	-0.01	-0.03	0.55	1.09	0.55	1.07
12	0.35	20	304.9	89.0	1.21	3.59	2.09	6.20	6.01	26.1	2.06	1.61	0.70	1.09	0.55	1.07
13	0.35	20	305.4	90.0	1.23	3.63	2.13	6.20	6.04	25.6	1.85	1.76	0.70	1.09	0.55	1.07
14	0.35	20	306.0	91.0	1.21	3.58	2.14	6.34	6.04	25.3	1.84	1.77	0.70	1.09	0.55	1.07
15	0.35	20	306.3	91.5	1.24	3.68	2.19	6.48	6.07	24.5	1.65	1.99	0.70	1.09	0.55	1.07
16	0.35	20	306.8	92.3	1.51	4.46	2.16	6.39	6.00	23.7	1.42	2.22	0.70	1.09	0.55	1.07
17	0.35	20	307.2	93.2	1.63	4.84	2.05	6.06	5.93	23.1	1.32	2.32	0.70	1.09	0.55	1.07
18	0.35	20	307.6	94.0	1.80	5.34	2.16	6.39	5.83	22.6	1.51	2.13	0.70	1.09	0.55	1.07
19 (2)	0.35	20	309.1	94.8	2.81	8.31	2.14	6.34	5.73	22.6	2.54	1.13	0.66	1.09	0.55	1.07
20	0.35	20	308.5	95.5	2.31	6.85	2.11	6.25	5.73	21.7	1.64	1.96	0.66	1.09	0.55	1.07
21	0.35	20	308.9	96.2	2.91	8.62	2.16	6.39	5.58	19.5	1.54	2.13	0.66	1.09	0.55	1.07
22	0.31	18	308.9	96.2	1.28	3.80	2.14	6.34	6.19	27.2	2.49	1.55	0.69	1.09	0.55	1.07
23	0.31	18	309.9	96.2	1.28	3.80	2.13	6.30	6.12	27.0	2.49	1.52	0.69	1.09	0.55	1.07
24	0.31	18	308.9	96.2	1.25	3.70	2.09	6.20	6.05	26.5	2.49	1.53	0.69	1.09	0.55	1.07
25	0.31	18	309.9	96.2	1.30	3.85	2.16	6.39	6.05	25.9	2.49	1.52	0.69	1.09	0.55	1.07
26	0.31	18	308.9	96.2	1.33	3.95	2.16	6.39	5.95	25.4	2.25	1.76	0.69	1.09	0.55	1.07
27	0.31	18	308.9	96.2	1.46	4.31	2.09	6.20	5.81	24.6	2.03	1.99	0.69	1.09	0.55	1.07
28	0.31	18	308.9	96.2	1.77	5.23	2.08	6.16	5.77	23.6	1.93	2.06	0.69	1.09	0.55	1.07
29	0.31	18	308.9	96.2	2.07	6.12	2.13	6.30	5.60	22.2	1.95	2.04	0.69	1.09	0.55	1.07
30	0.31	18	308.9	96.2	2.90	8.60	2.09	6.16	5.52	19.9	1.65	2.32	0.69	1.09	0.55	1.07
31 (2)	0.31	18	308.9	96.2	3.97	11.77	2.11	6.25	5.35	19.9	1.55	2.41	0.69	1.09	0.55	1.07
32	0.28	16	304.9	89.0	1.10	3.25	1.64	4.86	6.72	19.9	2.95	5.15	0.69	1.09	0.55	1.07
33	0.28	16	305.4	90.0	1.11	3.30	1.64	4.86	6.72	19.9	2.95	5.15	0.69	1.09	0.55	1.07
34	0.28	16	306.0	91.0	1.13	3.35	1.67	4.95	6.72	19.9	2.95	5.15	0.69	1.09	0.55	1.07
35	0.28	16	306.3	91.5	1.13	3.34	1.55	4.58	6.72	19.9	2.95	5.15	0.69	1.09	0.55	1.07
36	0.28	16	306.8	92.3	1.16	3.44	1.59	4.72	6.72	19.9	2.95	5.15	0.69	1.09	0.55	1.07
37	0.28	16	307.2	93.2	1.16	3.44	1.61	4.77	6.72	19.9	2.95	5.15	0.69	1.09	0.55	1.07
38	0.28	16	307.6	94.0	1.53	4.52	1.64	4.86	6.72	19.9	2.95	5.15	0.69	1.09	0.55	1.07
39	0.28	16	308.1	94.8	2.02	5.97	1.47	4.35	6.72	19.9	2.95	5.15	0.69	1.09	0.55	1.07
40	0.28	16	308.5	95.5	1.29	3.83	1.43	4.22	6.72	19.9	2.95	5.15	0.69	1.09	0.55	1.07
41 (2)	0.28	16	308.9	96.2	1.59	4.71	1.61	4.77	6.72	19.9	2.95	5.15	0.69	1.09	0.55	1.07

(1) Apparent Measurement Error in Tank Static Pressure

(2) No Step Slot Boundary Layer Removal

(3) Data Were Corrected According to Post-Test Gauge Calibration

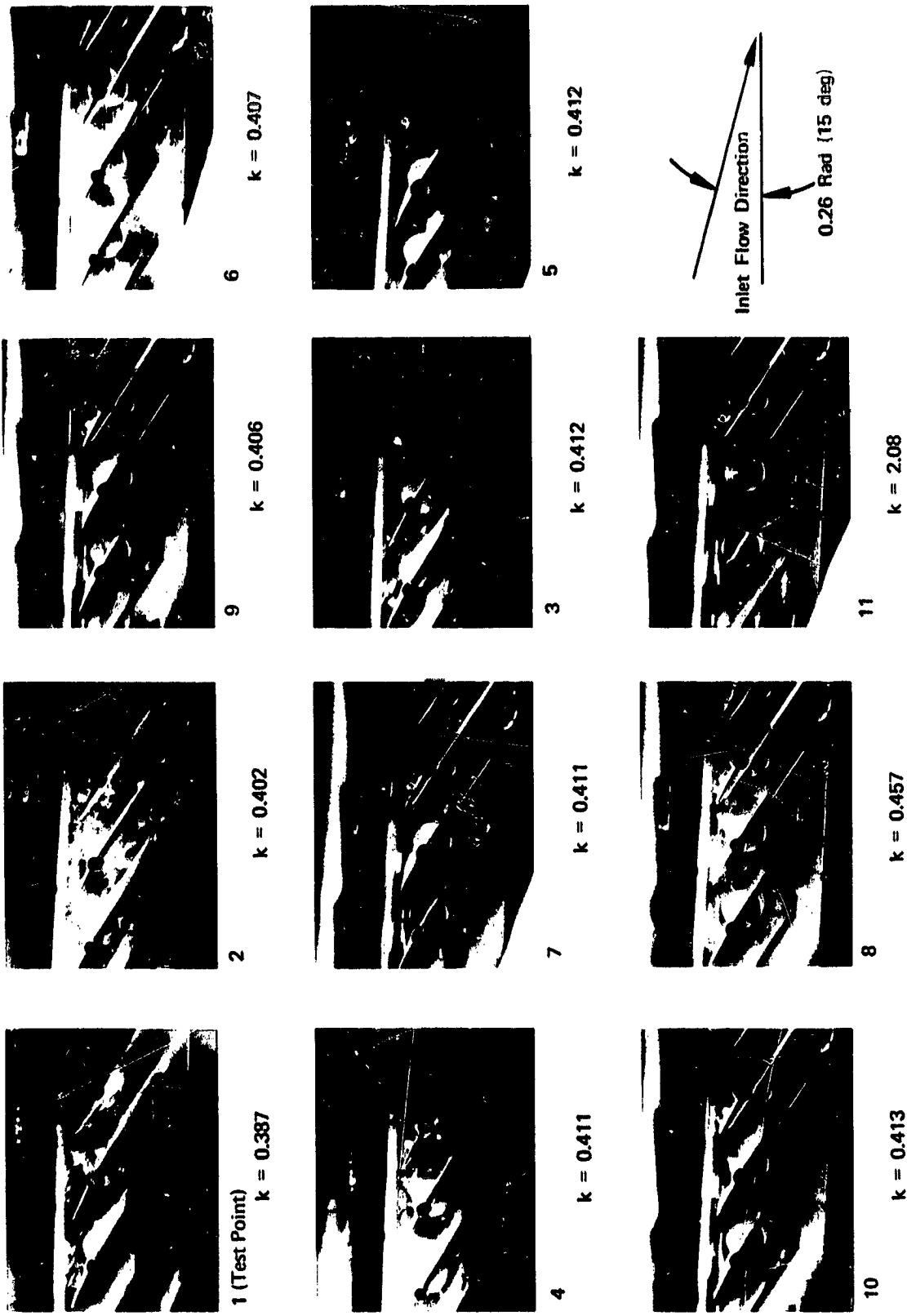
#### 4.1.6.1 Cavity Geometry

Profile and top view photographs of the cascade for the 0.28-rad (16-deg) incidence, 6.56-m/s (approximately) inlet velocity series of test points are shown in figures 12 and 13. The photographs are arranged in order of increasing cavitation number on each figure, and the test points, from table 2, are indicated under each photograph. Flow is from left to right. Counting hydrofoils from left to right, the profile photographs show the trailing edges of foil 2 and foils 3, 4, and 5 and the leading edge of foil 6. The top view shows the leading edge suction surfaces of foils 2 (in part), 3, 4, 5, and 6 (in part). The series of test points shown in the photographs illustrates the nature of the cascade cavitation and is representative of other series of points in that respect.

The degree of cavitation uniformity that could be established on the various foils and spanwise on each foil can be seen in figures 12 and 13. A fair degree of uniformity was accomplished with the small cavities, but the degree of attainable uniformity was not as good for the larger cavity size. The variation in cavitation patterns is believed to be indicative of variations in flow angle and/or velocity. The patterns were made as uniform as possible during the setting of each test point through adjustment of the cascade side walls and discharge tail boards. Additional control is possible for noncavitating test points through the variation of tunnel step slot boundary layer removal flow (figure 7), but these slots cavitated when significant cavitation developed in the cascade and sufficient flow for two-dimensional cascade conditions was not believed to be established. The cavitation off the edges of the step slots can be seen in figure 13.

The observed cascade nonuniformity and the occurrence of pressure surface cavitation at high incidence angles (0.23 rad, 13 deg) led to the conclusion that there were local variations in incidence angle and velocity within the cascade, and that the average incidence angle was lower than the indicated geometric angle. It is also probable that incidence angle varied with cavitation number. It was not possible either to correct these conditions (through the design of a new cascade inlet nozzle) or to measure the actual conditions (which would have required sophisticated instrumentation such as a laser velocimeter) within the scope of the program. Cascade cavitation was generally unsteady, and this unsteadiness also varied from one blade to another. The unsteadiness seemed to be random and had no relation to cavity size. In light of these uncertainties, the cascade cavity geometry test data were considered to indicate only qualitative trends, and it was evaluated with the uncertainties in mind.

A listing of the test points, measured cavity lengths, and heights is given in table 3. Cavity lengths for blades 2, 3, and 4 were measured from the top view photographs at the foil midspan, where boundary layer effects would be minimal. Blade 4 cavity length and cavity height were measured from the profile photographs. This blade was the only one close to a true profile in these photographs. Cavity height was measured from the blade suction surface in a direction perpendicular to the pressure surface. All measurements were corrected for viewing angle. Cavity length measurements from the top view are missing from the table in some cases where the cavity closure was under the adjacent foil and could not be measured. In such cases, the foil "4" profile length measurement was used to establish length.



33 Figure 12. Cascade Cavitation Looking at Hydrofoil Profiles - Incidence = 0.28 rad (16 deg), Velocity  $\approx 6.56$  m/s (21.5 ft/sec) FD 62670



Figure 13. Cascade Cavitation Looking at Top of Cascade - Incidence = 0.28 rad (16 deg), Velocity  $\approx$  6.56 m/s (21.5 ft/sec) FD 62671

Table 3. Measured Cavity Lengths and Heights

Test Point	Incidence Angle, $i$ rad deg	Cavitation Number, $k$	Cavity Height, $h$ in.		Cavity Length, $l$				cm in. Average of Top			
			cm (Foil 4)	in. (Foil 4)	cm (Foil 2 Top)	in. (Foil 2 Top)	cm (Foil 3 Top)	in. (Foil 3 Top)		cm (Foil 4 Top)	in. (Foil 4 Profile)	
1	0.29	16	0.55	0.22	(1)	(1)	(1)	(1)	>20	>8.0	(1)	(1)
2	0.29	16	0.3	0.12	(1)	(1)	(1)	(1)	12.3	4.8	>6.60	>2.6
3	0.28	16	0.412	0.08	(1)	(1)	(1)	(1)	6.10	2.4	>6.10	>2.4
4	0.28	16	0.411	0.12	(1)	(1)	(1)	(1)	6.10	2.4	>6.10	>2.4
5	0.25	16	0.7	0.28	(1)	(1)	1.87	3.1	7.37	2.9	>7.37	>2.9
6	0.28	16	0.407	0.37	(1)	(1)	5.33	2.1	(1)	(1)	>5.33	>2.1
7	0.28	16	0.411	0.35	6.60	2.6	4.57	1.8	5.84	2.3	5.59	2.2
8	0.28	16	0.457	0.30	5.33	2.1	2.54	1.0	3.81	1.5	3.31	1.5
9	0.28	16	0.406	0.33	2.03	0.8	3.30	1.3	4.57	1.8	3.30	1.3
10	0.28	16	0.55	0.22	1.27	0.5	2.79	1.1	2.79	1.1	2.29	0.9
11	0.28	16	0	0	0	0	0	0	0	0	0	0
12	0.35	20	0.65-0.90	0.26-0.35	(1)	(1)	(1)	(1)	(1)	(1)	11.0	4.3
13	0.35	20	0.5	0.20	(1)	(1)	(1)	(1)	(1)	(1)	1.4	2.9
14	0.35	20	0.334	0.35	7.37	2.9	6.96	2.7	6.10	2.4	3.7	1.5
15	0.35	20	0.9-1.0	0.35-0.39	6.60	2.6	8.64	3.4	3.81	1.5	4.3	1.7
16	0.35	20	0.458	0.39	5.33	2.1	5.59	2.2	3.81	1.5	4.3	1.7
17	0.35	20	0.6-0.9	0.24-0.35	4.83	1.9	4.83	1.9	4.83	1.9	2.1	0.93
18	0.35	20	0.583	0.39	3.05	1.2	1.78	0.7	2.54	1.0	1.5	0.71
19	0.35	20	0	0	0	0	0	0	0	0	0	0
20	0.35	20	0.6	0.24	(1)	(1)	(1)	(1)	(1)	(1)	1.2	0.47
21	0.35	20	1.079	-	(2)	(2)	(2)	(2)	(2)	(2)	(2)	(2)
22	0.31	18	0.6-0.7	0.24-0.28	(1)	(1)	(1)	(1)	(1)	(1)	>20	>8.0
23	0.31	18	0.330	0.26	(1)	(1)	(1)	(1)	(1)	(1)	>20	>8.0
24	0.31	18	0.319	0.37	6.35	2.5	5.59	2.2	7.11	2.8	6.1	2.4
25	0.31	18	0.333	0.35	6.35	2.5	5.59	2.2	5.08	2.0	5.5	2.2
26	0.31	18	0.349	0.43	5.59	2.2	5.08	2.0	4.32	1.7	4.0	1.6
27	0.31	18	0.417	0.35	5.84	2.3	5.08	2.0	4.32	1.5	6.1	2.4
28	0.31	18	0.521	0.8	No Photo						4.3	1.7
29	0.31	18	0.698	0.16	3.05	1.2	3.05	1.2	2.54	1.0	2.5	1.0
30	0.31	18	1.118	0.08	(1)	(1)	(1)	(1)	(1)	(1)	1.2	0.5
31	0.31	18	1.608	0	0	0	0	0	0	0	0	0
32	0.28	16	0.384	0.12	(1)	(1)	(1)	(1)	(1)	(1)	>20	>8.0
33	0.28	16	0.396	0.08	(1)	(1)	(1)	(1)	(1)	(1)	0	0
34	0.28	16	0.381	0.16	(1)	(1)	0.76	0.3	3.30	1.3	3.1	1.2
35	0.28	16	0.403	0.20	2.79	1.1	4.83	1.9	3.30	1.3	4.3	1.7
36	0.28	16	0.404	0.5	4.83	1.9	2.54	1.0	2.03	0.8	3.7	1.5
37	0.28	16	0.392	0.24	4.06	1.6	4.83	1.9	2.79	1.1	3.7	1.5
38	0.28	16	0.598	0.16	(1)	(1)	(1)	(1)	(1)	(1)	2.5	1.0
39	0.28	16	0.992	0	(2)	(2)	0	0	0	0	0.6	0.24
40	0.28	16	0.455	0.12	5.84	2.3	3.30	1.3	2.79	1.1	3.7	1.5
41	0.28	16	0.627	0	0	0	0	0	0	0	0	0

(1) Cavity Termination, W. Under Adjoining Foil or Too Indistinct for Measurement

(2) Cavitation Was Slight and Extremely Irregular Along the Foil Span

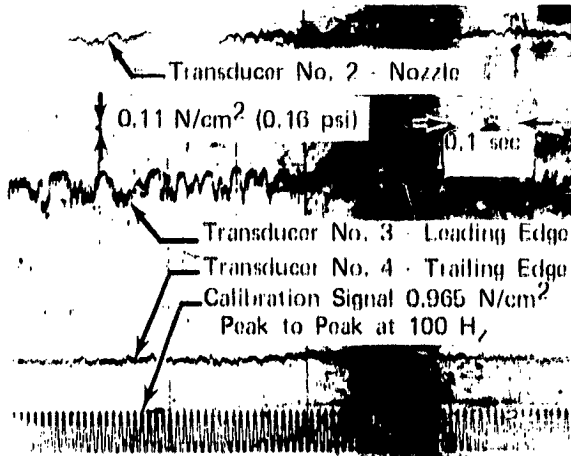
The boundary layer bleed slot valves were closed to observe what effect boundary layer bleed would have on the cavitation pattern for three points, listed as test points No. 19, 31, and 41 in table 3. When the bleed valves were closed (no other action was taken), the cavitation pattern changed significantly. The suction surface cavities, which had been from 8 to 26% chord in length, became very small misty patches, and pressure surface cavities formed. The pressure surface cavities were also very small misty patches at test points No. 19 and 31; however, at test point No. 41 they were about 20% chord in length. Water velocity approaching the cascade remained relatively constant, while static pressure increased, resulting in an increase in cavitation number. The increase in cavitation number explains the reduction in cavity size on the blade suction surfaces; however, the appearance of pressure surface cavitation indicates a change in flow angle (incidence) or in uniformity as well. This shows a qualitative dependence of the cavitation pattern on bleed flow. Cavitation was observed on the slot lip at the lower cavitation numbers, but blade pressure surface cavitation did not occur in the incidence range selected (0.28 to 0.35 rad, 16 deg to 20 deg) when the bleed valves were open.

Measured cavity length and height data are shown plotted and correlated with predictions in paragraph 5.1.2.

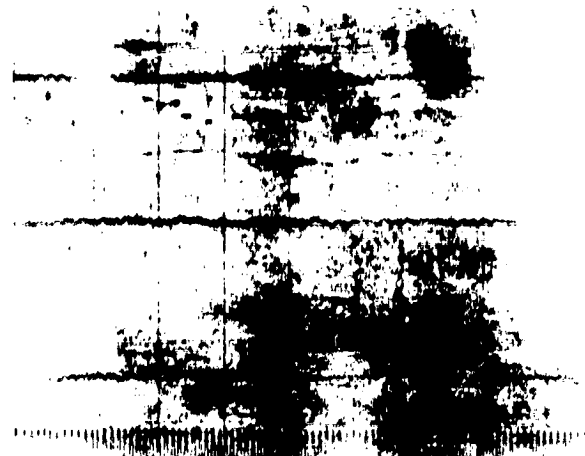
#### 4.1.6.2 Cascade Instability

A summary of the cascade leading edge transducer amplitude (No. 3 in figure 5) and visual observations of cavity motion made during the tests are presented in table 4. An equipment malfunction that was unnoticed while the test points were being recorded caused the loss of tape recorded pressure data for points 1 through 18. The leading edge transducer was the only one to show a significant amplitude during the tests. The upstream transducers (No. 2) and the trailing edge transducer (No. 4) were similar to transducer No. 1, typically showing a peak-to-peak amplitude of  $0.1 \text{ N/cm}^2$  (0.15 psi) and never exceeding  $0.2 \text{ N/cm}^2$  (0.30 psi). The  $0.1 \text{ N/cm}^2$  amplitude is the level of normal tunnel vibration under noncavitating conditions. O-graph traces of transducers No. 2, 3, and 4 at test points No. 28, 30, 36, 37, and 40 are shown in figure 14. These traces are typical and show both the highest and lowest amplitudes recorded at valid test points. It will be noted in table 4 that test point No. 19 has the highest amplitude; however, this point and test points No. 31 and 41 were conducted with the boundary layer bleed slot valves closed, which caused cavitation to occur on the blade pressure surfaces. These three "bleeds off" points are not typical and were not considered in the cascade instability investigation.

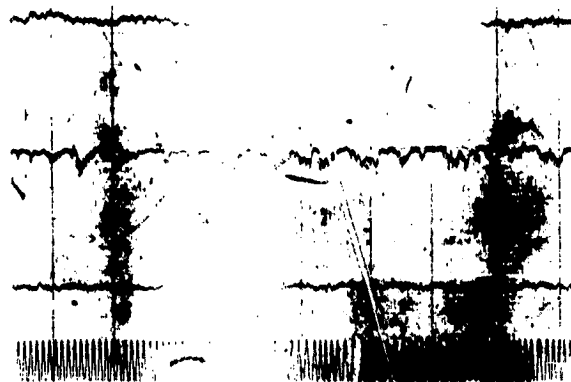
In table 4 the visual observation of cavitation is listed as unsteady or very unsteady at almost all test points. Also, it will be noted that the visual observations do not agree well with the leading edge transducer amplitudes. The reason for this is that the blade cavities almost never appeared steady in the sense of having a definite collapse point. The collapse point was continually moving in a random fashion. Nor was it possible to distinguish a smooth streamline separating the vapor cavity from the surrounding water. The cavity profile was generally irregular and changed shape in a random fashion. To an observer, the irregular shape and random motion gave the impression of unsteady flow, even though the pressure oscillations were no greater than for noncavitating flow.



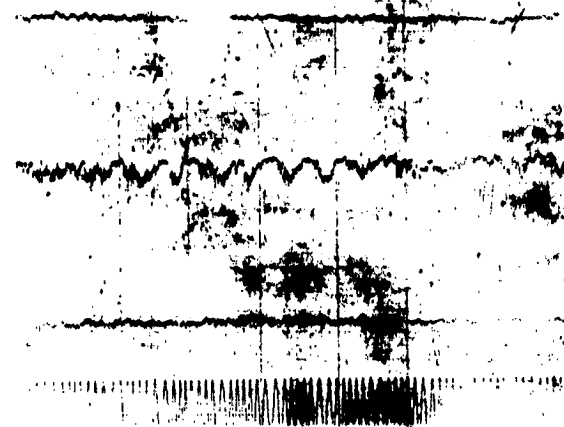
28  $i = 0.31$  Rad (18 deg)  $k = 0.521$



30  $i = 0.31$  Rad (18 deg)  $k = 1.118$



36  $i = 0.28$  Rad (16 deg)  $k = 0.404$



37  $i = 0.28$  Rad (16 deg)  $k = 0.392$



40  $i = 0.28$  Rad (16 deg)  $k = 0.455$

Figure 14. Typical Cascade Tunnel Dynamic Pressure Oscillographs

FD 62669

Table 4. Cascade Dynamic Pressure Data and Observed Cavity Motion

Test Point	Incidence Angle, $i$ rad	Incidence Angle, $i$ deg	Inlet Velocity, $V$ m/s	Inlet Velocity, $V$ ft/sec	Cavitation Number, $k$	Cavity Length, % Chord	Dynamic Pressure Amplitude, $P-P$ $N/cm^2$	Dynamic Pressure Amplitude, $P-P$ $lb/in^2$	Frequency, Hz	Visual Observation of Cavitation
1	0.28	16	~6.56	~21.5	0.387	100	NA <sup>(2)</sup>	NA	NA	Steady
2	0.28	16	~6.56	~21.5	0.402	43	NA	NA	NA	Very Unsteady
3	0.28	16	~6.56	~21.5	0.412	40	NA	NA	NA	Unsteady
4	0.28	16	~6.56	~21.5	0.411	40	NA	NA	NA	Very Unsteady
5	0.28	16	~6.56	~21.5	0.412	50	NA	NA	NA	Very Unsteady
6	0.28	16	~6.56	~21.5	0.407	35	NA	NA	NA	Very Unsteady
7	0.28	16	~6.56	~21.5	0.411	37	NA	NA	NA	Unsteady
8	0.28	16	~6.56	~21.5	0.457	25	NA	NA	NA	Steady
9	0.28	16	~6.56	~21.5	0.406	22	NA	NA	NA	Steady
10	0.28	16	~6.56	~21.5	0.413	15	NA	NA	NA	Steady
11	0.28	16	~6.56	~21.5	2.080	0	NA	NA	NA	Noncavitating
12	0.35	20	~6.56	~21.5	0.354	70 ± 30	NA	NA	NA	Very Unsteady
13	0.35	20	~6.56	~21.5	0.350	48 ± 12	NA	NA	NA	Unsteady
14	0.35	20	~6.56	~21.5	0.334	45	NA	NA	NA	Unsteady
15	0.35	20	~6.56	~21.5	0.338	42	NA	NA	NA	Steady
16	0.35	20	~6.56	~21.5	0.458	32	NA	NA	NA	Unsteady
17	0.35	20	~6.56	~21.5	0.539	32	NA	NA	NA	Unsteady
18	0.35	20	~6.56	~21.5	0.583	16	NA	NA	NA	Steady
19	0.35	20	~6.56	~21.5	1.051	Slight	0.55	0.80	25	B/L Bleedoff
20	0.35	20	~6.56	~21.5	0.827	8	0.10	0.15	(1)	Very Unsteady
21	0.35	20	~6.56	~21.5	1.079	Slight	0.10	0.15	(1)	Intermittent
22	0.31	18	~6.56	~21.5	0.328	>130	0.21	0.30	14	Unsteady
23	0.31	18	~6.56	~21.5	0.330	80 ± 20	0.21	0.30	15	Very Unsteady
24	0.31	18	~6.56	~21.5	0.319	42	0.21	0.30	30	Unsteady
25	0.31	18	~6.56	~21.5	0.333	37	0.10	0.15	(1)	Very Unsteady
26	0.31	18	~6.56	~21.5	0.349	32	0.21	0.30	18	Very Unsteady
27	0.31	18	~6.56	~21.5	0.417	32	0.21	0.30	14	Very Unsteady
28	0.31	18	~6.56	~21.5	0.521	28	0.48	0.70	24	Very Unsteady
29	0.31	18	~6.56	~21.5	0.698	18	0.10	0.15	(1)	Unsteady
30	0.31	18	~6.56	~21.5	1.118	8	0.10	0.15	(1)	Very Unsteady
31	0.31	18	~6.56	~21.5	1.608	Slight	0.41	0.59	30	B/L Bleedoff
32	0.28	16	~5.64	~18.5	0.384	95 ± 35	0.14	0.20	14	Very Unsteady
33	0.28	16	~5.64	~18.5	0.386	75 ± 25	0.14	0.20	10	Very Unsteady
34	0.28	16	~5.64	~18.5	0.381	11	0.14	0.20	8	Unsteady
35	0.28	16	~5.64	~18.5	0.403	24	0.21	0.30	18	Pulsating, Foils 1 and 2
36	0.28	16	~5.64	~18.5	0.404	21	0.35	0.51	20	Steady
37	0.28	16	~5.64	~18.5	0.392	26	0.35	0.51	23	Pulsating, Foils 1 and 2
38	0.28	16	~5.64	~18.5	0.598	16	0.10	0.15	(1)	Steady
39	0.28	16	~5.64	~18.5	0.992	0	0.10	0.15	(1)	Intermittent
40	0.28	16	~5.64	~18.5	0.455	26	0.28	0.41	10	Steady
41	0.28	16	~5.64	~18.5	0.627	0	0.28	0.41	23	B/L Bleedoff

(1) Frequency Was Not Apparent on Oscillograph

(2) NA = Not Available

Amplitudes and frequencies recorded by the leading edge transducer are plotted against cavitation number in figure 15. This figure reveals no discernible trend of either amplitude or frequency. At cavitation numbers greater than 0.55, only normal vibration is present. Between 0.55 and 0.30, both amplitude and frequency are random. Also shown in figure 15 for comparison is the highest amplitude recorded by Acosta and Wade (6). The present leading edge amplitudes are of the same order of magnitude as those measured by Acosta; however, Acosta recorded trailing edge amplitudes of the same order of magnitude as the leading edge, while the present trailing edge amplitudes never changed significantly from normal vibration levels, as shown in the O-graph traces of figure 14. The reason may be the proximity of the trailing edge transducer to the plenum tank, which effectively absorbed pressure oscillations.

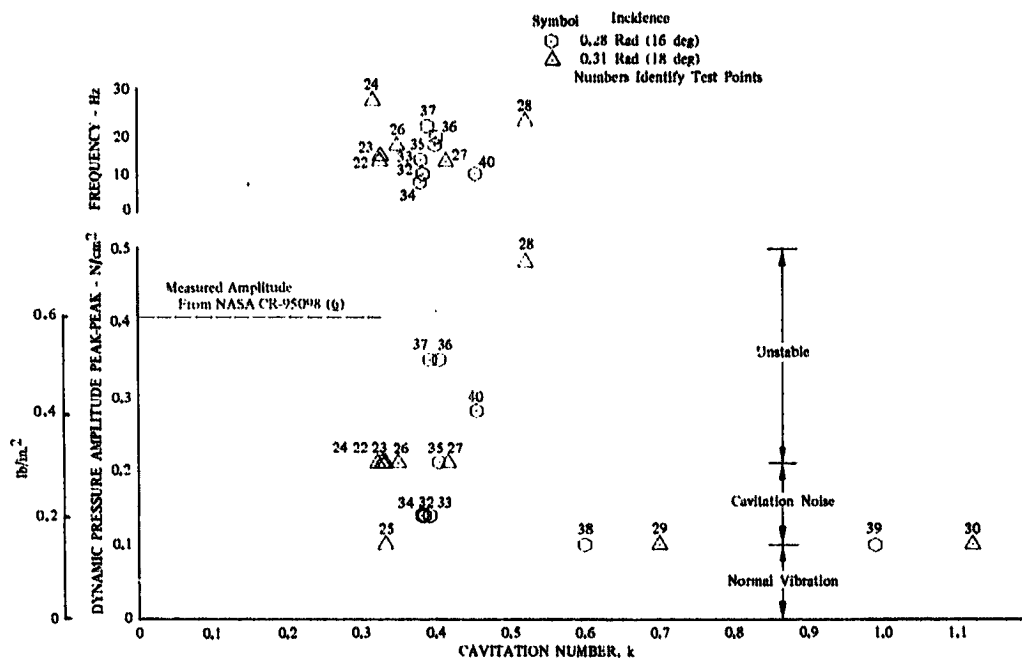


Figure 15. Variation of Cascade Dynamic Pressure Data With Cavitation Number DF 90794

Cavitation is generally unsteady in the sense of continuous irregular motion of the cavity, particularly in the collapse zone. However, unsteady cavitation does not necessarily mean that the flow is unstable. In experimentally determining whether a cavitating flow through a cascade or an inducer is stable or unstable the viewpoint adopted is that the flow is unstable only if upstream and downstream flowrates and pressures, or internal flowrates and pressures, vary in some regular pattern. This definition includes blade-to-blade propagation of cavitation and unisonous cavity oscillation as being unstable, and is intended to distinguish between these two phenomena and cavitation noise generated by random irregular cavity motion, which is considered stable.

Flow through the cascade was certainly unsteady, as witnessed by the irregularities in cavity shape shown in the photographs and the visual observations noted in table 4. However, from this evidence it is difficult to characterize a given test point as stable or unstable in the sense of propagating cavitation or of

unisonous cavity oscillation. The best single description of the cavitation pattern would have to be "random unsteadiness of each cavity." If overall flowrate were oscillating significantly, one would expect to see most, if not all, of the cavities changing size in unison. Only at two test points (No. 36 and 37) was any regular pulsation of cavity size observed, and then only blades No. 1 and 2 were involved. On the other hand, it was not apparent that any type of blade-to-blade propagation was occurring. Rather, complete randomness of the motion of each cavity was the most prominent observable feature of the flow. Of course it is difficult to determine by eye whether two or more cavities are oscillating in unison if a random unsteadiness is superimposed on the unisonous motion, so visual observation is not always a reliable indication of stable or unstable flow. Whether a given operating point was stable or unstable must be decided primarily from the leading edge pressure transducer traces.

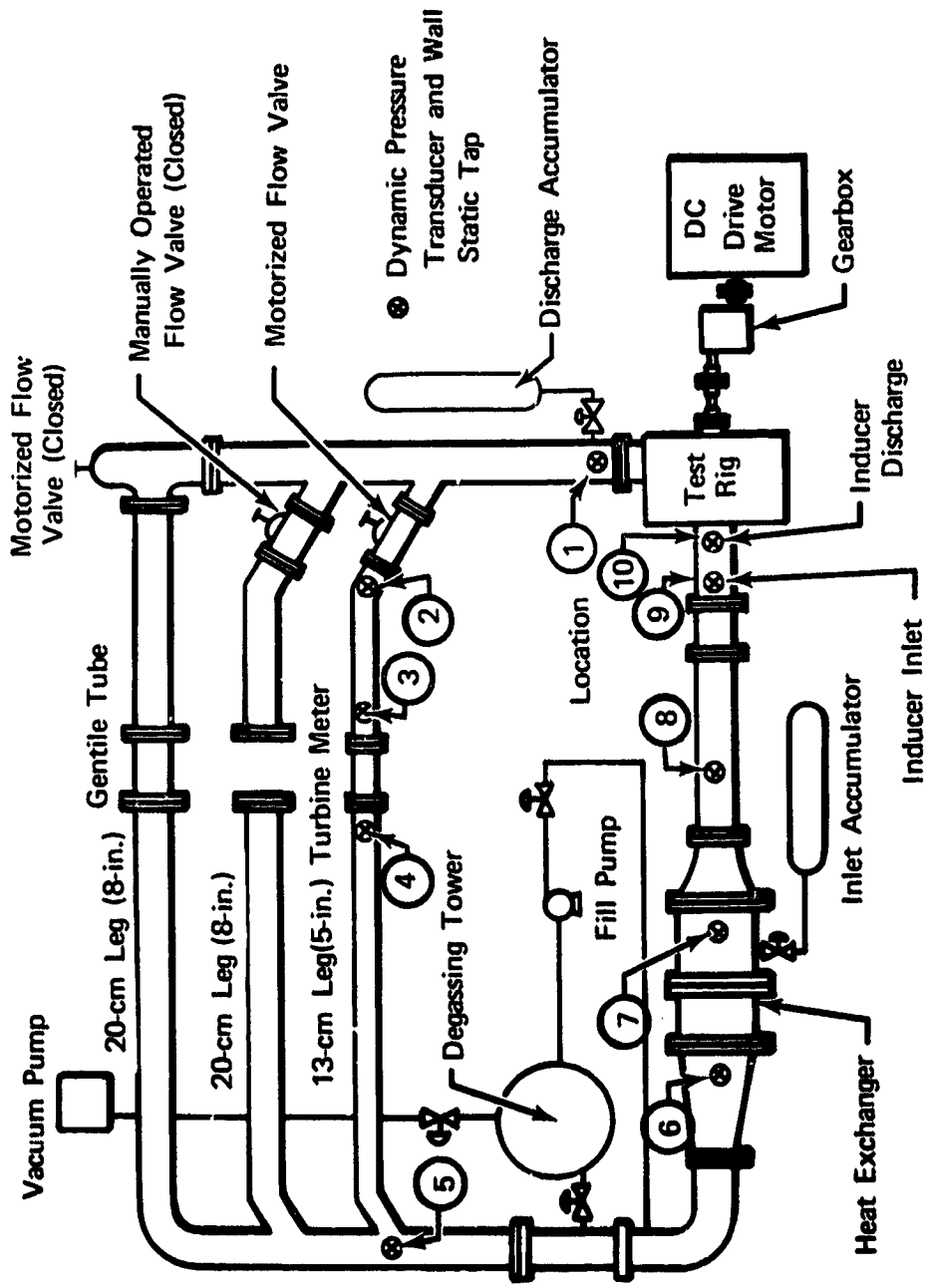
In figure 15 the leading edge transducer amplitudes have been divided into three bands in an attempt to make a distinction between normal tunnel vibration, cavitation noise, and unstable flow. Normal vibration levels were easily identified by the amplitudes recorded at the higher cavitation numbers. The dividing point between cavitation noise and unstable flow was not easily identified, and has been arbitrarily selected as the level separating the majority of the test points from the four test points showing the highest amplitudes. If any point were unstable, one would expect it to be one of the points with highest amplitude. A comparison of the visual observations, which are listed in table 4, with the four highest pressure amplitude points (No. 28, 36, 37, and 40) shows no particular correlation between the dynamic pressure data and the observations. Test point No. 28 is listed as very unsteady, No. 36 as steady, No. 37 as pulsating, and No. 40 as steady. Figure 15, therefore, shows the only possible distinction between the experimentally stable and unstable test points. The points are discussed further and correlated with predictions in paragraph 5.2.

## 4.2 INDUCER EXPERIMENT

### 4.2.1 Facility

The test facility used for the rotating inducer instability tests was P&WA<sup>TM</sup> FRDC test stand D-34, a schematic of which is shown in figure 16. The 13-cm (5-in.) inside leg of the loop was used for all testing.

The test rig is driven by a 250-hp dc motor through a 2.33:1 ratio gearbox, providing output speeds to 9000 rpm. Rig speed is automatically regulated to within 0.03% by control of the dc output of the motor-generator set supplying drive motor power. The test loop uses demineralized water and has a heat exchanger for control of loop water temperature. A complete degassing system is available for the deaeration of the test loop water. Loop pressures are controlled by either the inlet or discharge accumulator system, depending on the inlet pressure required. The inlet accumulator is used for inlet pressures above atmospheric, and the discharge accumulator is used for lower than atmospheric pressures. A schematic typical of both accumulator systems is shown in figure 17. Inlet pressures down to approximately 2 N/cm<sup>2</sup> (2.9 psi) are possible. Flowrate is controlled by a motorized flow valve located in the 13-cm (5-in.) leg and measured with a turbine-type flowmeter located downstream of the flow valve.



FD 59365A

Figure 16. Inducer Test Loop

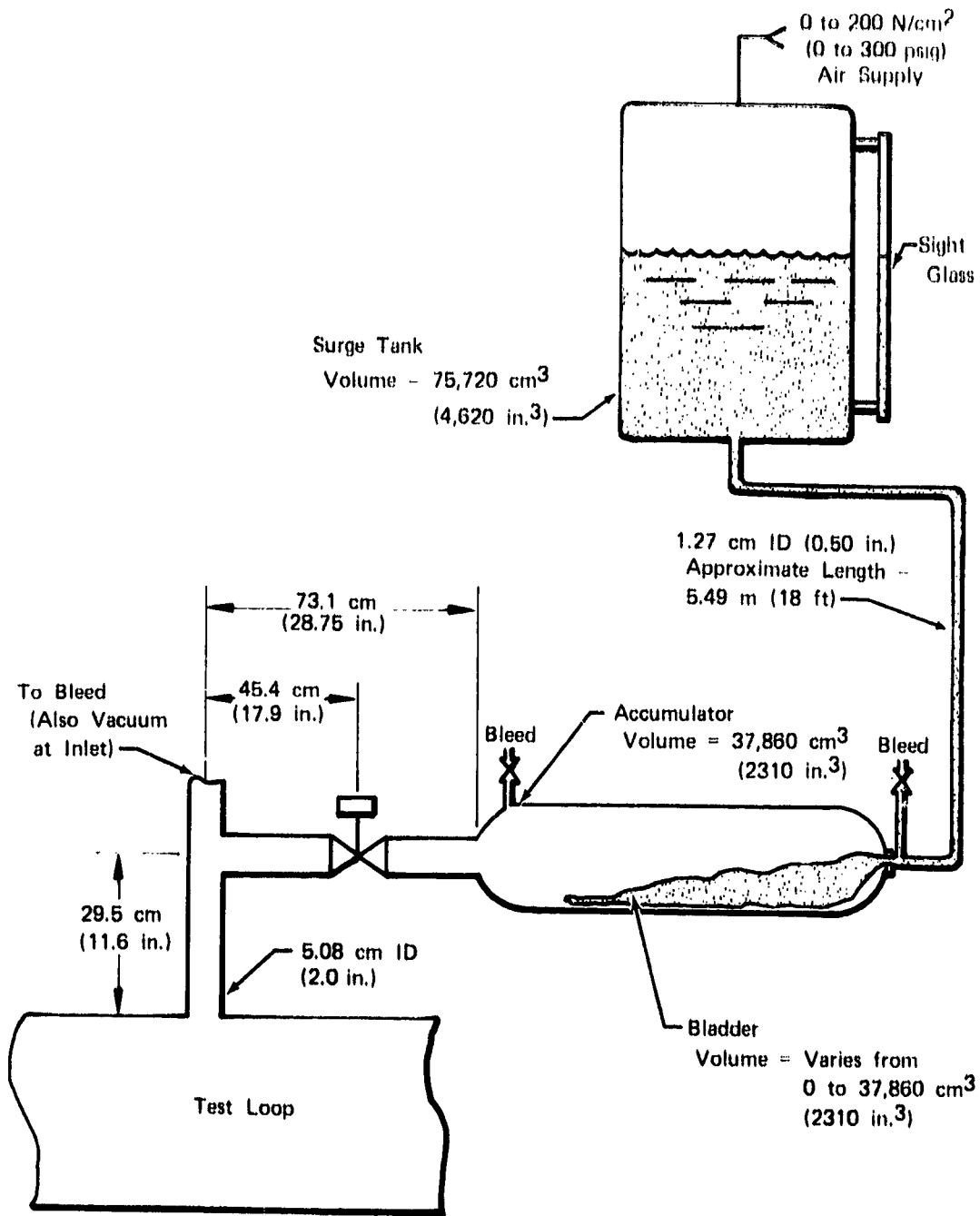


Figure 17. Accumulator System Schematic

FD 59366

The inducer test rig design is shown in figure 18. The inducer housing was made of transparent acrylic and thus permitted observation of the inducer cavitation. The inducer is overhung from its bearings in the inlet line and inlet flow is unobstructed. Figure 19 shows an overall view of the rig on the test stand.

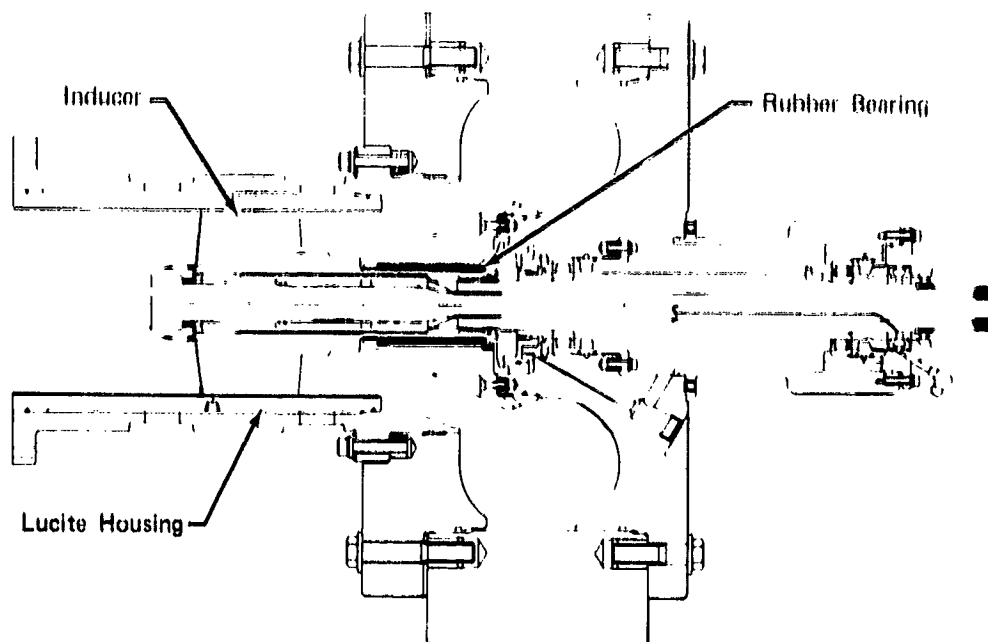


Figure 18. Inducer Test Rig

FD 63041

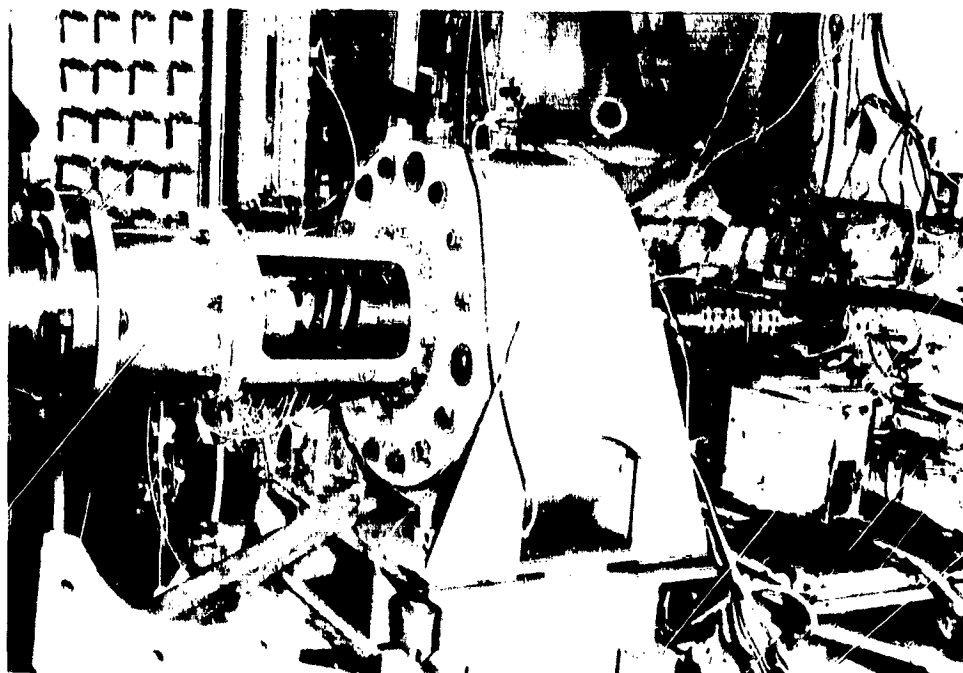


Figure 19. Inducer Installed in Test Facility

FE 89984

#### 4.2.2 Inducers

The two inducers used in the test program were fabricated in the inducer load and stress project, NASA Contract NAS3-11210, as reported in (1). The inducers were identical except that the first inducer had a radial leading edge, while the second inducer was swept back at a cone angle of 0.28 rad (16 deg), in the manner shown in figure 20. The contour cut was moved axially forward the distance "Y" to provide for the fitting of the blade leading edge into the hub. This sweepback produced the leading edge contour shown in figure 21. As the figure shows, the swept leading edge inducer had pressure tap tubing installed in the blades for the previous program. The blade surface around the tubing was filled with epoxy to provide a smooth surface.

The inducer had three blades with inlet tip blade angles of 0.14 rad (8 deg). The blading was hollow to a solidity of approximately 1.0, at which point camber was applied exponentially. The sweep cutback was within the blade hollow portion at all radii, so that blade leading edge metal angle was the same for the radial and swept leading edge inducers. Both inducers were machined from titanium. Table 5 summarizes the basic inducer design parameters.

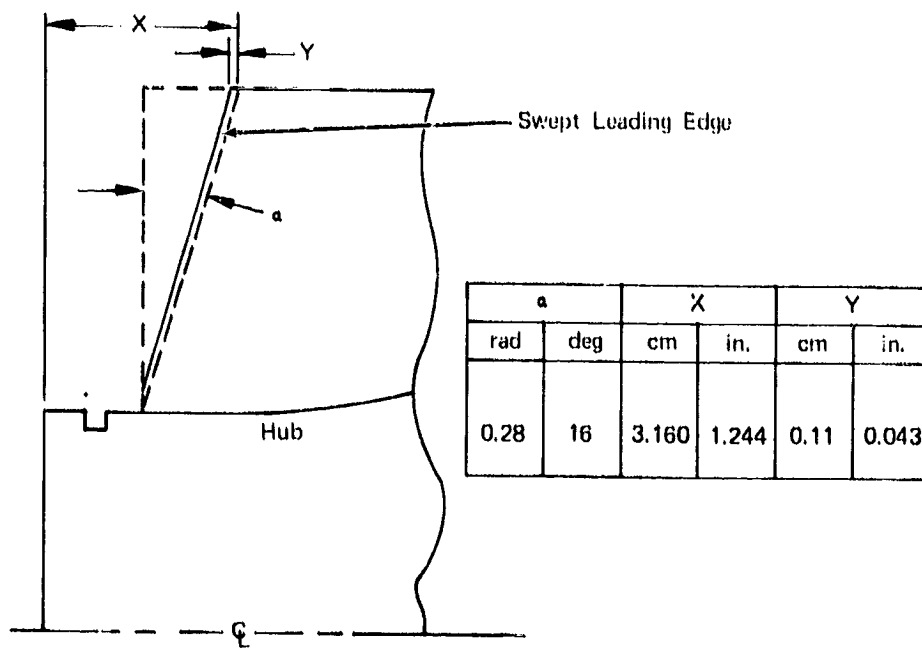


Figure 20. Definition of Inducer Leading Edge Sweepback Angle

FD 61210A

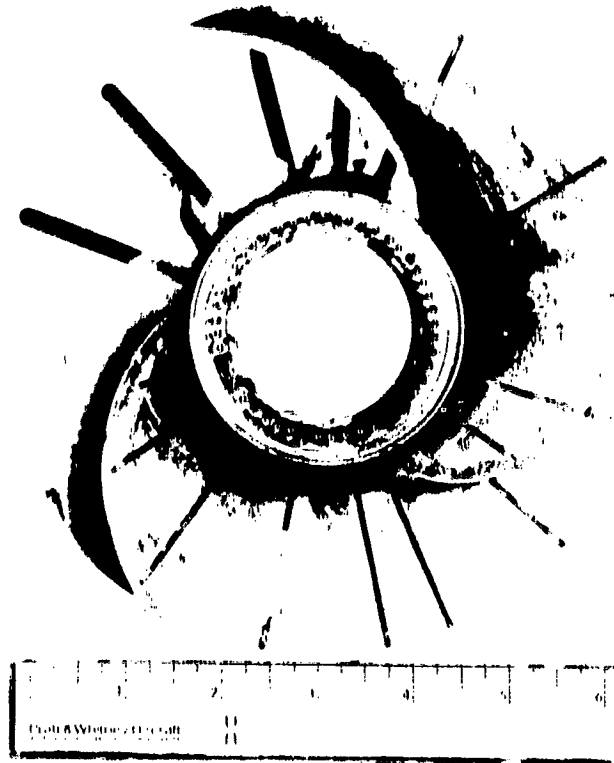


Figure 21. Inducer With 0.28 rad (16 deg) Leading  
Edge Sweepback

FE 113407

Table 5. Inducer Design Parameters

Inlet Hub Diameter, cm (in.)	7.11	(2.80)
Discharge Hub Diameter, cm (in.)	9.49	(3.74)
Tip Diameter (Constant), cm (in.)	17.80	(7.00)
Blade Thickness (Constant), cm (in.)	0.330	(0.130)
Inlet Tip Blade Angle, rad (deg)	0.140	(8.0)
Inlet Hub Blade Angle, rad (deg)	0.339	(19.35)
Discharge Tip Blade Angle, rad (deg)	0.180	(10.0)
Discharge Hub Blade Angle, rad (deg)	0.318	(18.25)
Inlet Tip Blade Wedge Angle, rad (deg)	0.140	(8.0)
Tip Leading Edge Radius, cm (in.)	0.081	(0.032)
Number of Blades	3	
Design Flow Coefficient, $\bar{\Phi}$	0.070	
Design Head Coefficient, $\bar{\Psi}$	0.240	

#### 4.2.3 Instrumentation

Inducer performance instrumentation was located as shown in figure 22. Inlet total pressure was measured approximately 89 cm (35 in.) upstream of the inducer leading edge with a Kiel probe located at the inlet pipe centerline. A traverse wedge probe was used near the inducer leading edge to monitor inlet flow angle and flow velocity at a radius near the inducer tip (8.66 cm, 3.41 in.). Discharge total and static pressure and flow angle were gathered with another traverse wedge probe. For nontraversing tests, the probe was set at a radius that was representative of mass averaged total head. Both inlet and exit probes were air calibrated before installation, and static pressure readings were corrected accordingly. Static pressures at the upstream measurement station and immediately upstream and downstream of the inducer were measured with static wall taps. All pressures were read from precision,  $\pm 0.25\%$  F.S., pressure gages.

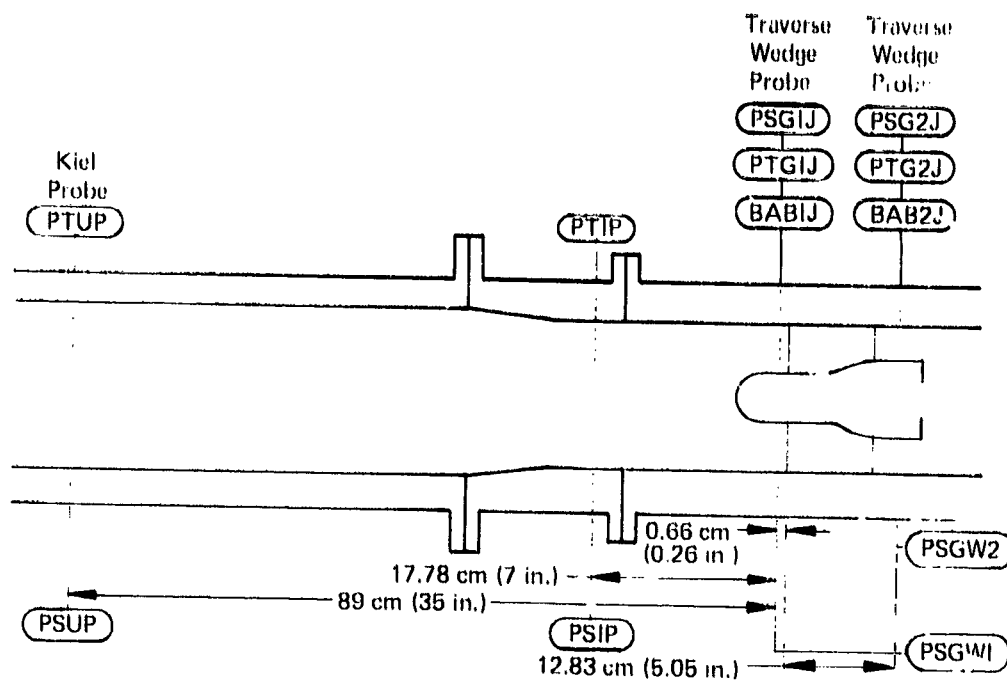


Figure 22. Inducer Pressure Instrumentation Locations

FD 63042

Dynamic pressure measurements were taken with piezoelectric transducers\* mounted flush with the inside walls at the locations shown in figure 16. The ten locations were selected to provide complete coverage of the inducer-flow loop system. Output of the transducers was recorded on magnetic tape. Static pressures from flush-mounted static wall taps were also gathered at each of the ten locations and read from gages.

\*Kistler Model 601 H

A turbine-type flowmeter located downstream of the flow throttling valve in the 13-cm (5-in.) log was used to measure flowrate. Readout was on a digital counter. Water temperature was measured with a chromel-alumel thermocouple located upstream of the inducer inlet. Inducer speed was measured by electronically counting the output of a magnetic transducer that sensed the passing frequency of a 60-tooth gear on the rig drive shaft. That signal was multiplied by a preset value and transmitted to a panel-mounted digital counter.

Table 6 summarizes the instrumentation and the estimated maximum error associated with each reading.

#### 4.2.4 Test Procedure

Since the inducers and the test rig that were used in this program were used in previous programs, the tests were numbered consecutively from the previous programs. This program represented the eighth series of tests and each test is designated 8.XX with the "XX" indicating the test number for this program.

##### 4.2.4.1 Performance Tests

Prior to the start of instability testing, noncavitating performance tests were conducted on the radial leading edge inducer to supplement the data reported in (1). Performance data were available for flow coefficients of 0.096, 0.090, and 0.084 and additional data were required for 0.070. The available data had also been obtained with blade pressure instrumentation on the inducer, and the effects of the instrumentation on performance were unknown. (The radial inducer used in this program had no blade instrumentation.)

The performance tests were conducted by setting a speed, flow, and inlet pressure, and all other instrumentation were recorded. Total pressure, static pressure, and flow angle were manually traversed at each of seven radial stations (spaced at equal area increments) at the inducer inlet and exit. In total, three flow coefficients (0.096, 0.084, and 0.070) were explored. The speed was a constant 513.1 rad/s (4900 rpm) and inlet pressure a constant 20.7 N/cm<sup>2</sup> gage (30.0 psig).

##### 4.2.4.2 Accumulator Evaluation

Before the instability testing was started, the effects of the test loop pressure control accumulators on the response of the total inducer-test loop system was determined. Various combinations of "hard" and "soft" (water or air in the bladder) accumulators were tried while pressure oscillations were being generated with the radial leading edge inducer. A schematic typical of the inlet and discharge accumulator systems is shown in figure 17. The Kistler transducers, mounted in the water loop at the locations shown in figure 16, were used to measure dynamic data during the time the different combinations of accumulators were being tried. Subsequent analysis of the dynamic pressure data showed it to be independent of the accumulator configurations. Dynamic pressure amplitudes as high as  $\pm 4$  N/cm<sup>2</sup> ( $\pm 6$  psi) were generated at the inducer discharge (location 10), diminishing to approximately  $\pm 1$  N/cm<sup>2</sup> ( $\pm 1.5$  psi) at location 3. Negligible pressure amplitudes were measured at locations 4, 5, 6, and 7. The amplitude at location 8 was approximately  $\pm 1$  N/cm<sup>2</sup> ( $\pm 1.5$  psi), and data at location 9 were obscured by high pressure amplitudes at blade passing frequency.

Table 6. Inducer Test Instrumentation

Symbol	Parameter	Sensor	Readout	Range	Maximum Error
AN	Speed	Magnetic Transducer	Counter	-	0.1 rad/s (1 rpm) 2%
Q	Flow	Turbine Flowmeter	Counter	94,600 cm <sup>3</sup> /s (1500 gpm)	
T	Temperature	Thermocouple	Meter	-	1.1°K (2°F)
PSUP	Pressure-Static, Upstream	Wall Tap	Gage	69 N/cm <sup>2</sup> (100 psia)	0.25% F.S.
PTUP	Pressure-Total, Upstream	Kiel Probe	Gage	69 N/cm <sup>2</sup> (100 psia)	0.25% F.S.
PSIP	Pressure-Static, Inlet	Wall Tap	Gage	69 N/cm <sup>2</sup> (100 psia)	0.25% F.S.
PTIP	Pressure-Total, Inlet	Kiel Probe	Gage	69 N/cm <sup>2</sup> (100 psia)	0.25% F.S.
PSGW1	Pressure-Static, Wall	Wall Tap	Gage	69 N/cm <sup>2</sup> (100 psia)	0.25% F.S.
PSGW2	Pressure-Static, Wall	Wall Tap	Gage	69 N/cm <sup>2</sup> (100 psia)	0.25% F.S.
PSK1-7	Pressure-Static, Wall	Wall Tap	Gage	69 N/cm <sup>2</sup> (100 psia)	0.25% F.S.
PDK1-10	Pressure-Dynamic, Wall	Piezoelectric Transducer	Tape	10,300 N/cm <sup>2</sup> (15,000 psia)	10%
PSG1J	Pressure-Static, Inlet Traverse	Wedge Probe	Gage	69 N/cm <sup>2</sup> (100 psia)	0.25% F.S.
PTG1J	Pressure-Total, Inlet Traverse	Wedge Probe	Gage	69 N/cm <sup>2</sup> (100 psia)	0.25% F.S.

Table 6. Inducer Test Instrumentation (Continued)

Symbol	Parameter	Sensor	Readout	Range	Maximum Error
PSG2J	Pressure-Static, Exit Traverse	Wedge Probe	Gage	110 N/cm <sup>2</sup> (160 psia)	0.25% F.S.
PTG2J	Pressure-Total, Exit Traverse	Wedge Probe	Gage	110 N/cm <sup>2</sup> (160 psia)	0.25% F.S.
BAB1J	Flow Angle-Inlet Traverse	Wedge Probe	Vernier	6.3 rad (360 deg)	0.09 rad (0.5 deg)
BAB2J	Flow Angle-Exit Traverse	Wedge Probe	Vernier	6.3 rad (360 deg)	0.09 rad (0.5 deg)

There was negligible time lag between the signals at locations 10 and 2 (from upstream to downstream of the discharge accumulator), and the amplitude at location 2 was only slightly lower than that at location 10. Because the accumulators had negligible effect, the tests were conducted with the "hard" accumulator configuration since it was the most convenient to use.

#### 4.2.4.3 Instability Tests

The demineralized water used in the flow loop was deaerated prior to each instability test as it was transferred from the storage tank to the test loop. The water was pumped into a 0.38-m<sup>3</sup> (100-gal) degassing tower, where it was heated to 120°F and held for 10 to 15 minutes while a vacuum pump evacuated the tower and the empty test loop to approximately 2 N/cm<sup>2</sup> absolute (2.9 psia). The water was then transferred from the degassing tower to the loop, while the loop was maintained under the 2 N/cm<sup>2</sup> (2.9 psia) vacuum. Approximately three towers of water were required to complete a loop fill. Once the test loop was filled, the vacuum line valve was closed and pressure, supplied by the tower-to-loop transfer pump, was allowed to build to the pump discharge limit (approximately 17 N/cm<sup>2</sup>, 25 psia), and all high spots in the test loop were bled of trapped air from existing bleed valves and pressure gage lines were purged of air bubbles. The transfer pump valves were then closed and the inlet accumulator system pressurized with air to permit the control of the loop pressure from the control room. At this point the loop was ready for operation.

Prior to the start of each test, a check was made of the air content of the loop water to determine how effective the deaeration procedure had been. The rig was run at approximately 314 rad/s (3000 rpm) with the flow throttling valve wide open and an inlet pressure of about 17 N/cm<sup>2</sup> absolute (25 psia), as controlled by the inlet accumulator. The inlet accumulator system was then isolated from the loop with a valve; the discharge accumulator system was brought up to a pressure equal to the loop static pressure at the point where the discharge accumulator joins the loop; the valve between the discharge accumulator and the loop was opened; and rig inlet pressure was controlled through regulation of the inducer discharge pressure. The water level in the discharge surge tank sight glass was noted at this point (figure 17), and the inducer inlet pressure was reduced from 17 N/cm<sup>2</sup> (25 psia) to approximately 6 N/cm<sup>2</sup> absolute (9 psia), which was the loop limit at that inducer speed. The change in water level in the sight glass was then noted again. The amount of water rise in the tank corresponded to the change in volume of the test loop system. An increase in volume of approximately 0.0037 m<sup>3</sup> (0.13 ft<sup>3</sup>) in the surge tank (this increase corresponds to an increase of 0.35% of the volume in the total loop system) was found to be the facility limit in previous programs and as such was the goal for the deaeration process. If the water was found to be sufficiently deaerated, as evidenced by less than a 0.0037 m<sup>3</sup> (0.13 ft<sup>3</sup>) increase in surge tank water volume, the inlet pressure was increased above ambient and the test run was started. Otherwise, the loop was drained and the deaeration process repeated.

Instability tests were conducted by setting rotative speed at 513.1 rad/s (4,900 rpm) and flow correspondent to one of the three selected flow coefficients (0.090, 0.084, or 0.070), and dropping inlet total pressure from approximately 24.8 N/cm<sup>2</sup> (36 psia) to a point where head rise fell off by approximately 20%.

Approximately 12 points were selected in this range to define the shape of the head rise vs cavitation number curve and to identify the range of unstable operation. A complete set of steady and dynamic pressure data were taken at each point. The cavitation was also observed and noted through the acrylic housing with the aid of a strobe light.

#### 4.2.5 Data Reduction

Inducer performance data were defined as the head rise and efficiency between the upstream measurement station (Loop Station "8", PTUP in figure 22) and the discharge measurement station (Loop Station "9", PTG2 in figure 22). The Kiel probe at Station "8" was sufficiently far upstream that prerotation did not effect its readings, while the wedge probe at the inducer inlet (Station "9", PTG1 in figure 22) was effected by prerotation. Inlet conditions were calculated from the data as follows:

Upstream Total Pressure:	$P_8 = \text{PTUP}$ (Corrected for Gage Height)
Inlet Total Head:	$\bar{H}_1 = H_9 = P_8/\rho$
Inlet Absolute Velocity (Assumed Axial):	$\bar{V}_1 = Q/A_1$
Inlet Static Head:	$\bar{h}_1 = \bar{H}_1 - V_1^2/2g$
Inlet Tip Relative Velocity:	$V_1' = \sqrt{\bar{V}_1^2 + U_t^2}$
Inlet Tip Relative Velocity Head:	$q_1' = V_1'^2/2g$
Tip Cavitation Number:	$\bar{k} = (\bar{h}_1 - h_v)/q_1'$
Inlet Tip Flow Coefficient:	$\bar{\phi} = \bar{V}_1/U_t$

Discharge conditions were calculated from the measured data at seven radial measurement stations, as follows:

Discharge Total Head:	$H_d = \frac{\text{PTG2J}}{\rho}$ (corrected for gage height)
Discharge Static Head:	$h_d = \frac{\text{PSG2J}}{\rho}$ (corrected for static pressure and gage height)
Discharge Flow Angle:	$\beta_d = \text{BAB2J}$
Discharge Velocity:	$V_d = \sqrt{2g(H_d - h_d)}$
Discharge Axial Velocity:	$V_{zd} = V_d \sin \beta_d$
Discharge Tangential Velocity:	$V_{ud} = V_d \cos \beta_d$

$$\begin{aligned} \text{Average Discharge Total Head: } \bar{H}_d &= \frac{\sum_{R_t}^{R_h} V_{zd} R \Delta R}{\sum_{R_t}^{R_h} V_{zd} R \Delta R} \\ \text{Average Discharge Ideal Head: } \bar{H}_{id} &= \frac{\sum_{R_t}^{R_h} V_{zd} R \frac{U V_{ud}}{g} \Delta R}{\sum_{R_t}^{R_h} V_{zd} R \Delta R} \\ \text{Average Head Coefficient: } \bar{\psi} &= \frac{g(\bar{H}_d - \bar{H}_l)}{U_t^2} \\ \text{Average Efficiency: } \bar{\eta} &= \frac{(\bar{H}_d - \bar{H}_l)}{\bar{H}_{id}} \end{aligned}$$

(Assumes  $V_{ul} = 0$ )

Inlet total pressure, static pressure, and flow angle were measured at the inducer inlet tip and were reduced as follows:

$$\begin{aligned} \text{Inlet Total Head: } H_t &= \frac{PTG1J}{\rho} \text{ (corrected for gage height)} \\ \text{Inlet Static Head: } h_t &= \frac{PSG1J}{\rho} \text{ (corrected for gage height)} \\ \text{Inlet Flow Angle: } \beta_t &= BAB1J \\ \text{Inlet Velocity: } V_t &= \sqrt{2g(H_t - h_t)} \\ \text{Inlet Axial Velocity: } V_{zt} &= V_t \sin \beta_t \\ \text{Inlet Tangential Velocity: } V_{ut} &= V_t \cos \beta_t \end{aligned}$$

Nomenclature is defined in the Appendix. Measurements and calculations were performed using the English system of units and were converted to the SI for presentation in this report.

The magnetic-tape-recorded, piezoelectric, transducer data were reduced with the aid of a spectrum analyzer. A block diagram of the system used is shown in figure 23. The input (test data on the magnetic tape) was input to an amplifier and multiplied by some factor N. This amplification was necessary to ensure that the data entering the spectrum analyzer were within the analyzer input level limits. The spectrum analyzer contained an internal 50 Hz low-pass filter with a 0.16 Hz noise bandwidth. A 10-sec record length of transducer data was put into the spectrum analyzer's memory after passing through this filter.

This information was converted to a frequency vs amplitude output with a resolution of 0.1 Hz. After passing through an attenuator to null out the effects of the first amplifier, the output was scaled for plotting purposes and then plotted on paper by a Moseley X-Y recorder. The resultant plots had a frequency scale of 0 to 50 Hz, and are accurate at all frequencies above 0.3 Hz, which is the lower limit of the data response and reduction system.

Input to the amplifier and output of the scaler were monitored with oscilloscopes, as shown in figure 23, to ensure correct system operation. Prior to the taped data being input, a calibration signal of known amplitude and frequency was injected into the system and proper functioning of the entire setup was checked. The tape reproducer was identical to the recorder used to gather the data at the test stand, thus ensuring that what came off the tape was identical to what went on.

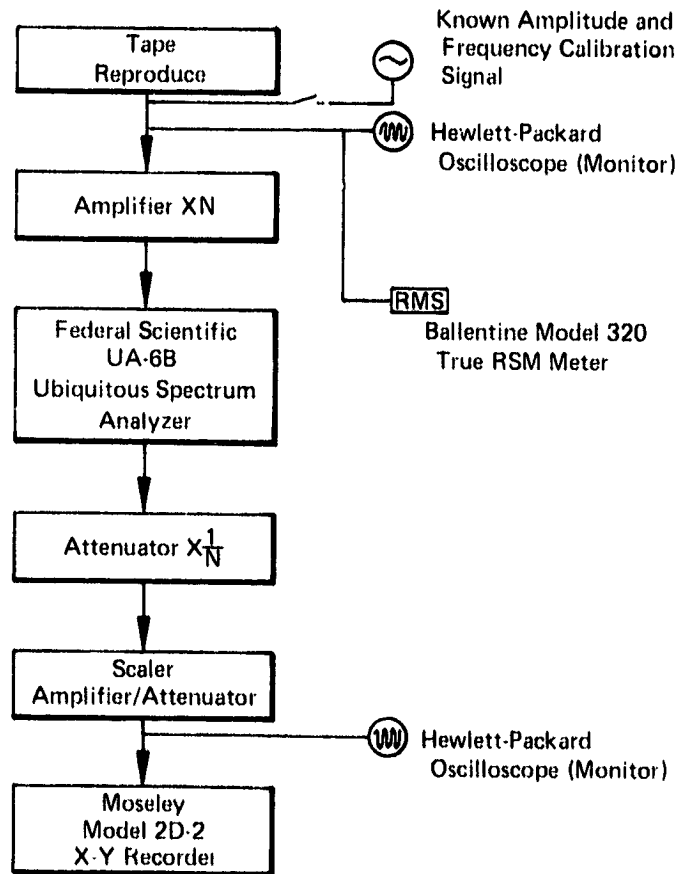


Figure 23. Data Tape Analyzer System

FD 63040

#### 4.2.6 Test Results

A list of inducer tests and test point conditions is given in table 7. The first three tests (8.01, 8.02, and 8.03), were noncavitating performance tests for the radial leading edge inducer; tests 8.04 through 8.08 were radial inducer stability tests; and tests 8.09 through 8.11 were swept inducer stability tests.

Table 7. Summary of Inducor Test Points

Test No.	Speed		Flow		Inlet Total Pressure		Water Temperature		Comments
	rad/s	rpm	cm <sup>3</sup> /s	gpm	N/cm <sup>2</sup>	psig	°K	°F	
Radial Loading Edge Inducor									
8.01	513.1	4900	91,600	1450	20.7	30.0	302.4	85	Noncavitating Performance Test
8.02	513.1	4900	80,260	1272	20.7	30.0	304.1	88	Noncavitating Performance Test
8.03	513.1	4900	66,890	1060	20.7	30.0	305.7	91	Noncavitating Performance Test
8.04	513.1	4900	85,940	1362	14.6	21.2	302.4	85	Test loop water contained excessive amount of air (0.0148 m <sup>3</sup> , 4 gal, registered during deaeration test, as compared with 0.0037 m <sup>3</sup> , 1 gal, for all subsequent runs).
	513.1	4900	85,940	1362	11.2	16.2	303.0	86	
	513.1	4900	85,940	1362	8.0	11.6	304.1	88	
	513.1	4900	85,940	1362	3.8	5.5	304.7	89	
	513.1	4900	85,940	1362	1.0	1.4	305.2	90	
	513.1	4900	85,940	1362	0.3	0.4	305.2	90	
	513.1	4900	85,940	1362	-0.3	-0.45	305.2	90	
	513.1	4900	85,940	1362	-1.0	-1.4	305.2	90	
	513.1	4900	85,940	1362	-2.1	-3.0	305.2	90	
	513.1	4900	85,940	1362	-2.4	-3.5	305.2	90	
8.05	513.1	4900	80,260	1272	15.0	21.8	302.4	85	Discharge accumulator system developed small line leak during test, thereby causing difficulty in holding low pressure test points steady.
	513.1	4900	80,260	1272	8.1	11.7	302.4	85	
	513.1	4900	80,260	1272	4.8	6.9	303.6	87	
	513.1	4900	80,260	1272	0.7	1.0	304.7	89	
	513.1	4900	80,260	1272	-0.9	-1.3	305.2	90	
	513.1	4900	80,260	1272	-2.0	-2.9	305.2	90	
	513.1	4900	80,260	1272	-2.4	-3.5	305.2	90	
	513.1	4900	80,260	1272	-3.1	-4.5	305.2	90	
	513.1	4900	80,260	1272	-4.8	-6.9	305.2	90	
	513.1	4900	80,260	1272	-6.0	-8.7	305.2	90	
8.06	513.1	4900	66,890	1060	14.8	21.5	300.6	82	Normal
	513.1	4900	66,890	1060	8.1	11.7	303.0	86	
	513.1	4900	66,890	1060	4.7	6.8	303.6	87	
	513.1	4900	66,890	1060	1.2	1.7	304.1	88	
	513.1	4900	66,890	1060	0.8	1.2	304.1	88	
	513.1	4900	66,890	1060	-0.6	-0.9	304.7	89	
	513.1	4900	66,890	1060	-1.8	-2.6	304.7	89	
	513.1	4900	66,890	1060	-2.4	-3.5	305.2	90	
	513.1	4900	66,890	1060	-4.4	-6.4	305.2	90	
	513.1	4900	66,890	1060	-5.7	-8.3	305.2	90	
	513.1	4900	66,890	1060	-5.9	-8.6	305.2	90	
	513.1	4900	66,890	1060	-6.1	-8.9	305.2	90	

Table 7. Summary of Inducer Test Points (Continued)

Test No.	Speed		Flow		Inlet Total Pressure		Water Temperature		Comments
	rad/s	rpm	cm <sup>3</sup> /s	gpm	N/cm <sup>2</sup>	psig	°K	°F	
Radial Leading Edge Inducer									
8.07	513.1	4900	85,940	1362	15.0	21.7	302.4	85	Repeat of test 8.04 with water deaerated to stand limit.
	513.1	4900	85,940	1362	7.9	11.5	304.1	88	
	513.1	4900	85,940	1362	4.5	6.5	304.1	88	
	513.1	4900	85,940	1362	1.0	1.5	304.1	88	
	513.1	4900	85,940	1362	-0.5	-0.7	304.1	88	
	513.1	4900	85,940	1362	-1.1	-1.6	304.1	88	
	513.1	4900	85,940	1362	-1.8	-2.6	304.1	88	
	513.1	4900	85,940	1362	-2.4	-3.5	304.1	88	
	513.1	4900	85,940	1362	-3.1	-4.5	304.1	88	
	513.1	4900	85,940	1362	-4.8	-7.0	304.1	88	
513.1	4900	85,940	1362	-5.6	-8.2	304.1	88		
8.08	513.1	4900	80,260	1272	14.9	21.6	304.1	88	Repeat of test 8.05 at lower pressures with properly functioning discharge accumulator system.
	513.1	4900	80,260	1272	1.1	1.6	304.1	88	
	513.1	4900	80,260	1272	-2.6	-3.8	304.1	88	
	513.1	4900	80,260	1272	-4.0	-5.8	304.1	88	
	513.1	4900	80,260	1272	-5.6	-8.2	304.1	88	
	513.1	4900	80,260	1272	-5.8	-8.4	304.1	88	
	513.1	4900	80,260	1272	-5.8	-8.4	304.1	88	
0.28 rad (16 deg) Swept Leading Edge Inducer									
8.09	513.1	4900	85,940	1362	15.0	21.7	296.3	74	Normal
	513.1	4900	85,940	1362	8.1	11.7	296.3	74	
	513.1	4900	85,940	1362	4.6	6.7	296.3	74	
	513.1	4900	85,940	1362	0.3	0.4	296.8	75	
	513.1	4900	85,940	1362	-1.7	-2.4	296.8	75	
	513.1	4900	85,940	1362	-2.2	-3.2	297.4	76	
	513.1	4900	85,940	1362	-2.5	-3.7	297.4	76	
	513.1	4900	85,940	1362	-4.3	-6.3	297.4	76	
	513.1	4900	85,940	1362	-5.0	-7.2	298.0	77	
	513.1	4900	85,940	1362	-6.2	-9.0	298.6	78	
8.10	513.1	4900	80,260	1272	14.8	21.5	300.6	82	Normal
	513.1	4900	80,260	1272	8.1	8.1	301.8	84	
	513.1	4900	80,260	1272	4.7	6.8	303.0	86	
	513.1	4900	80,260	1272	1.2	1.8	303.6	87	
	513.1	4900	80,260	1272	0.3	0.4	303.6	87	
	513.1	4900	80,260	1272	-1.7	-2.5	304.1	88	
	513.1	4900	80,260	1272	-2.5	-3.6	304.1	88	
	513.1	4900	80,260	1272	-4.1	-6.0	304.1	88	
	513.1	4900	80,260	1272	-4.8	-7.0	304.7	89	
	513.1	4900	80,260	1272	-5.9	-8.5	304.1	88	
513.1	4900	80,260	1272	-7.2	-10.5	304.7	89		

Table 7. Summary of Inducor Test Points (Continued)

Test No.	Speed		Flow		Inlet Total Pressure		Water Temperature		Comments
	rad/s	rpm	cm <sup>3</sup> /s	gpm	N/cm <sup>2</sup>	psig	°K	°F	
8.11	513.1	4900	66,890	1060	14.8	21.5	299.7	80	Inducor housing split midway through test, forcing termination.
	513.1	4900	66,890	1060	8.0	11.6	301.2	83	
	513.1	4900	66,890	1060	4.6	6.7	301.8	84	
	513.1	4900	66,890	1060	1.2	1.8	302.4	85	
	513.1	4900	66,890	1060	0	0	303.0	86	

Inducor head rise coefficient and efficiency data are plotted against flow coefficient in figure 24. The radial inducer data are from tests 8.01 through 8.03 and the swept inducer data are from the previous program reported in (1). Radial inducer test data, with and without blade instrumentation, were found to agree almost exactly with previous data at the two flow coefficients that were repeated (0.096 and 0.084). It can therefore be concluded that the pressure instrumentation that was on the radial inducer blades for the previous tests of (1), and also on the swept inducer tested in this program, had a negligible effect on overall performance.

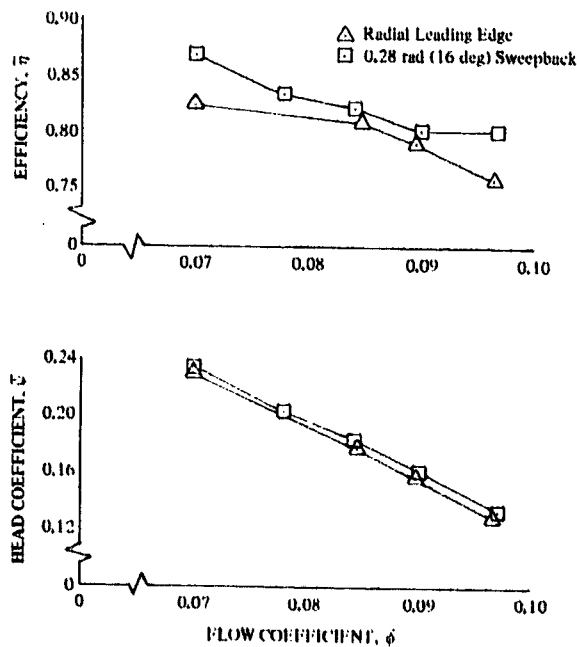


Figure 24. Noncavitating Inducor Performance

DF 91153

Tests 8.04 through 8.08 were radial leading edge inducer stability tests. The inducer was operated at a rotational speed of 513 rad/s (4900 rpm) and flows of 85,940, 80,260, and 66,890 cm<sup>3</sup>/s (1300, 1272, and 1060 gpm). Inlet tip flow coefficients at these conditions were 0.090, 0.084, and 0.070, respectively. In all cases the objective was to drop inlet pressure to the point where head rise fell off by at least 20%. Originally three tests were to be conducted, one at each flow coefficient, but the degeneration attempt prior to test 8.04 represented the first time that the components of the degeneration system had been operated for some time, and several small problems showed up in the procedure. As a result, the loop water contained more dissolved air than that which was present during the later tests. (Refer to the comments on table 7.) In addition, during test 8.04 a loose coupling was noticed in the drive train after a cavitation number of 0.058 was reached, and the test was terminated above the head falloff point. For these reasons, test 8.07 repeats the conditions of test 8.04. Test 8.08 was conducted to supplement test 8.05 at the low end of the cavitation number scale because the discharge accumulator system developed a small leak on the surge tank side during the first test at this flow coefficient. This leak made it difficult to hold precise test points at low inlet pressures.

Cavitating performance data for the radial leading edge inducer are shown in figure 25. Regions of observed test loop surging are indicated on the curves. It was impossible to reach head falloff at the 0.090 flow coefficient as the inducer loop system became uncontrollable at a cavitation number of approximately 0.030. Large flow fluctuations of approximately 38,000 cm<sup>3</sup>/s (600 gpm) at approximately two cycles per minute prevented operation at lower cavitation numbers. The results of test 8.04 have been omitted from these curves since the loop water contained four times the amount of air that was present in all subsequent tests, and this excess air casts doubts on the usefulness of the data for test to test comparisons. Surge regions were characterized by a cyclic chugging sound and by alternate lengthening and shortening of the tip clearance cavitation. Blade surface cavitation could not be clearly seen through the tip clearance cavitation. Two regions of surging were noted in the radial leading edge tests. The first region started at a cavitation number of approximately 0.07 and completely ceased at a lower cavitation number before the start of the second surging region. The first region was always relatively mild as compared with the second. The second surging region ceased just prior to head falloff for the 0.070 and 0.084 flow coefficients; however, as stated previously, it became very severe at the 0.090 flow coefficient and was accompanied by large test loop flow fluctuations.

The 0.28 rad (16 deg) leading edge inducer was tested in runs 8.09 through 8.11 in the same manner as the radial inducer. These test points are also summarized in table 7. Again it was impossible to reach a head falloff condition at 0.090 flow coefficient. The same fluctuations that occurred with the radial inducer occurred again below a cavitation number of 0.027. During the final test, 8.11, the acrylic inducer housing split and forced the termination of the run after the fifth data point. The housing had been experiencing very heavy cavitation damage near the blade leading edge area during the course of the program. Cavitation performance data for the swept leading edge inducer are shown in figure 26. Regions of observed test loop surging are again indicated on the curves. The swept inducer exhibited only one surging region that occurred over approximately the same range of cavitation numbers as the second region of the radial leading edge inducer. Surging with the swept inducer was milder than that which was observed with the radial inducer.

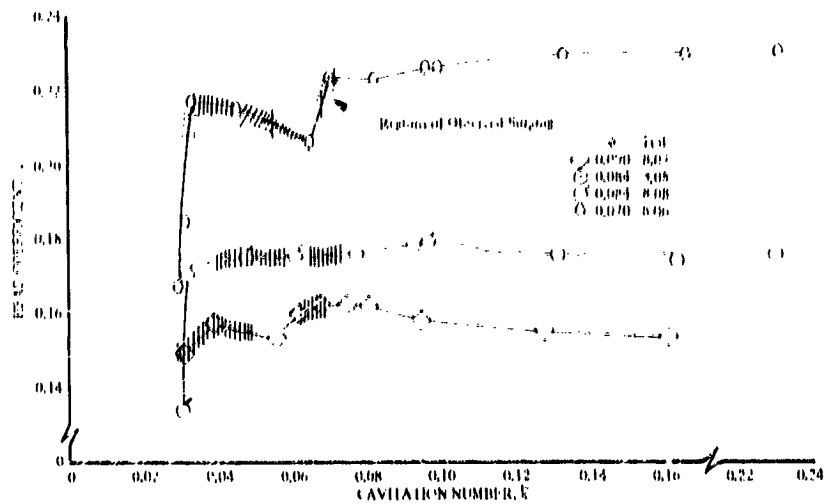


Figure 25. Cavitating Performance, Radial Leading Edge Inducer DF 91154

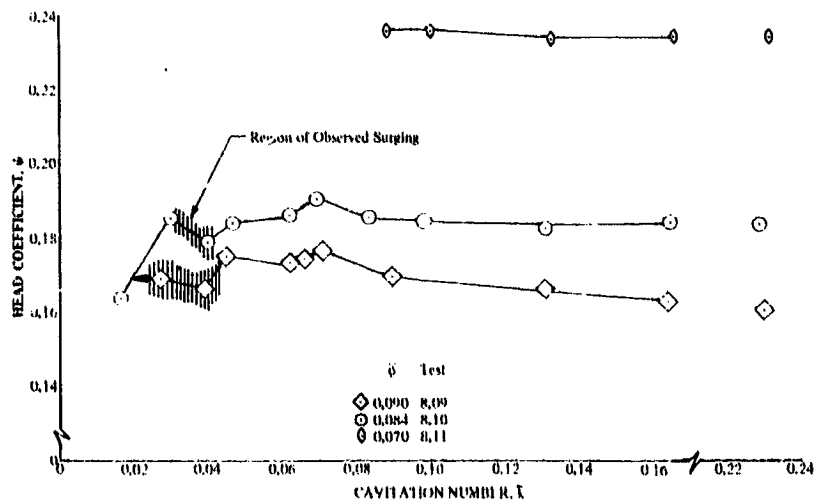


Figure 26. Cavitating Performance, 0.28 rad (16 deg) Swept Leading Edge Inducer DF 91155

The cavitating performance data are shown as the ratio of head rise over noncavitating head rise ( $\lambda$ ) in figures 27 and 28 for the radial and swept inducers, respectively. Both figures show that head rise increased before falling off for the 0.090 flow coefficient, is relatively constant to an abrupt falloff point for the 0.084 flow coefficient, and decreases from the noncavitating value for the 0.070 flow coefficient.

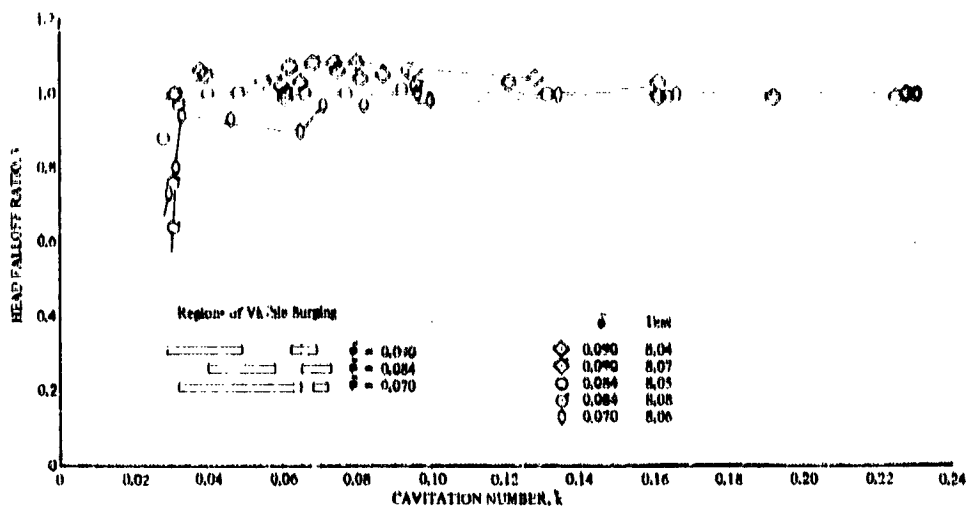


Figure 27. Normalized Cavitating Performance, Radial Leading Edge Inducer

DF 91156

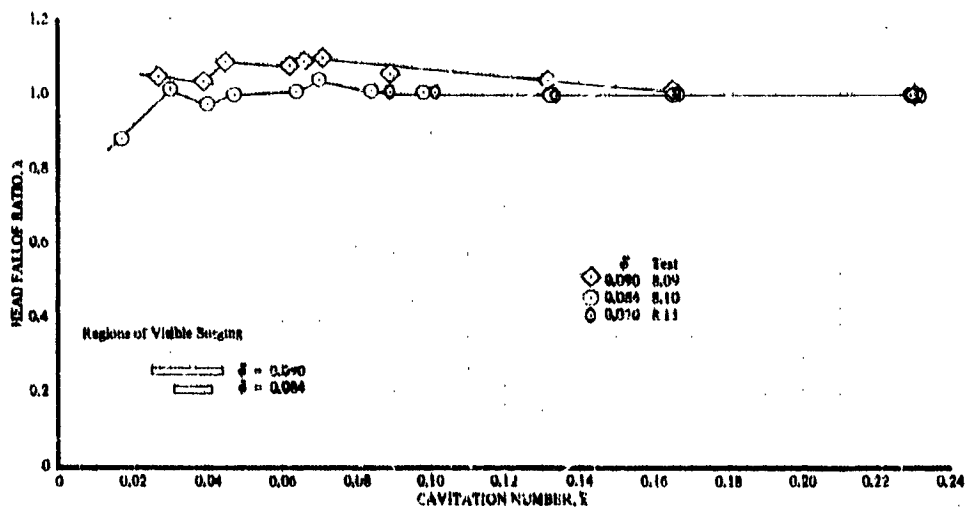


Figure 28. Normalized Cavitating Performance, 0.28 rad (16 deg) Swept Leading Edge Inducer

DF 91157

An oscillograph trace of the tape recorded dynamic pressure data for test 8.04 at its lowest pressure point ( $\bar{k} = 0.038$ ) is shown in figure 29. This trace is typical of the relatively high amplitude measured instabilities found in all tests, and it was used to gain an appreciation of the form of the pressure signals and of their relationship to one another. The transducer positions are shown on figure 16. The discharge transducers (10 and 1) show the highest amplitudes and are similar except that No. 10, which is nearer the inducer, shows a significant 82 Hz component (rotational speed) in spite of the 50 Hz low pass filter. No. 1 has a cleaner signal (with regard to the desired cavitation instability) and was selected as the representative transducer for data correlating purposes. No. 8, in the inducer inlet line, shows a measurable signal at the same low frequency and in phase with the signal from No. 1 and also has an 82 Hz component. This signal was also considered to adequately represent the instability. Transducer No. 9, at the inducer inlet, had its data completely obscured by blade passing frequency (246 Hz).

Spectrum analysis plots of the discharge transducer signal (No. 10) over a 0.3 to 50 Hz range are shown in figures 30 through 37. One figure shows the plots for all the test points of a given test. The plots generally show that the dynamic pressure signal is made up of a well-defined, fundamental frequency with harmonics. The harmonics frequently are of higher amplitude than the fundamental frequency. Note that amplitude scales are not the same for all of the plots.

The inlet transducer (No. 8) spectrum plots were uniformly similar to those from the discharge transducer except that they were of lower amplitude. Several of the inlet plots that had significant amplitudes are shown in figure 38.

Since the discharge transducer signal was found to adequately represent the system dynamic pressure data, the amplitude and frequency of its fundamental component were plotted against cavitation number for each flow coefficient. These data are shown for the radial leading edge inducer in figure 39 and for the swept leading edge inducer in figure 40. Amplitude data are plotted even where the spectrum is apparently composed primarily of noise, while frequency data are plotted only where a significant frequency could be identified on the spectrum plot. For points where the pressure amplitudes were low, the identification of a fundamental frequency required engineering judgment; figures 39 and 40 should be evaluated with this in mind. The frequency curves are quite smooth, however, which lends considerable confidence to the accuracy of the spectrum data interpretation. The location of the observed surge regions is indicated on the figures. Surge regions were characterized by visual and audible flow oscillations, as described previously.

Both the radial and the swept inducers have identifiable discrete pressure oscillations at relatively high cavitation numbers (0.16 to 0.23). The amplitudes tend to gradually increase as cavitation number is lowered until the second observed surge region of the radial inducer and the only surge region of the swept inducer (figures 25 and 26) is reached. At this point there is a sudden increase in pressure amplitude. There is no particular correlation between the pressure amplitude data and the first observed surge region of the radial inducer; however, these surges were relatively mild and often difficult to detect so pressure amplitudes would not be expected to be particularly high. Pressure amplitudes were generally considerably lower for the swept inducer than for the radial.

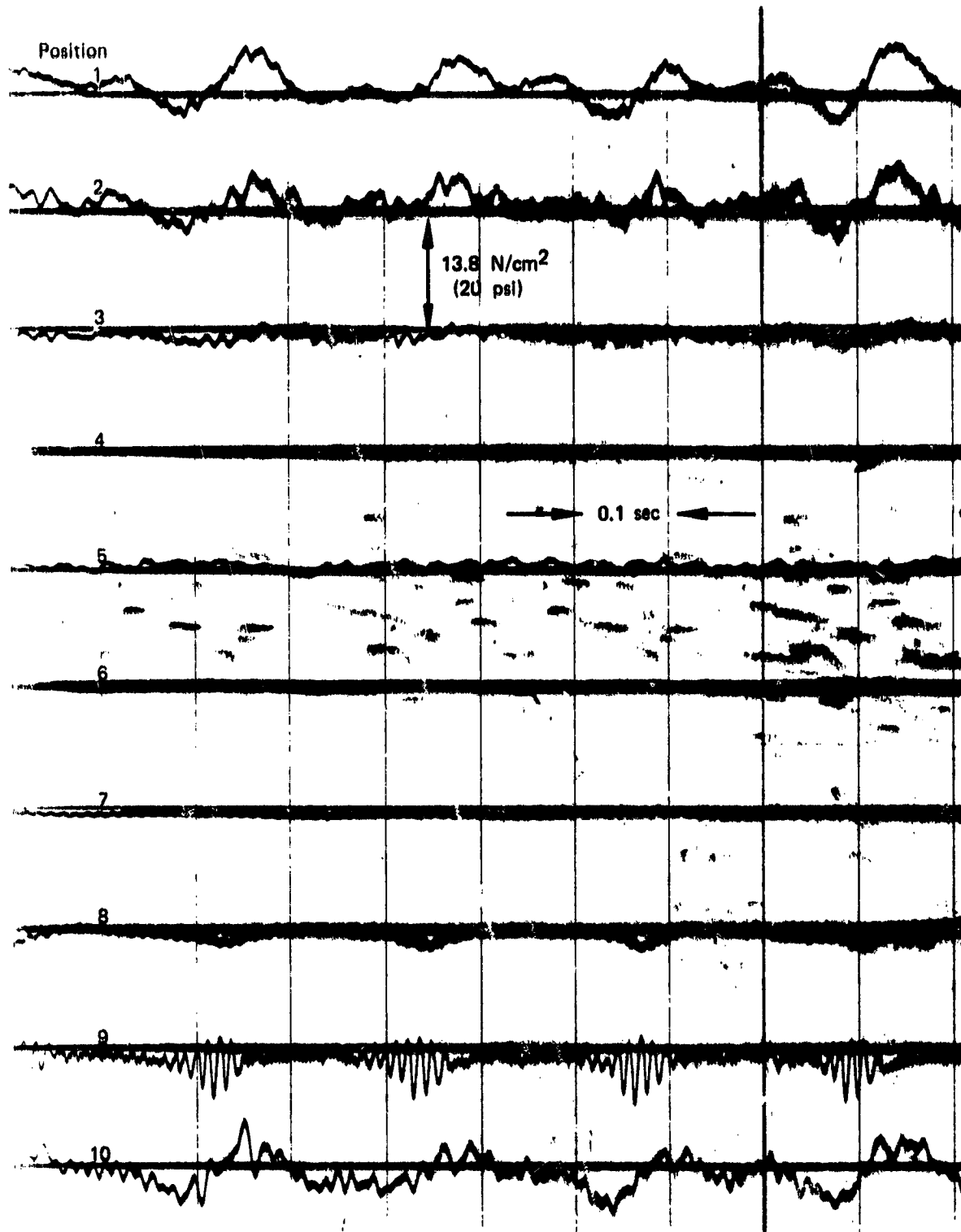


Figure 29. Oscillograph Tracing Typical of inducer Instability; Test 8.04,  $513.1 \text{ rad/s}$  (4900 rpm),  $\bar{\phi} = 0.090$ ,  $\bar{k} = 0.038$  FD 63039

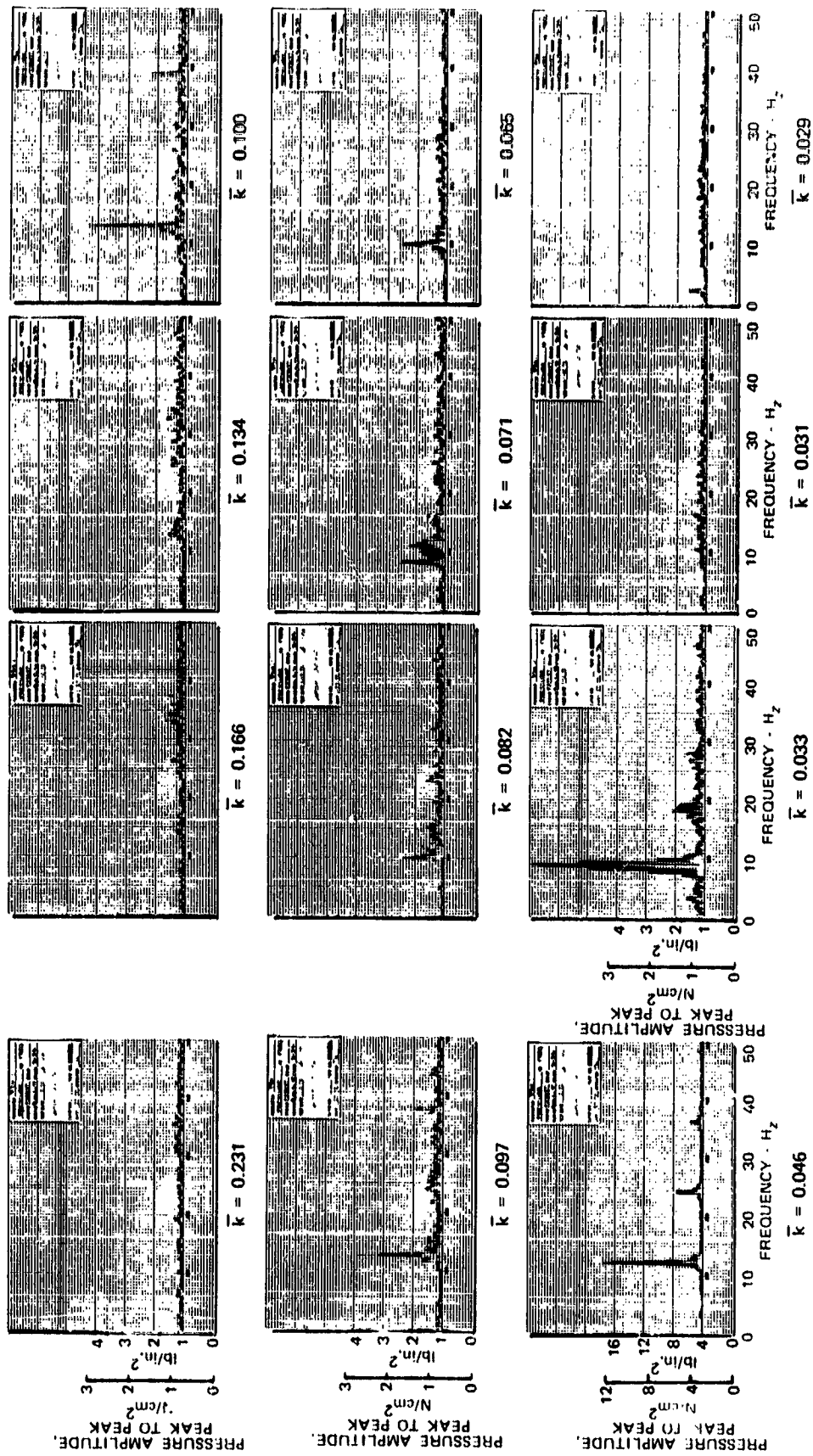


Figure 30. Inducer Discharge Dynamic Pressure Spectrum Plots; Radial Leading Edge,  
 $\phi = 0.070$  (Test 8.06)

FD 62545

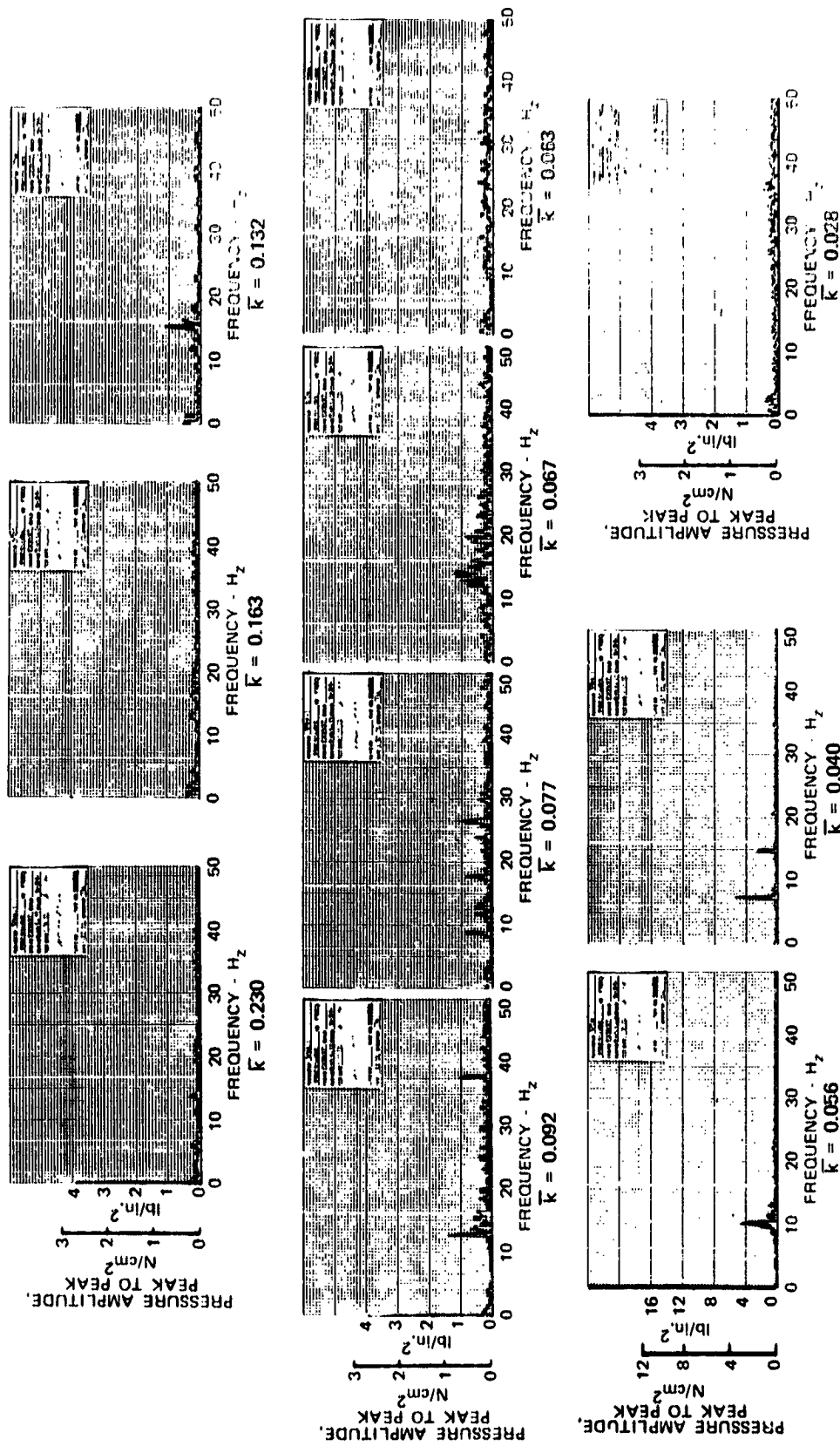


Figure 31. Inducer Discharge Dynamic Pressure Spectrum Plots; Radial Leading Edge,  $\phi = 0.084$  (Test 8.05) FD 62544

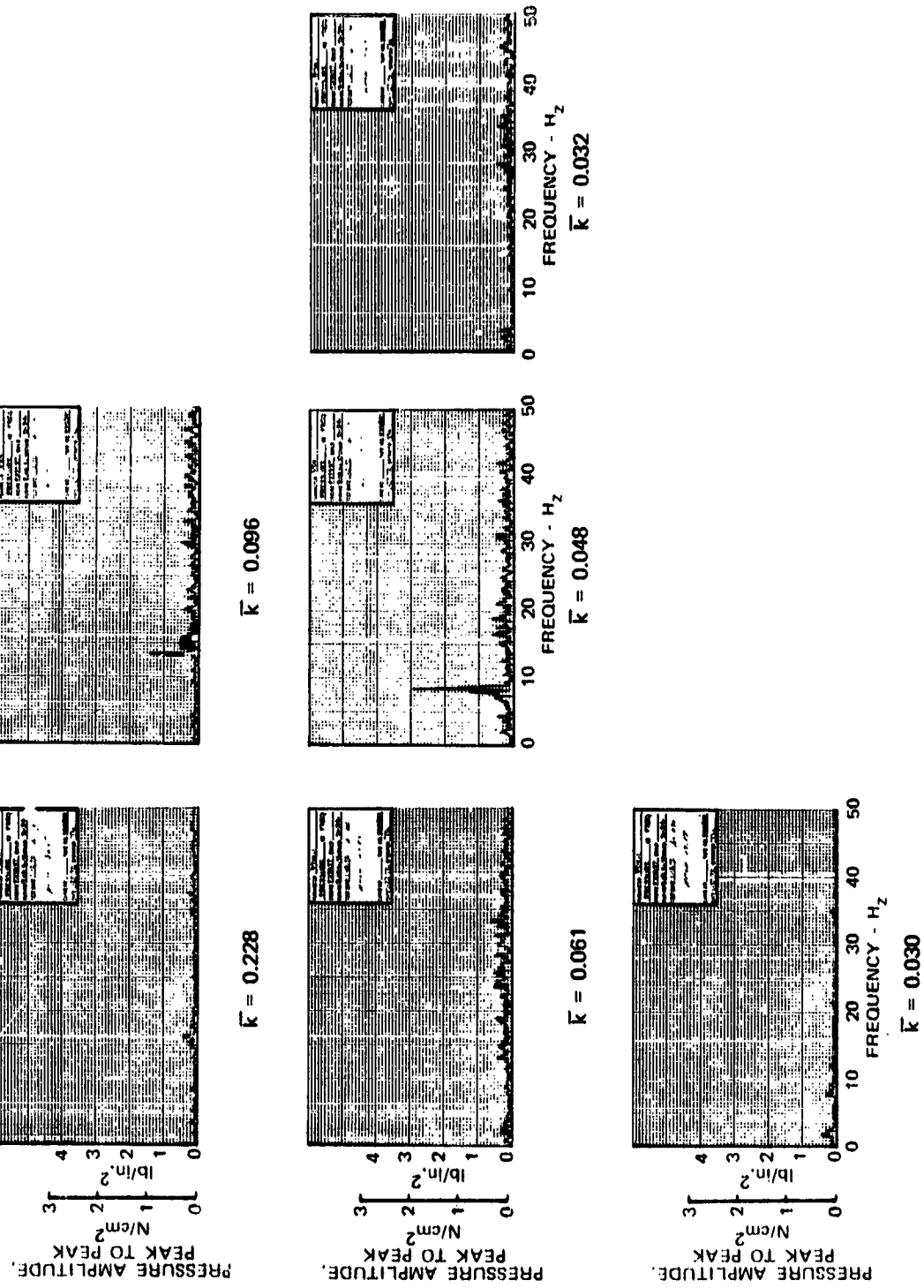
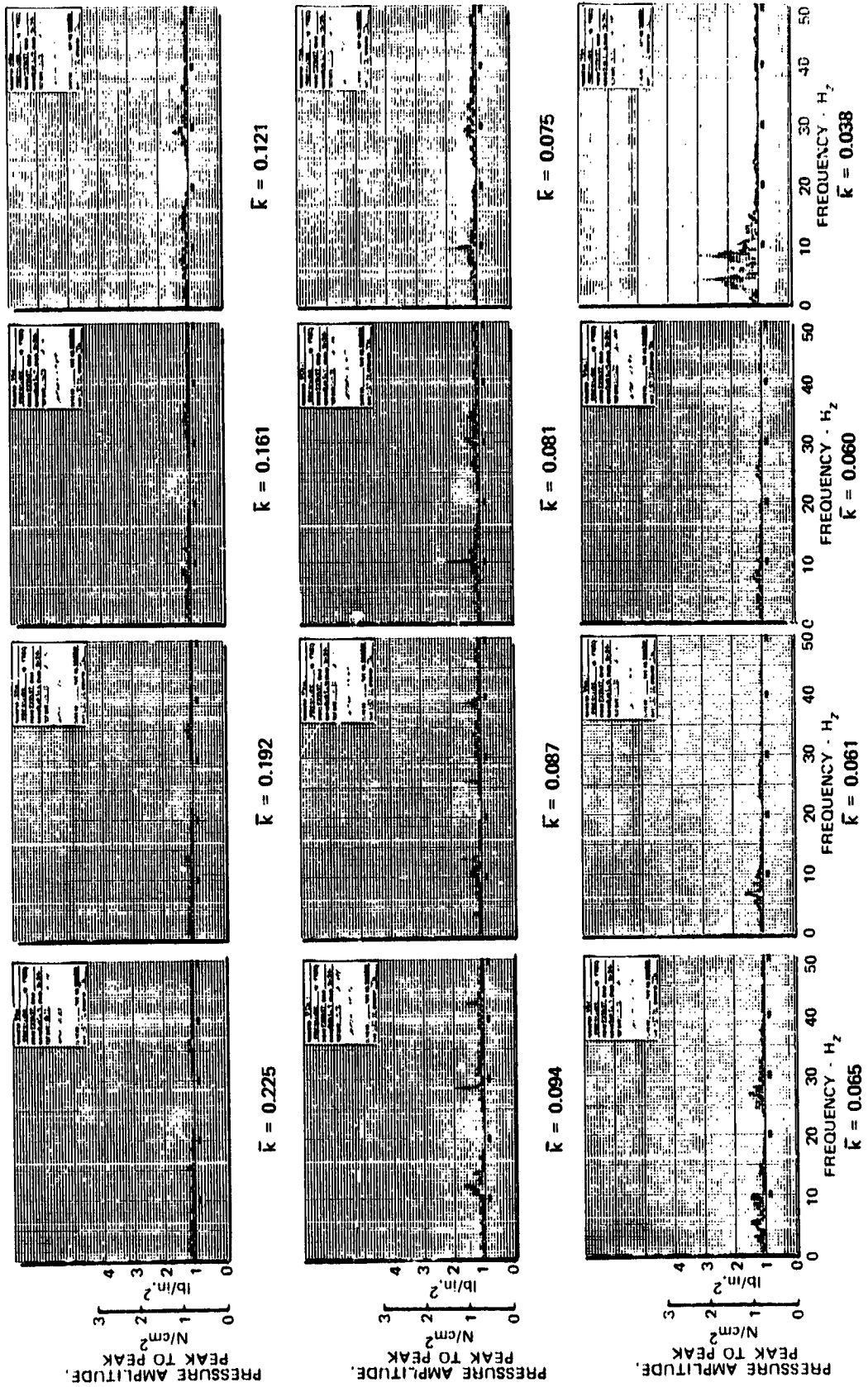


Figure 32. Inducer Discharge Dynamic Pressure Spectrum Plots; Radial Leading Edge,  $\phi = 0.084$  (Test 8.08)

FD 62547



FD 62543

Figure 33. Inducer Discharge Dynamic Pressure Spectrum Plots; Radial Leading Edge,

$\bar{\phi} = 0.090$  (Test 8.04)

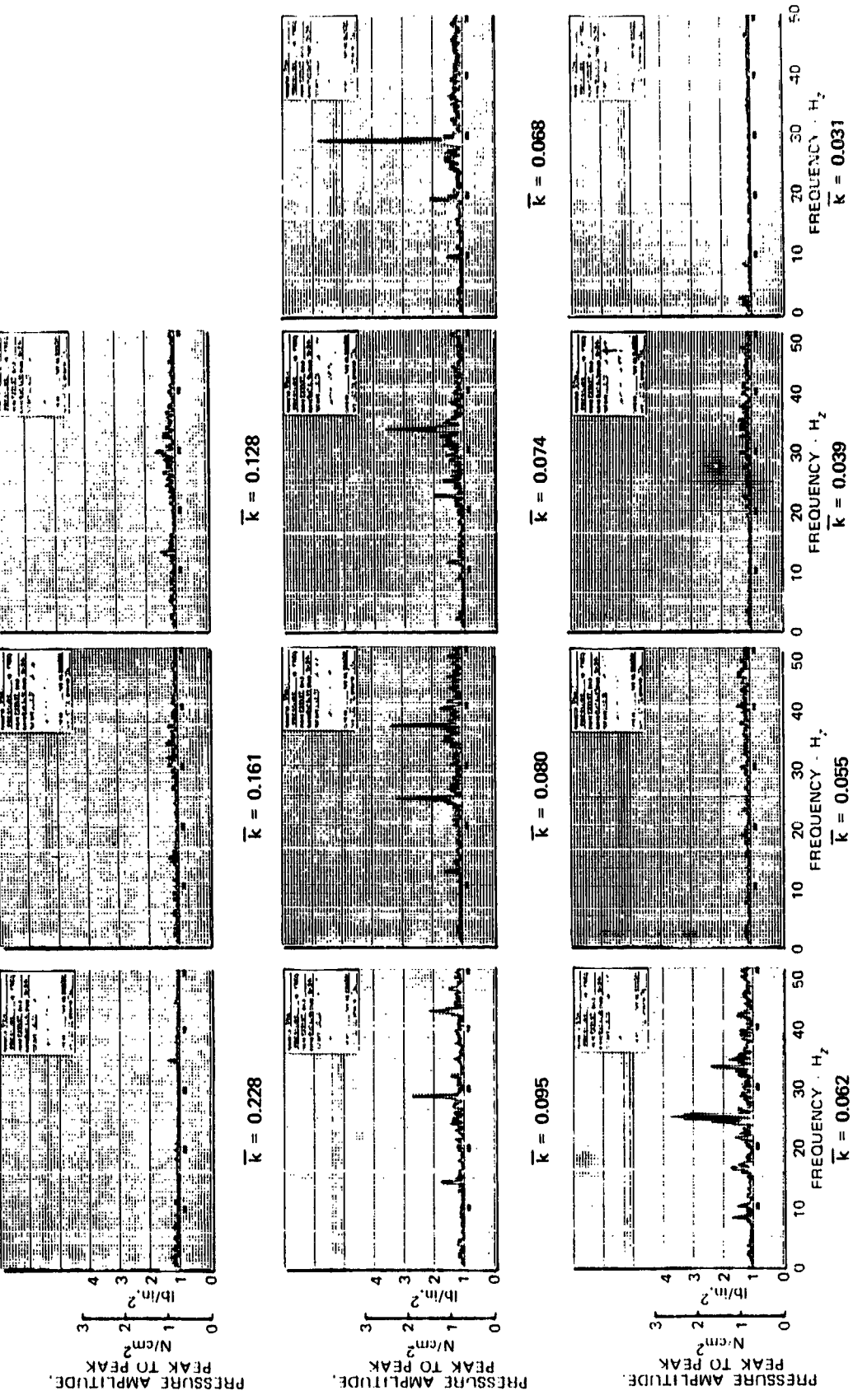


Figure 34. Inducer Discharge Dynamic Pressure Spectrum Plots; Radial Leading Edge,  $\bar{\phi} = 0.090$  (Test 8.07) FD 62546

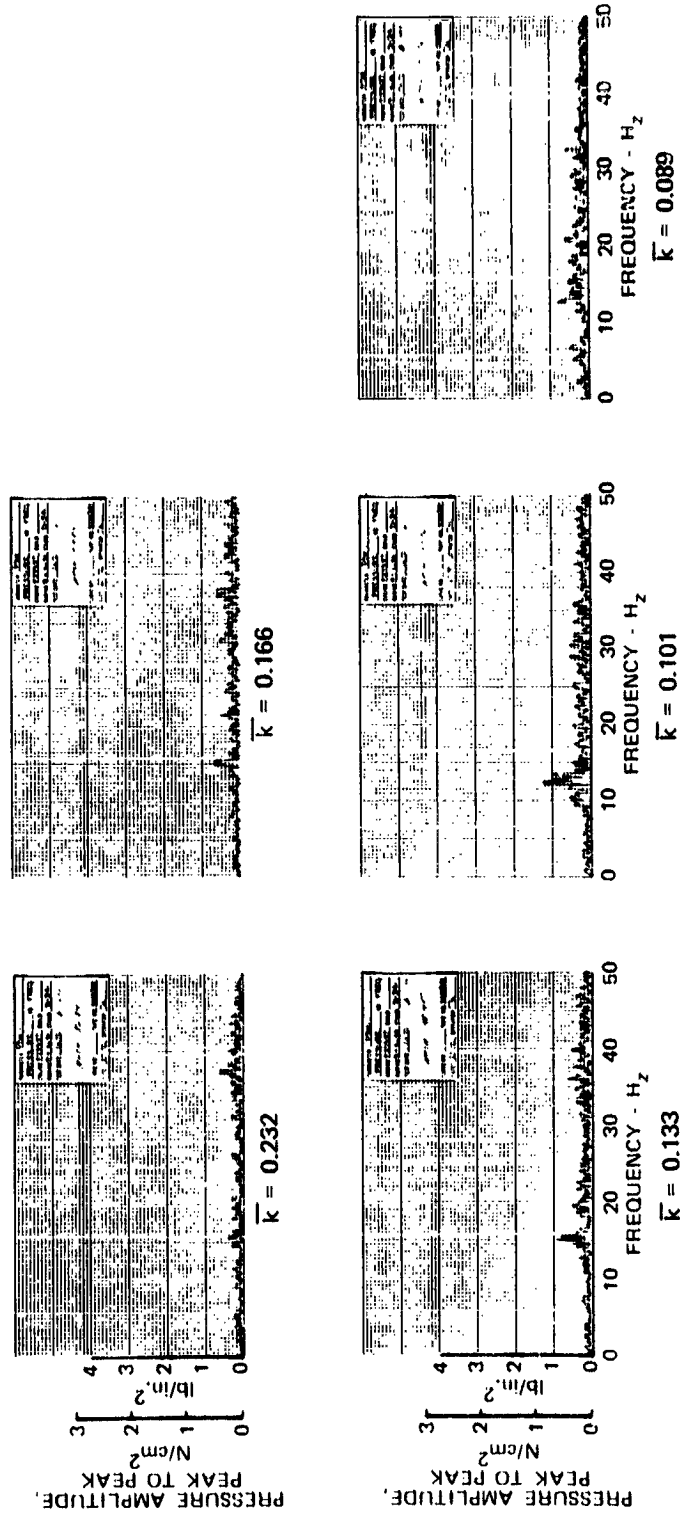


Figure 35. Inducer Discharge Dynamic Pressure Spectrum Plots; Swept Leading Edge,  $\phi = 0.070$  (Test 8.11) FD 62550

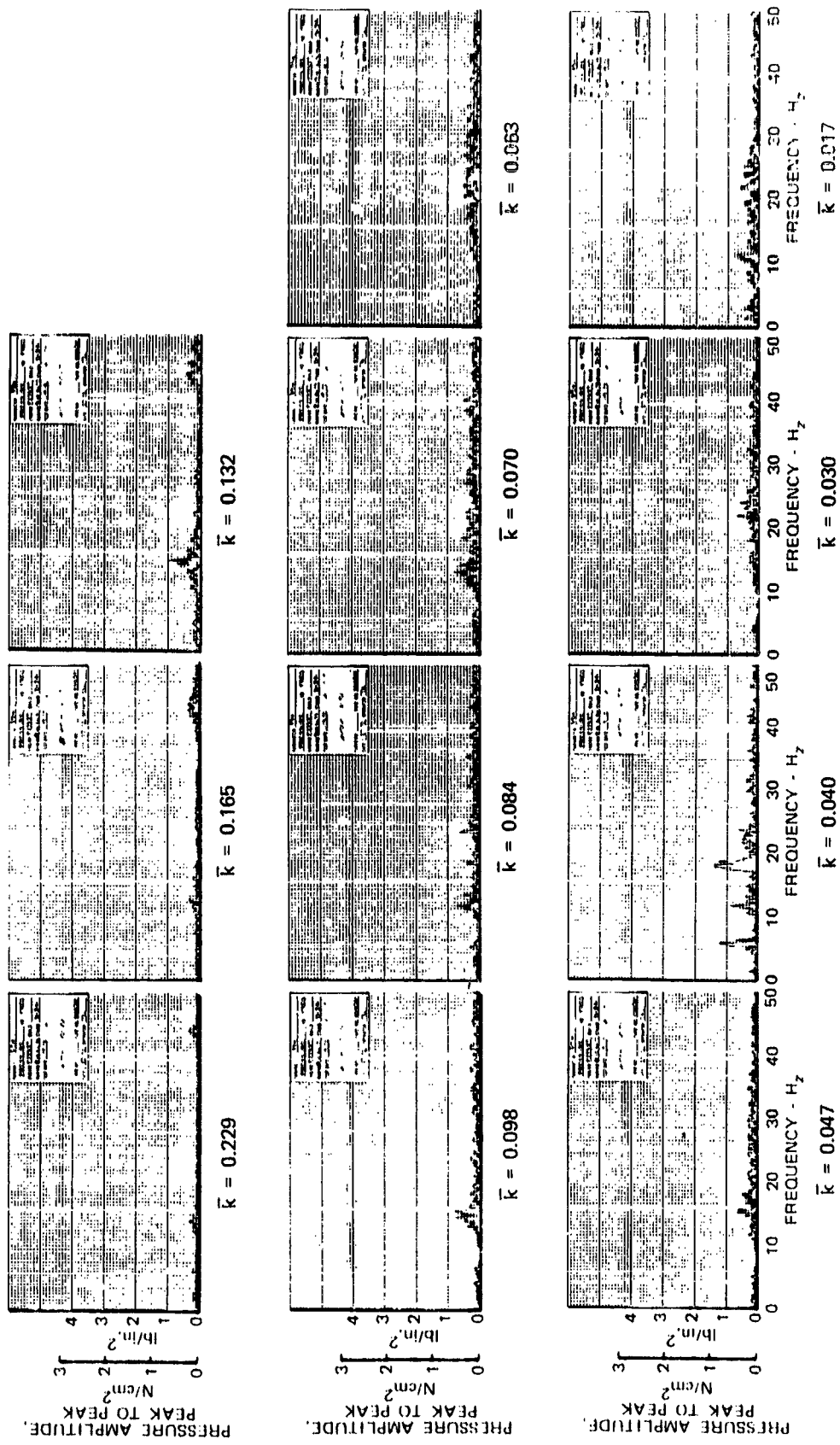


Figure 36. Inducer Discharge Dynamic Pressure Spectrum Plots; Swept Leading Edge,  $\bar{\phi} = 0.084$  (Test 8.10)

FD 62549

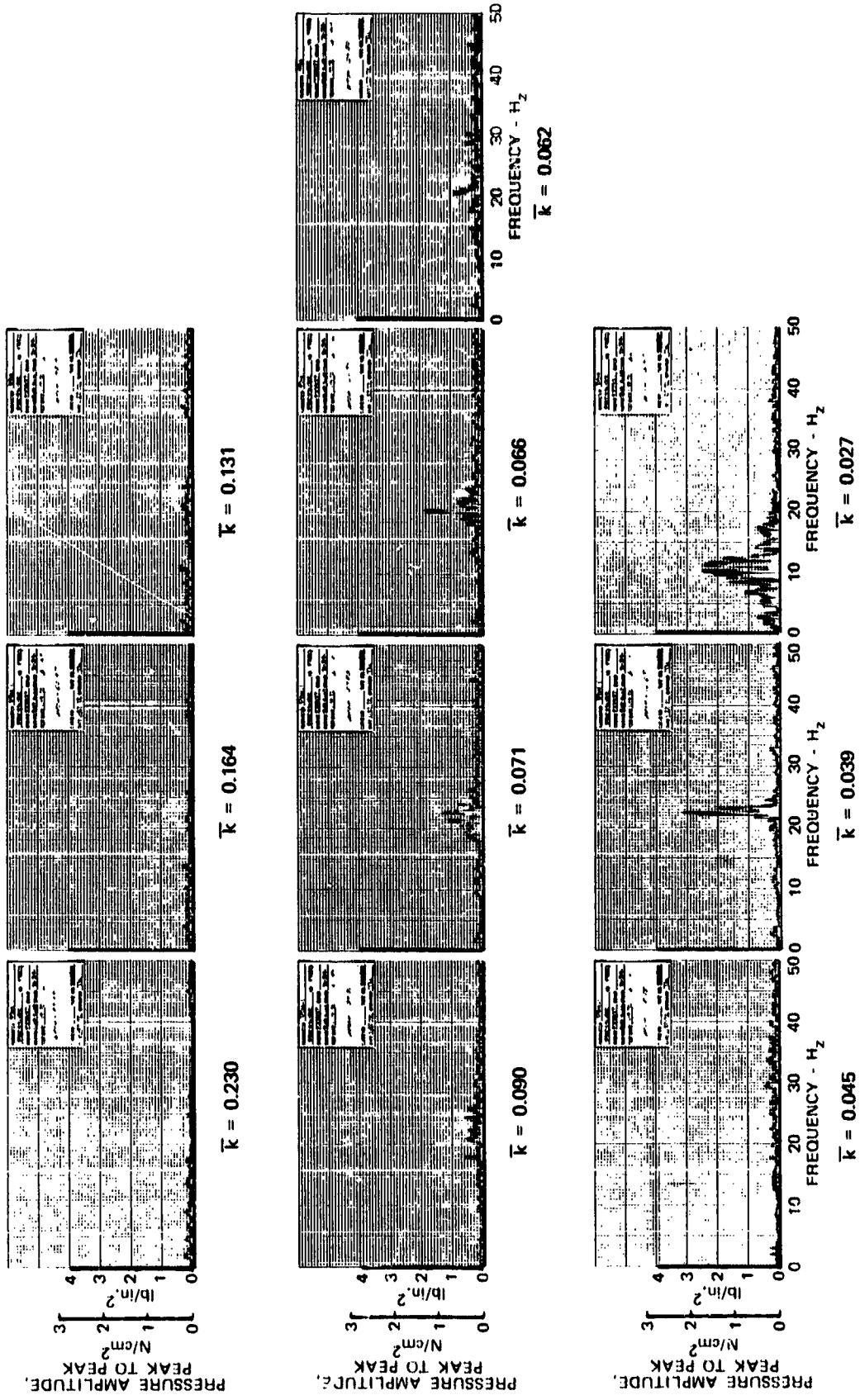


Figure 37. Inducer Discharge Dynamic Pressure Spectrum Plots; Swept Leading Edge,  $\bar{\phi} = 0.090$  (Test 8.09)

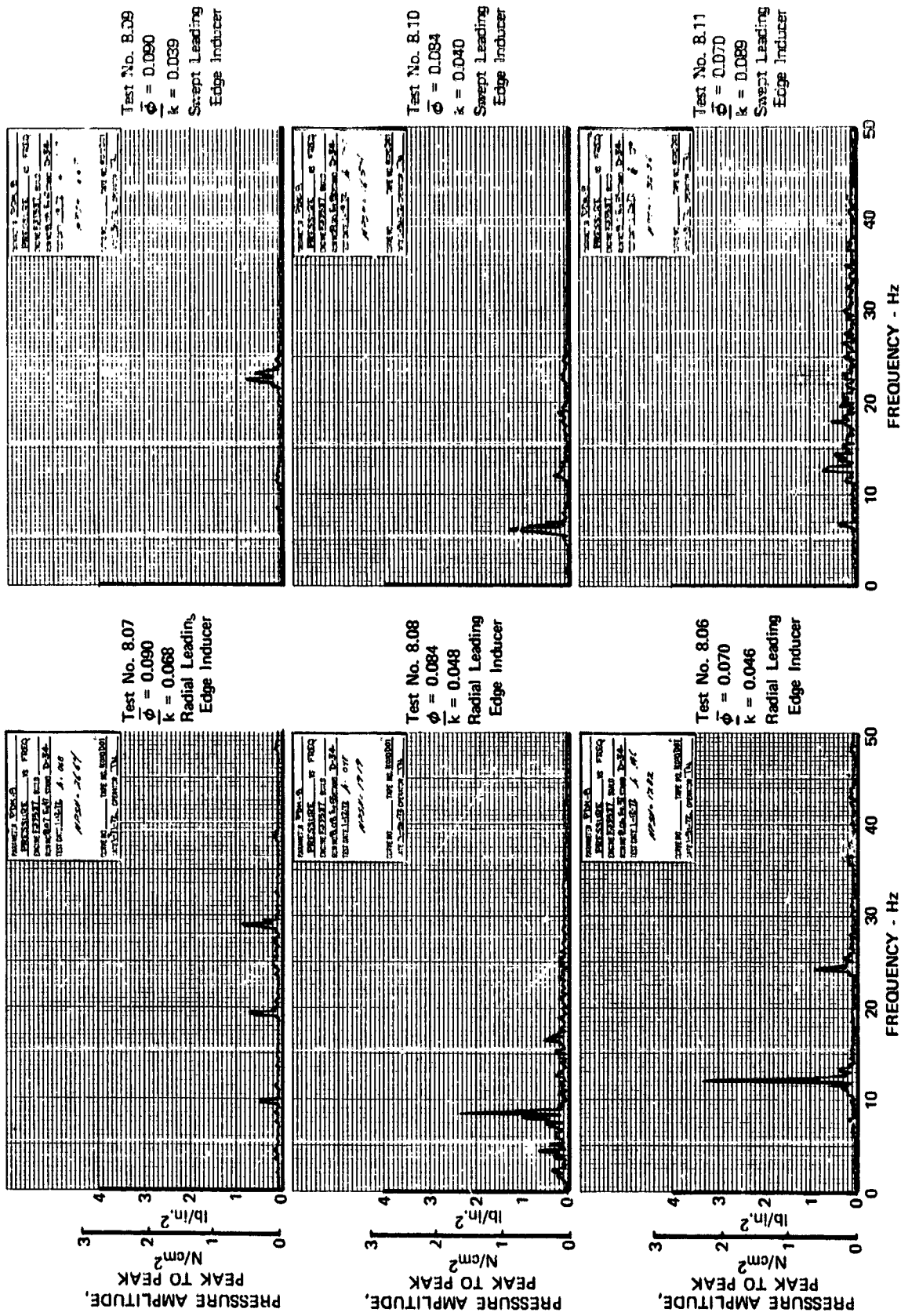


Figure 38. Inducer Inlet Dynamic Pressure Spectrum Plots; Typical Points

FD 62542

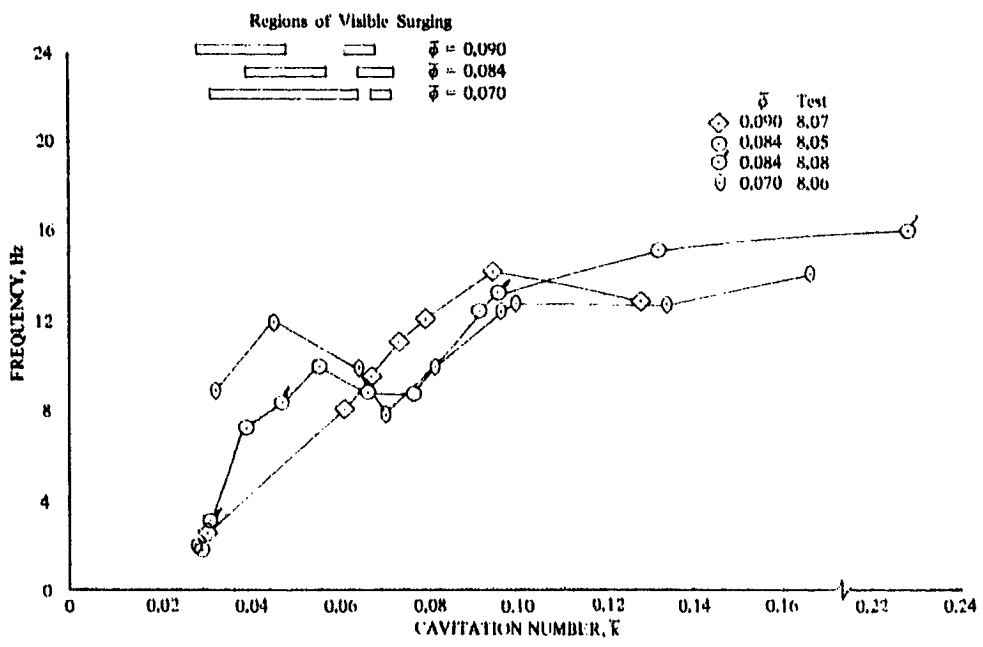
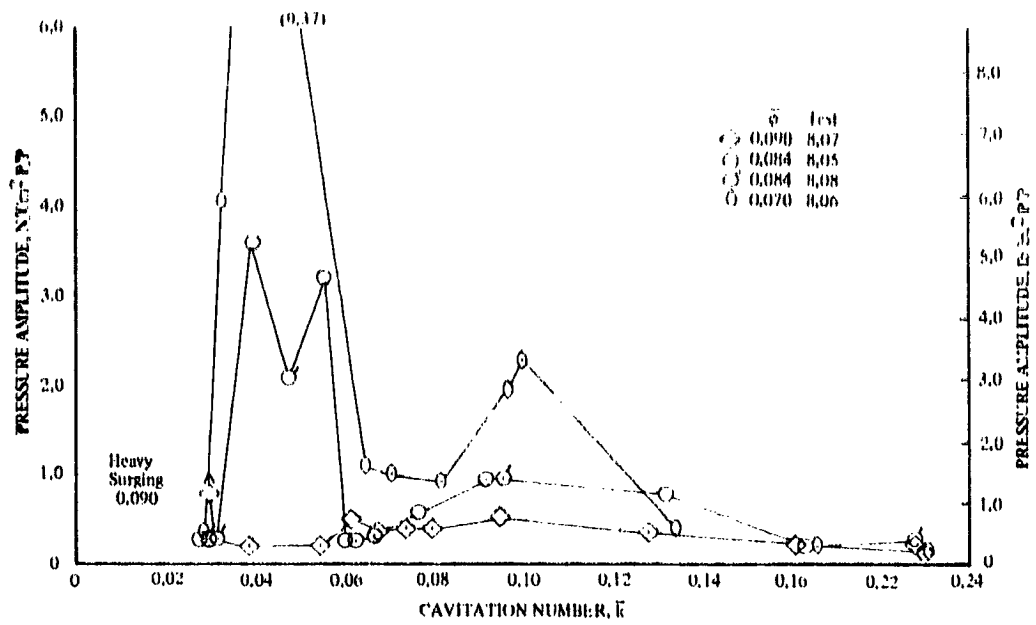


Figure 39. Variation of Inducer Discharge Dynamic Pressure Data With Cavitation Number, Radial Leading Edge

DF 91158

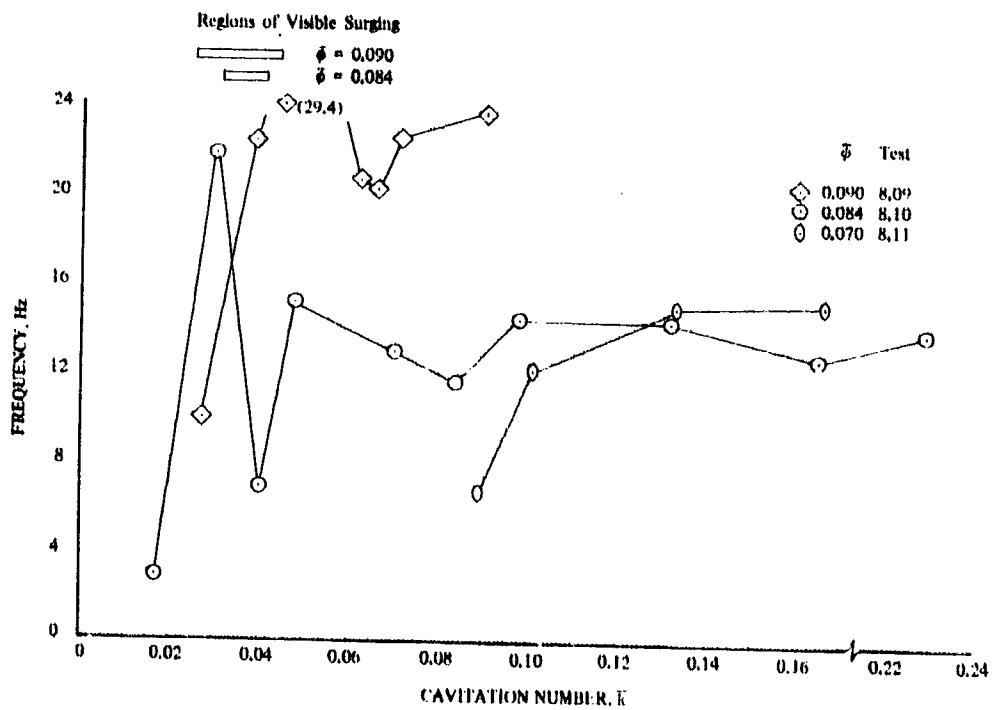
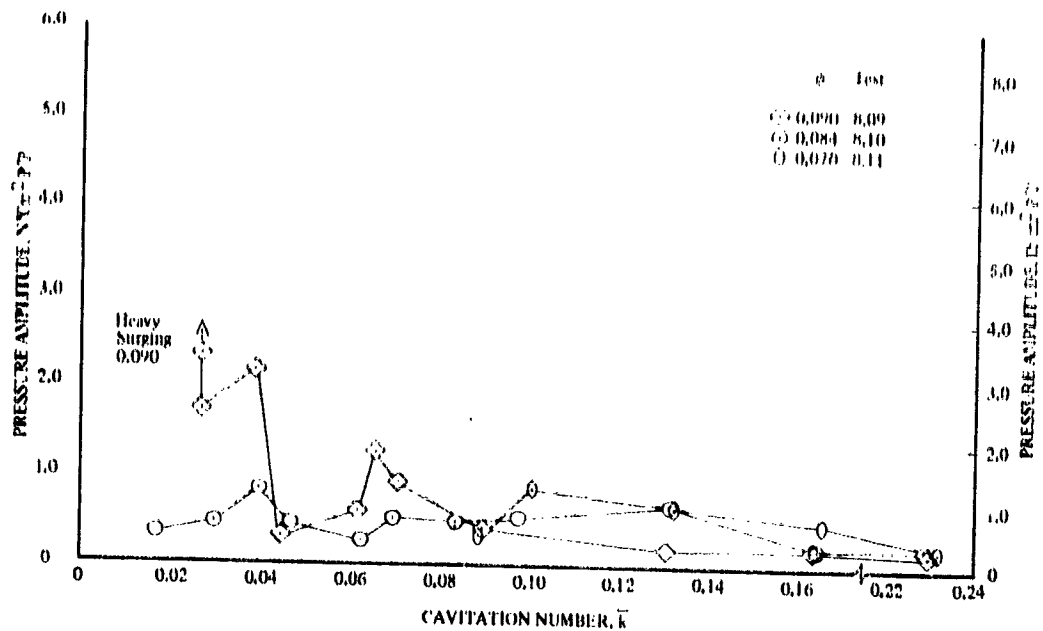


Figure 40. Variation of Inducer Discharge Dynamic Pressure Data With Cavitation Number, 0.28 rad (16 deg) Swept Leading Edge

DF 91159

Frequencies tend to decrease gradually to a cavitation number of approximately 0.09 for the radial inducer, and then to decrease more rapidly. The first surge region occurred when frequencies were in the 8 to 10 Hz range. Frequencies were generally higher for the swept inducer and a rapid decrease with cavitation number starts at a lower cavitation number (0.06 to 0.03).

Considering the variation of the data with flow coefficients, the radial inducer shows a definite amplitude increase as flow coefficient decreases (at cavitation numbers where the measured amplitudes were reasonably large); the swept inducer data are limited and do not show a definite relationship. The radial inducer shows no particular relationship of frequency to flow coefficient, while the swept inducer shows a definite reduction of frequency with flow coefficient.

A sight glass had been installed in the test loop at the inducer inlet accumulator (No. 7 in figure 16) for the accumulator evaluation tests. The level of water in this glass was noted for tests 8.06, 8.08, and 8.09 and a free surface was observed to suddenly form at an inlet pressure of approximately  $-4.5 \text{ N/cm}^2$  ( $-6.5 \text{ psig}$ ,  $k \approx 0.06$ ). The formation of this surface was attributed to the flashing of air from solution and is therefore indicative of the achieved degree of water deaeration. Since the deaeration procedure was the same for all tests, it can be assumed that the free surface generally formed at the same inlet pressure for all tests. This inlet pressure approximately corresponds to the cavitation number at which the second surge region for the radial inducer and the only surge region for the swept inducer were noted. Hence, there was a sudden change in the test loop system that coincided with the observed surge regions.

The general effects of air in the loop system on the pressure signals can be evaluated by considering the spectrum plots for test 8.04 (figure 33) with those for test 8.07 (figure 34). Both tests were run with the radial inducer at a flow coefficient of 0.090, but test 8.04 was not considered satisfactory because the water initially had approximately four times as much air in solution as did test 8.07 and all other tests. Spectrum plots for test 8.04 show noticeably less well defined signal frequency components than the plots for test 8.07, and test 8.04 had relatively high amplitude, low frequency oscillations at a cavitation number of 0.038, whereas test 8.07 did not at a nearly comparable cavitation number of 0.039. The amplitude and frequency of the signals are plotted against cavitation number in figure 41. The data for the two tests are similar except that test 8.04 tends to show slightly lower frequency oscillations and its pressure amplitude increases at a higher cavitation number.

Inducer inlet fluid tangential velocities, which were measured near the inducer tip, are shown plotted against cavitation number in figure 42 for the radial leading edge inducer. The probe was located at a radius of 8.66 cm (3.41 in.) and was 0.66 cm (0.26 in.) upstream of the leading edge. Tip radius was 8.96 cm (3.50 in.). Tangential velocity generally decreased with decreasing cavitation number and reached zero at a cavitation number of 0.06 to 0.07 for all flow coefficients, the same range of cavitation numbers at which the first surge region was observed. Although not plotted, fluid through-flow velocity decreased along with tangential velocity. The rate of decrease with cavitation number was gradual to a cavitation number of approximately 0.10, at which point velocity decreased more rapidly.

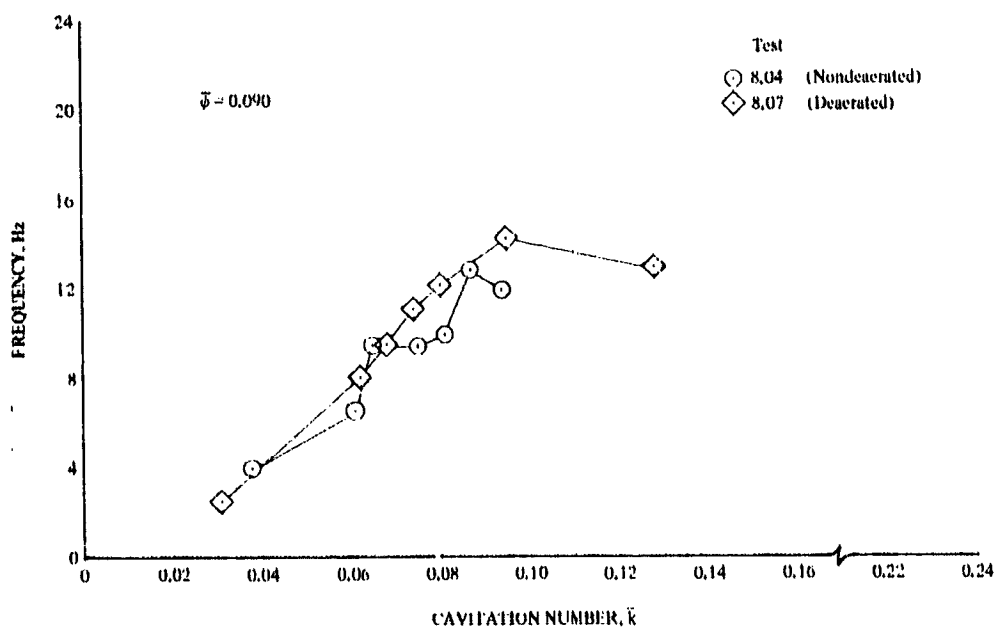
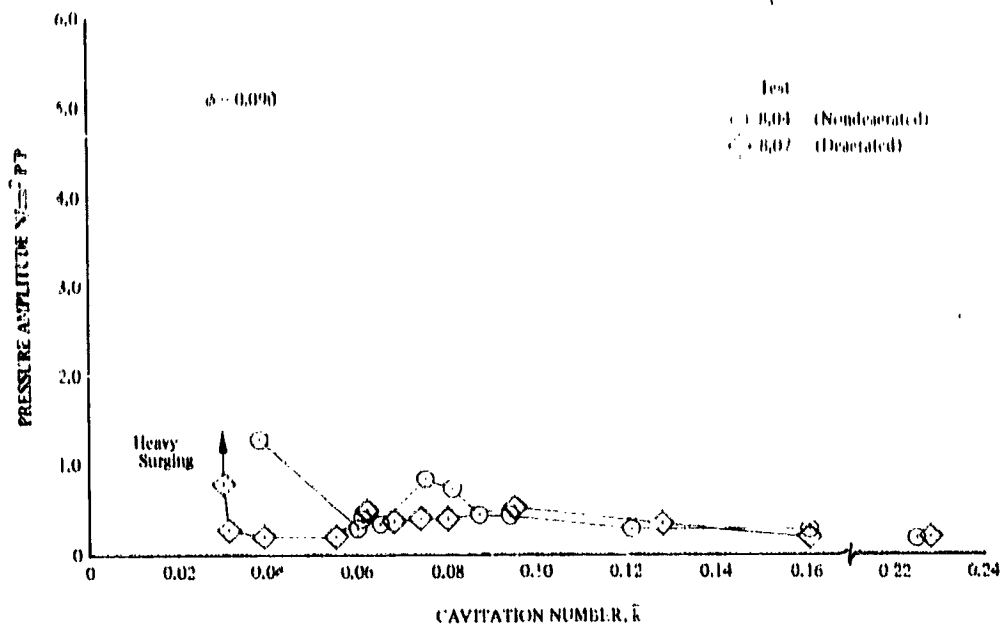


Figure 41. Comparison of Relatively Deaerated With Nonde aerated Dynamic Pressure Data, Radial Loading Edge DF 91160

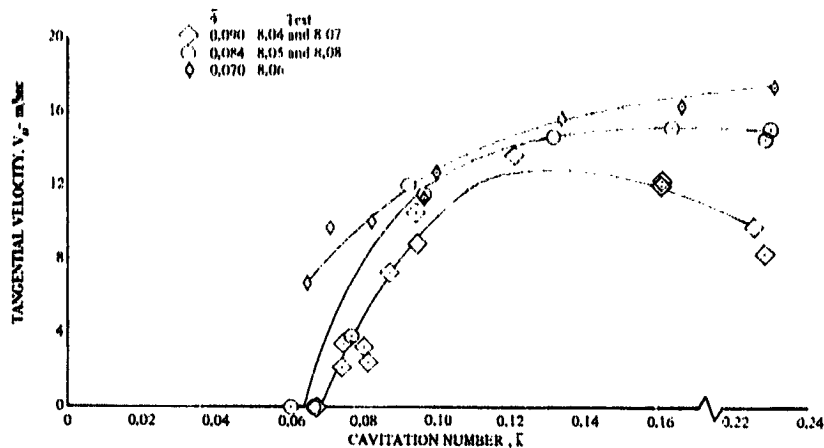


Figure 42. Variation of Inlet Tip Prerotation With Cavitation Number, Radial Leading Edge Inducer DF 91161

Tangential velocity data for the swept inducer are shown in figure 43. The probe was at the same radius but the sweepback of the blades resulted in the probe being 2.20 cm (0.87 in.) upstream of the leading edge tip. Data were not taken for all the swept inducer test points because of the time required and the observed high rate of cavitation damage to the inducer housing. The data show the same trend as the radial data, decreasing to zero at a cavitation number of 0.06 to 0.07. Velocities were lower for the swept inducer than for the radial, but this may be at least partly explained by the probe location, which was approximately three times further upstream of the leading edge.

Test results are discussed further and correlated with predictions in paragraph 5.3.

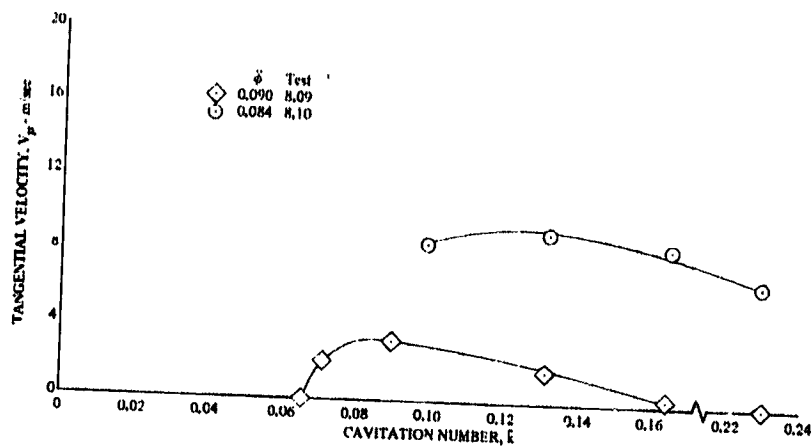


Figure 43. Variation of Inlet Tip Prerotation With Cavitation Number, 0.28 rad (16 deg) Swept Leading Edge Inducer

DF 91162

## SECTION 5 ANALYSIS AND DATA CORRELATION

Three sets of experimental data were correlated with predictions: measured hydrofoil cascade suction surface cavity geometry data, measured cascade tunnel pressure oscillation data, and measured inducer loop instability data. The cascade geometry data were correlated against predictions made through the use of an inducer internal flow analysis, cascade tunnel dynamic pressure data were correlated with tunnel system model predictions, and inducer loop dynamic pressure data were correlated with inducer system model predictions. The analyses and results of each of the correlation efforts are reported in the following subsections.

### 5.1 CAVITATION CAVITY GEOMETRY

#### 5.1.1 Analytic Model

The analytic cavity model was formulated in the inducer flow analysis reported in (1) and is based on the concept of a distinct vapor cavity on the blade suction surface which displaces an otherwise incompressible liquid. The liquid and vapor are assumed to be separated by centrifugal effects both in the meridional and blade-to-blade directions. Such a cavity is illustrated in figure 44. The coordinates of the vapor-liquid interface (which defines the cavity) are calculated to the point of maximum cavity height in an iterative process where the flow forces associated with the cavity are calculated and equated to the change in momentum parallel to the blades, and the radial streamlines are located to satisfy radial equilibrium. The cavity is assumed to collapse linearly from the point of maximum height in a manner that is based on empirical data. The profile of such a cavity is shown in figure 45. Significant dimensions are:

$c$  = Length from blade leading edge to point of maximum height along the blade chord

$b$  = Length of collapse region along the blade chord

$h$  = Cavity height normal to the blade chord measured from the suction surface

$l$  = Length from blade leading edge to end of cavity along the blade chord

$\delta_w$  = Angle of the cavity collapse (or wake) relative to the blade chord.

The cavity model is similar to the models of Stripling and Acosta (19) and Jakobsen (24) who applied conformal mapping to obtain an exact solution for two-dimensional, ideal flow. These models do not account for real effects, however, which occur in viscous, three-dimensional flow and which are accounted for in the cavity model of (1). Viscous effects influence the cavity through boundary layer blockage and drag forces. Three-dimensional effects consist of (1) centrifugal forces, (2) streamline relocation, and (3) changes in passage width and height.

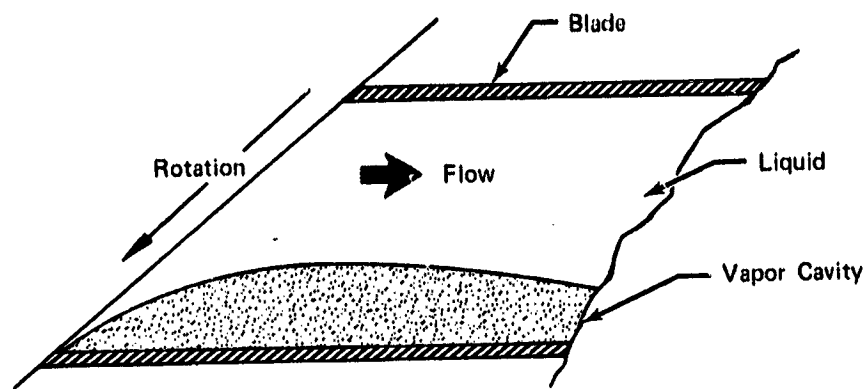


Figure 44. Distinct Vapor Cavity on Inducer Blade Suction Surface

FD 62906

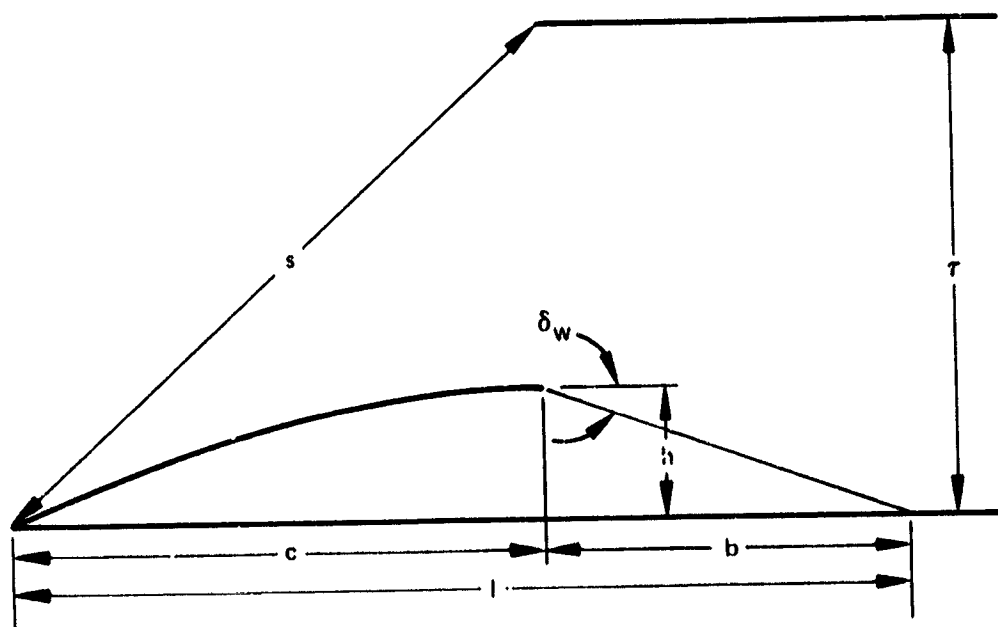


Figure 45. Cavitation Cavity Profile

FD 62907

The analytic formulation of the cavity model is given in (1) and it is included in the inducer hydrodynamic computer program listed in Volume II of that report. Correlations of the model's predictions with test data and refinements to the model that were made in this program are reported in the following subsections.

### 5.1.2 Correlation of Cavity Model Predictions and Refinements of Model

Cavity model predictions were correlated with predictions from the equations of Stripling and Acosta (19), with cascade test data that were reported in Section 4.1, and with inducer test data from (1) to define areas of the model that required refinement. In this correlation effort, the dimensions shown on the cavity profile of figure 45 were assumed to define the cavity. Since Stripling provides an exact solution of the cavity profile to the point of maximum height for ideal two dimensional flow with zero blade thickness, their predictions were correlated with cavity model predictions of height (h) and length to maximum height (c) for the same zero blade thickness, ideal flow cascade. Cavity model predictions for such a cascade will differ from those for a real flow and real cascade but the degree of correlation provides an indication of the cavity model's general accuracy.

The data correlations and model refinements are discussed in the following paragraphs for each of the significant dimensions. Cavity model predictions of height were found to be reasonably accurate, length to maximum height was in error but correctable through adjustment of the empirical collapse function, and overall length predictions correlated reasonably well with the available test data.

#### 5.1.2.1 Cavity Height

Comparisons of cavity height predictions (dimension h in figure 45) with predictions from Stripling and Acosta are shown in figure 46 for the hydrofoil cascade and in figure 47 for an inducer cascade. Actual height is divided by blade spacing [7.6 cm, (3.0 in.) for the hydrofoil cascade and 18.6 cm (7.3 in.) for the inducer cascade] and plotted against cavitation number. The inducer cascade is geometrically similar to the tip streamline geometry of the inducer that was tested as reported in (1). Cavity model predictions for both cascades were generated for an inviscid, two-dimensional flow and zero thickness blades to provide a direct comparison with exact Stripling and Acosta predictions. Since the Stripling and Acosta model is an exact solution, the degree of correlation is an indication of the model's accuracy for the selected cascades and flow conditions. Figure 46 shows the cavity height correlation for the ideal hydrofoil cascade at a single incidence angle (0.28 rad, 16 deg). The correlation between the two prediction models is good over the entire range of cavitation numbers. Figure 47 shows the height correlation for the ideal inducer cascade for three incidence angles. At high cavitation numbers (1.0-0.2), the correlation for all incidence angles is good and at low cavitation numbers the cavity model predicts cavity heights approximately 10% lower than those from Stripling. The low prediction is consistent for all incidence angles. The indicated degree of correlation for both cascades is considered satisfactory and the wide difference between the blade stagger angles and incidence angles for the two cascades indicates that the cavity model is applicable to a wide range of geometries and flow conditions.

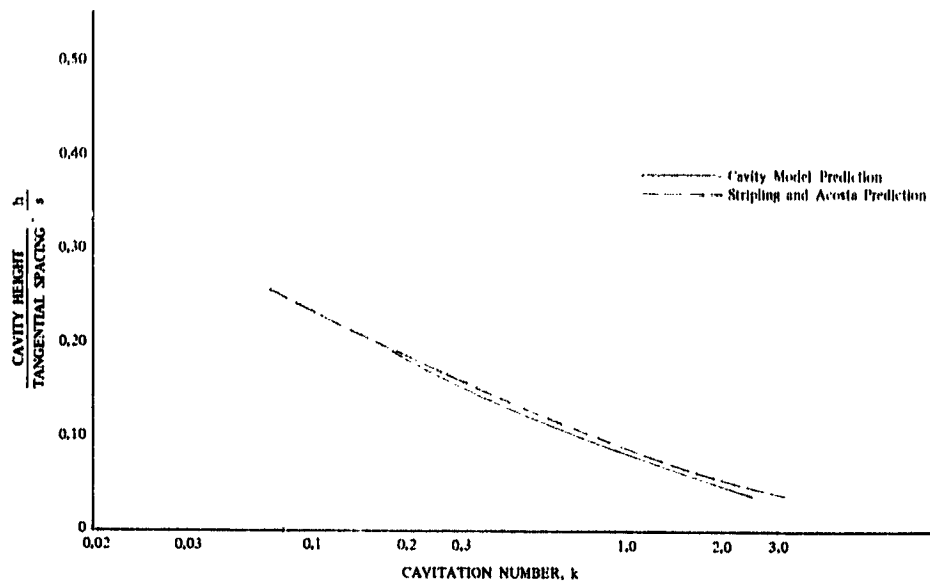


Figure 46. Comparison of Cavity Height Predictions With Exact Predictions; Ideal Hydrofoil Cascade  $i = 0.78$  rad (16 deg) DF 91076

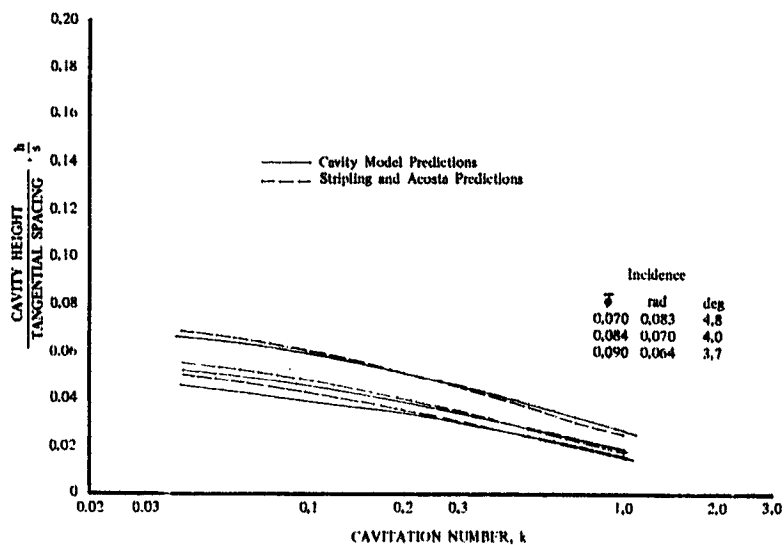


Figure 47. Comparison of Cavity Height Predictions With Exact Predictions, Ideal Inducer Cascade DF 91092

Cavity model predictions of cavity height are compared with the hydrofoil cascade test data in figure 48. The measured and predicted cavity height data in this figure are from the suction surface of the hydrofoil. Test data scatter is attributed to difficulties experienced in taking accurate measurements from the photographs, to the fact that cavitation was unsteady for nearly all test points, to observed blade-to-blade nonuniformity, and to possible variations in incidence angle with cavitation number (due to choking of the boundary layer removal slots). Measured data were at indicated incidence angles of 0.28, 0.31, and 0.35 rad (16, 18, 20 deg) and the predicted data are shown for 0.28 and 0.17 rad (16 and 10 deg). Cavity height predictions fall within the band of the measured data scatter in spite of the lower incidence angles for the predictions. This result is consistent with observed pressure surface cavitation at relatively high incidence angles and the conclusion that actual cascade incidence angles were less than the value measured from the geometric settings.

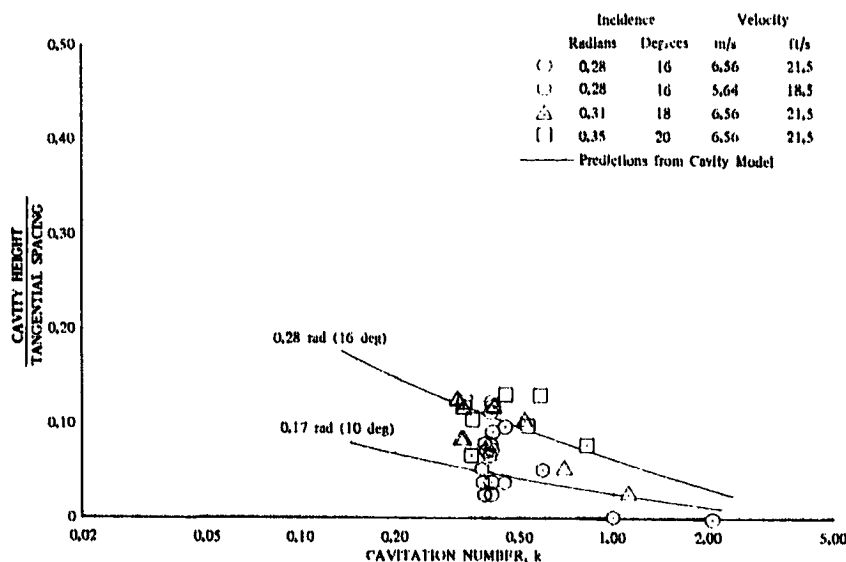


Figure 48. Comparison of Cavity Height Predictions With Cascade Test Data DF 89778

The good correlation between height predictions from the cavity model and the exact predictions from Stripling and Acosta for ideal two-dimensional flow led to the conclusion that the model's predictions of cavity height are satisfactory. The hydrofoil cascade test data were not sufficiently accurate for quantitative correlation and refinement of the model (as was originally intended) but the model's predictions are in qualitative agreement with the data. This agreement also tends to substantiate the accuracy of the height predictions.

#### 5.1.2.2 Cavity Length to Maximum Height

Length to maximum cavity height (dimension  $c$  in figure 45) is precisely predictable, by the method of Stripling and Acosta, for an ideal two-dimensional flow. Thus, while this length was not measurable in either the hydrofoil cascade or the inducer test program of (1), a comparison of ideal flow predictions from

the two cavity models is an additional indication of the inducer program cavity model's accuracy.

Comparisons of length to maximum height predictions are shown in figure 49 for the ideal hydrofoil cascade and in figure 50 for the ideal inducer cascade. The band that is indicated for the inducer program cavity model predictions is a result of the finite difference solution and it defines the limits of the length prediction at a given cavitation number. The predicted band was not shown in the height predictions of figures 47 and 48 because height changes more gradually than length and the band is small. The cavity model's prediction of length to maximum height for the ideal hydrofoil cascade generally shows the same trend with cavitation number as the Stripling and Acosta prediction but the model's prediction is longer than the exact Stripling and Acosta solution. Cavity model predictions for the ideal inducer cascade are considerably longer than the Stripling predictions at high cavitation numbers but they approach the Stripling predictions as cavitation number decreases and the two are equal at a cavitation number of approximately 0.04. The predicted variation of cavity length with incidence is similar for both prediction models. These results indicate that the cavity model generally predicts longer than actual lengths to maximum height. This is considered to be an important deficiency in the cavity model and refinements were considered to improve the correlation. The calculations of cavity height and length to maximum height are integral with the inducer internal flow analysis, however, and any refinements in the calculations would require major rework of that analysis. A simpler, more easily implemented, approach was taken wherein the cavity collapse length ( $b$  in figure 45) was adjusted to make predictions of overall length agree with the test data. This approach was possible because the trend of the length to maximum height predictions was correct and the cavity model's prediction of length to maximum height was not enough longer than the Stripling and Acosta exact length to require collapse angles ( $\delta_w$  in figure 45) of greater than 1.57 rad (90 deg). The error in cavity volume which is accepted through this approach is a small percentage of the overall volume as will be illustrated in the following subsections.

### 5.1.2.3 Cavity Collapse

The cavity collapse model that was reported in (1) assumed that the cavity collapsed in a turbulent wake, which was bounded by a straight line from the point of maximum cavity height to the blade surface. Such a collapse was shown in figure 45. The angle of the line relative to the blade surface ( $\delta_w$  in figure 45) was assumed to be a function of normal cavity height and to vary inversely with the cavity profile blockage. The wake angle function was defined empirically from the available overall cavity length measured data.

The empirical collapse angle function was reexamined in this program in an effort to improve the correlation between predicted and measured inducer overall cavity length. The work of other investigators was reviewed to determine if the assumed form of the collapse function was correct. Abbott and Kline (25) studied the zone of flow separation behind a backward facing step, a situation that is physically similar to flow in the wake region of a cavitation cavity. Figure 51 shows the experimental configuration that was used by Abbott and Kline along with their test results. Their results indicated that the length of the wake region was solely a function of the step height, which is consistent with our assumption that the cavity wake characteristics are a function of the cavity height. If the collapse is assumed

to be linear (a necessary approximation in view of the lack of any data concerning the actual shape) from the step to the wall, an effective collapse angle can be calculated ( $\arctan h/b$ ). This was done and the resulting plot of collapse angle vs passage blockage is shown in figure 52. Abbott's results are shown as data points and the original cavity model collapse function is shown as a dashed line. Both the Abbott data and our collapse function agree in that low cavity heights (or steps) have high collapse angles (very abrupt collapse) and high cavities have low collapse angles (very gradual collapse). There is a rapid transition from low to high collapse angle as the cavity height increases. The quantitative levels of the Abbott data and our own collapse function are different and there are several possible explanations for this. The step of Abbott is not exactly similar to the cavity in that the step represents a solid flow boundary. Abbott's data are also representative of fully developed flow to which the step is perpendicular and which is confined by sidewalls. In the inducer the cavities may collapse on the uncovered part of the blade where the flow is not confined and the flow will contain velocity and pressure gradients. These flow differences would be expected to result in a quantitative difference in the collapse angle functions.

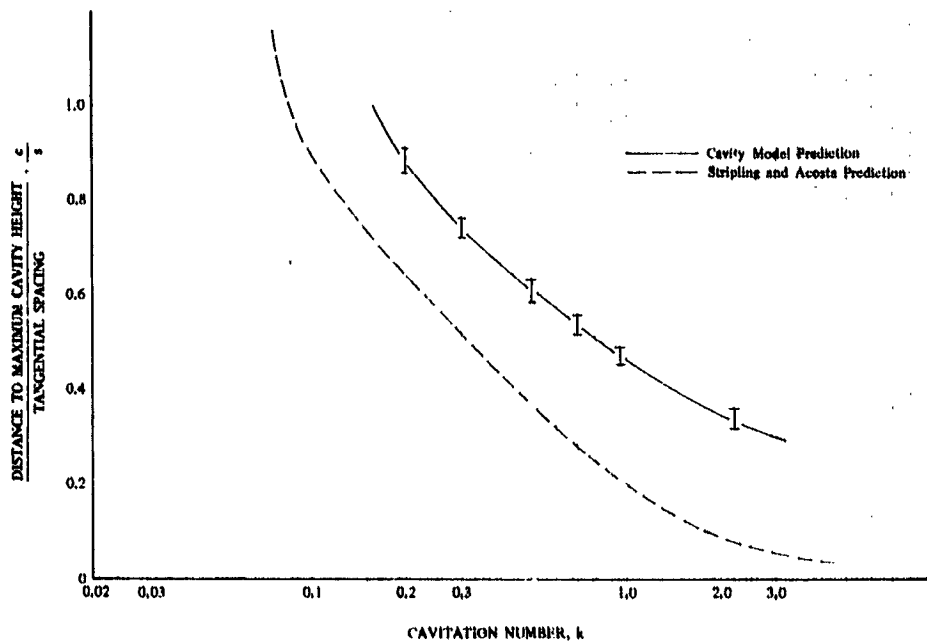


Figure 49. Comparison of Cavity Length-to-Maximum DF 91080 Height Predictions With Exact Predictions; Ideal Hydrofoil Cascade,  $i = 0.78$  rad (16 deg)

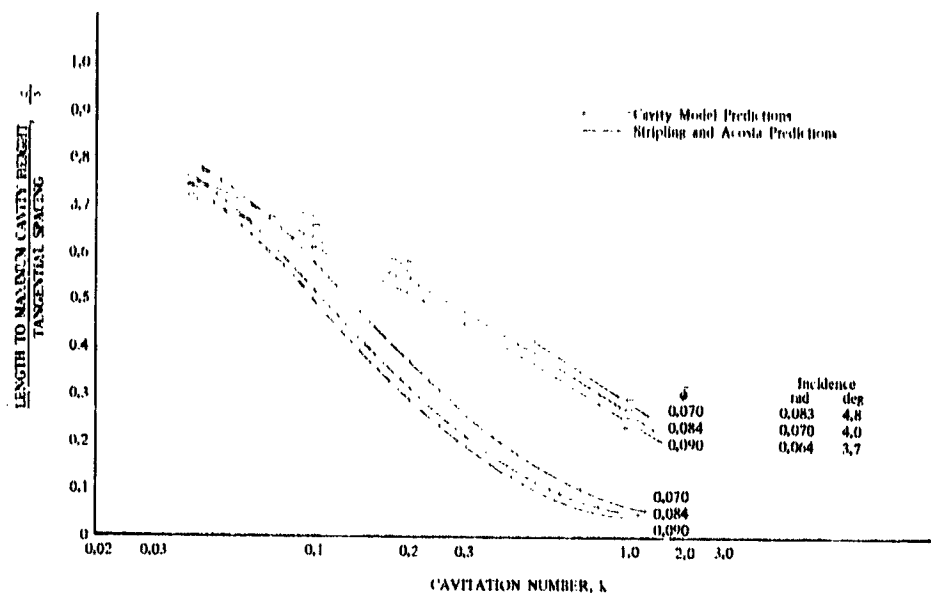


Figure 50. Comparison of Cavity Length to Maximum DF 91081  
Height Predictions With Exact Predictions,  
Ideal Inducer Cascade

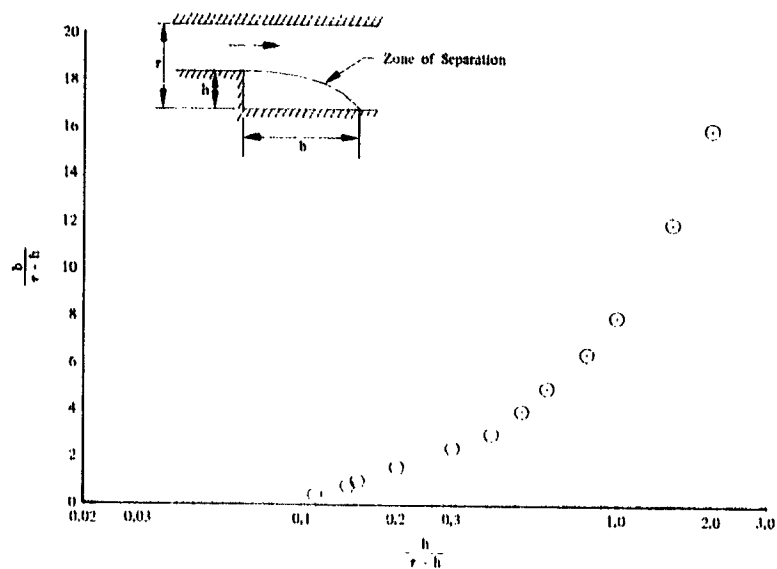


Figure 51. Flow Separation Downstream of a Back- DF 91079  
ward Facing Step (Data From Abbott and  
Kline)

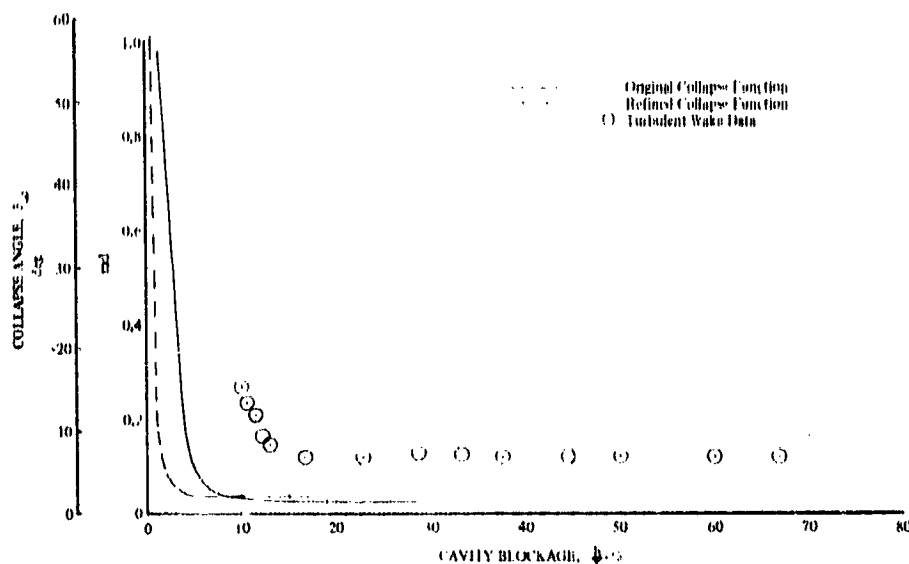


Figure 52. Flow Separation Data Compared With Empirical Cavity Collapse Function

DF 91152

The general agreement of the cavity collapse angle function with the Abbott data was considered to substantiate the form of the cavity model collapse angle function. Accordingly, the original angle function was adjusted to bring overall cavity length predictions into agreement with the test data. The final function is shown as a solid line in figure 52. Note that the use of overall cavity length measured data to define the function effectively compensates for the inaccuracy in length to maximum cavity height predictions that were discussed in the previous subsection. The error in profile area that is accepted through this approach can be appreciated by considering figure 53, which shows cavity profiles in an ideal inducer cascade. The solid profile is the one that would be predicted by the cavity model and the dashed line is the Stripling profile to maximum height along with the linear collapse to the same point as that of the cavity model. The area error is approximately 13% for the small and 12% for the large cavity, values which are considered quite satisfactory.

#### 5. 1. 2. 4 Cavity Overall Length

Predicted overall cavity lengths, generated using the collapse model of figure 52, are compared with inducer test data from (1) in figures 54 and 55. Figure 54 is for the inducer tip measurement streamline and figure 55 is for the midspan streamline. The available test data are limited and the cavity model cannot be fully substantiated, particularly with regard to the length variation with flow coefficient. A degree of confidence in the model's prediction as a function of flow coefficient is gained, however, when the correlation for both the tip and midspan streamlines is considered. There is a difference in incidence angle at these two streamlines because of the difference in blade angle and wheel speed. The incidence and blade angle differences would be predicted to have a significant effect on the cavity profiles, as would a difference in flow coefficient. A tabulation of blade and flow angles at these two streamlines is given in table 8.

Flow angles assume no prerotation and all angles are measured from the tangential direction. For the 0.090 tip flow coefficient, the flow coefficient at which most of the blade pressure data were taken, incidence angles at tip, and midspan were 0.052 rad (3.0 deg) and 0.072 (4.1 deg). Blade angles are 0.148 rad (8.5 deg) and 0.202 rad (11.6 deg). The difference in incidence angle between these streamlines approximately corresponds to a change in flow coefficient of from 0.000 to 0.070 at the tip streamline station.

Cavity length predictions are compared with the cascade test data in figure 56. Predicted data are shown for incidence angles of 0.28 and 0.17 rad (16 and 10 deg) and measured data are at indicated incidence angles of 0.28, 0.31, and 0.35 rad (16, 18, and 20 deg). Predicted lengths are longer than the measured lengths in spite of the lower incidence angles. This result is consistent with the results of the cavity height correlation and with the presumed lower than measured test incidence angles. If predicted data are accurate, the measured data indicate that actual incidence was less than 0.17 rad (10 deg) for the tests.

#### 5.1.2.5 Cavity Volume

Cavity volume predictions were generated for the radial leading edge inducer with the refined cavity model over a range of inlet tip flow coefficients and cavitation numbers. The volumes were calculated through radial integration of the predicted profile area. The resulting volume function or map, which was subsequently used in the instability analysis is shown in figure 57.

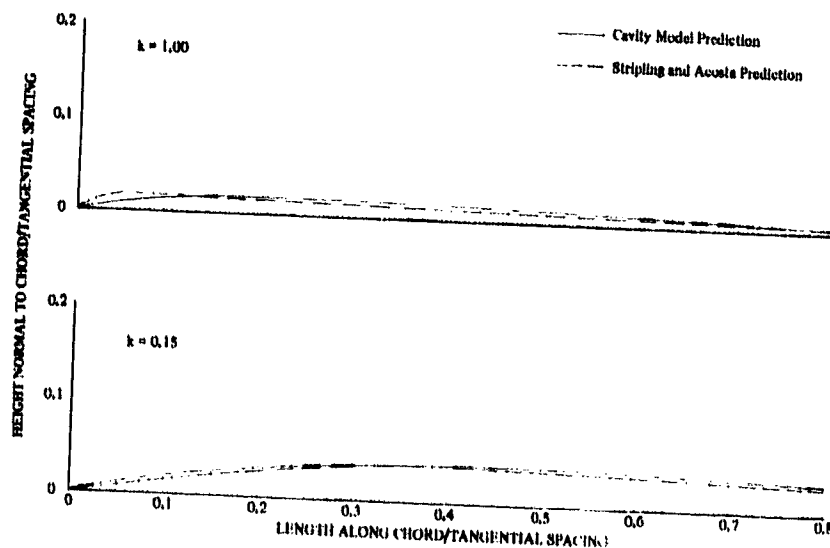


Figure 53. Comparison of Cavity Profiles for an Inducer Cascade ( $\beta^* = 0.15$  rad, 8.83 deg;  $l = 0.07$  rad, 3.8 deg)

DF 91000

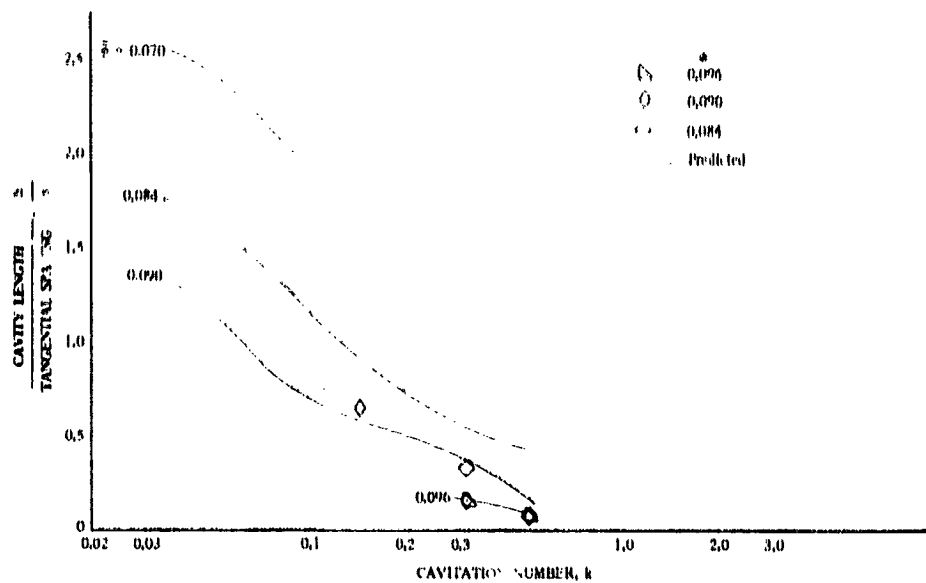


Figure 54. Comparison of Cavity Length Predictions With Inducer Test Data, Tip Streamline DF 91077

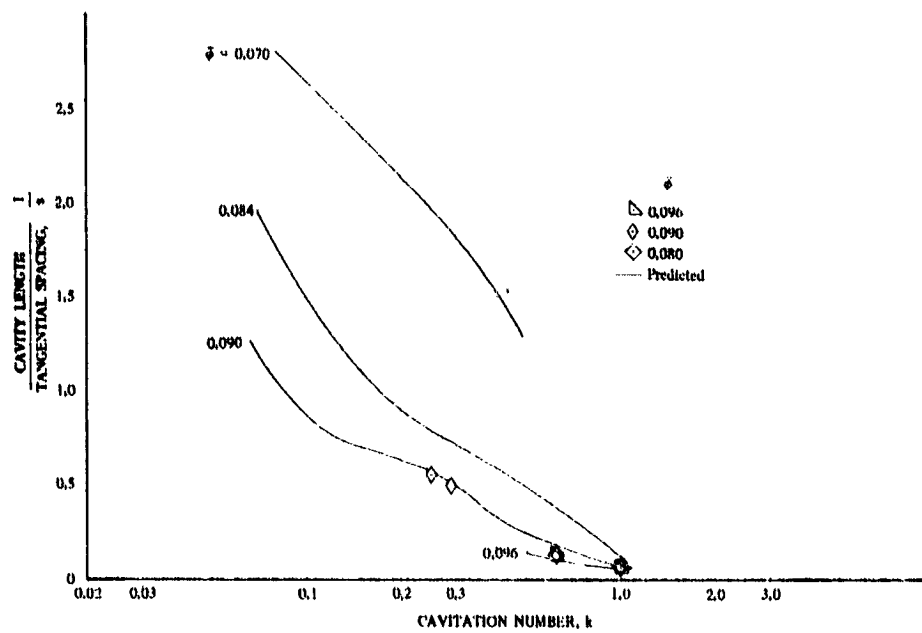


Figure 55. Comparison of Cavity Length Predictions With Inducer Test Data; Midspan Streamline DF 91078

Table 8. Blade and Flow Angles for Inducer Measurement Streamlines

Inlet Tip Flow Coefficient	Tip Streamline						Midspan Streamline					
	Blade Angle		Relative Flow Angle		Incidence Angle, $\alpha$		Blade Angle		Relative Flow Angle, $\beta$		Incidence Angle, $\alpha$	
	rad	deg	rad	deg	rad	deg	rad	deg	rad	deg	rad	deg
0.096	0.148	8.5	0.101	5.8	0.047	2.7	0.202	11.6	0.140	8.0	0.063	3.6
0.000	0.148	8.5	0.096	5.5	0.052	3.0	0.202	11.6	0.131	7.5	0.072	4.1
0.084	0.148	8.5	0.089	5.1	0.069	3.9	0.202	11.6	0.122	7.0	0.080	4.6
0.070	0.148	8.5	0.075	4.3	0.073	4.2	0.202	11.6	0.101	5.8	0.101	5.8

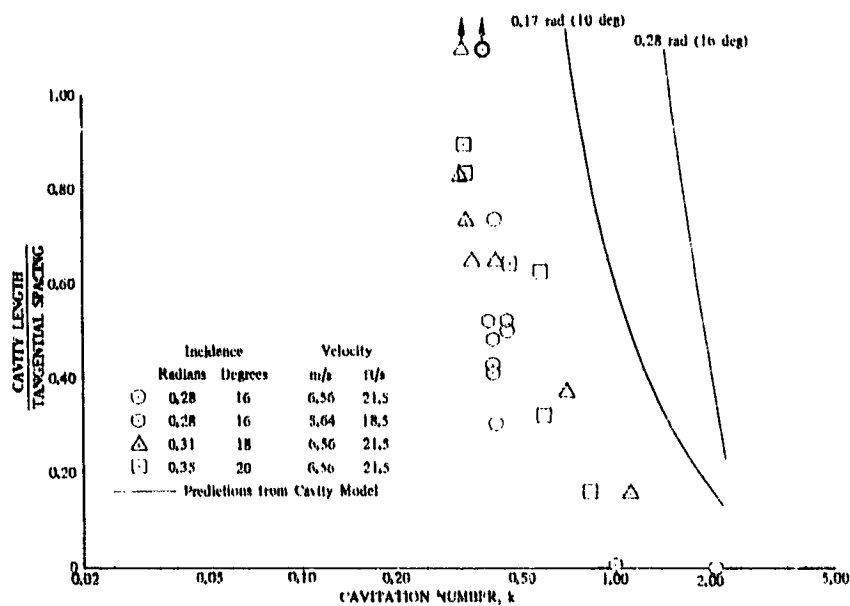


Figure 56. Comparison of Cavity Length Predictions With Cascade Test Data DF 89779

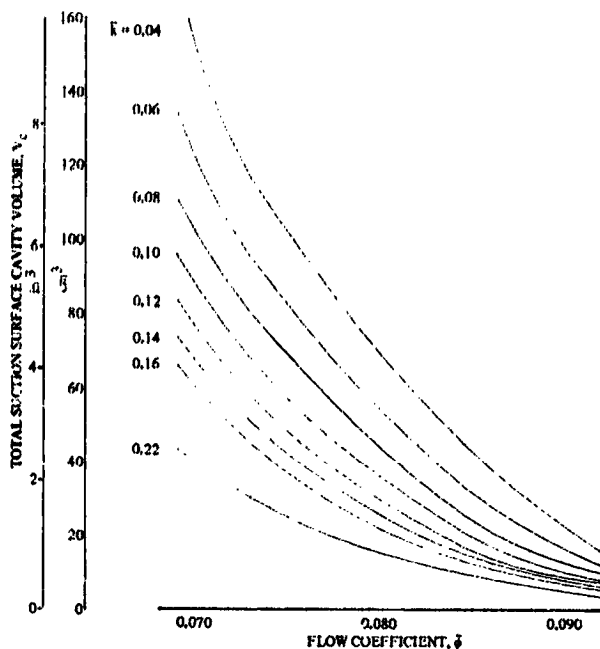


Figure 57. Predicted Suction Surface Cavity Volume, DF 90999  
Radial Leading Edge Inducer

Sweepback tends to reduce cavity length as shown in the measured data plot of figure 58. It can be assumed that volume is proportional to length so that volume also decreases with sweepback. This relationship of cavity volume to sweepback was used to evaluate instability data for the swept inducer instead of a more rigorous regeneration of swept inducer cavity volumes and stability predictions because of convergence problems which were being experienced with the inducer internal flow computer program. The computer program was being refined to include swept inducers concurrently in a related program (26). This approach was adequate for our purposes where an instability prediction technique was to be validated and the cavity volume predictions for swept inducers will be obtainable when the work of (26) is completed.

## 5.2 CASCADE TUNNEL INSTABILITY

### 5.2.1 Analytic Model

A dimensional schematic of the cascade tunnel is shown in figure 59. A linear dynamic model of the facility was prepared to investigate the characteristics of cascade flow that could cause an instability. The model was based on the assumptions that the flow past each cascade blade is identical, causing the cavities to oscillate in unison; and blade-to-blade pressure and flow distortion and cavitation propagation along the cascade do not occur. No propagation was evident during the tests.

A simplified model of the complete facility was prepared so that the essential features of an instability could be investigated. Referring to the schematic of figure 59, it is apparent that the plenum tank, being large and containing a free surface, could be considered a point of constant pressure (infinite compliance). If some plane in the nozzle could also be considered a point of constant pressure, these two points become boundaries that isolate the nozzle and cascade from the remainder of the facility. Only that portion of the facility from the chosen nozzle plane through the cascade to the plenum tank requires modeling. The validity of treating a plane in the nozzle as a constant pressure boundary was later substantiated by the test data.

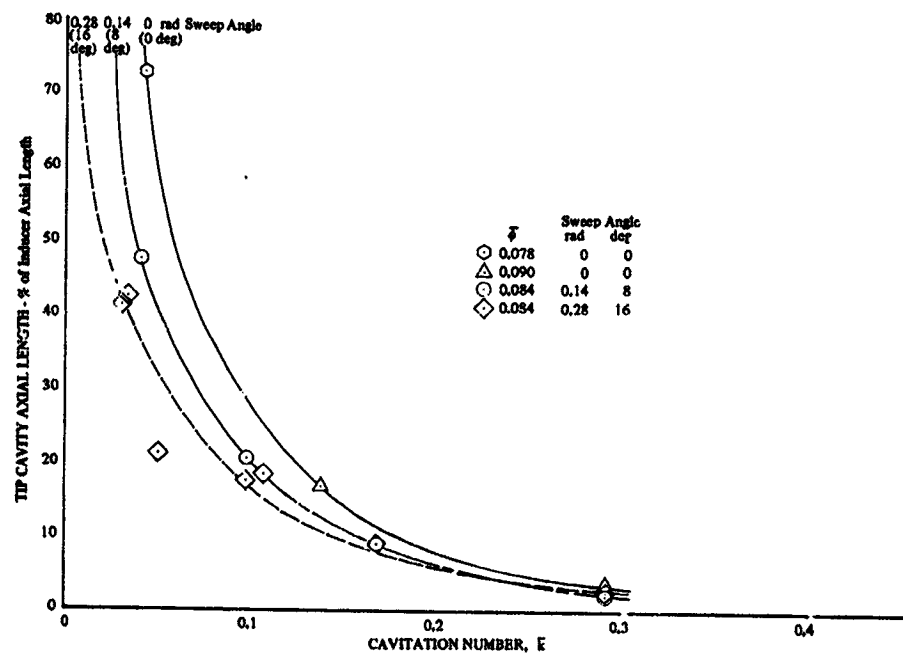
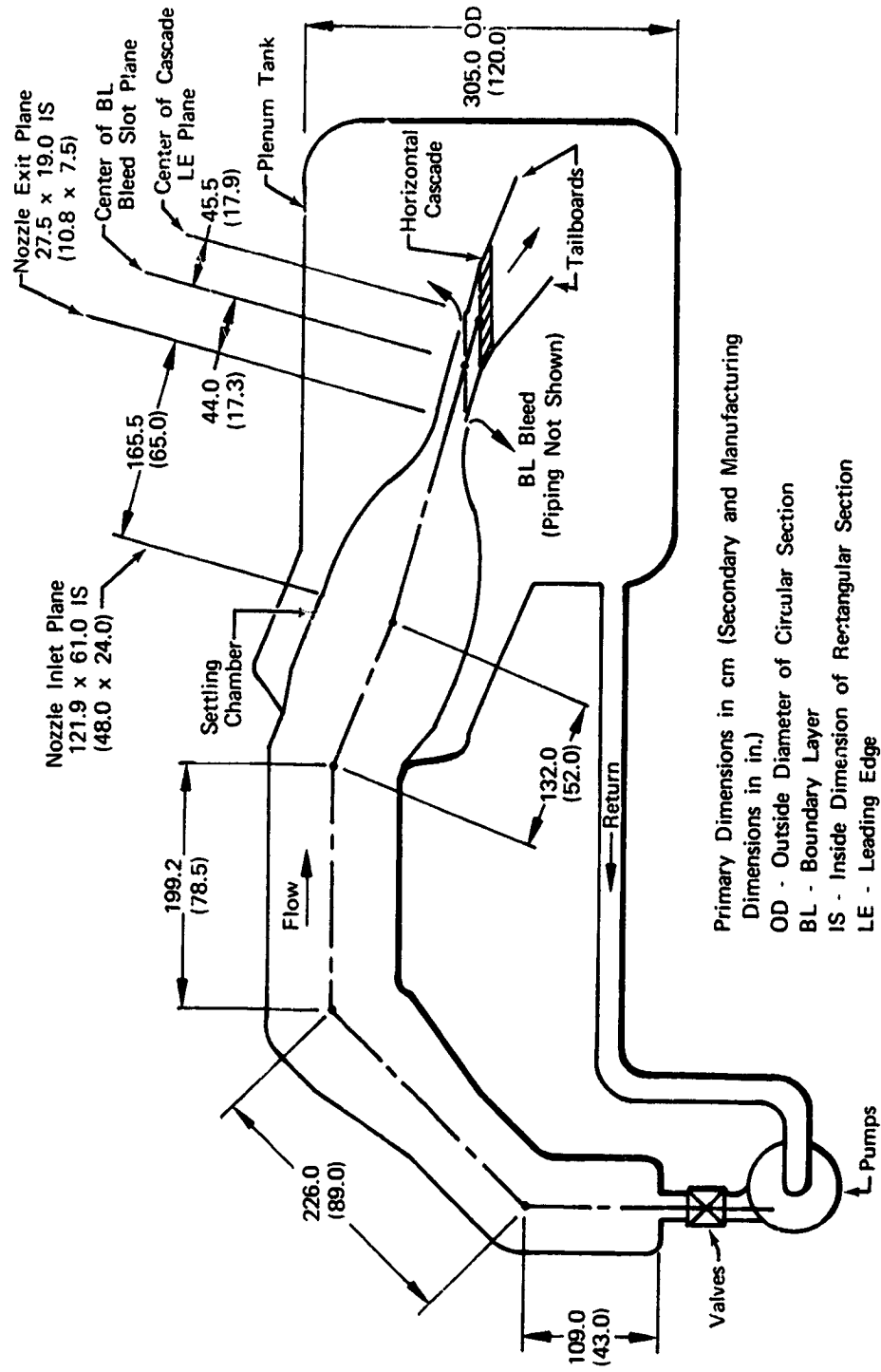


Figure 58. Measured Effect of Sweep Angle on Inducer DF 90996 Cavity Length



Primary Dimensions in cm (Secondary and Manufacturing  
 Dimensions in in.)  
 OD - Outside Diameter of Circular Section  
 BL - Boundary Layer  
 IS - Inside Dimension of Rectangular Section  
 LE - Leading Edge

Figure 59. Cascade Tunnel Dimensions

FD 58633

A schematic of that portion of the cascade facility chosen for modeling is shown in figure 60. The model consists of:

1. A constant pressure boundary at static pressure ( $p_n$ ) across which a fluid of constant density ( $\rho$ ) is flowing.
2. A rigid nozzle length ( $l_i$ ) and inlet and exit cross sectional areas ( $A_n$  and  $A_i$ ) measured normal to the flow direction. Flow through the nozzle ( $W_i$ ) is considered incompressible, frictionless, and one-dimensional at each cross section.
3. A cascade and tailboard section with a total-to-total pressure loss ( $D$ ) that is dependent on the instantaneous value of inlet static pressure ( $p_i$ ), inlet flowrate ( $W_i$ ), and discharge flowrate ( $W_d$ ). Pressure drop is measured from the cascade leading edge plane to the tank pressure ( $p_t$ ).
4. A cavitation cavity on each cascade hydrofoil suction surface that results in a total cavity volume ( $V_c$ ) that is dependent on the instantaneous values of inlet static pressure ( $p_i$ ) and inlet flowrate ( $W_i$ ).
5. A large plenum tank at constant pressure ( $p_t$ ).

The model neglects the boundary layer bleed system, which has the effect of an upstream compliance, and neglects fluid compressibility and wall expansion in the nozzle, which would require that the nozzle be broken into several calculation sections (or "lumps") for accurate modeling. However, it is unlikely that either of the neglected effects would make a difference in determining whether flow through the cascade is stable or unstable.

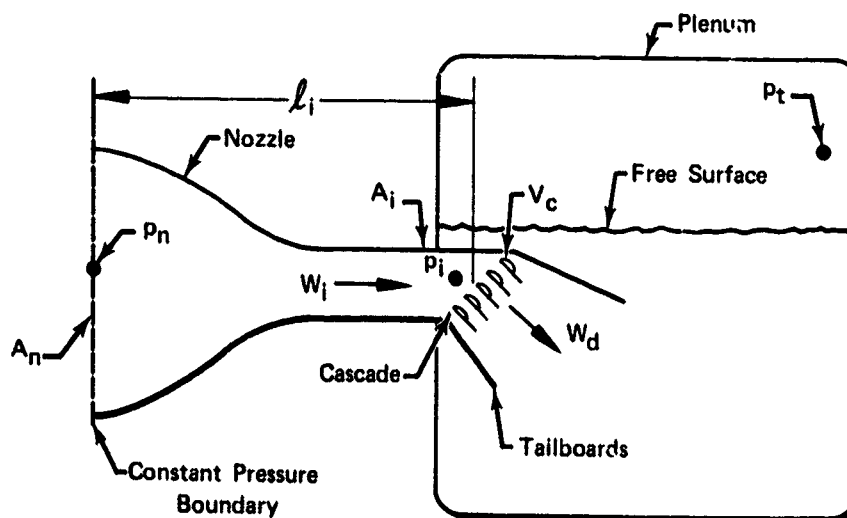


Figure 60. Cascade Instability Model

FD 61195

For small amplitude oscillations, dynamic behavior of the model can be described, and the onset of an instability can be predicted, by treating linear perturbations about the steady-state operating point. A set of linear algebraic and differential equations results. Letting ( $\Delta$ ) denote a linear perturbation and ( $\dot{\bullet}$ ) denote the derivative with respect to time ( $d/dt$ ), the equations (general and linearized), which represent the model, are:

Nozzle:

$$p_n - p_i = \left[ \frac{1}{A_i^2} - \frac{1}{A_n^2} \right] \frac{W_i^2}{2\rho} + \frac{dW_i}{dt} \int_0^{l_i} \frac{dx}{A}$$

$$-\Delta p_i = \left[ \frac{1}{A_i^2} - \frac{1}{A_n^2} \right] \frac{W_i}{\rho} \Delta W_i + \Delta \dot{W}_i \int_0^{l_i} \frac{dx}{A} \quad (1a)$$

Cavity Volume:

$$V_c = \text{function}(p_i, W_i)$$

$$\Delta V_c = \frac{\partial V_c}{\partial p_i} \Delta p_i + \frac{\partial V_c}{\partial W_i} \Delta W_i \quad (2a)$$

Continuity:

$$W_i = W_d - \rho \frac{dV_c}{dt}$$

$$\Delta W_i = \Delta W_d - \rho \Delta \dot{V}_c \quad (3a)$$

Cascade Pressure Drop:

$$p_i + \frac{W_i^2}{2\rho A_i^2} = p_t + D$$

$$\Delta p_i + \frac{W_i}{\rho A_i^2} \Delta W_i = \Delta D \quad (4a)$$

$D = \text{function}(p_i, W_i, W_d)$

$$\Delta D = \frac{\partial D}{\partial p_i} \Delta p_i + \frac{\partial D}{\partial W_i} \Delta W_i + \frac{\partial D}{\partial W_d} \Delta W_d \quad (5a)$$

The coefficients in each of the above linearized equations are taken to be constants evaluated at the steady-state operating point, where  $W_i = W_d = W$ , the steady-state flowrate. Substituting equation (2a) into (3a) and (4a) into (5a), and taking the

Laplace transform ( $S =$  Laplace variable) of each equation, a set of equations is obtained in which some convenient definitions can be made

$$-\Delta p_l = \left[ \frac{1}{A_l^2} - \frac{1}{A_n^2} \right] \frac{W}{\rho} \Delta W_l + S \Delta W_l \int_0^{l_l} \frac{dx}{A} \quad (1b)$$

$$\Delta W_l = \Delta W_d - \rho \frac{\partial V_c}{\partial p_l} S \Delta p_l - \rho \frac{\partial V_c}{\partial W_l} S \Delta W_l \quad (3b)$$

$$\left[ 1 - \frac{\partial D}{\partial p_l} \right] \Delta p_l + \left[ \frac{W}{\rho A_l^2} - \frac{\partial D}{\partial W_l} \right] \Delta W_l - \frac{\partial D}{\partial W_d} \Delta W_d = 0 \quad (5b)$$

The following definitions are made:

Inlet Resistance:

$$R_l = \frac{W}{\rho} \left[ \frac{1}{A_l^2} - \frac{1}{A_n^2} \right]$$

Inlet Inertance:

$$L_l = \int_0^{l_l} \frac{dx}{A}$$

Pressure Compliance:

$$C_p = -\rho \frac{\partial V_c}{\partial p_l}$$

Flow Compliance:

$$C_w = -\rho \frac{\partial V_c}{\partial W_l}$$

Pressure Gain:

$$G_p = 1 - \frac{\partial D}{\partial p_l}$$

Flow Gain:

$$G_w = \frac{W}{\rho A^2} - \frac{\partial D}{\partial W_l}$$

Cascade Internal Resistance:

$$R_c = \frac{\partial D}{\partial W_d}$$

Substituting these definitions into equations (1b, 3b, and 5b) allows the characteristic equation to be obtained in the form:

$$[R_c L_i C_p] S^2 + [R_c (R_i C_p - C_w) + G_p L_i] S + [R_c + R_i G_p - G_w] = 0 \quad (7)$$

An operating point will be stable if all roots of the characteristic equation have negative real parts, indicating a tendency of the flow to return to an equilibrium state if momentarily disturbed. Otherwise the operating point is unstable. Because this characteristic equation is of the second order the roots will have negative real parts (indicating a stable operating point) only if all three coefficients in brackets have the same sign. Conversely, the operating point will be unstable if any coefficient vanishes or takes on a sign different from the other two. Therefore, to determine stability, it was necessary to evaluate each term making up the coefficients of equation (7). These terms were evaluated at the steady-state operating point from the definitions of equation (6).

Inlet Resistance and Inertance ( $R_i$  and  $L_i$ ):

If inlet resistance is written in terms of the inlet velocity head ( $q_i$ ) where:

$$q_i = \frac{W^2}{2\rho A_i^2}$$

The expression for resistance is:

$$R_i = \frac{2q_i}{W} \left[ 1 - \frac{A_i^2}{A_n^2} \right]$$

Since both terms are positive it is apparent that  $R_i$  is always positive.

When inlet inertance is defined in terms of a "mean nozzle area" ( $\bar{A}$ ) such that

$$L_i = \int_0^{l_i} \frac{dX}{A} = \frac{l_i}{\bar{A}}$$

It is also apparent that  $L_i$  is a positive number at all operating points.

Pressure and Flow Compliance ( $C_p$  and  $C_w$ ):

According to the cascade flow model of Stripling and Acosta (19) for fixed geometry and fixed incidence, the maximum cavity height ( $h$ ) and length ( $c$ ) from the blade leading edge to the point of maximum cavity height (figure 45) are functions only of cavitation number ( $k$ ) where:

$$k = \frac{p_l - p_v}{q_l} \quad (p_v = \text{vapor pressure}) \quad (8)$$

In (19), both  $h$  and  $c$  are shown to increase as  $k$  is lowered and to decrease as  $k$  is raised. The experimental measurements of cavity height and total length show the same trend. It is reasonable to expect that total cavity volume ( $V_c$ ) will also be a function only of cavitation number, for fixed

geometry and incidence, and will follow a trend identical to the length and height as shown in figure 61. If we assume that the cascade incidence is fixed at any operating point, whether steady or unsteady, then the terms  $C_p$  and  $C_w$  can be calculated (using equation (8)) as:

$$C_p = -\rho \frac{\partial v_c}{\partial p_i} = \frac{-\rho}{q_i} \frac{dv_c}{dk}$$

$$C_w = -\rho \frac{\partial v_c}{\partial W_i} = \frac{2\rho k}{W} \frac{dv_c}{dk}$$

Since  $dv_c/dk$  is always negative,  $C_p$  is always positive and  $C_w$  is always negative.

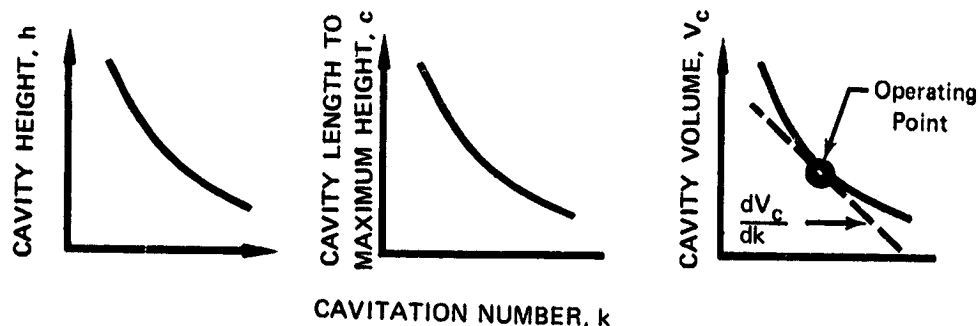


Figure 61. Cascade Cavity Relationships

FD 62908

Pressure and Flow Gain ( $G_p$  and  $G_w$ ):

The cascade total pressure drop ( $D$ ) at any cavitating steady-state operating point can be written as the product of the noncavitating pressure drop ( $D_{nc}$ ), at the same flowrate but high inlet pressure, and a dimensionless pressure drop ratio ( $\lambda$ ).

$$D = \lambda D_{nc}$$

This equation serves as the definition of  $\lambda$  and as the means for calculating its value at any operating point. The noncavitating pressure drop ( $D_{nc}$ ) will be a function only of flowrate ( $W$ ) for fixed geometry and incidence. We assume that  $\lambda$  is a function only of cavitation number ( $k$ ). Then at any steady-state operating point:

$$D(k, w) = \lambda(k) D_{nc}(W)$$

To adapt this equation to the cascade instability model, we assume that the same relationship holds under nonsteady conditions, with  $\lambda$  always equal to the steady-state value of  $\lambda$  that would exist at the instantaneous cavitation number, and  $D_{nc}$  always equal to the steady-state value of  $D_{nc}$  that would

exist at the instantaneous discharge flowrate. Then at any unsteady operating point:

$$D(k, W_d) = \lambda(k) D_{nc}(W_d)$$

$$\frac{\partial D}{\partial p_1} = D_{nc} \frac{\partial \lambda}{\partial p_1} = \frac{D_{nc}}{q_1} \frac{d\lambda}{dk}$$

$$\frac{\partial D}{\partial W_1} = D_{nc} \frac{\partial \lambda}{\partial W_1} = \frac{-2k D_{nc}}{W} \frac{d\lambda}{dk}$$

Defining a noncavitating pressure loss coefficient ( $C_{nc}$ ):

$$D_{nc} = C_{nc} q_1$$

$$G_p = 1 - \frac{\partial D}{\partial p_1} = 1 - C_{nc} \frac{d\lambda}{dk}$$

$$G_w = \frac{W}{\rho A_1^2} - \frac{\partial D}{\partial W_1} = \frac{2q_1}{W} \left[ 1 + k C_{nc} \frac{d\lambda}{dk} \right]$$

$G_p$  and  $G_w$  can be positive or negative depending upon the sign and magnitude of  $(d\lambda/dk)$ .

Cascade Internal Resistance ( $R_c$ ):

$$R_c = \frac{\partial D}{\partial W_d} = \lambda \frac{\partial D_{nc}}{\partial W} = \lambda \frac{\partial (C_{nc} q_1)}{\partial W} = 2\lambda C_{nc} \frac{q_1}{W}$$

$R_c$  is positive at all operating points.

The terms making up the coefficients of the characteristic equation (7) can be summarized as follows:

$$R_1 = \frac{2q_1}{W} \left[ 1 - \frac{A_1^2}{A_n^2} \right] > 0$$

$$L_1 = \frac{\ell_1}{A} > 0$$

$$C_p = \frac{-\rho}{q_1} \frac{dV_c}{dk} > 0$$

$$C_w = \frac{2\rho k}{W} \frac{dV_c}{dk} < 0 \quad (9)$$

$$\begin{array}{l}
 G_p = 1 - C_{nc} \frac{d\lambda}{dk} \quad \geq 0 \\
 G_w = \frac{2q_l}{W} \left[ 1 + k C_{nc} \frac{d\lambda}{dk} \right] \quad \geq 0 \\
 R_c = 2\lambda C'_{nc} \frac{q_l}{W} \quad > 0
 \end{array}
 \left. \vphantom{\begin{array}{l} G_p \\ G_w \\ R_c \end{array}} \right\} \begin{array}{l} \text{depend upon the sign of} \\ \frac{d\lambda}{dk} \end{array}$$

The first coefficient in the characteristic equation (7),  $R_c L_l C_p$ , is therefore positive at all operating points and the other two coefficients,  $[R_c(R_l C_p - C_w) + G_p L_l]$  and  $[R_c + R_l G_p - G_w]$  must also be positive for an operating point to be stable. Therefore, an operating point will be unstable if:

$$R_c(R_l C_p - C_w) + G_p L_l \leq 0 \quad (10a)$$

or if:

$$R_c + R_l G_p - G_w \leq 0 \quad (11a)$$

Referring to equations (9), (10a) and (11a), it is apparent that the only way an instability can occur is for  $G_p$  to be negative in equation (10a) or for  $R_l G_p - G_w$  to be negative in equation (11a), since  $L_l$ ,  $R_c$  and  $R_l C_p - C_w$  are always positive. Therefore, the model indicates that cascade instabilities result from the gains ( $G_p$  and  $G_w$ ), which are related to the term  $d\lambda/dk$ , the slope of the pressure drop ratio curve. Stable and unstable forms of this curve are shown in figure 62.

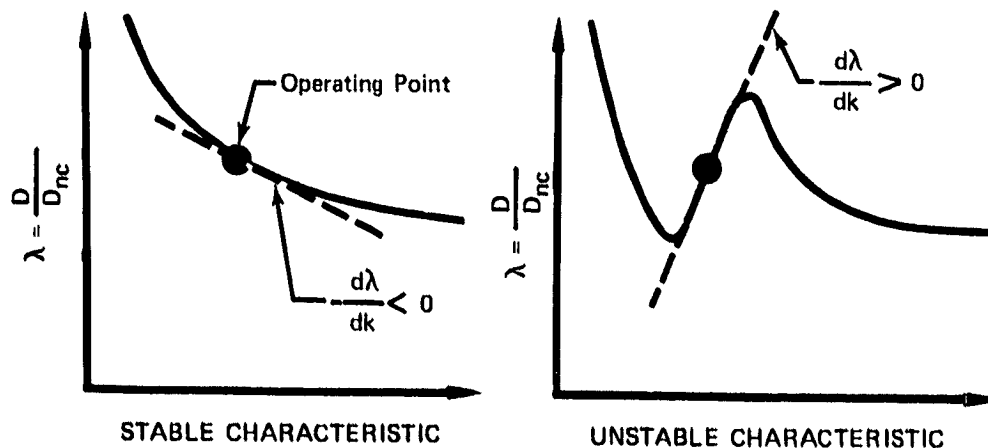


Figure 62. Cascade Pressure Drop Ratio Curves  
(Cavitating/Noncavitating)

FD 62909

In the stable characteristic, the curve is flat at high cavitation numbers and turns upward smoothly as cavitation number is lowered, indicating that the cascade becomes a greater restriction to flow as cavitation increases. In the unstable characteristic, the curve is also flat at high cavitation numbers, but has an inflection as cavitation number is lowered. The requirement that the loss curve have an inflection for a cascade instability to occur was also found by Acosta (6). The slope of a loss curve inflection that would be required to

cause an instability was defined by substituting from equation (9) into equations (10a) and (11a). An operating point would be unstable if:

$$\frac{d\lambda}{dk} \geq \frac{1}{C_{nc}} + \frac{2\lambda\bar{A}}{\ell_1 A_1^2} \left[ 1 - \frac{A_1^2}{A_n^2} + k \right] \left( \frac{-dV_c}{dk} \right) \quad (10b)$$

or if:

$$\frac{d\lambda}{dk} \geq \frac{\lambda - \frac{1}{C_{nc}} \left( \frac{A_1^2}{A_n^2} \right)}{1 - \frac{A_1^2}{A_n^2} + k} \quad (11b)$$

The right side of equation (10b) is positive at all operating points. In equation (11b) the order of magnitude of the terms is:

$$\lambda \sim 1$$

$$C_{nc} \sim 1$$

$$A_1^2/A_n^2 \sim 0.01$$

so that the right side of equation (11b) is also positive at all operating points.

Therefore, the model predicts that an operating point can be unstable only if  $d\lambda/dk$  is positive and has a magnitude greater than that required by either equation (10b) or (11b). Referring to the pressure drop ratio curves of figure 62, the model predicts that a cascade with the stable characteristic will be stable at all operating points, while a cascade with the unstable characteristic will be unstable on that part of the inflection having a positive slope, if the slope is sufficiently steep. The magnitude of the slope required for an instability can be estimated by approximating the values of the terms. These were estimated as follows:

$$\lambda \sim 1$$

$$C_{nc} \sim 1$$

$$A_1^2/A_n^2 \sim 0.01$$

$$k \sim 0.4$$

$$\bar{A} \sim 600 \text{ cm}^2 \text{ (93 in}^2\text{)}$$

$$\ell_1 \sim 1.6 \text{ m (5.3 ft)}$$

$$A_1 \sim 500 \text{ cm}^2 \text{ (78 in}^2\text{)}$$

$$dV_c/dk \sim -2000 \text{ cm}^3 \text{ (-122 in}^3\text{)}$$

The value of  $dV_c/dk$  was estimated by fitting a circular arc from the blade leading edge through the maximum height point, defined by  $e$  and  $h$  in figure 45, and back to the blade to define a completely circular cavity. Then, at an incidence of 0.28 rad (16 deg), the total cavity volume was calculated for  $k = 0.4$  and  $k = 0.404$ , and  $dV_c/dk$  was approximated as  $\Delta V_c/\Delta k$ . Substituting the above values into equation (10b) and (11b) we obtain the following estimates for the slope required to cause an instability.

$$\frac{d\lambda}{dk} \geq 1.1 \quad (10c)$$

$$\frac{d\lambda}{dk} \geq 0.7 \quad (11c)$$

The required slopes are approximately equal, so that the instability model predictions can be summarized as stating that an operating point in the neighborhood of  $k = 0.4$  will be unstable if  $d\lambda/dk$  has a positive slope greater than about 1.0. We would therefore expect to find an inflection in the experimental pressure drop ratio curves, similar to figure 62, at each of the four test points shown as unstable in figure 15.

#### 5.2.2 Comparison of Cascade Instability Predictions to Test Results

The measured cascade pressure drop ratios from inlet total to the plenum free surface are plotted against cavitation number in figure 63. Estimated maximum uncertainties in cavitation number ( $\pm 2\%$ ) and in pressure drop ( $\pm 10\%$ ) are sufficiently small to allow identification of inflections in the curves. In figure 63 there is an inflection in the curve for 0.28 rad (16 deg) incidence at a cavitation number of about 0.4, and in the curve for 0.35 rad (20 deg) incidence at a cavitation number of about 0.35. The curve for 0.31 rad (18 deg) incidence does not show an inflection. This is probably due to an insufficient number of data points between test points No. 26 and 27, where an inflection would be expected. The positive slopes of the two identified inflections are much greater than 1.0, so, according to the instability model prediction, we would expect to see instabilities at all operating points that lie on the positive slope portions of the inflections. Therefore, at 0.28 rad (16 deg) incidence, unstable operating points are predicted to be No. 2, 3, 4, 5, 6, 9, 35, and 36, and at 0.35 rad (20 deg) incidence, No. 12 and 13. All other operating points at these two incidences are predicted to be stable. Definite predictions cannot be made for 0.31 rad (18 deg) incidence since the inflection cannot be identified; however, it probably occurs between test points No. 26 and 27, and we would expect test points to the left of No. 26 and to the right of No. 27 to be stable.

Comparing the predicted unstable points with the visual observations of table 4, most of the predicted unstable points are listed as unsteady, very unsteady, or pulsating. However, No. 9 and 36 are listed as steady. Also, many of the predicted stable points are listed as very unsteady. There is, therefore, no apparent correlation between predictions and visual observations. This might have been expected since there was also no correlation between observations and measured pressure amplitudes.

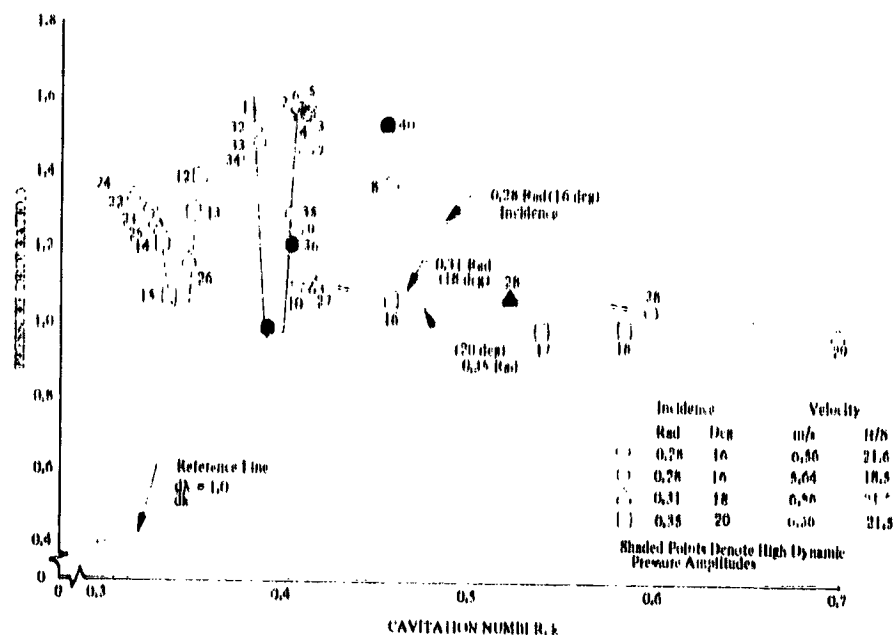


Figure 63. Cascade Pressure Drop Ratio, Cavitating to Noncavitating DF 91001

The test data points (28, 36, 37, and 40) with the highest cascade inlet dynamic pressure amplitudes (0.28 to 0.46 N/CM<sup>2</sup>, 0.4 to 0.7 psi) are shaded on figure 63. Points 36 and 37 could fall on the positive slope portion of the 0.28 rad (16 deg) incidence curve and might be expected to be unstable. Points 28 and 40 are removed from a positive slope area, however, and the relatively high dynamic pressure amplitudes for these points cannot be explained by our instability model. There are also many points on the positive slope portions of the curves that would be predicted to be unstable but which had relatively low dynamic pressure amplitudes.

Since there was apparently little correlation between predicted unstable operating regions and the test data, an estimate was made of the dynamic pressure amplitude that might be expected at an unstable operating point. An "order or magnitude" estimate was sufficient for this purpose, and it was made using the linearized equations of the tunnel model. (It should be noted that a linearized prediction of pressure amplitude is very approximate, and that an analog solution would be required in a thorough analysis.) Since very small amplitudes were used to form a relationship between changes in static pressure ( $\Delta p_1$ ) and changes in cavitation number ( $\Delta k$ ) as follows:

$$\Delta p_1 = -(R_1 + L_1 S) \Delta W_1$$

$$\Delta k = \frac{1}{q_1} \Delta p_1 - \frac{2k}{W} \Delta W_1$$

$$\frac{\Delta p_1}{\Delta k} = \frac{\left(\frac{W}{2k}\right) (R_1 + L_1 S)}{1 + \frac{W}{2 q_1 k} (R_1 + L_1 S)}$$

Using the definitions of equation (9) for  $(R_1)$  and  $(L_1)$  and with  $W = A_1(2 \rho q_1)^{1/2}$ :

$$\frac{\Delta p_1}{\Delta k} = \frac{\frac{q_1}{k} \left(1 - \frac{A_1^2}{A_n^2}\right) + \frac{l_1}{k} \frac{A_1}{A} \left(\frac{\rho q_1}{2}\right)^{1/2} S}{1 + \frac{1}{k} \left(1 - \frac{A_1^2}{A_n^2}\right) + \frac{l_1}{k} \frac{A_1}{A} \left(\frac{\rho}{2 q_1}\right)^{1/2} S}$$

Assuming that cavitation number varies sinusoidally at the frequency of test point No. 36 (20 Hz), then using the same approximation previously used for an incidence of 0.28 rad (16 deg), and additionally ( $q_1 \approx 0.2 \text{ N/cm}^2$ ), and ( $A_1 \approx 0.05 \text{ m}^2$ ), and ( $\rho \approx 1000 \text{ kg/m}^3$ ), an estimate of 0.2 N/cm<sup>2</sup> was obtained for the magnitude of  $(\Delta p_1/\Delta k)$ .

At an unstable operating point (No. 36 for example) we could expect cavitation number to vary in figure 63 so that the instantaneous operating point oscillates from one negative slope portion of the curve, where operation is stable, through the positive slope portion, where operation is unstable, and over to the other negative slope portion, where operation is again stable. This would require cavitation number to vary from 0.39 to 0.41. For this variation in cavitation number,  $\Delta p_1 = 2(0.2)(0.41 - 0.39) = 0.008 \text{ N/cm}^2$  (peak-to-peak) (0.012 psi). This value is approximately two orders of magnitude lower than any recorded dynamic pressure data.

An estimate of expected cavity length variation was made by assuming that total cavity length was twice the length to maximum height (c) predicted by Stripling and Acosta (19). For swings in cavitation number between 0.39 and 0.41, total cavity length would vary from 44% chord to 42% chord, a movement that would be difficult to detect and that was considerably exceeded for all cavitating test points.

Our conclusion concerning the cascade tunnel instability correlation is that any instabilities that may have occurred were obscured by normal cavitation oscillations. Cascade tunnel test results are therefore inconclusive in regard to substantiation of the model as a means for predicting instabilities. An analog model of the complete system would allow more accurate predictions of unstable frequency and amplitude, but the complexity of the system and the erratic, nonperiodic nature of the test data make it doubtful that such a model could be correlated with the data. Further modeling of the cascade tunnel was, therefore, not considered justified.

## 5.3 INDUCER INSTABILITIES

### 5.3.1 Analytic Model

A drawing of the inducer test loop, showing significant features and dimensions, is shown in figure 64 and a schematic of the dynamic model that was prepared to represent the system is shown in figure 65. The circled whole numbers refer to static and dynamic pressure measurement stations. Decimal numbers refer to calculation stations between measurement stations. Pressure drops around the loop are represented by resistances (R), fluid inertia by inertances (L), and fluid and pipe wall elasticity by compliances (C), using the standard lumped parameter modeling technique for hydraulic lines. Air pockets were treated as increases in local compliance and, since a linear analysis was used, the resistances were linearized about the steady operating point.

Frequency response analyses of the dead-end lines showed that the proper relationship of pressure to flowrate at the junctions could be obtained at frequencies up to about 30 Hz by treating the dead-end lines as simple compliances. The first closed-end resonance frequency of the longest section of the line in the inner loop treated as a lumped parameter is 135 Hz, as determined from the one-dimensional wave equations. Generally, experience with dynamic models has shown that the lumped parameter modeling technique is accurate at frequencies up to 10% to 20% of the first resonance. The model would therefore accurately follow a sine wave input up to about 20 Hz, and become progressively less accurate at higher frequencies. This accuracy was considered sufficient to model the instability, since the fundamental oscillation was found to be less than 20 Hz.

Equations were written to define the "through flow" or branch portions of the test loop in terms of the measured change in static pressure between two points, as listed in equations (12) below. Compliance at the node locations indicated in figure 65 was accounted for by relating it to the difference between entering and leaving flow, as listed in equations (13), and the inducer interfaces with the test loop system were defined through the inlet and discharge mass flowrates ( $W_8$ ) and ( $W_9$ ) and the inlet and discharge static pressures ( $p_9$  and  $p_{10}$ ), as shown in equations (14) and (15). All equations represent linear perturbations of pressure and flow about the steady-state operating point, the conventional  $\Delta$  having been omitted for clarity.  $S$  = Laplace variable representing  $d/dt$ . Other symbols are defined in the Appendix.

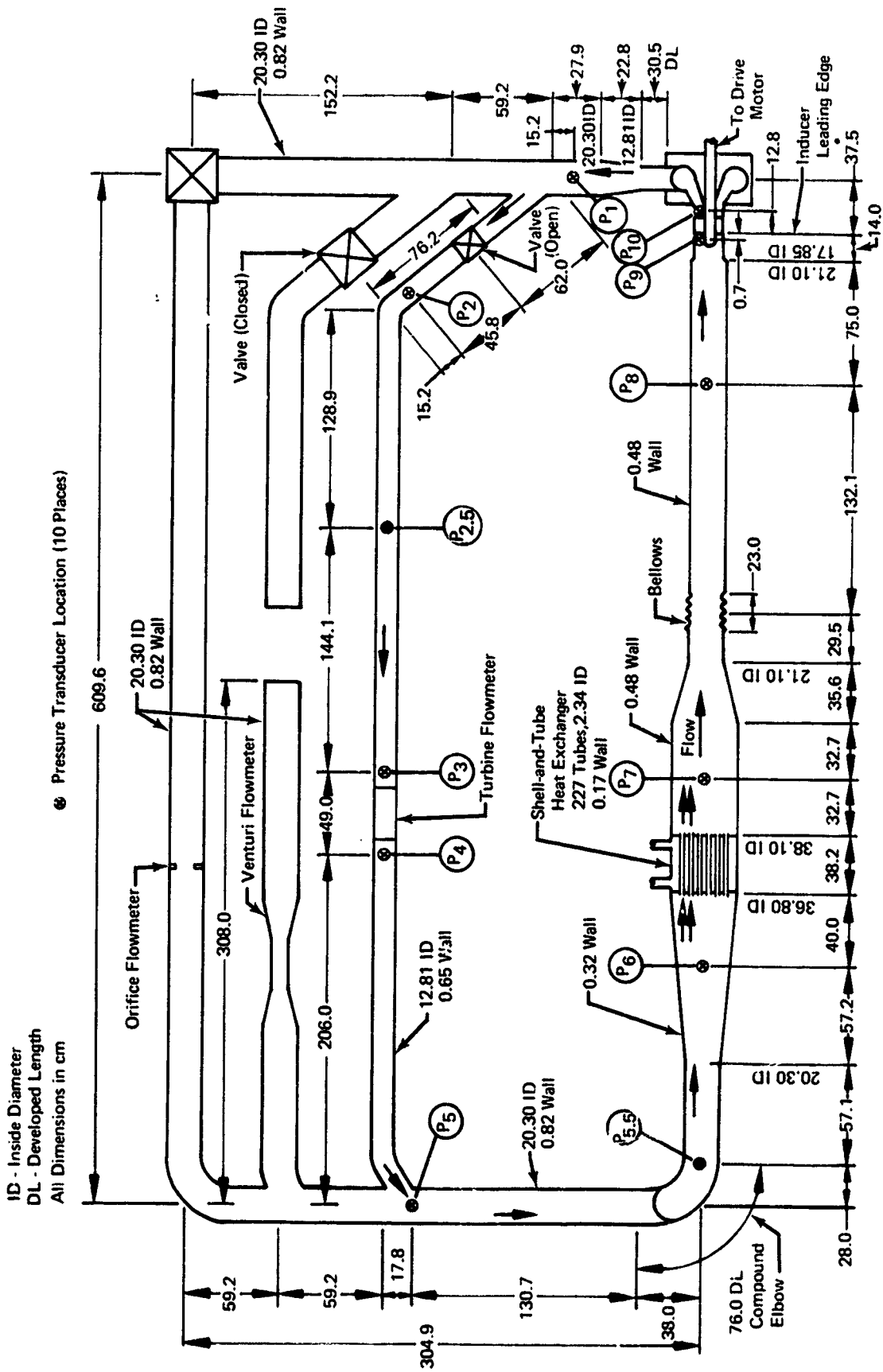


Figure 64. Dimensions of Inducer Water Loop

FD 62367

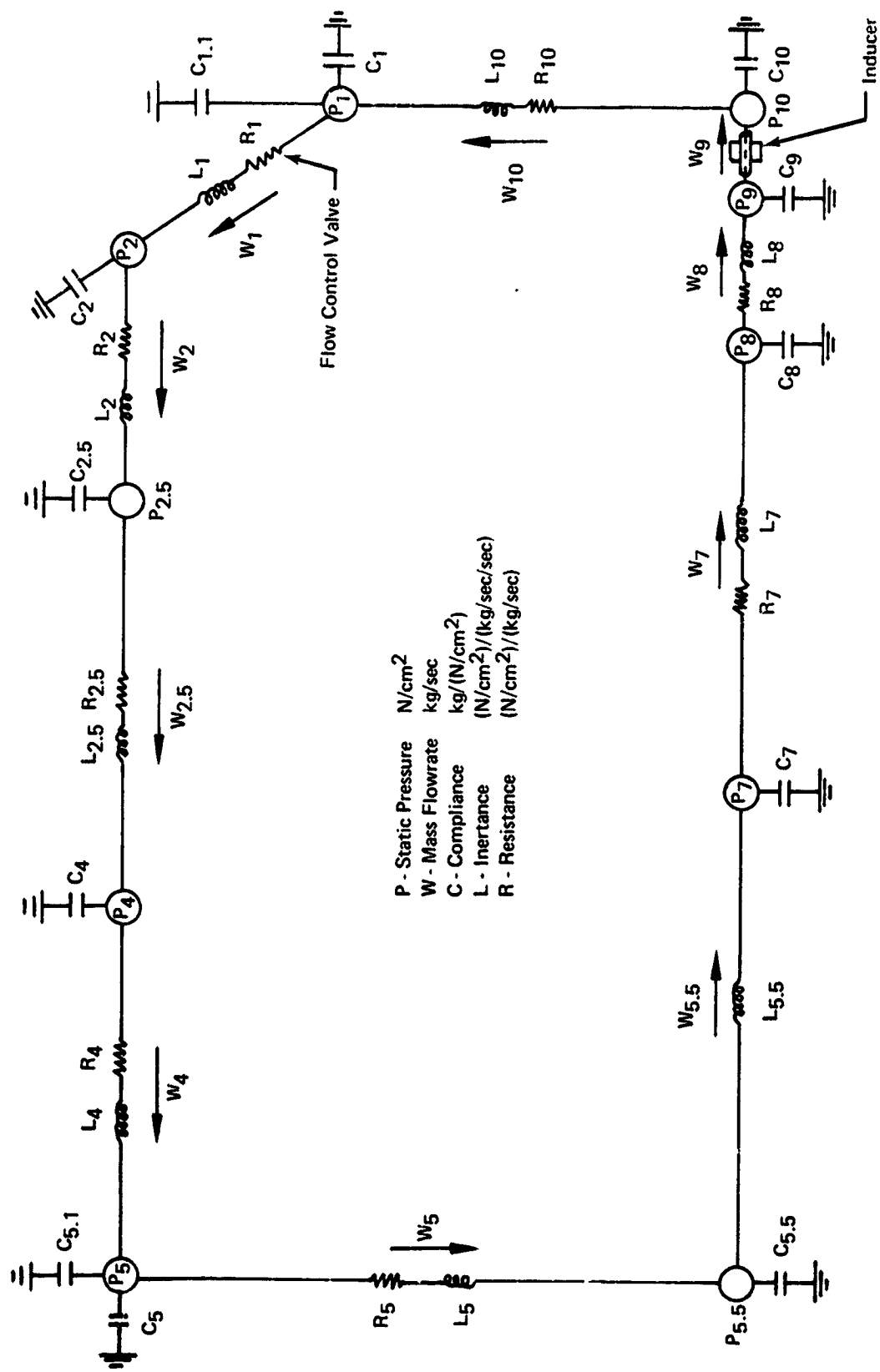


Figure 65. Schematic of Inducer Loop Dynamic Model

FD 62370

$$\begin{aligned}
p_{10} - p_1 - R_{10} W_{10} - L_{10} SW_{10} &= 0 \\
p_1 - p_2 - R_1 W_1 - L_1 SW_1 &= 0 \\
p_2 - p_{2.5} - R_2 W_2 - L_2 SW_2 &= 0 \\
p_{2.5} - p_4 - R_{2.5} W_{2.5} - L_{2.5} SW_{2.5} &= 0 \\
p_4 - p_5 - R_4 W_4 - L_4 SW_4 &= 0 \\
p_5 - p_{5.5} - R_5 W_5 - L_5 SW_5 &= 0 \\
p_{5.5} - p_7 - L_{5.5} SW_{5.5} &= 0 \\
p_7 - p_8 - R_7 W_7 - L_7 SW_7 &= 0 \\
p_8 - p_9 - R_8 W_8 - L_8 SW_8 &= 0
\end{aligned}
\tag{12}$$

$$\begin{aligned}
W_9 - W_{10} - C_{10} Sp_{10} &= 0 \\
W_{10} - W_1 - (C_1 + C_{1.1}) Sp_1 &= 0 \\
W_1 - W_2 - C_2 Sp_2 &= 0 \\
W_2 - W_{2.5} - C_{2.5} Sp_{2.5} &= 0 \\
W_{2.5} - W_4 - C_4 Sp_4 &= 0 \\
W_4 - W_5 - (C_5 + C_{5.1}) Sp_5 &= 0 \\
W_5 - W_{5.5} - C_{5.5} Sp_{5.5} &= 0 \\
W_{5.5} - W_7 - C_7 Sp_7 &= 0 \\
W_7 - W_8 - C_8 Sp_8 &= 0
\end{aligned}
\tag{13}$$

$$W_8 - W_9 - C_w SW_8 - (C_p + C_9) Sp_9 = 0 \tag{14}$$

$$p_{10} - G_p p_9 - G_w W_8 + R_p W_9 = 0 \tag{15}$$

These equations constitute the inducer system analytic model.

The values that were calculated for (L) and (C) from the known test loop geometry, the calculated pipe compliance, and the bulk modulus of water at the measured temperatures are tabulated in table 9. Resistances (R) at the test flow coefficients, which were calculated from the measured static pressures, are also tabulated. Discharge valve resistance was a variable (since inducer head rise varied with cavitation number), and its resistance is plotted against cavitation number in figure 66 for the radial leading edge inducer.

The inducer portion of the system dynamic model is illustrated in table 10. The variables that defined the inducer in equations (14) and (15) were obtained, as indicated in the table, from the measured head vs flow map (figure 24), the measured head vs cavitation number map (figure 27), and the predicted cavity volume map (figure 57). The cavity volume map of figure 57 represents blade surface cavitation only, and, to account for tip vortex cavitation, it would be necessary to plot the sum of both forms of cavitation. The derivation of the equations that represent the inducer are discussed in the following paragraphs.

Table 9. Values of Inducer Loop Inertance, Compliance, and Resistance

Position (Subscript)	Inertance, L $\frac{N/cm^2}{kg/s}$	Compliance, C $\frac{kg/s}{(N/cm^2)/s}$	Resistance, R $\frac{N/cm^2}{kg/s}$		
			$\phi = 0.070$	$\phi = 0.084$	$\phi = 0.090$
1	$8.36 \times 10^{-3}$	$0.54 \times 10^{-4}$	(1)	(1)	(1)
1.1	(2)	$5.56 \times 10^{-4}$	(2)	(2)	(2)
2	$11.20 \times 10^{-3}$	$0.76 \times 10^{-4}$	$4.66 \times 10^{-2}$	$5.64 \times 10^{-2}$	$6.10 \times 10^{-2}$
2.5	$15.00 \times 10^{-3}$	$1.01 \times 10^{-4}$	$11.58 \times 10^{-2}$	$13.91 \times 10^{-2}$	$15.01 \times 10^{-2}$
4	$16.00 \times 10^{-3}$	$1.35 \times 10^{-4}$	$-3.01 \times 10^{-2}$	$-3.51 \times 10^{-2}$	$-3.76 \times 10^{-2}$
5	$6.40 \times 10^{-3}$	$1.45 \times 10^{-4}$	$2.71 \times 10^{-2}$	$3.01 \times 10^{-2}$	$3.52 \times 10^{-2}$
5.1	(2)	$19.30 \times 10^{-4}$	(2)	(2)	(2)
5.5	$4.10 \times 10^{-3}$	$3.80 \times 10^{-4}$	(2)	(2)	(2)
7	$5.49 \times 10^{-3}$	$19.90 \times 10^{-4}$	$1.07 \times 10^{-2}$	$1.29 \times 10^{-2}$	$1.41 \times 10^{-2}$
8	$2.71 \times 10^{-3}$	$3.04 \times 10^{-4}$	$0.54 \times 10^{-2}$	$0.65 \times 10^{-2}$	$0.71 \times 10^{-2}$
9	(2)	$3.32 \times 10^{-4}$	(2)	(2)	(2)
10	$3.87 \times 10^{-3}$	$3.21 \times 10^{-4}$	$5.11 \times 10^{-2}$	$6.01 \times 10^{-2}$	$6.56 \times 10^{-2}$

(1) Variable. (See figure 66.)  
(2) Not Used in Model.

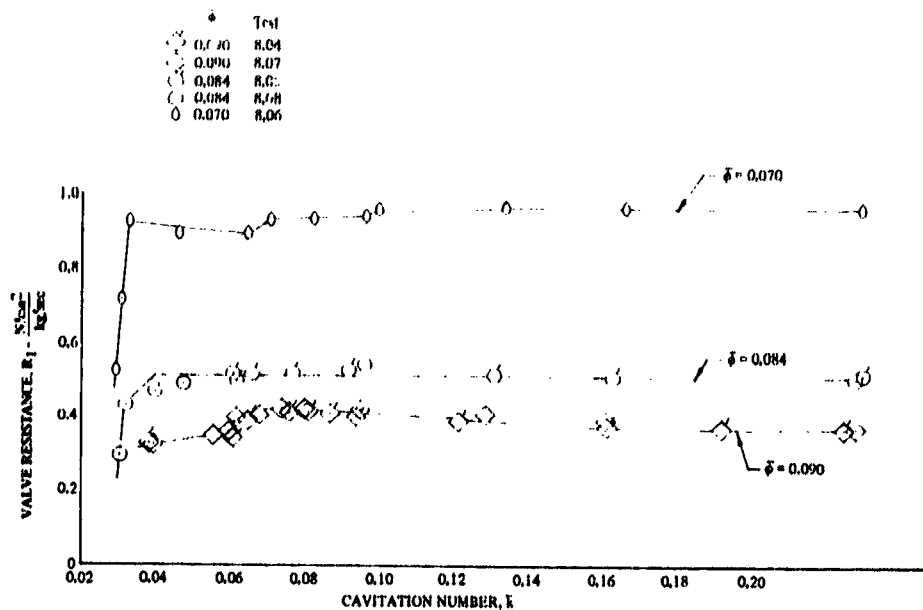


Figure 66. Discharge Throttling Valve Linear Resistance, Radial Inducer

DF 91007

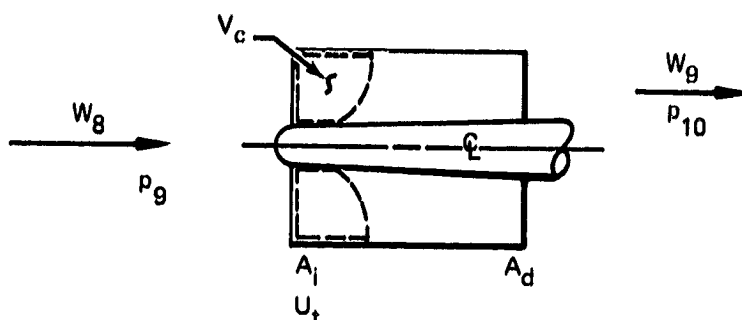
Under steady-state conditions, inducer performance can be written (assuming constant speed):

$$\begin{aligned}
 P_r &= \lambda P_{rnc} \\
 \lambda &= f_1(P_g, W) \\
 P_{rnc} &= f_2(W)
 \end{aligned}
 \tag{16}$$

Under dynamic conditions, inlet flowrate ( $W_8$ ) can differ from discharge flowrate ( $W_9$ ) because cavity volume can change. Inducer pressure rise becomes a function of both flowrates. It is assumed that the above relationship for inducer pressure rise is valid under dynamic conditions if the steady-state flowrate ( $W$ ) is replaced by inlet flowrate ( $W_8$ ) in " $f_1$ ," and by discharge flowrate ( $W_9$ ) in " $f_2$ ." Then under dynamic conditions inducer performance can be written:

$$\begin{aligned}
 P_r &= \lambda P_{rnc} \\
 \lambda &= f_1(P_g, W_8) \\
 P_{rnc} &= f_2(W_9)
 \end{aligned}
 \tag{17}$$

Table 10. Inducer Representation In Dynamic Model



Performance	$\Delta p_{10} = G_p \Delta p_9 + G_w \Delta W_8 - R_p \Delta W_9$	
Continuity	$\Delta W_8 - \Delta W_9 = -\rho \Delta \dot{V}_c$	
Cavity Volume	$-\rho \Delta V_c = C_p \Delta p_9 + C_w \Delta W_8$	
Pressure Gain	$G_p = \frac{\partial p_{10}}{\partial p_9} = 1 + \frac{2\bar{\psi}}{1 + \bar{\phi}^2} \frac{\partial \lambda}{\partial \bar{k}}$	] Head Falloff Map
Flow Gain	$G_w = \frac{\partial p_{10}}{\partial W_8} = \frac{U_t}{A_1} \left\{ \bar{\phi} - 2\bar{\psi}k \left( \frac{\bar{\phi}}{1 + \bar{\phi}^2} \right) \frac{\partial \lambda}{\partial \bar{k}} + \bar{\psi} \frac{\partial \lambda}{\partial \bar{\phi}} \right\}$	
Pump Resistance	$R_p = -\frac{\partial p_{10}}{\partial W_9} = \frac{U_t}{A_1} \left\{ \left( \frac{A_1}{A_d} \right)^2 \bar{\phi} - \lambda \frac{\partial \bar{\psi}}{\partial \bar{\phi}} \right\}$	] Head Flow Map
Pressure Compliance	$C_p = -\rho \frac{\partial V_c}{\partial p_9} = -\frac{2}{U_t^2 (1 + \bar{\phi}^2)} \frac{\partial V_c}{\partial \bar{k}}$	] Cavity Volume Map
Flow Compliance	$C_w = -\rho \frac{\partial V_c}{\partial W_8} = \frac{1}{A_1 U_t} \left\{ 2\bar{k} \left( \frac{\bar{\phi}}{1 + \bar{\phi}^2} \right) \frac{\partial V_c}{\partial \bar{k}} - \frac{\partial V_c}{\partial \bar{\phi}} \right\}$	

In these equations, " $f_1$  and  $f_2$ " still denote the head falloff and head vs flow maps obtained from steady-state tests or predictions. For linear perturbations about the steady-state operating point, inducer discharge static pressure ( $p_{10}$ ) can be written:

$$\Delta p_{10} = \Delta p_9 + \Delta p_r + \Delta q_8 \cdot \Delta q_9 \quad (18)$$

$$\Delta p_r = \frac{\partial p_r}{\partial p_9} \Delta p_9 + \frac{\partial p_r}{\partial W_8} \Delta W_8 + \frac{\partial p_r}{\partial W_9} \Delta W_9 \quad (19)$$

The symbol ( $\Delta$ ) denotes a linear perturbation about the steady-state operating point. Inlet and discharge velocity heads are denoted by  $q_8$  and  $q_9$ , respectively. Each coefficient in equation (19) is considered to be a constant, evaluated at the steady-state operating point. From the relationships of equation (17), the coefficients in equation (19) can be evaluated as:

$$\begin{aligned}\frac{\partial P_r}{\partial p_9} &= P_{rnc} \frac{\partial \lambda}{\partial p_9} = f_2 \frac{\partial f_1}{\partial p} \\ \frac{\partial P_r}{\partial W_8} &= P_{rnc} \frac{\partial \lambda}{\partial W_8} = f_2 \frac{\partial f_1}{\partial W} \\ \frac{\partial P_r}{\partial W_9} &= \lambda \frac{\partial P_{rnc}}{\partial W_9} = f_1 \frac{\partial f_2}{\partial W}\end{aligned}\tag{20}$$

The velocity heads can be written:

$$\begin{aligned}q_8 &= \frac{W_8^2}{2 \rho A_1^2} \\ q_9 &= \frac{W_9^2}{2 \rho A_d^2} \\ \Delta q_8 &= \frac{W}{\rho A_1^2} \Delta W_8 \\ \Delta q_9 &= \frac{W}{\rho A_d^2} \Delta W_9\end{aligned}\tag{21}$$

Substituting equation (20) into equation (19) and equations (19) and (21) into equation (18), Inducer performance becomes:

$$\begin{aligned}\Delta p_{10} &= \left[ 1 + f_2 \frac{\partial f_1}{\partial p} \right] \Delta p_9 + \\ &\left[ \frac{W}{\rho A_1^2} + f_2 \frac{\partial f_1}{\partial W} \right] \Delta W_8 - \\ &\left[ \frac{W}{\rho A_d^2} - f_1 \frac{\partial f_2}{\partial W} \right] \Delta W_9\end{aligned}\tag{22}$$

The three coefficients in equation (22) can be interpreted as a "pressure gain" ( $G_p$ ), a "flow gain" ( $G_w$ ), and a "pump internal resistance" ( $R_p$ ), so that equation (22) can be written:

$$\Delta p_{10} = G_p \Delta p_g + G_w \Delta W_g - R_p \Delta W_g \quad (23)$$

The three coefficients could be evaluated directly from the head falloff and head vs flow maps and known operating point if the maps were available in terms of pressure and flowrate. Since the maps are available in terms of cavitation number ( $\bar{k}$ ), flow coefficient ( $\bar{\phi}$ ), and noncavitating head coefficient ( $\bar{\psi}$ ), it is convenient to redefine the functions " $f_1$  and  $f_2$ " in these terms.

$$\begin{aligned} \lambda &= f_1(\bar{k}, \bar{\phi}) \\ \bar{\psi} &= f_2(\bar{\phi}) \end{aligned} \quad (24)$$

Use is made of the following standard relationships:

$$\begin{aligned} \bar{k} &= \frac{p_g - p_v}{\rho q'} \\ \bar{\phi} &= \frac{\bar{V}_t}{U_t} \\ \bar{V}_t &= \frac{W}{\rho A_t} \end{aligned} \quad (25)$$

$$q' = \frac{\rho}{2} (U_t^2 + \bar{V}_t^2)^{1/2}$$

$$P_{rnc} = \rho \bar{\psi} U_t^2$$

The coefficients ( $G_p$ ,  $G_w$  and  $R_p$ ) in equation (23) can then be obtained in the equivalent form shown in table 10. Values for these coefficients that were calculated for the radial leading edge inducer are given in figures 67, 68, and 69.

Continuity at the inducer involves changes in the total volume ( $V_c$ ) of cavitation present. For linear perturbations, the liquid being stored in the inducer is:

$$\Delta W_g - \Delta W_g = \frac{d}{dt} (-\rho \Delta V_c) \quad (26)$$

The instantaneous cavity volume is assumed to be a function ( $f_3$ ) of inlet static pressure and inlet flowrate, where " $f_3$ " denotes the steady-state cavity volume map.

$$V_c = f_3(p_g, W_g) \quad (27)$$

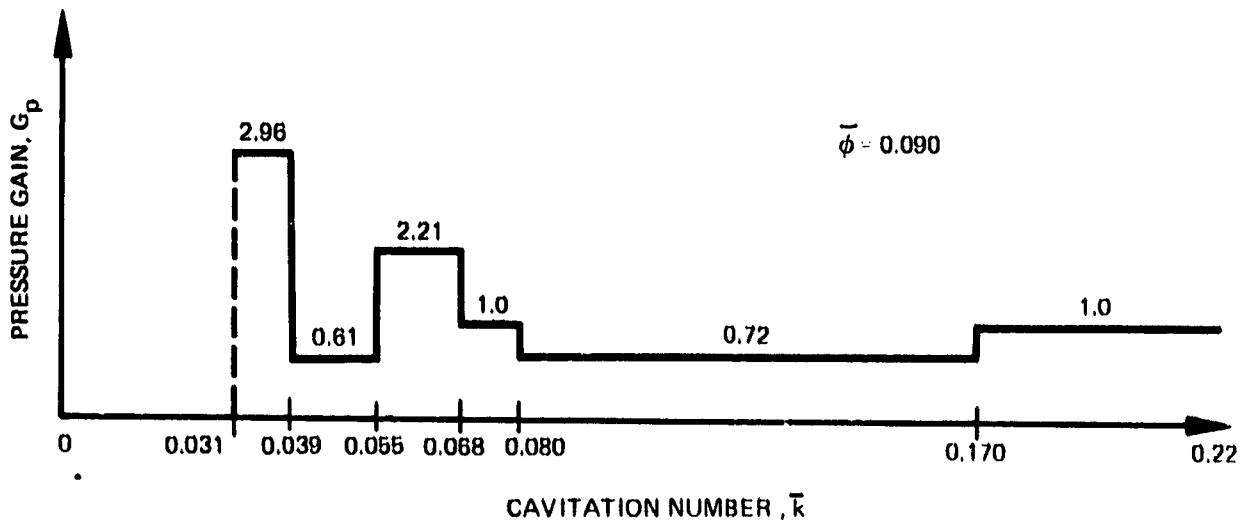
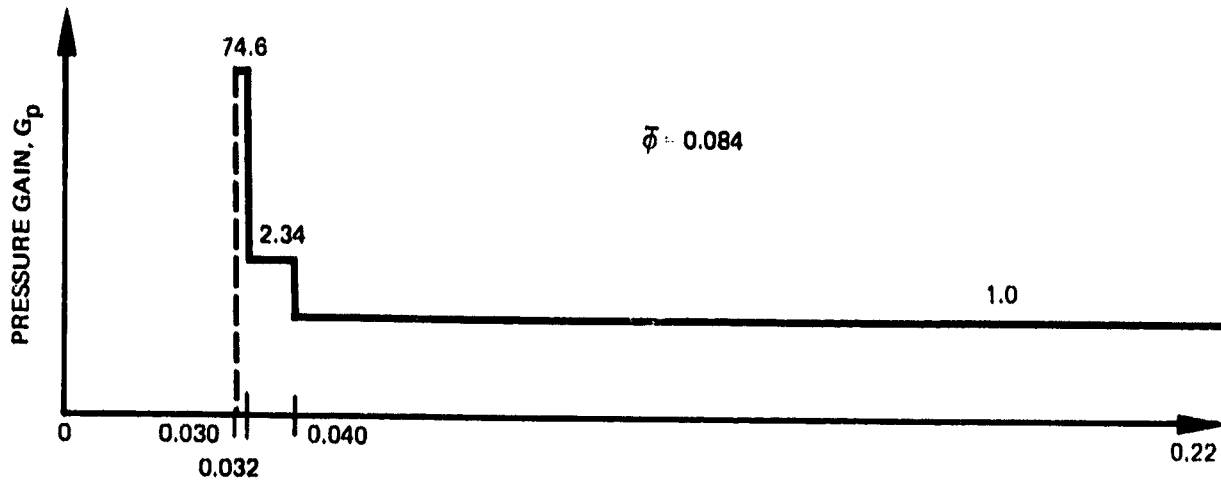
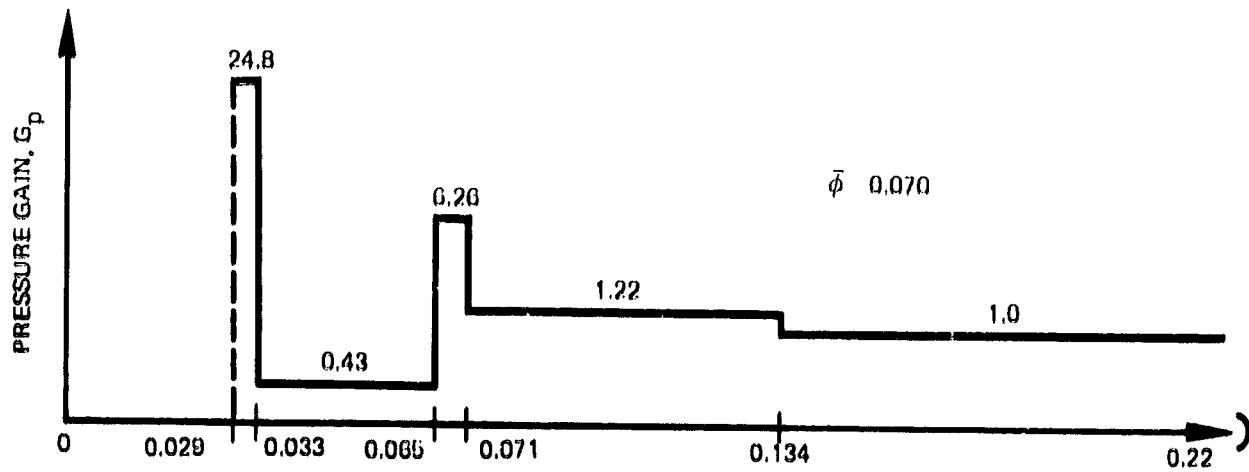


Figure 67. Pressure Gains; Radial Leading Edge Inducer

FD 62366

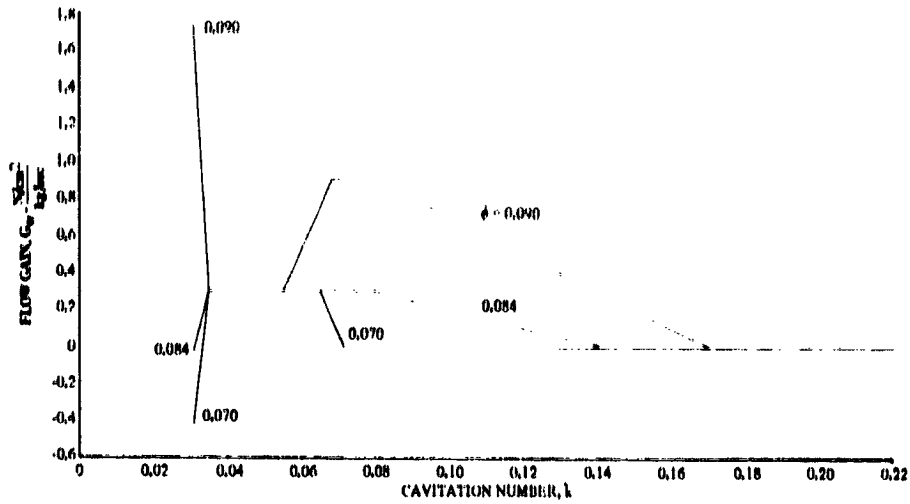


Figure 68. Flow Gains, Radial Leading Edge Inducer DF 91008

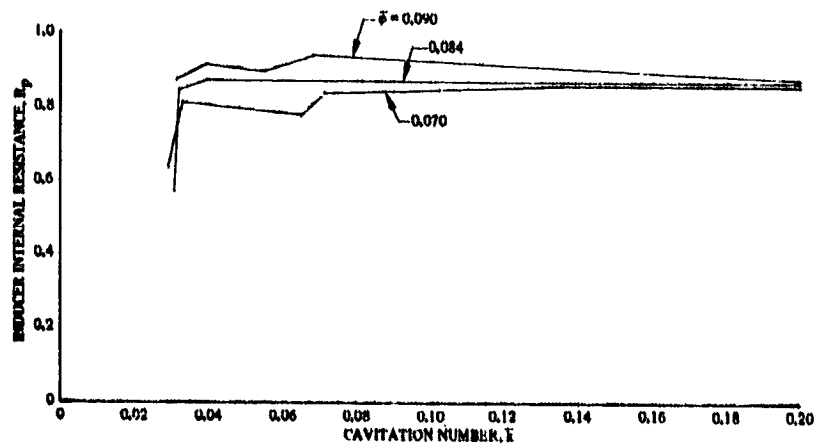


Figure 69. Internal Resistance, Radial Leading Edge Inducer DF 91009

For linear perturbations:

$$\Delta V_c = \frac{\partial V_c}{\partial p_0} \Delta p_0 + \frac{\partial V_c}{\partial W_R} \Delta W_R \quad (28)$$

The liquid being stored in the inducer becomes:

$$-\rho \Delta V_c = -\rho \frac{\partial V_c}{\partial p_0} \Delta p_0 - \rho \frac{\partial V_c}{\partial W_R} \Delta W_R \quad (29)$$

The two coefficients in equation (29) can be interpreted as a pressure compliance ( $C_p$ ) and a flow compliance ( $C_w$ ), so that equation (29) can be written:

$$-\rho \Delta V_c = C_p \Delta p_0 + C_w \Delta W_R \quad (30)$$

The two coefficients,  $C_p$  and  $C_w$ , could be evaluated directly from the cavity volume map if the map were available in terms of pressure and flowrate. Since the map is available in terms of cavitation number and flow coefficient, it is convenient to redefine the function " $f_3$ " in these terms:

$$V_c = f_3(\bar{k}, \bar{\phi}) \quad (31)$$

The coefficients  $C_p$  and  $C_w$  in equation (30) can then be obtained in the equivalent form shown in table 10. Values that were calculated for the radial leading edge inducer are given in figures 70 and 71.

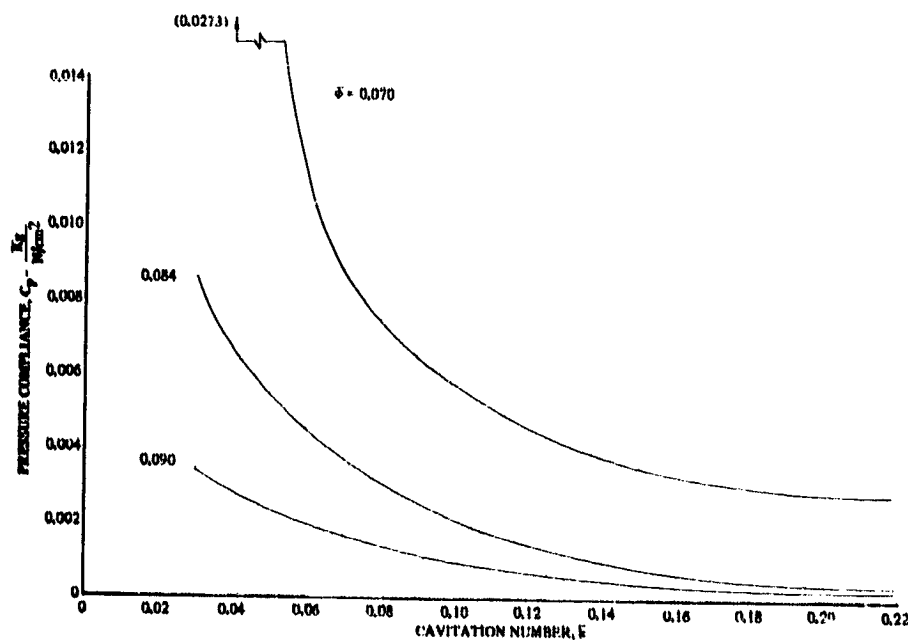


Figure 70. Pressure Compliance, Radial Leading Edge Inducer

DF 91010

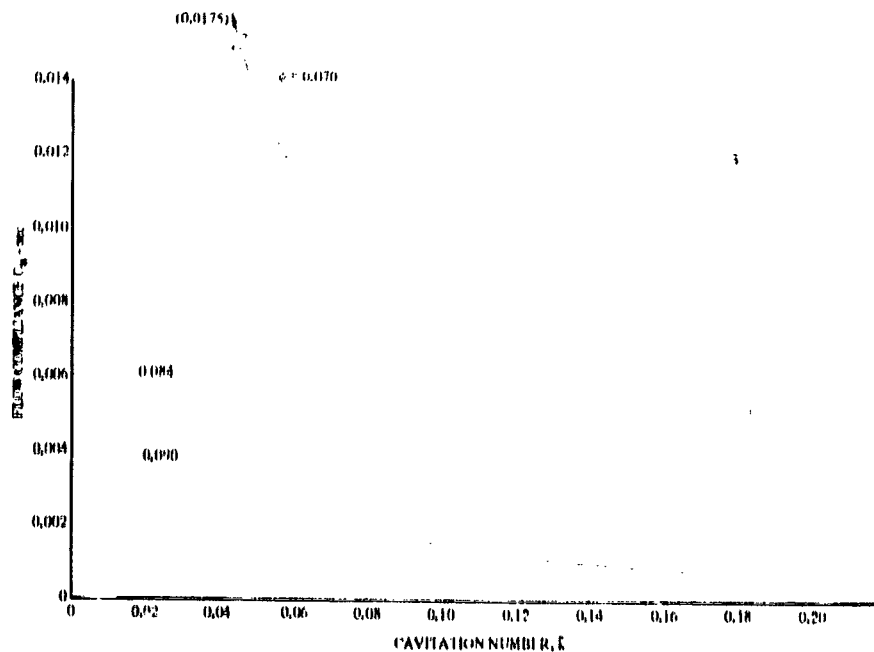


Figure 71. Flow Compliance, Radial Leading Edge Inducer

DF 91011

Equations (23), (26), and (30) completely define the inducer dynamics and complete the model description. Predictions were generated by simultaneous solution of the inducer equations and equations (12) and (13) that describe the test loop hydraulic system.

### 5.3.2 Model Predictions

Model predictions were generated in the form of a damping ratio ( $\zeta$ ) and an undamped natural frequency ( $\omega$ ) that corresponded to each root in the characteristic equation of the water loop. Graphical definitions of  $\zeta$  and  $\omega$  are given in figure 72. The roots indicate the manner in which the water loop would respond to a disturbance. If "y(t)" represents an arbitrary parameter in the water loop, such as inducer discharge pressure, each pair of complex roots indicates an oscillatory response of the form:

$$y(t) = e^{-\zeta\omega t} \sin(\omega\sqrt{1-\zeta^2}t)$$

and each real root indicates a ramping response of the form:

$$y(t) = e^{-\zeta\omega t}$$

The overall response is the sum of the response from each root. The actual form of the disturbance (sine wave, pulse, etc.) would add additional terms to the overall response; however, the roots indicate the response that is characteristic of the water loop and determine whether the water loop would respond in a stable or unstable manner. Therefore, to analyze the stability of the water loop it is only necessary to examine the roots of the characteristic equation for evidence of unstable response. The disturbance required to initiate unstable response is always present in the form of normal vibration and need not be considered.

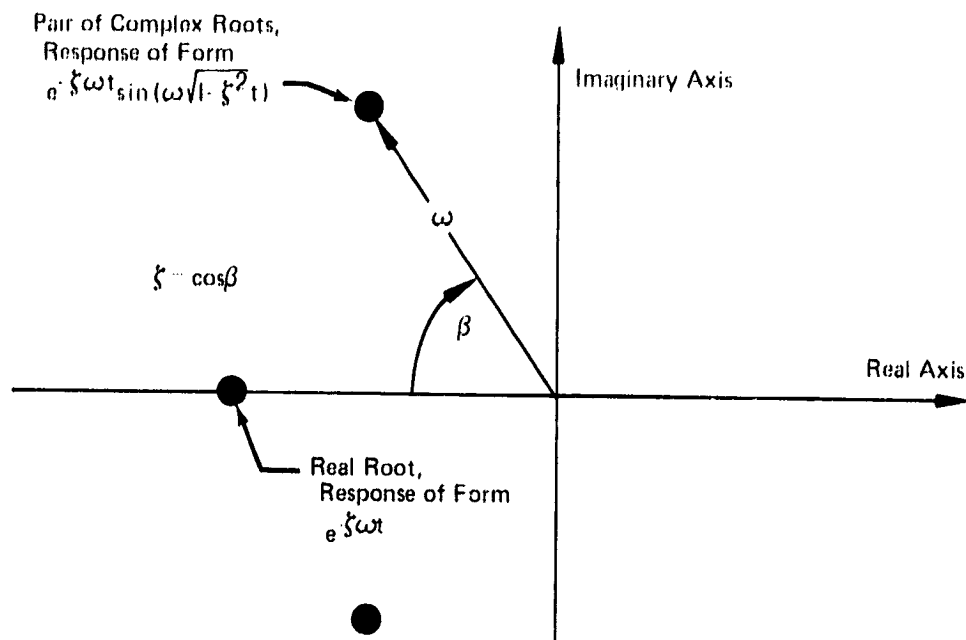


Figure 72. Definitions of Damping Ratio and Natural Frequency in the Complex Plane FD 63062

Positive damping ratio ( $\zeta$ ) indicates a decaying oscillatory amplitude or a decaying ramp, which is stable behavior. When damping ratio is negative, the water loop is predicted to be unstable; and when it is positive, the loop is predicted to be stable. The form of the unstable behavior is indicated by whether the damping ratio is obtained from a complex root pair (oscillatory behavior) or from a real root (ramping behavior).

The convention used is that damping ratio always lies between  $-1.0 \leq \zeta \leq 1.0$ . For a complex root pair, damping ratio can be interpreted as the ratio of actual damping to critical damping of a second order system, such as a spring-mass-damper system, where critical damping is the value at which oscillations would cease. For a real root, damping ratio is either  $\pm 1.0$ , indicating whether the root lies to the left or right of the origin (figure 72).

Actual oscillatory frequency for a complex root is given by the damped natural frequency ( $\omega \sqrt{1-\zeta^2}$ ); however, since the magnitude of damping ratio for the complex roots is generally very small, the frequency can be approximated by the undamped natural frequency ( $\omega$ ). For a real root, natural frequency does not imply oscillatory behavior, but locates the distance the root lies from the origin (figure 72).

Since the equations used to describe the water loop are linear, amplitudes reached at unstable operating points cannot be predicted. A linear analysis can only determine whether a given operating point will be stable or unstable, and, if unstable, indicate whether the initial behavior will be an oscillation or a ramp. There is no direct relationship between damping ratio obtained from a linear analysis and oscillation amplitude reached by the actual nonlinear system.

However, a qualitative relationship usually exists in that a large negative damping ratio indicates that oscillation amplitude would grow much more rapidly than a small negative damping ratio, indicating a tendency toward a more severe instability. It is therefore reasonable to expect that damping ratio will be an indicator of relative oscillation amplitude.

Actual oscillation amplitude can be predicted by solution of the nonlinear equations describing water loop dynamic motion on an analog computer. Non-linearities arise from pressure drops around the water loop and from the nonlinear relationship between cavity volume, pressure, and flowrate. A linear analysis was selected over the nonlinear approach because it allows greater flexibility in identifying destabilizing effects through parametric studies and is, therefore, a more powerful tool for evaluating model validity. An additional nonlinear simulation would have complemented the analysis but was outside the scope of effort.

Instability predictions were generated for the radial leading edge inducer and later qualitatively extended to the swept inducer during the data correlation effort. The only significant difference between the inducer systems was the smaller cavitation volume of the swept inducer.

Noncavitating values of  $\zeta$  and  $\omega$  are listed in table 11 in order of increasing frequency. Damping ratios are all positive and therefore correctly indicate that the system is stable under noncavitating conditions. Roots 1 and 10 are real roots and represent ramping behavior of the water loop, while roots 2 through 9 are complex roots and represent oscillatory behavior. Root 2 represents the basic low frequency, oscillatory behavior of the loop and was found to show the greatest change with cavitation number. Root 1 was found to indicate a runaway instability in the head breakdown region.

Table 11. Noncavitating Values of Damping Ratio and Natural Frequency, Radial Leading Edge Inducer

Root Number	$\bar{\phi} = 0.070$		$\bar{\phi} = 0.084$		$\bar{\phi} = 0.090$	
	Natural Frequency, Hz $\omega$	Damping Ratio $\zeta$	Natural Frequency, Hz $\omega$	Damping Ratio $\zeta$	Natural Frequency, Hz $\omega$	Damping Ratio $\zeta$
1	4.5	1.0000	3.6	1.0000	3.3	1.0000
2	44.7	0.0180	44.7	0.0152	44.7	0.0148
3	63.2	0.0525	63.2	0.0531	63.2	0.0536
4	110	0.0209	110	0.0125	110	0.0098
5	145	0.0309	145	0.0316	145	0.0321
6	172	0.0008	172	0.0009	172	0.0010
7	195	0.0140	195	0.0094	195	0.0079
3	245	0.0102	245	0.0102	245	0.0104
9	295	0.0124	295	0.0072	295	0.0055
10	1106	1.0000	1100	1.0000	1097	1.0000

Oscillatory type instability predictions are shown in figures 73, 74, and 75 over a range of cavitation number from 0.22 to 0.04 for flow coefficients of 0.070, 0.084, and 0.090. Roots 2, 3, 6, and 8 have negative damping ratios (an instability is predicted) over nearly the entire range of cavitation number. Other oscillatory roots had positive damping ratios. Inducer headrise was assumed to be unaffected by cavitation over this range, and the negative damping predictions are, therefore, representative of "continuity" mechanism instabilities. The measured shape of the head falloff curve did not significantly affect predictions in this range of cavitation number. The air that was observed to form in the heat exchanger was accounted for in the analysis and is shown on the curves along with predictions made with no air. The noncavitating values of the roots are indicated on the right of the figures.

Root 2 is the most important because it represents the basic low frequency, oscillatory behavior of the system. Root 3 is only slightly higher in frequency, but its damping ratio does not show as substantial a change with cavitation number as that of root 2. Roots 6 and 8 are of such a high frequency that they are not considered significant to any instabilities. The root 2 damping ratio curve intercepts zero damping at a cavitation number above 0.27. The curves show a gradual drop in damping ratio with cavitation number to the point of air formation in the heat exchanger. At that point, there is an abrupt drop in damping ratio. Natural frequency also gradually drops with cavitation number to the point of air formation, at which point it drops abruptly. The natural frequencies and damping ratios generally decrease with flow coefficient, signifying that oscillatory frequencies would decrease and amplitudes become more severe as flow coefficient was reduced.

Root 1, which represents a ramping type instability, also varied with cavitation number. Since this root is strongly dependent on the shape of the head falloff curve, the measured maps from figure 27 were used to generate predictions. Predictions are shown in figure 76 for the flow coefficients of 0.070 and 0.090; 0.084 was similar to 0.070 and was omitted for clarity. The predictions are shown in the form of damping ratio and natural frequency as a matter of convention. These terms are ambiguous for ramping-type instabilities, and they do not imply oscillatory behavior. A reduction in natural frequency toward zero indicates a tendency toward transition from stable to unstable operation. The predictions therefore show that a ramping instability should occur for the 0.090 flow coefficient at  $k = 0.035$ . The other two flow coefficients are predicted to be stable, but they are tending to go unstable, as evidenced by the dropping natural frequency prediction.

Model predictions are correlated with inducer test data in the next paragraph, and the degree of correlation is evaluated through parametric treatment of the variables in paragraph 5.3.4.

### 5.3.3 Correlation of Model Predictions With Test Results

Model predictions for the lowest frequency oscillatory root (root 2) are compared with test data for the flow coefficients ( $\phi$ ) of 0.070, 0.084, and 0.090 in figures 77, 78, and 79. Test data are from figure 39 and are the lowest measured frequency component. The measured range of cavitation number (0.22 to 0.03) and the measured head falloff curves were used in the model. Predictions are for the radial leading edge inducer, and test data are for both the swept and radial inducers. The noncavitating predicted values of damping ratio ( $\zeta$ ) and natural frequency ( $\omega$ ) are indicated on the right of the curves.

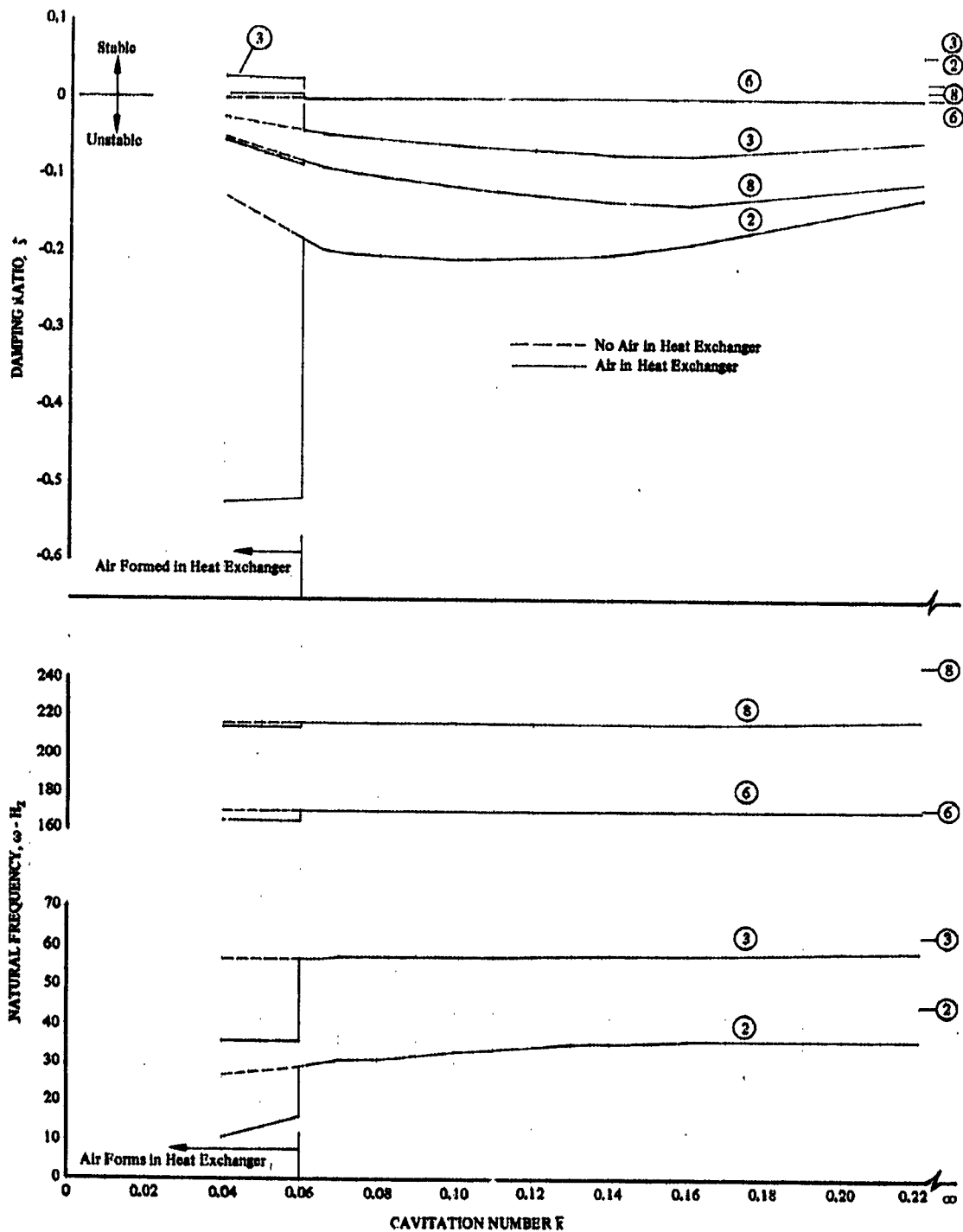


Figure 73. Linear Model Predictions of Inducer Loop DF 91002  
 Oscillatory Characteristics With No Head  
 Falloff; Radial Leading Edge Inducer;  
 $\phi = 0.070$

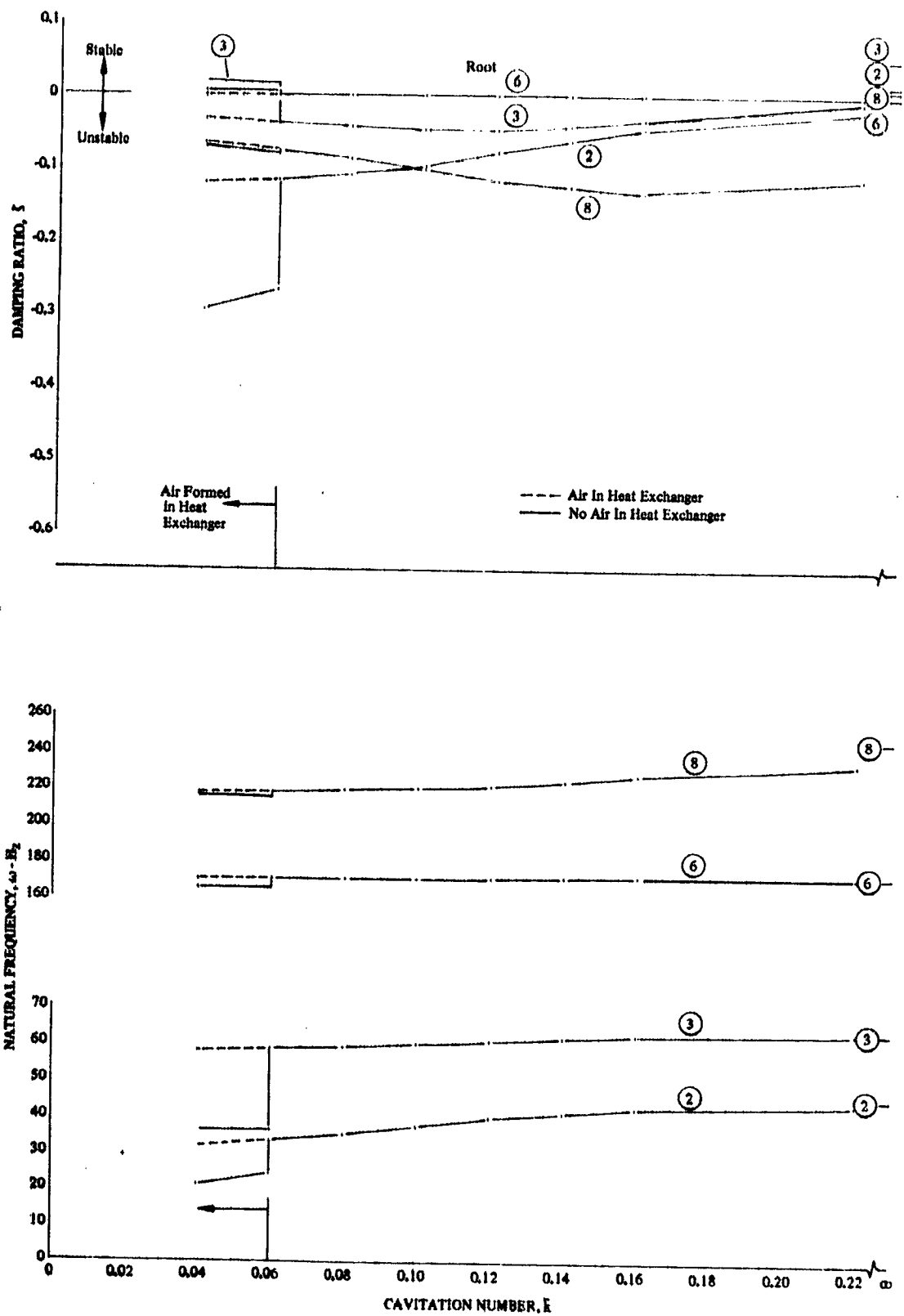


Figure 74. Linear Model Predictions of Inducer Loop Oscillatory Characteristics With No Head Falloff; Radial Loading Edge Inducer;  $\phi = 0.084$

DF 91003

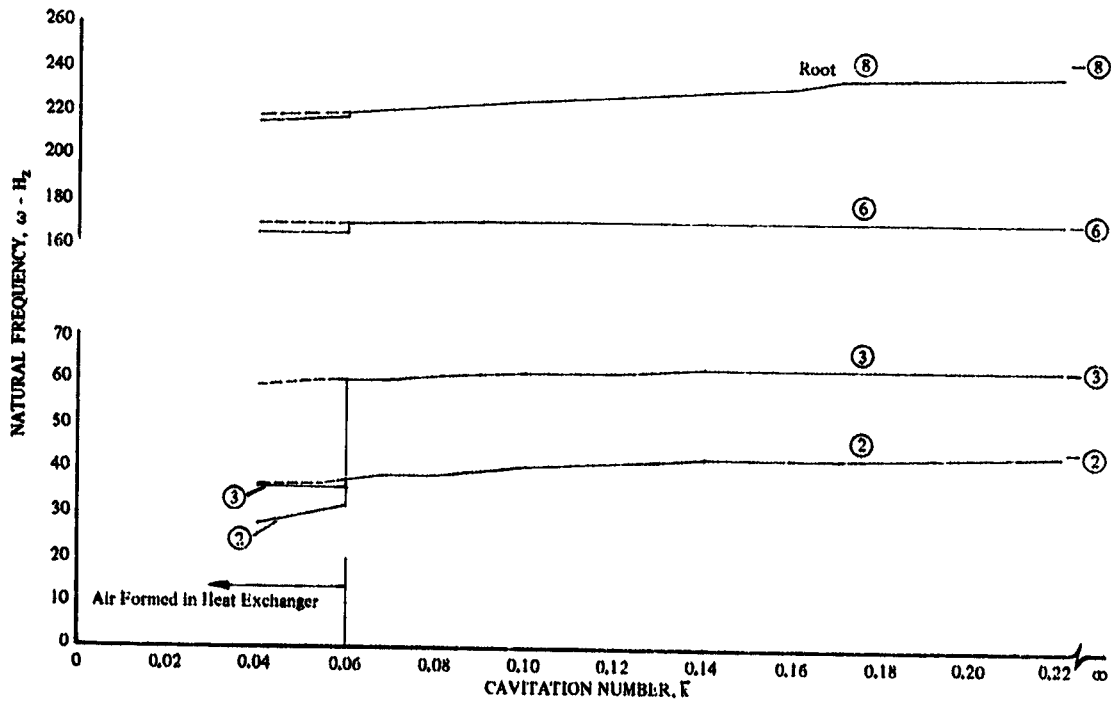
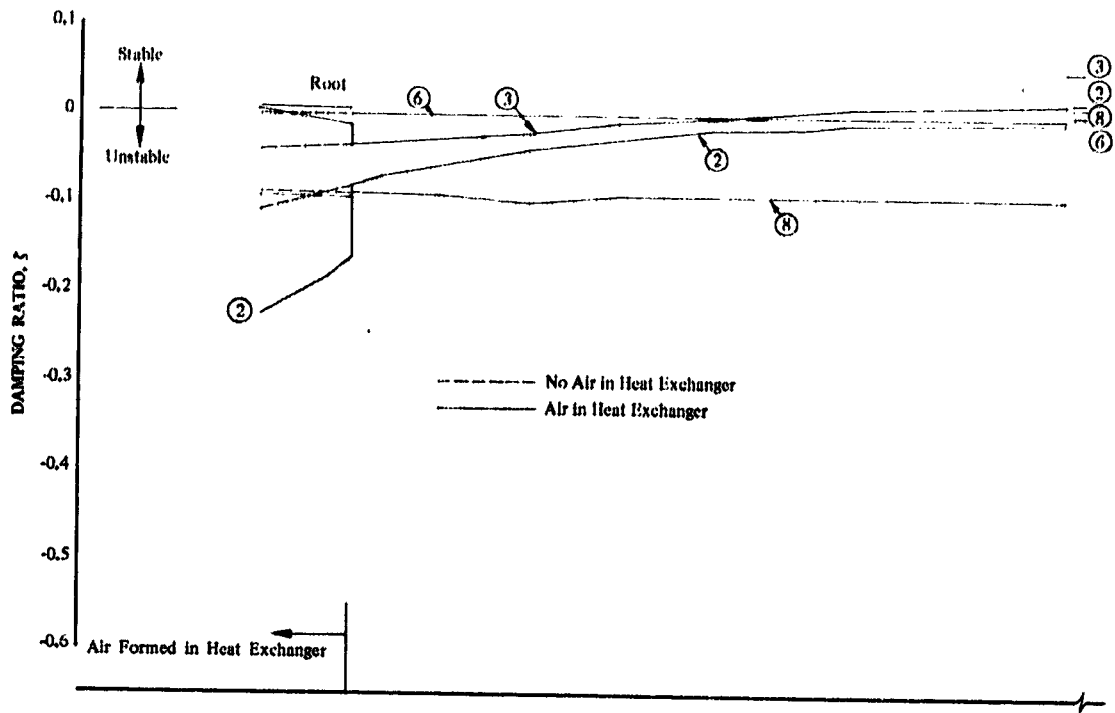


Figure 75. Linear Model Predictions of Inducer Loop Oscillatory Characteristics With No Head Falloff; Radial Leading Edge Inducer;  $\phi = 0.090$

DF 91004

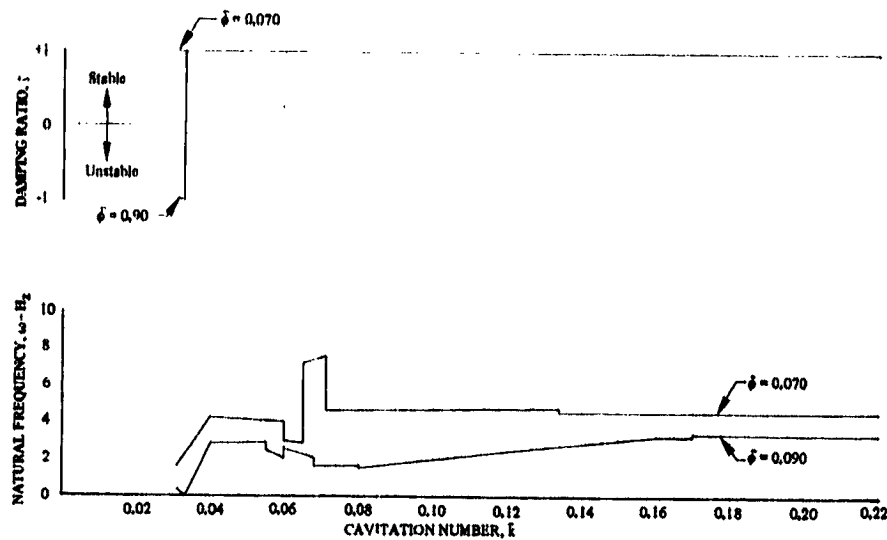


Figure 76. Linear Model Predictions of Inducer Loop Ramping Characteristics, Radial Leading Edge Inducer

DF 91015

The model predictions for the radial inducer correlate favorably with the oscillatory test data in that:

1. The negative damping ratio curve indicates that the loop is predicted to be unstable at all test points, and oscillations were measured at all test points.
2. The predicted drop in damping ratio at  $\bar{k} = 0.06$ , when air formed in the heat exchanger, coincides with the measured sudden increase in oscillation amplitude.
3. The predicted rise in damping ratio toward stable operation below  $\bar{k} = 0.04$  coincides with the measured decrease in oscillation amplitude.
4. The relative magnitude of damping ratio at the three flow coefficients when air formed in the heat exchanger agrees with the relative magnitude of measured amplitude.

Predicted frequency is higher than measured and shows more change with flow coefficient than measured, but has the proper trend of decreasing frequency with decreasing cavitation number.

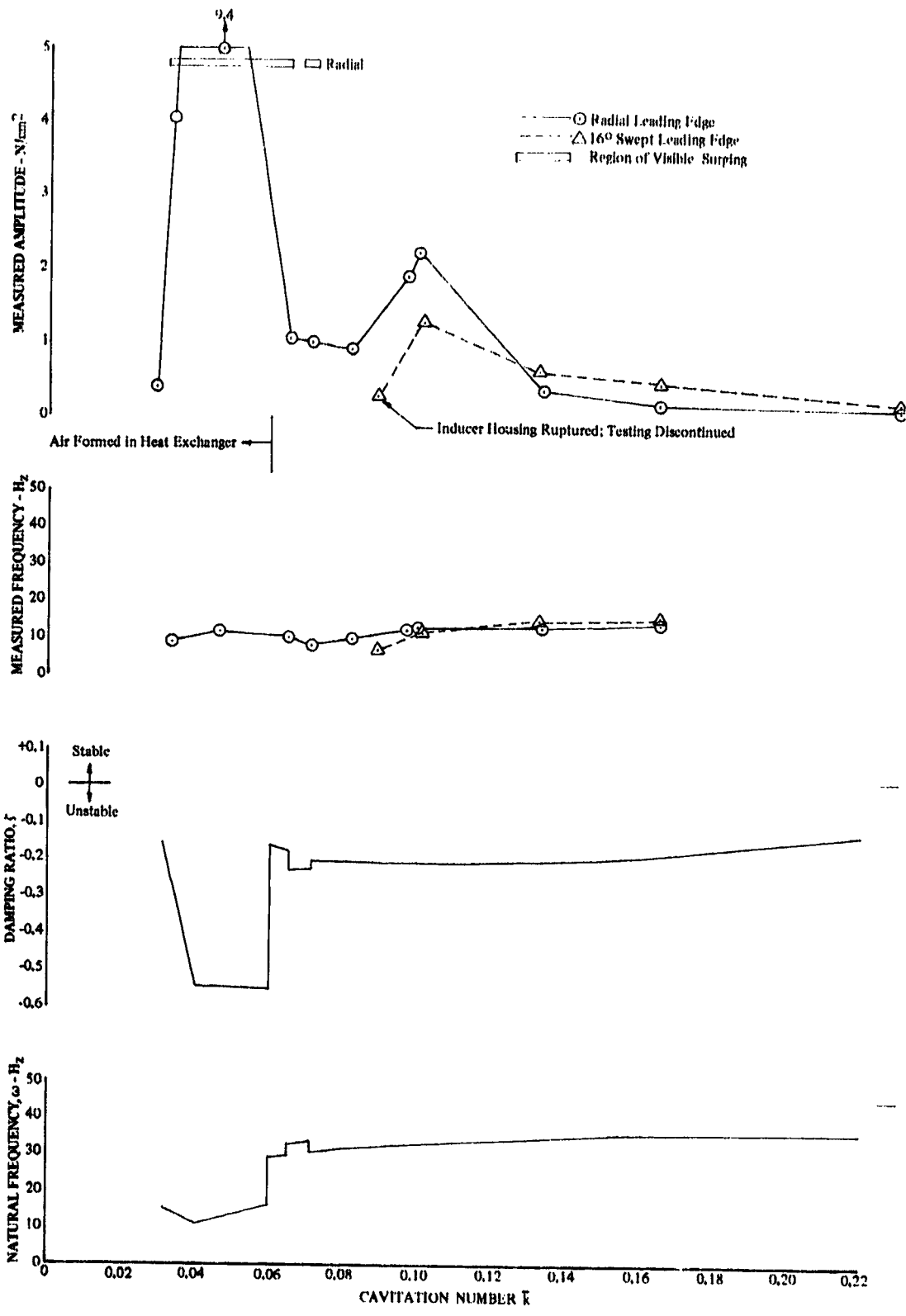


Figure 77. Comparison of Inducer Instability Predictions With Test Results,  $\bar{\phi} = 0.070$

DF 91014

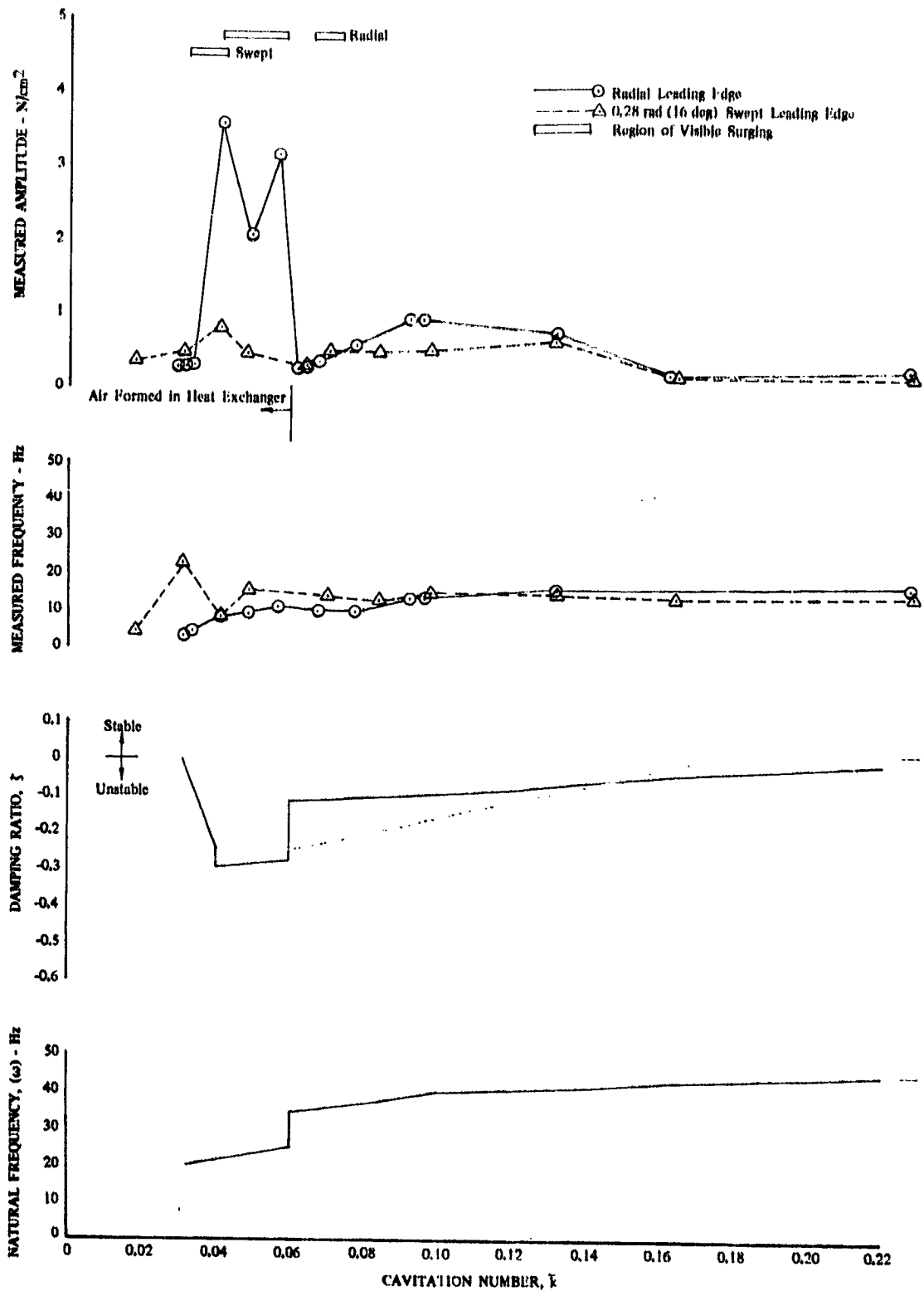


Figure 78. Comparison of Inducer Instability Predictions With Test Results,  $\phi = 0.084$

DF 91013

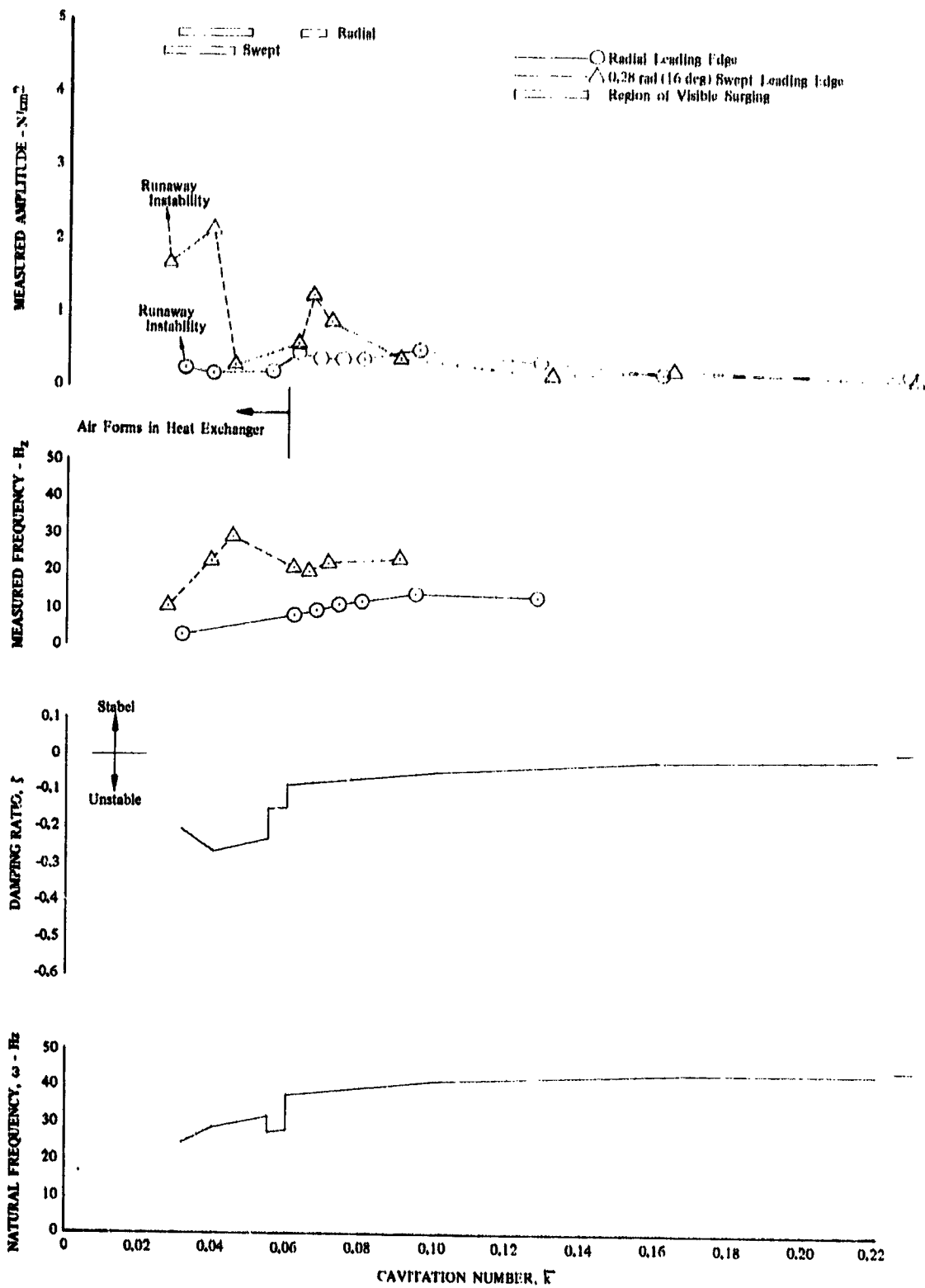


Figure 79. Comparison of Inducer Instability Predictions With Test Results,  $\bar{\phi} = 0.090$

DF 91012

A runaway instability, making it impossible to hold a steady-state operating point, occurred at a flow coefficient of 0.090 but not at the two lower flow coefficients. A real root of the loop characteristic equation (root 1), an indicator of ramping behavior, predicted that a runaway instability should occur at  $\bar{\phi} = 0.090$  but not at the two lower flow coefficients. The predictions were shown in figure 76. The figure shows an abrupt decrease in damping ratio at a cavitation number of 0.035 for the 0.090 flow coefficient, indicating a transition to unstable ramping operation. The observed runaway instability occurred at a cavitation number of approximately 0.032.

The effect of leading edge sweepback on measured cavity length was shown in figure 58. The data are limited, but they consistently show that the cavities become shorter as sweepback is increased. The effect of sweepback on system dynamics is therefore to provide a smaller suction surface cavity at a given cavitation number. Swept inducer system oscillatory characteristics would therefore be predicted to resemble radial inducer characteristics if the two were compared with the swept inducer operating at a cavitation number that was lower than the radial inducer, such that cavity volume for the two inducers was the same. This qualitative prediction is consistent with the test data, which showed lower amplitude pressure oscillations and higher frequencies at a given cavitation number for the swept inducer.

Prerotation of the inducer inlet flow can effect stability through its effect on the head flow map, the head falloff map, and the cavity volume map. Model parameters that were derived from those maps include pump resistance ( $R_p$ ), pressure gain ( $G_p$ ), flow gain ( $G_w$ ), pressure compliance ( $C_p$ ) and flow compliance ( $C_w$ ). Since  $R_p$ ,  $G_p$ , and  $G_w$  were obtained from measured data, the effect of any prerotation that occurred in the tests is already included.  $C_p$  and  $C_w$  were obtained from the predicted cavity volume map, however, and do not include prerotation effects directly. The cavity volume calculation does include an empirical length adjustment, but the inducer data used for the adjustment were insufficient to empirically account for prerotation. Prerotation would tend to reduce incidence angle and cause the cavitation cavities to be smaller than predicted, thereby reducing  $C_p$  and  $C_w$ .

From figure 42, it can be seen that prerotation, as measured at a radius near the inducer tip, was greater for the low flow coefficients and decreased as flow coefficient increased. Actual cavity size would therefore tend to differ from the predicted "zero prerotation" cavities more at low flow coefficients, and there would be less spread in cavity volume with pressure and flow ( $C_p$  and  $C_w$ ) than predicted. The use of reduced  $C_p$  and  $C_w$  values in the model equations would result in predictions that show less spread in damping ratio and natural frequency with flow coefficient than the predictions of figures 77, 78, and 79. The new predictions would agree more closely with test results that show very little spread in amplitude and frequency with flow coefficient at cavitation numbers ( $\bar{k}$ ) above 0.06 (where prerotation was measured). Prerotation ceased below  $\bar{k} = 0.06$ , and a spread with flow coefficient in the test amplitudes and frequencies and in model predictions then occurred. However, below  $\bar{k} = 0.06$  the trend of test frequency with flow coefficient for the radial inducer is opposite to predictions, for reasons which are not presently understood. For the swept inducer, the expected trend of increasing frequency with increasing flow coefficient occurred below  $\bar{k} = 0.06$ . Above  $\bar{k} = 0.06$  the fundamental oscillation component for the swept inducer was not sufficiently distinct to identify its frequency, so that a trend of frequency with flow coefficient could not be identified.

The only significant area in which the predictions do not correlate closely with the test data is the magnitude of the oscillatory frequency. In an effort to resolve the frequency difference, the test procedure and facility were examined to identify any unaccounted for system compliances that could have affected predicted frequencies. Before being filled, the water loop was evacuated to  $2.1 \text{ N/cm}^2$  (3 psia). Previously degenerated water was then pumped into the loop until loop pressure reached  $17 \text{ N/cm}^2$  (25 psia). This pressure was maintained while bleed valves in high parts of the loop were opened to expel trapped air. A review of the bleed valve locations revealed that one area, in an unused loop leg, could have had a trapped air pocket because the valve location was not at the top of the pipe. The section of the loop in question is shown in figure 80. Approximately  $5050 \text{ cm}^3$  (1.33 gal) of air at  $2.1 \text{ N/cm}^2$  (3 psia) could have been trapped by the venturi throat and compressed to  $625 \text{ cm}^3$  (0.26 gal) at  $17 \text{ N/cm}^2$  (25 psia) during the bleed process. These water levels are shown in the pipe cross section of figure 81. The air pocket would remain trapped by the venturi throat since loop pressure was not again lowered to  $2.1 \text{ N/cm}^2$  during the test. Such an amount of air is consistent with an observed increase in total loop fluid volume (as determined by a change in discharge accumulator surge tank level) of approximately  $3785 \text{ cm}^3$  (1.0 gal) when loop pressure was lowered from 26 to 10  $\text{N/cm}^2$  (38 to 15 psia). The trapped air would account for  $655 \text{ cm}^3$  (0.17 gal) of this volume change.

The effect of the trapped air on the system was calculated at a flow coefficient of 0.084 and a cavitation number of 0.16. Trapped air volume under these conditions would be  $530 \text{ cm}^3$  (0.14 gal). Model predictions of damping ratio and natural frequency as functions of air volume at the location shown in figure 80 are shown in figure 82. Air volume has a negligible effect on damping ratio, but it has a large effect on frequency. The calculated amount of air would lower the system natural frequency from 42 to 27 Hz, as compared with a measured frequency of 16 Hz. As little as 15% of the calculated amount of air would lower the natural frequency from 42 to 34 Hz. It is probable that nearly the total calculated amount of air was trapped and that the air accounts for part of the difference between predicted and measured frequencies.

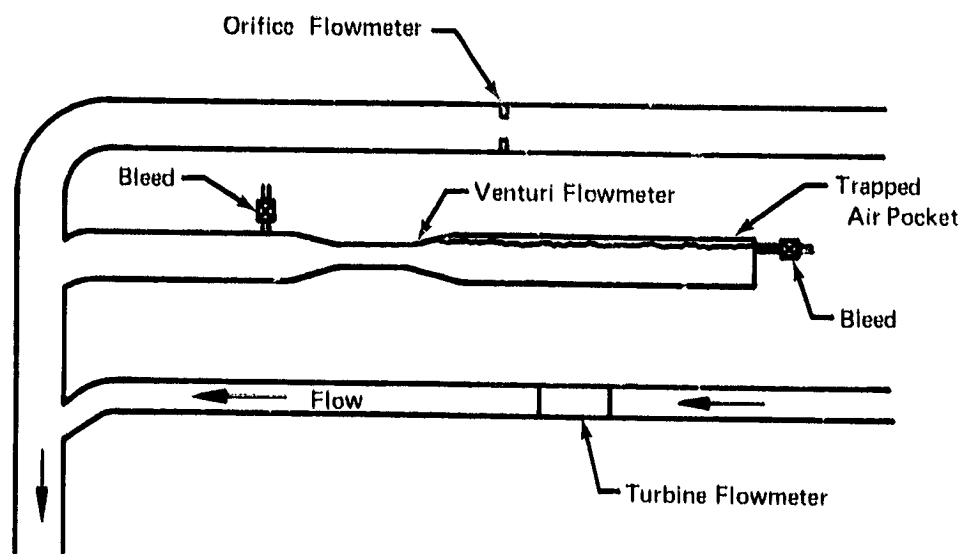


Figure 80. Location of Trapped Air Pocket

FD 62368

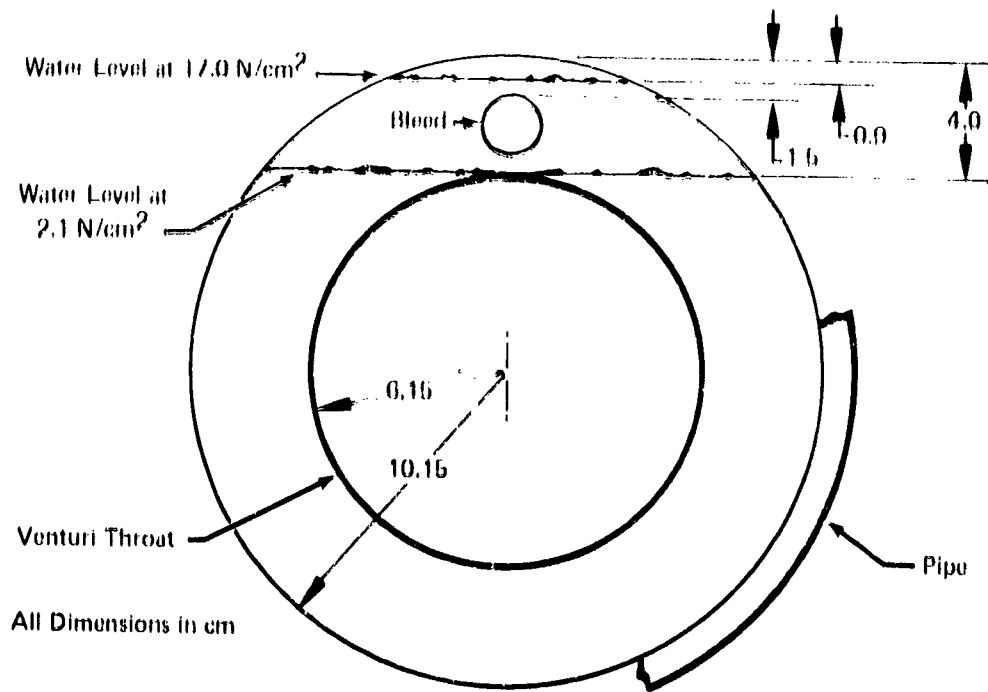


Figure 81. Pipe Section at Trapped Air Pocket

FD 62369

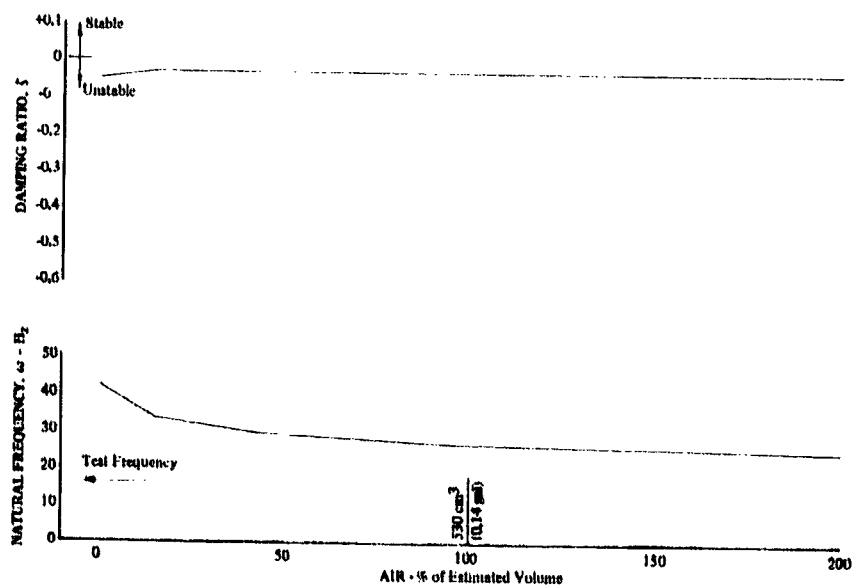


Figure 82. Effect of Trapped Air On Oscillatory Predictions; Radial Leading Edge Inducer;  $\bar{\phi} = 0.084$ ,  $\bar{k} = 0.16$

DF 91005

The remaining difference between predicted and measured frequencies could be accounted for by additional compliances, such as entrained air in the water, tip vortex cavitation, and/or nonlinearities in the cavity volume curves. The fact that test loop total fluid volume increased by approximately 3785 cm<sup>3</sup> (1.0 gal) when pressure was reduced from 20 to 10 N/cm<sup>2</sup> (28 to 15 psia) gives an indication that additional compliances were present. This volume increase has been accounted for as follows:

	<u>cm<sup>3</sup></u>	<u>gal</u>
Pipe and Water Compressibility	110	0.03
Blade Surface Cavitation ( $\bar{\phi} = 0.84$ )	80	0.02
Trapped Air in Loop Leg	<u>655</u>	<u>0.17</u>
	845	0.22

Thus, there remains approximately 2900 cm<sup>3</sup> (0.8 gal) of unaccounted for displacement, indicating the presence of additional compliances, which, if included in the model, would certainly lower predicted natural frequencies. Tip clearance cavitation would form a part of this unaccounted for compliance; its effect on damping ratio and frequency are shown in figure 83 for the  $\bar{\phi} = 0.084$ ,  $\bar{k} = 0.16$  condition. The effect of tip clearance cavitation would be to increase pressure compliance an amount that is currently indeterminate. An increase from the nominal value of 0.00067 (which represents predicted blade suction surface cavitation only) to 0.084 would lower the natural frequency from 28 Hz to the measured 16 Hz. Intuitively, such an increase due to tip clearance cavitation alone seems high, but it should be remembered that there is a substantial amount of unaccounted for compliance that would lower frequency regardless of its source.

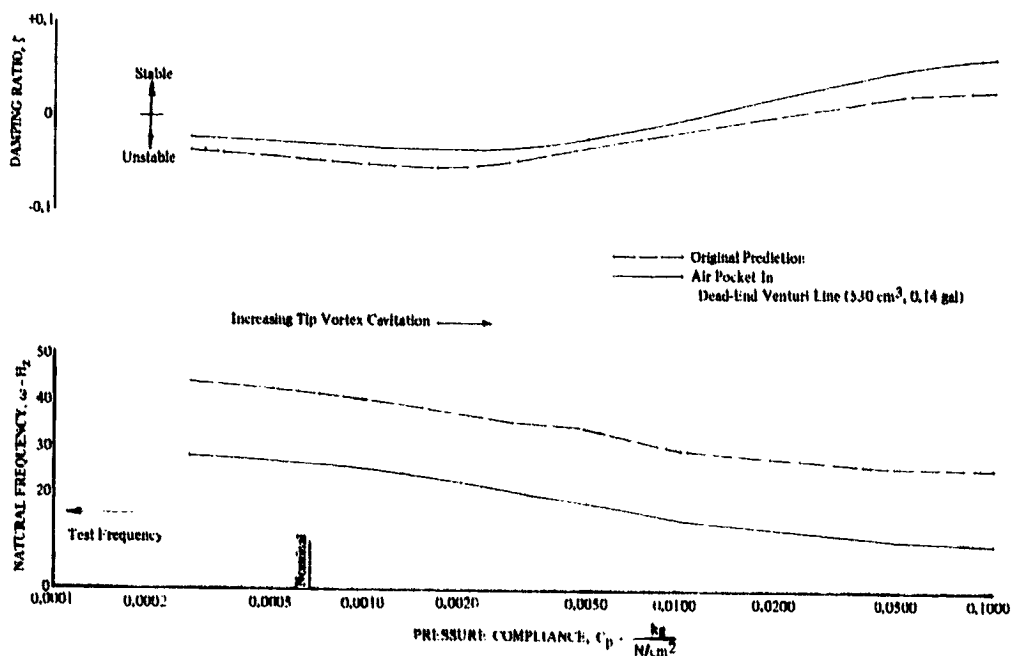


Figure 83. Effect of Pressure Compliance on Oscillatory Predictions; Radial Loading Edge Inducer;  $\bar{\phi} = 0.084$ ,  $\bar{k} = 0.16$

DF 91016

### 5.3.4 Parametric Effects of System Variables on Stability

Several parametric studies were conducted during which the sensitivity of instability predictions to various system parameters was evaluated. The purposes of the studies were to (1) provide quantitative information concerning possible inaccuracies in the predictions that may have resulted from inaccuracies in parameter definition and (2) identify potentially "stabilizing" system changes. The results of these studies are discussed in the following paragraphs.

#### 5.3.4.1 Inlet and Discharge Line Inertance and Resistance

The effect of inlet and discharge line inertances ( $L_8$  and  $L_{10}$ ) on predicted damping ratio and natural frequency is shown in figure 84 at a flow coefficient of 0.084 and a cavitation number of 0.16. Increasing these inertances is equivalent to increasing the line lengths between stations 8-9 and stations 10-1 of figure 64. An inlet inertance increase from nominal to five times nominal results in only slightly lower damping ratios and natural frequencies. The same increase in discharge inertance has a negligible effect on the predictions. A similar lack of sensitivity was found for pump resistance ( $R_p$ ), which is proportional to slope of the head vs flow map, and for control valve resistance ( $R_1$ ) over the same order of magnitude range, although these curves are not shown. These results are valid for our closed-loop system only. An open-loop system, such as a rocket engine feed system, was found to be sensitive to inlet line length in another study (27). The above comments refer to oscillatory instabilities. Ramping instabilities are sensitive to pump resistance ( $R_p$ ) and control valve resistance ( $R_1$ ) in that a decrease in these resistances reduces system resistance and head required to maintain flow. This reduction makes it easier for head available to jump above head required and initiate a runaway instability.

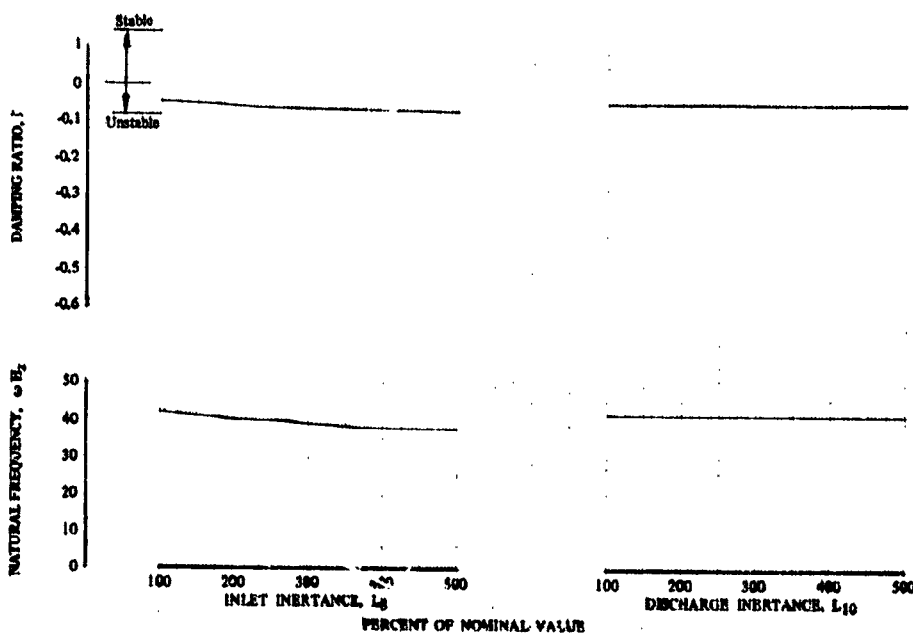


Figure 84. Effect of Line Inertances on Oscillatory Predictions;  $\phi = 0.084$ ,  $\bar{k} = 0.16$

DF 91006

### 5.3.4.2 Cavitation Pressure Compliance ( $C_p$ )

Pressure compliance is a measure of the cavitation volume response to static pressure changes. The effect of pressure compliance on predictions was shown in figure 83 for  $\bar{\phi} = 0.084$  and  $\bar{k} = 0.16$ . An increase in compliance from the nominal 0.0067 to 0.010 would cause system to be stable and would lower oscillatory frequency from 27 to 15 Hz. More than the indicated nominal pressure compliance was known to be present in the inducer loop, the additional compliance being attributed to tip clearance cavitation. Further additions in pressure compliance could be obtained with an accumulator at the inducer inlet. A highly significant finding with respect to pressure compliance was that it alone cannot cause an instability. If cavity volume changed only in response to changes in static pressure, the system would be stable.

### 5.3.4.3 Cavitation Flow Compliance ( $C_w$ )

Flow compliance is a measure of the change in cavitation volume with flowrate. The effects of flow compliance at  $\bar{\phi} = 0.084$  and  $\bar{k} = 0.16$  are shown in figure 85. A reduction of flow compliance from the nominal 1.7 to 0.25 ms would stabilize the system. Flow compliance has a negligible effect on frequency. Tip vortex cavitation would contribute some flow compliance above the nominal but the amount is indeterminate. Flow compliance is the predicted destabilizing parameter above head breakdown. If it is set to zero, the system is predicted to be stable regardless of the values of other parameters.

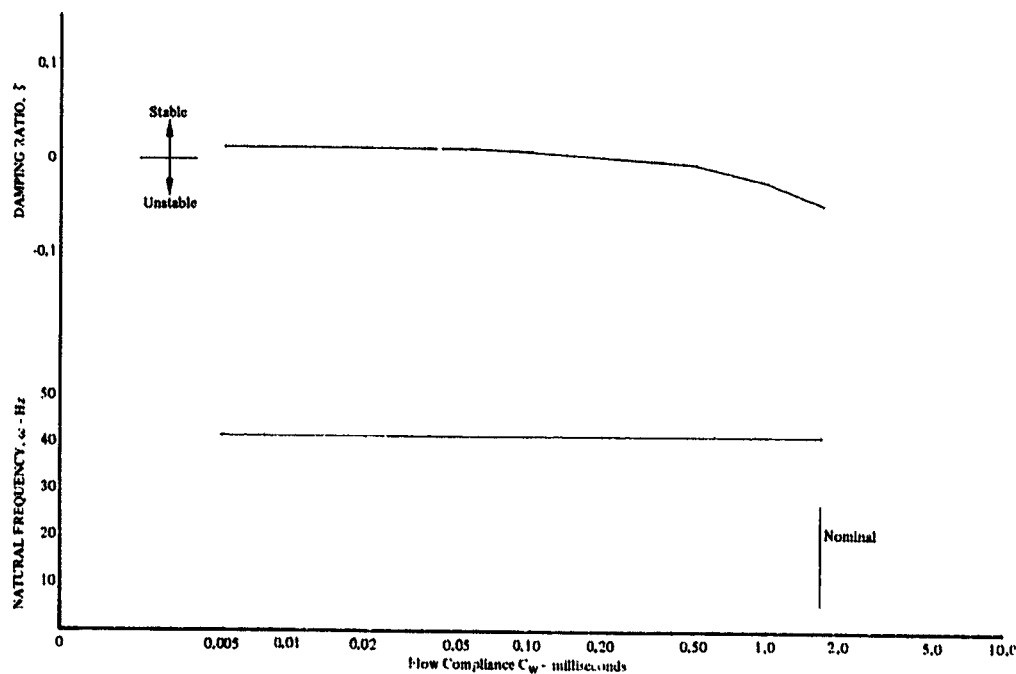


Figure 85. Effect of Flow Compliance on Oscillatory Predictions; Radial Leading Edge Inducer;  $\bar{\phi} = 0.084$ ,  $\bar{k} = 0.16$  DF 91017

#### 5.3.4.4 Inducer Pressure Gain ( $G_p$ )

Pressure gain is a measure of the change in inducer head rise with inlet pressure. The only area where pressure gain was sufficient to significantly affect predictions was in the head falloff area. It was therefore evaluated for flow coefficients of 0.090 and 0.070 at a cavitation number of 0.04. The sensitivity of oscillatory predictions to pressure gain in this area is shown in figure 86. The values of  $G_p$  for a  $\bar{k}$  of 0.04 and 0.031 are indicated on the curves for reference. An increase in pressure gain is equivalent to a reduction in cavitation number because the inducer head rise drops increasingly rapidly as cavitation number is reduced. As pressure gain is increased (cavitation number reduced), the model predicts a return toward stable operation. Frequency is predicted to decrease for  $\bar{\phi} = 0.090$  and to increase for  $\bar{\phi} = 0.070$ . Pressure gain is the parameter that causes the predicted damping ratio in figures 77, 78, and 79 to rise toward stable operation below  $\bar{k} = 0.04$ , a prediction that compared favorably with measured data.

Pressure gain has an overall stabilizing effect on ramping behavior of the test loop.

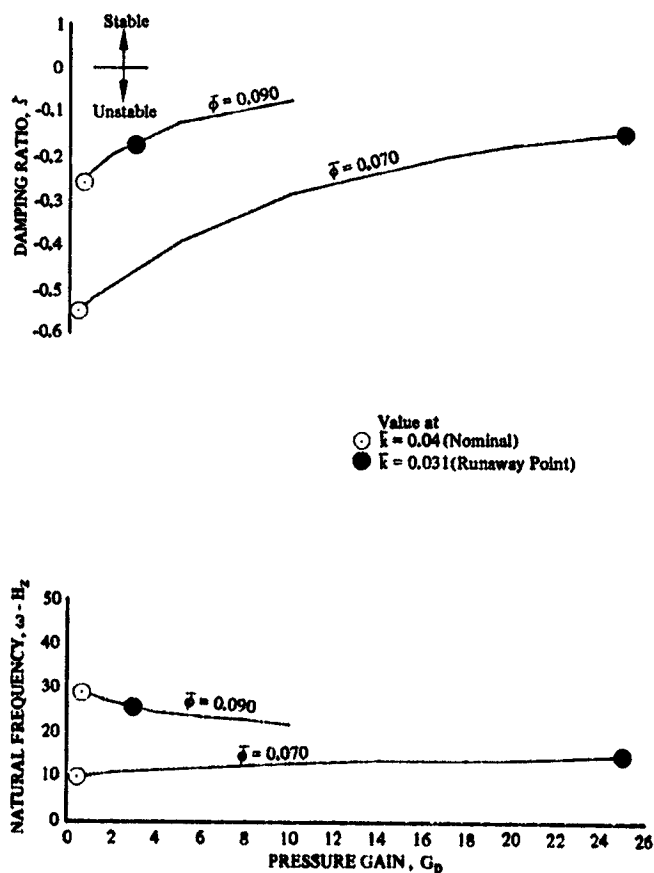


Figure 86. Effect of Pressure Gain on Oscillatory Predictions; Radial Leading Edge Inducer;  $\bar{k} = 0.04$

DF 91018

### 5.3.4.5 Flow Gain ( $G_w$ )

Flow gain is a measure of the change in inducer head rise with inlet flowrate. The effects of flow gain on system oscillatory behavior are shown in figure 87 for flow coefficients of 0.070 and 0.090, and a cavitation number of 0.04 and 0.031 are shown for reference. The curves show that flow gain has a relatively small effect on oscillatory damping ratio and frequency. Flow gain has a strong influence on ramping behavior, however, as shown in figure 88. The values of flow gain for the  $\bar{k} = 0.04$  and 0.031 points are indicated. As cavitation number is lowered from 0.04 to 0.031, flow gain decreases at  $\bar{\phi} = 0.070$  (and at 0.084, which is not shown) and increases at  $\bar{\phi} = 0.090$ . The increase in flow gain at  $\bar{\phi} = 0.090$  is sufficient to cause the model to predict a transition from stable to unstable operation. The decrease in flow gain with cavitation number at the other flow coefficients is stabilizing. This predicted behavior correlates with radial inducer test data where a ramping-type instability was observed for  $\bar{\phi} = 0.090$ , but not for other flow coefficients.

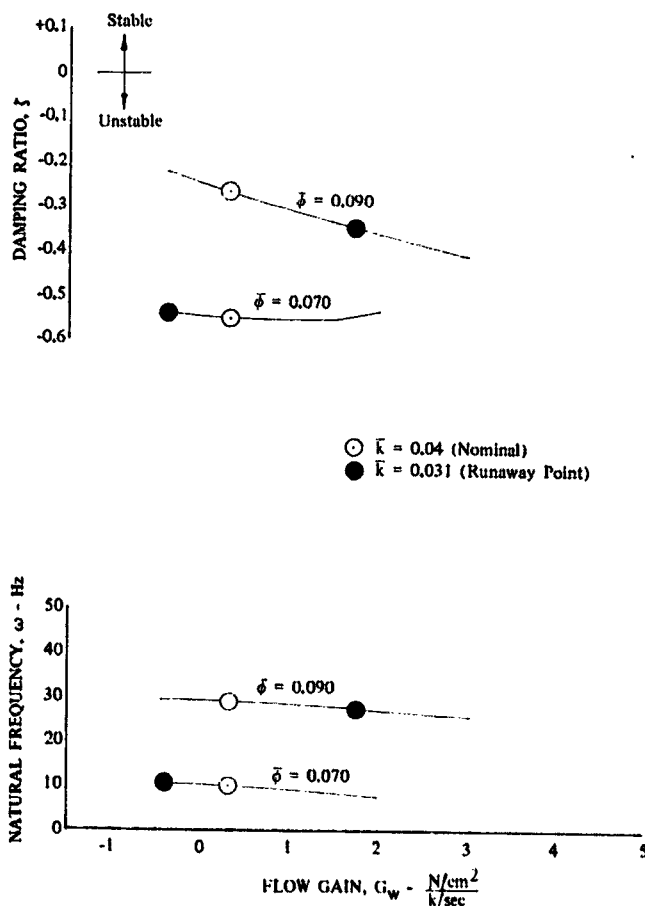


Figure 87. Effect of Flow Gain on Oscillatory Predictions; Radial Leading Edge Inducer;  $\bar{k} = 0.04$

DF 91208

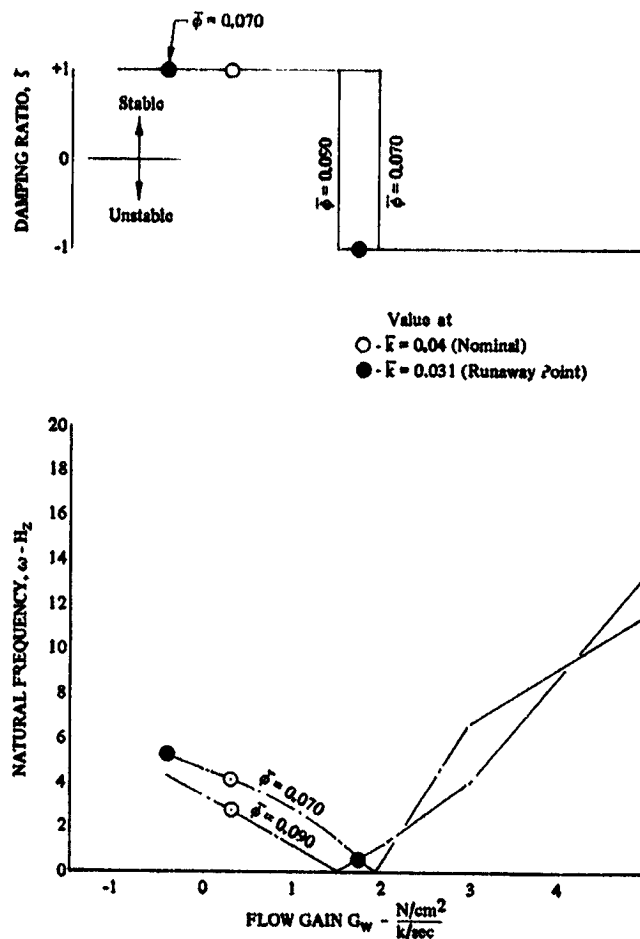


Figure 88. Effect of Flow Gain on Ramping Predictions; Radial Leading Edge Inducer;  $k = 0.04$

DF 91019

In spite for the stabilizing effect of flow gain at  $\bar{\Phi} = 0.070$ , a tendency toward a runaway instability below  $k = 0.04$  was predicted in figure 76. (The reduction in natural frequency indicates that the real root damping ratio is approaching a transition from +1.0 to -1.0.) The reason for the predicted tendency toward instability was that inducer head rise decreased below  $k = 0.04$ , which caused the control valve resistance ( $R_1$ ) and the inducer internal resistance to decrease. The decrease in  $R_1$  and  $R_p$  is a destabilizing effect for the runaway instability since it reduces system resistance and head required to maintain flow. This reduction makes it easier for head available to jump above head required and initiate an instability.

#### 5.3.4.6 Inlet Line Compliance ( $C_7$ )

The addition of inlet line compliance to the system model at a point some distance upstream of the inducer (location 7) is comparable to changing the model from a closed to an open loop, wherein the inlet line becomes more similar to an

engine inlet line. The effect of a high compliance (open loop) on damping ratio and natural frequency predictions is shown in figure 89. The solid line is the original prediction (with no air in the heat exchanger), and the dashed line is for high inlet line compliance. The prediction indicates that the transition from stable to unstable for the two systems would occur at approximately the same  $k$  ( $< 0.22$ ), but that the open loop would probably experience greater amplitudes. The damping ratios and natural frequencies shown in figure 89 are for the lowest frequency oscillatory root that showed significant change with cavitation number for each system. Unlike the closed-loop system, the next to lowest frequency root in the open-loop system (at high cavitation numbers) showed greatest change and became the lowest frequency root at low cavitation numbers.

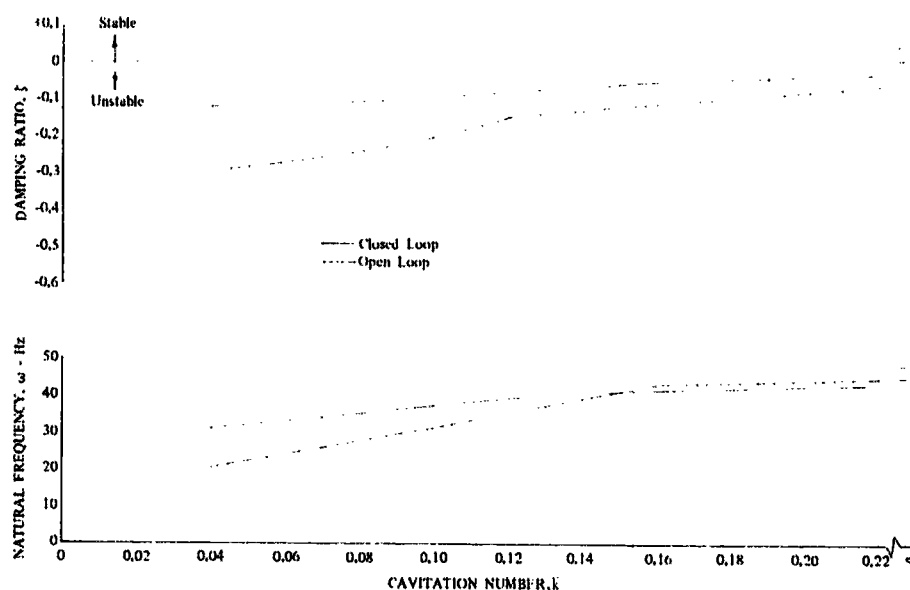


Figure 89. Effect of Inlet Line Compliance on  
Oscillatory Predictions; Radial Leading  
Edge Inducer,  $\bar{\phi} = 0.084$

DF 91264

#### 5.4 SIMPLIFIED INDUCER SYSTEM MODEL

A somewhat complex set of equations (12, 13, ---) was used to describe the inducer test loop in paragraph 5.3.1. This complexity resulted in accurate response predictions but, unfortunately, it also obscured the significance of the major parameters affecting stability. A simplified system model is described in this section to permit more apparent analytic interpretation of the roles played by pressure gain ( $G_p$ ), flow gain ( $G_w$ ), pump resistance ( $R_p$ ), pressure compliance ( $C_p$ ), and flow compliance ( $C_w$ ). The influence of the hydraulic system parameters, such as inlet line resistance ( $R_g$ ) and inertance ( $L_g$ ) and discharge valve resistance ( $R_1$ ), can also be easily interpreted.

The inducer test loop of figure 16 can be simplified by assuming that: a large supply tank exists at location 8; a large discharge tank exists at location 2; all compliances, except that due to cavitation, are negligible; and the discharge tank is sufficiently close to the inducer discharge to make any inertance between

the two negligible. The resulting simplified model is shown in figure 90 and can be described by:

1. Large supply tank maintained at constant pressure ( $p_g$ )
2. Rigid inlet line having resistance ( $R_g$ ) and inductance ( $L_g$ )
3. Cavitation cavity at inducer inlet having a total volume ( $V_c$ ) that is dependent upon the instantaneous values of inlet static pressure ( $p_g$ ) and inlet mass flowrate ( $W_g$ )
4. Inducer (or pump) turning at constant speed creating discharge static pressure ( $p_{10}$ ) that is dependent upon the instantaneous values of inlet static pressure ( $p_g$ ), inlet flowrate ( $W_g$ ), and discharge flowrate ( $W_9$ )
5. Rigid discharge line of negligible inductance containing a discharge valve with resistance ( $R_1$ )
6. Large discharge tank maintained at constant pressure ( $p_2$ ).

The linearized equations describing this system can be obtained from equations 12, 13, ---. With the simplifying assumptions these become:

$$\text{Inlet line: } \Delta p_g = -R_g \Delta W_g - L_g \dot{\Delta W}_g$$

$$\text{Continuity: } \Delta W_g - \Delta W_9 = -\rho \dot{\Delta V}_c$$

$$\text{Cavitation: } -\rho \dot{\Delta V}_c = C_p \Delta p_g + C_w \Delta W_g$$

$$\text{Performance: } \Delta p_{10} = G_p \Delta p_g + G_w \Delta W_g - R_p \Delta W_9$$

$$\text{Discharge line: } \Delta p_{10} = R_1 \Delta W_9$$

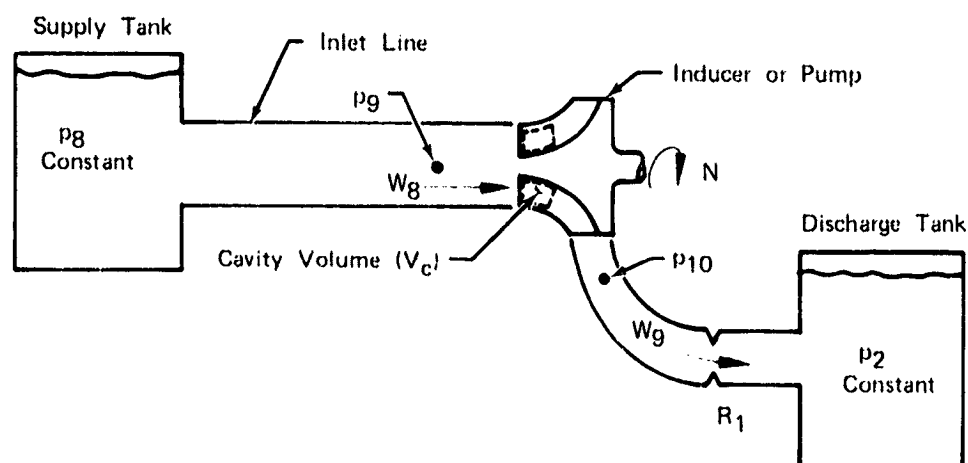


Figure 90. Simplified Inducer System Model

FD 63340

The eight constants in the above equations are represented graphically in figure 91. All constants are obtained from the known geometry and operating point; the steady-state head-flow, head falloff, and cavity volume maps; and the relationships of equations (17 and 27). Figure 91(a) is the conventional inducer head falloff map. Figure 91(b) is constructed from figure 91(a) by first plotting head falloff ratio ( $\lambda$ ) vs steady-state flowrate (W) for the operating point inlet pressure ( $p_g$ ) and multiplying by noncavitating pressure rise ( $P_{rnc}$ ). Figure 91(c) is constructed by multiplying the noncavitating head-flow map ( $P_{rnc}$ ) by the operating point head falloff ratio ( $\lambda$ ). Figures 91(d) and 91(e) are the predicted cavity volume maps. Figures 91(f) and 91(g) are predicted or measured static pressure drop curves for the inlet and discharge lines, respectively. Figure 91(h) is constructed from the known geometry of the inlet line. The terms  $(U_t \bar{\phi}/A_i)$  and  $(U_t \bar{\phi}/A_i)(A_i/A_d)^2$  in figures 91(b) and 91(c) result from the velocity heads at inducer inlet and discharge and the fact that the maps represent inducer total-to-total pressure rise while it is static pressure at inducer inlet and discharge that is used in the equations describing the system.

The five simplified system equations can be solved simultaneously to obtain the equation of motion for a typical parameter, such as cavity volume ( $V_c$ ):

$$\begin{aligned} &\{(R_p + R_1)L_8 C_p\} \ddot{\Delta V}_c + \{(R_p + R_1)(R_8 C_p - C_w) + G_p L_8\} \dot{\Delta V}_c + \\ &\{(R_p + R_1) + R_8 G_p - G_w\} \Delta V_c = 0 \end{aligned}$$

The condition for a cavitation-induced instability is easily seen through analogy with the spring-mass-damper system of figure 92. The equation of motion for such a system is:

$$M \ddot{X} + B \dot{X} + K X = 0$$

The following analogy between the inducer system and the spring-mass-damper system can be made:

$$\begin{aligned} \text{Mass:} & \quad M \sim (R_p + R_1)L_8 C_p \\ \text{Damper:} & \quad B \sim (R_p + R_1)(R_8 C_p - C_w) + G_p L_8 \\ \text{Spring:} & \quad K \sim (R_p + R_1) + R_8 G_p - G_w \end{aligned}$$

Either system will be unstable if the damper or the spring constant becomes negative. The model then indicates that a cavitation-induced instability will occur when:

$$C_w > R_8 C_p + \frac{G_p L_8}{R_p + R_1} \quad (32)$$

or when:

$$G_w > R_8 G_p + R_p + R_1 \quad (33)$$

Equation (32), involving cavity volume changes, represents the "continuity" mechanism of an instability, while equation (33), involving inducer performance, represents the "performance" mechanism mentioned in paragraph 3.1.

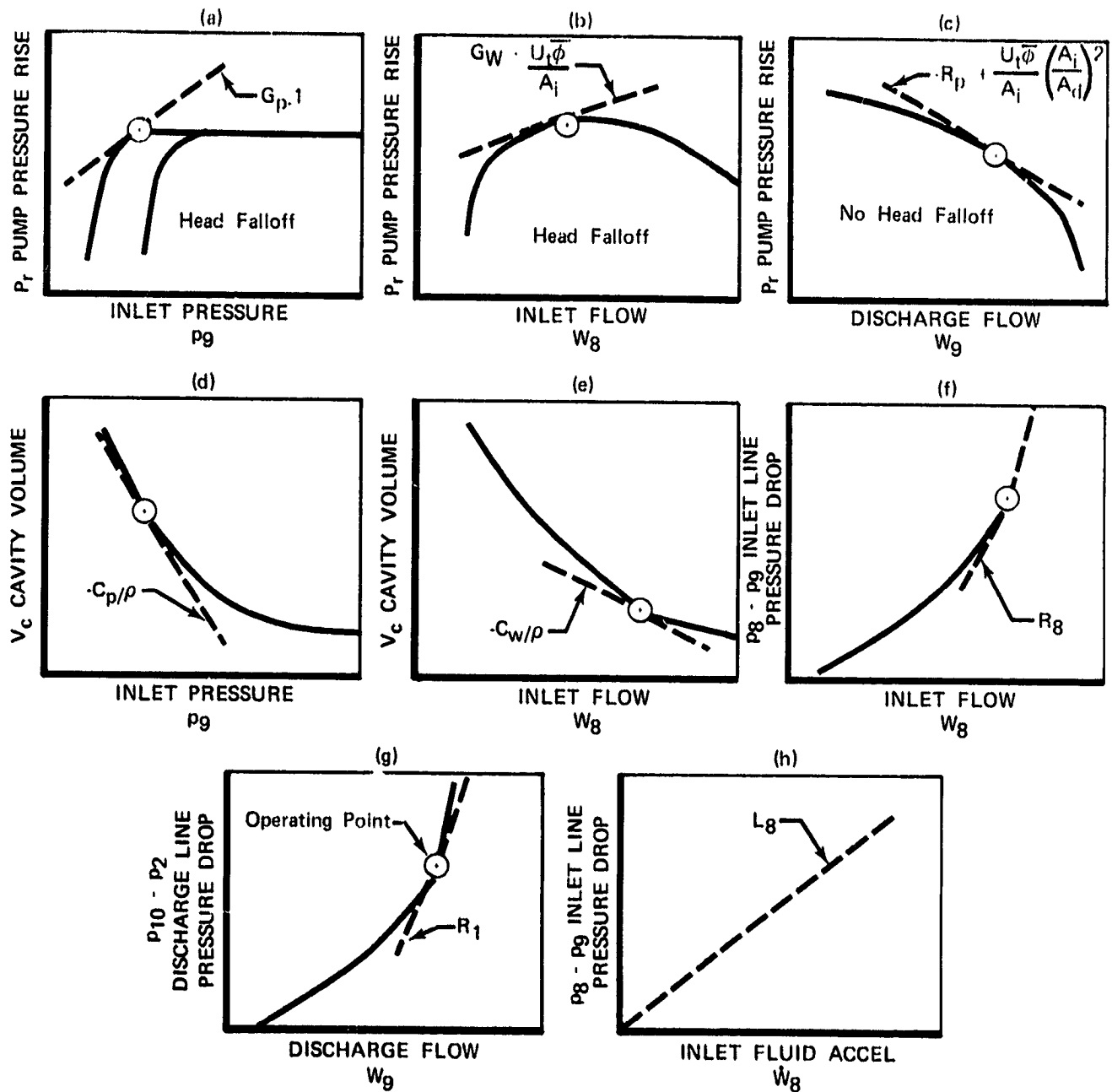
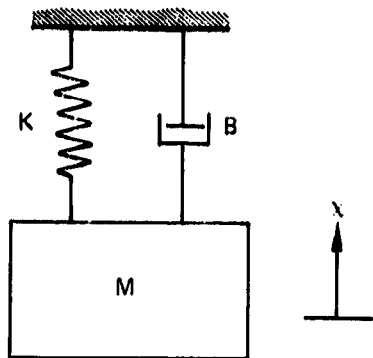


Figure 91. Graphical Representation of System Parameters

FD 63339



M = Mass  
 K = Spring Constant  
 B = Damper Coefficient  
 x = Position From Equilibrium

Figure 92. Spring-Mass-Damper System

FD 51471

Above head breakdown  $G_p = 1$  and  $G_w$  approaches zero. Equation (33) does not predict an instability, since  $(R_p + R_1)$  and  $R_8$  are positive numbers. However equation (32) predicts that an instability will occur if:

$$C_w > R_8 C_p + \frac{L_8}{R_p + R_1} \quad (34)$$

Both flow compliance ( $C_w$ ) and pressure compliance ( $C_p$ ) are zero under non-cavitating conditions. Since inlet line inertance ( $L_8$ ) is a positive number, we see that noncavitating flow is predicted to be stable, a necessary condition for an instability model. As cavitation number is lowered, both  $C_w$  and  $C_p$  increase (always positively). An instability starts when flow compliance ( $C_w$ ) reaches a value that satisfies equation (34). When cavitation number is lowered to the head breakdown point, pressure gain ( $G_p$ ) takes on a large positive value. Referring to equation (32), this is seen to be a stabilizing influence and explains why oscillations have generally been noted to disappear when head breakdown begins.

In the head breakdown region, flow gain ( $G_w$ ) can also take on large positive values. An instability related to inducer performance will start if  $G_w$  reaches a value that satisfies equation (33). This type of instability occurred in our tests, making it impossible to set a steady-state operating point.

Frequency of oscillation at the initial instant of the instability can be estimated as the system undamped natural frequency. By analogy to the spring-mass-damper system the natural frequency is:

$$\omega = \sqrt{K/M} = \sqrt{\frac{(R_p + R_1) + R_8 G_p - G_w}{(R_p + R_1) L_8 C_p}}$$

Since the operating point of interest is usually above head breakdown ( $G_p = 1$  and  $G_w$  approaches zero) and since inlet line resistance is usually negligible ( $R_8 = 0$ ), this reduces to:

$$\omega = \sqrt{1/L_8 C_p} \quad (35)$$

Comparing equation (35) with equation (34), with  $R_8 = 0$ , it can be seen that for a given pump (known  $R_p$ ) and given hydraulic system (known  $L_8$  and  $R_1$ ), flow compliance ( $C_w$ ) determines the operating point at which the instability starts, and pressure compliance ( $C_p$ ) determines the oscillation frequency. Thus, it is necessary to define inducer cavitation in terms of both flowrate and pressure.

The simplified system model qualitatively explains the occurrence of cavitation-induced instabilities and demonstrates that inducer cavitation and the hydraulic system in which the inducer operates are linked together to create the conditions under which an instability can occur. Both must be considered in an analysis of stability. The link also implies that stability can be achieved through changes to the hydraulic system as well as through changes to the inducer.

## SECTION 6 CONCLUSIONS AND RECOMMENDATIONS

### 6.1 CONCLUSIONS

- (1) A system model can explain the occurrence of self-induced instability in cavitating inducers and can be used to define stabilizing system changes. The model requires accurate definitions of inducer and system parameters in terms of resistance, inertance, and compliance. Frequency predictions are especially sensitive to pressure compliance.
- (2) Two mechanisms can cause inducer instabilities: (1) a "continuity" mechanism that is operable whenever flow-sensitive inducer cavitation is present; and (2) a "performance" mechanism that is usually operable only in the head breakdown region. Continuity instabilities are of primary interest because they can occur in the usual inducer operating region. Both instability mechanisms were observed and correlated satisfactorily with predictions in this program. Since blade suction surface cavitation is known to occur at inlet pressures well above those at which performance is affected, and this cavitation is inherently sensitive to flow perturbations, such cavitation is believed to be primarily responsible for "continuity" type instabilities. Tip clearance cavitation would contribute to "continuity" instabilities but the magnitude of the contribution is unknown. Tip clearance cavitation may also be stabilizing in overall effect if its sensitivity to flow is small relative to its sensitivity to pressure. This can only be proved by developing a tip vortex cavity model.
- (3) Predictions of conditions under which an instability may occur, the frequency of oscillations, and trends of the instability with changing conditions can be predicted with a linearized analysis. Predictions of amplitude and frequency after the start of oscillations would require an analog treatment of the nonlinear relationships. Both linear and analog analyses should be conducted to thoroughly define the instability, with the linear analysis being used to gain an appreciation of significant parameters and trends and the analog analysis to predict exact amplitudes and frequencies.
- (4) Cascade instabilities are also explainable through the use of a system model, but the test data generated in this program were inconclusive in that regard. The "performance" mechanism is believed to be the only operable mechanism in a two-dimensional cascade because incidence angle, which is analogous to inducer flow coefficient, would be constrained to a constant value, rendering the "continuity" mechanism inoperable. "Performance" type cascade instabilities require an inflection in the cascade loss vs inlet pressure relationship, and such an inflection was measured in this program.

### 6.2 RECOMMENDATIONS

- (1) A linearized model was used to generate predictions of operating conditions under which an instability would be expected and the trends of the instability with changes in the system and operating conditions. The model predicted the onset of oscillations at high cavitation numbers and

this was substantiated by test data. The measured amplitudes were relatively small, however, and did not increase appreciably until cavitation number was lowered a substantial amount. These low amplitudes may be quickly damped out and not cause any pressure oscillations in an actual engine system. It would be desirable, therefore, to generate instability frequency and amplitude predictions over the full range of cavitation number through the use of an analog model. We recommend that such an analog model of the inducer system be prepared and its predictions correlated with test data to further substantiate the modeling technique.

- (2) Experimental data that are available for substantiation of inducer blade suction surface cavity volume predictions are limited. Instability predictions are sensitive to the relationship of cavity volume to flowrate. Additional inducer tests and cavity model refinement effort are recommended to provide a more accurate, substantiated definition of suction surface cavity volume as a function of cavitation number and flow coefficient.
- (3) Tip clearance cavitation influences instabilities because of volume sensitivity to pressure and flowrate changes, but the magnitude of its effect is currently indeterminate. Analytical and experimental efforts to define these relationships is recommended.
- (4) Detailed model predictions have only been generated for the test loop system, and its general applicability to other systems and fluid should be demonstrated. At least one additional system in which instabilities have been measured should be modeled and the predictions correlated with test results.
- (5) Several system changes that appear to have a stabilizing influence have been identified in this program. These changes are tangential inlet flow injection, prewhirl inducing guide vanes, and added inducer inlet pressure compliance. Such changes should be further defined analytically and demonstrated systematically in a "baseline" system whose characteristics are well known. The objectives would be (1) to demonstrate that the changes resulted in the predicted stability trends and (2) to provide preliminary definition of inducer and/or system design changes that can be applied to obtain stability.

SECTION 7  
REFERENCES

- (1) "Study of Inducer Load and Stress," Final Report on Contract NAS3-11210, Volumes I and II, Pratt & Whitney Aircraft, NASA CR-72712, December 1970.
- (2) Wade, R. B. and Acosta, A. J., "Experimental Observations on the Flow Past a Plano-Convex Hydrofoil," Journal of Basic Engineering, March 1966, ASME Paper No. 65-WE-3.
- (3) Kaplan, P. and Lehman, A. F., "An Experimental Study of Hydroelastic Instabilities of Finite Span Hydrofoils under Cavitating Conditions," Oceanics Inc., Report No. 64-12, Contract NOns-88301, February 1964.
- (4) Besch, P. K., "Cavity-Induced Oscillation of a Two-Degree-of-Freedom Hydrofoil," ASME 1970 Cavitation Forum.
- (5) Wade, R. B. and Acosta, A. J., "Investigation of Cavitating Cascades," Journal of Basic Engineering, December 1967, ASME Paper No. 66-WA/FE-25.
- (6) Acosta, A. J. and Wade, R. B., "Experimental Study of Cavitating Hydrofoils in Cascade," NASA CR-95098, Final Report, Contract NAS NGR 05-002-059, February 1968.
- (7) Taylor, W. E., Murrin, T. A., and Columbo, R. M., "Systematic Two-Dimensional Cascade Tests, Volume I - Double Circular-Arc Hydrofoils," United Aircraft Research Laboratories, NASA CR-72498, Contract NAS3-4184, December 1969.
- (8) Acosta, A. J., "An Experimental Study of Cavitating Inducers," Second Symposium on Naval Hydrodynamics, Office of Naval Research, Dept. of the Navy, ACR-38, August 1958, also discussion by T. Iura, pg. 554.
- (9) Wood, G. M., "Visual Cavitation Studies of Mixed Flow Pump Impellers," Journal of Basic Engineering, March 1963, ASME Paper No. 62-Hyd-12.
- (10) Badowski, H. R., "An Explanation for Instability in Cavitating Inducers," ASME 1969 Cavitation Forum and author's reply to discussion in ASME 1970 Cavitation Forum.
- (11) Etter, R. J., "An Investigation of Tandem Row High Head Pump Inducers," Final Report, Hydronautics Inc., Technical Report 703-9, May 1970, Contract NAS8-20625.
- (12) Hartmann, M. J. and Soltis, R. F., "Observation of Cavitation in a Low Hub-Tip Ratio Axial Flow Pump," Gas Turbine Power and Hydraulic Conference, March 1960, ASME Paper No. 60-Hyd-14.

- (13) Hildebrand, A. G., "S-IVB Stage/J2 Engine POGO Testing," NASA MSFC IN-ASTN-TSJ-70-6, June 1970.
- (14) "Investigation of 17-Hertz Closed-Loop Instability on S-II Stage of Saturn V," Rocketdyne Report, Contract NAS8-19, August 1969.
- (15) Soltis, R. F., "Some Visual Observations of Cavitation in Rotating Machinery," NASA TN D-2681, July 1965.
- (16) Miller, C. D. and Gross, L. A., "A Performance Investigation of an Eight-Inch Hubless Pump Inducer in Water and Liquid Nitrogen," NASA TN D-3807, March 1967.
- (17) Yeh, H., "An Actuator Disk Analysis of Inlet Distortion and Rotating Stall in Axial Flow Turbomachines," Journal of the Aero/Space Sciences, November 1959.
- (18) Gross, L. A., "Oscillations Associated with Pump-Inducer Systems," Thesis for Master of Science in Mechanical Engineering, University of Alabama, 1966.
- (19) Stripling, L. B. and Acosta, A. .., "Cavitation in Turbopumps - Part 1," Journal of Basic Engineering, September 1962, ASME Paper No. 61-WA-112.
- (20) Sack, L. E. and Nottage, H. B., "System Oscillations Associated With Cavitating Inducers," Journal of Basic Engineering, December 1965, ASME Paper No. 65-FE-14.
- (21) "Study of Pump Discharge Pressure Oscillations," Rocketdyne Final Report, Contract NAS8-20143, October 1966.
- (22) Ghahremani, F. G., "Turbopump Cavitation Compliance," Aerospace Corp. Report No. TQR-0059 (6531-01)-2, September 1970.
- (23) "ICRPG Measurement Uncertainty Handbook for Liquid Rocket Engines," Pratt & Whitney Aircraft Report FR-2974B, April 1969.
- (24) Jakobsen, J. K., "Supercavitating Cascade Flow Analysis," Transactions of the ASME, Journal of Basic Engineering, (64-FE-11), December 1964.
- (25) Abbott, D. E. and Kline, S. J., "Experimental Investigation of Subsonic Turbulent Flow Over Single and Double Backward Facing Steps," Transactions of the ASME, Journal of Basic Engineering, September 1962.
- (26) "Study of Inducer Load and Stress," Final Report, Volume III, Pratt & Whitney Aircraft, NASA CR-72712, (In Preparation).
- (27) Murphy, R., "An Analytic Technique for Prediction of Pump Self-Induced Oscillation," Pratt & Whitney Aircraft Report FR-4444, March 1971.

APPENDIX  
NOMENCLATURE

Symbol	Definition	Unit
A	Cross-sectional area normal to cascade nozzle or inducer centerline	$L^2$
$\bar{A}$	Cascade nozzle mean cross sectional area $\left(\bar{A} = l_i / \int_0^{l_i} \frac{dx}{dA}\right)$	$L^2$
B	Damping coefficient	$FTL^{-2}$
b	Length of cavity collapse region	L
$C_{1...10}$	Compliance of inducer loop water and pipes	$MF^{-1}L^2$
$C_p$	Cavitation pressure compliance	$MF^{-1}L^2$
$C_w$	Cavitation flow compliance	$MM^{-1}T$
$C_{nc}$	Cascade noncavitating total pressure loss coefficient ( $C_{nc} = D_{nc}/q_i$ )	dimensionless
c	Length of cavity to point of maximum height	L
D	Cascade total pressure loss	$FL^{-2}$
$f_1, f_2, f_3$	Functions representing inducer head falloff, head vs flow, and cavity volume maps	
$G_p$	Pressure gain	dimensionless
$G_w$	Flow gain	$FL^{-2}M^{-1}T$
H	Total head	L
HI	Ideal Head	L
$H_r$	Total-to-total head rise	L
h	Maximum cavity height, step height, or static head	L
i	Fluid incidence angle	rad (deg)
K	Spring constant	$FL^{-1}$
k	Local or cascade cavitation number	dimensionless
$\bar{k}$	Inducer cavitation number based on average static pressure and tip relative velocity	dimensionless
l	Total length of cavity	L

Symbol	Definition	Unit
$l_i$	Cascade nozzle length	L
L	Fluid inertance of cascade inlet nozzle or inducer loop	$FL^{-2}M^{-1}T^2$
M	Mass	M
N	Rotative speed	$T^{-1}$
$P_r$	Inducer total-to-total pressure rise	$FL^{-2}$
p	Static pressure	$FL^{-2}$
Q	Volume flowrate	$L^3T^{-1}$
q	Fluid velocity pressure	$FL^{-2}$
$R_{1...10}$	Static-to-static resistance of inducer loop	$FL^{-2}M^{-1}T$
$R_c$	Cascade internal resistance	$FL^{-2}M^{-1}T$
$R_p$	Inducer internal resistance	$FL^{-2}M^{-1}T$
$R_i$	Cascade nozzle resistance	$FL^{-2}M^{-1}T$
S	Laplace variable	--
s	Inducer or cascade tangential blade spacing	L
$U_t$	Inducer tip speed	$LT^{-1}$
V	Fluid absolute velocity (Assumed axial at inducer inlet)	$LT^{-1}$
$V_c$	Total cavity volume	$L^3$
W	Mass flowrate	$MT^{-1}$
X	Coordinate along cascade nozzle centerline or of oscillating mass	L
$\beta$	Angle of characteristic equation root in the complex plane, or flow angle from axial	rad (deg)
$\delta_w$	Angle of cavity collapse	rad (deg)
$\Delta$	Denotes linear perturbation about steady-state operating point	
$\bar{\phi}$	Inducer inlet flow coefficient ( $\bar{\phi} = V_z/U_t$ )	dimensionless
$\zeta$	Damping ratio	dimensionless

Symbol	Definition	Unit
$\omega$	Undamped natural frequency	$T^{-1}$
$\rho$	Fluid density	$ML^{-3}$
$r$	Inducer normal blade spacing or step separation passage height	L
$\lambda$	Ratio of inducer head rise to noncavitating head rise or cascade pressure loss to noncavitating pressure loss	dimensionless
$\bar{\psi}$	Inducer average head rise coefficient ( $\bar{\psi} = g\bar{H}_r/U_t^2$ )	dimensionless

Superscripts:

-	Average value
'	Relative to inducer

Subscripts (unless otherwise indicated):

d	Condition at cascade or inducer discharge
h	Condition at inducer hub
i	Condition at cascade or inducer inlet
n	Condition at cascade nozzle inlet
nc	Noncavitating value
t	Condition above free surface in cascade plenum tank or condition at inducer tip
u	Component in tangential direction
v	Vapor pressure
z	Component in axial direction
1, 2, 3... 10	Condition at station in inducer loop